On the Use of Swept Frequency Alternating Current Potential Difference Method and Skin Effect to Detect Feature Geometry in Flawed Conductors

YUQIAN SI, BENG. (HONS)

March 2023

Abstract

In many engineering situations, the unavoidable occurrence of cracks compromises the integrity of the structural components and poses a threat to safety. Reliable identification of cracks is the prerequisite of structural integrity assessment and enables the accurate prediction of the service lifetime of components. Among the various technologies developed for non-destructive testing, potential difference (PD) methods have gained wide acceptance due to the easy implementation and the ability to provide accurate and continuous detection of cracks. PD methods rely on the principle that the resistance of a conductor containing a feature increases as the crack propagates. Depending on the type of operating current, PD methods are recognised as direct current potential difference (DCPD) and alternating current potential difference (ACPD). Compared with direct current distributed on the whole cross-section of the conductor in DCPD, alternating current (AC) in ACPD is confined to a narrower layer beneath the conductor surface, i.e. skin effect. Therefore, ACPD requires a lower excitation current yet is able to achieve higher sensitivity in detecting cracks especially near conductor surfaces.

Given constant material properties and measurement distances, DC resistance of a cracked conductor is solely determined by the cross-sectional area of the crack, i.e. DCPD is only able to identify the cross-sectional area, without offering other information such as the geometry and depth of crack. In contrast, ACPD results are determined by multiple factors including the frequency and crack geometry due to the fact that AC delineates the crack edge (or part of the edge) by taking advantage of the skin effect. The potential of ACPD methods in identifying cracks by utilising the skin effect, especially different cracks with the same cross-sectional area (beyond the capability of DCPD), has been investigated. In this work, swept frequency AC was supplied in experiments to obtain abundant ACPD results in a wide frequency range. The overall behaviour of ACPD results with swept frequencies were used to identify cracks. The primary aim was to validate and comprehend the capability of the swept ACPD method in detecting and distinguishing, firstly the shapes of the conductors with the same cross-sectional area (no crack-like feature), and secondly cracks/features with different opening geometries (i.e. widths) on the external surfaces and depths inside the conductors.

The first part of the investigation were focused on four samples made of non-magnetic material with the same gauge dimension and of different cross-sectional shapes. In the second part, five different features were manufactured at uniform

locations of five samples made of ferromagnetic material and with the same dimension to simulate cracks. AC and PD signals were input and measured from uniform positions on all the samples. Measured signals in the time interval were then converted to results in the frequency domain by the use of a MATLAB script. The detection capability of the ACPD method was investigated upon the performance of two types of processed results in the frequency range: PD measured from the uniform positions and internal impedance further calculated from processed results of AC and PD. Experimental methodology, particularly the reliability of the data processing, were validated by conducting several preliminary experiments.

Furthermore, the electromagnetic models of the ACPD samples have been approximated by a theoretical methodology involving several established theories and the numerical methodology of finite element analysis (FEA) via ANSYS. Several theoretical frameworks based on distinct principles were used to calculate internal impedance of the non-magnetic samples of various cross-sectional shapes. Finite element (FE) models were created to simulate the current distributions on the four cross-sectional shapes and around the five features. Internal impedance of the four non-magnetic samples approximated by FE models were compared with theoretical solutions to assess the reliability of the theories and evaluate the precision of FEA. Subsequently, FEA was used to approximate PDs from the uniform measurement path to compare with experimental results, and hence analyse the detection capability of the ACPD method. Moreover, FEA was applied to measure PDs from paths in the vicinity of the measurement path to provide error bars covering possibly measurement uncertainties in experiments. Eventually, the approximated current distributions (and electric fields) were employed to comprehend and elucidate the conclusions obtained from the experiments and FEA.

The swept ACPD method has been demonstrated by FEA to have the capability to distinguish between different cross-sectional shapes of non-magnetic conductors with the same cross-sectional area. The capability is attributed to the current crowding which refers to the current localisation around edges of conductors with polygonal cross-sections. The current crowding is apparent on the surfaces of non-magnetic conductors and shows an increasing intensity as the cross-sectional shape varying from circular to triangular. For the non-magnetic (SS316) samples with the same gauge size of 55 mm $\times$ 100 mm^2, PDs measured from the uniform positions on FE models of circular and triangular cross-sectional shapes reach 0.22 mV and 0.39 mV at 300 kHz (i.e. difference of 77%), respectively. However, this finding is only supported by FEA but has not been observed in experiments due to measurement uncertainties. This motivates the use of ferromagnetic conductors in feature detection experiments to reduce the effect of current crowding on surface measurements, i.e. the impact of measurement uncertainties on experimental results. Experimental results measured from the featured ferromagnetic samples show distinct differences between different features, which agrees well with FEA results. For example, PDs measured from the uniform positions on ferromagnetic

(EN1A) samples across three features, which have the same cross-sectional area of 9 mm^2 and various opening widths of 0.11, 0.21, and 0.42 to the sample size, reach 0.47, 0.72, and 1.08 mV at 50 kHz, respectively. This is due to the varying disturbances of different opening widths of features on the current distribution (or skin effect) around the features. Narrow openings lead to shallow current distributions, while wide openings result in deep penetration of current.

The present work has demonstrated the potential of the ACPD method in identifying surface features within ferromagnetic materials, which relies on the impact of the feature opening widths on the resulting current distributions. Future work may look to quantify the capability/limitation of the detection capability, for example, by constructing a current attenuation equation relating the current density along the feature depths to parameters of feature openings including dimensions, shapes, and positions. This may be used to determine the maximum detection depth of the ACPD method in identifying cracks/features with certain openings. Any situations within the detection region, e.g. unexpected propagating profiles and shorter depths (shorter than the maximum detection depths), may be detected by contrasting measured PDs with results predicted by the current attenuation equitation.

Acknowledgements

Contents

Nomenclature

Symbols

General

$\mathbf{A}$	Magnetic Vector Potential
$\mathbf{B}$	Magnetic Field Intensity
$\mathbf{D}$	Electric Flux Density
$\mathbf{E}$	Electric Field Intensity
f	Frequency of Signal
f_s	Sampling Frequency
$\mathbf{H}$	Magnetic Field Intensity
I	Total Current
I_{tol}	Determined Tolerance Value for Current Bands in Data Processing Script
J_0	Current Density at Conductor Surface
$\mathbf{J}$	Current Density Field
k_{xy}	Slope of Segments xy on Current Bands in Data Processing Script
L_{ac}	Internal Inductance at High Frequency
L_{dc}	Internal Inductance at Low Frequency
L_{ext}	External Inductance
L_{ind}	Known Inductance of Preliminary Inductor
L_{tol}	Total Inductance
p_{sim}	Parameter of Principle of Similitude
R_{ind}	Measured Resistance of Preliminary Inductor
R_{res}	Known Resistance of Preliminary Resistor
R_{ac}	Alternating Current Resistance at High Frequency
$\frac{R_{ac}}{R_{dc}}$	Resistance Ratio
R_{dc}	Direct Current Resistance at Low Frequency
R_k	Ratio between Two Segment Slopes in Data Processing Script
t	Time
V	Scalar Electric Potential/Steady Electrical Potential Field
$|Z|$	Modulus of Impedance
Z_{ser}	Total Impedance of Series Combined Resistor-Inductor Circuit

Z_{int}	Internal Impedance of Conductor
$Z_{int,ac}$	Internal Impedance of Conductor at High Frequency
$Z_{int,dc}$	Internal Impedance of Conductor at Low Frequency
Z_{par}	Total Impedance of Parallel Combined Resistor-Inductor Circuit
δ	Skin depth/Depth of Current Penetration
ϵ	Magnetic Permittivity of Conductors
θ	Phase Angle of Signal
θ_Z	Phase Angle of Impedance
μ	Magnetic Permeability of Conductors
ρ	Volume Density of Free Charge
σ	Electric Conductivity of Conductors
Φ	Magnetic Flux
ω	Angular Frequency

Calibrations of Potential Difference Methods

a	Depth of Propagating Crack Including Initial Notch
a_0	Initial Depth of Notch
c	Coordinate Proportionality Factor in Johnson's Formula
D_I	Distance between Current Input and Output Leads
D_V	Distance between Potential Difference Measurement Leads
L	Length of Specimen
r	Radius of Cylindrical Specimen
T	Thickness of Specimen
$u_0(a)$	Elliptic Coordinate at Slot Boundary in Johnson's Formula
$u_1(a)$	Elliptic Coordinate at measurement position in Johnson's Formula
V	Potential Difference across Propagating Crack
V_N	Normalised Potential Difference Excluding Measurement Uncertainty
V_0	Potential Difference across Initial Notches
W	Width of Specimen
Φ	Scalar Electric Potential Function
Ψ	Scalar Current Function

Theoretical Methodology for Internal Impedance

a_0	Side Length of Polygonal Cross-section
a_s	Side Length of Subsection
d, D	Geometric Mean Distance between Two Observation Positions
$F(f)$	Frequency-related Term in K_{cc}
$\mathbf{G}$	Distance/Geometric Matrix Representing Cross-sectional Shape

i	Fractional Current of Individual Subsection
$\mathbf{I}_p$	Eigenvectors of Matrix Equation in Modal Network Theory
$\mathbf{J}$	Current Matrix
J_{imp}	Impressed Current Density
$\mathcal{J}_0$	Zero-order Bessel Function
$\mathbf{K}$	Constant Matrix relating to J_{imp}
K_{cc}	Current Crowding Factor
K_{se}	Skin Effect Factor
l	Fractional Inductance of Individual Subsection
$\mathbf{L}$	Inductance Matrix
m_p	Time Constant in Modal Network Theory
n	Number of Corners of Polygonal Cross-section
N	Number of Subsections
$\mathcal{N}_0$	Zero-order Neumann Function
r	Fractional Resistance of Individual Subsection
r_0	Radius of Circular Cross-section/Effective Radius of Polygonal Cross-section
$\mathbf{R}$	Resistance Matrix
S_0	Area of Polygonal Cross-section
S_{ac}	Effective Area of Polygonal Cross-section at High Frequency
$\mathbf{U}$	Unit Matrix
w_1, w_2	Side Lengths of Rectangular Cross-section
x_{se}	Asymptotic Coefficient of Skin Effect in Payne's Equation
$\boldsymbol{\alpha}_p$	Average Component Value in Modal Network Theory
$\boldsymbol{\gamma}$	Eigenvalues of Matrix Equation in Modal Network Theory
θ	Interior Angle of Polygonal Cross-section
Ω	Frequency-dependent Term in Modal Network Theory
$\boldsymbol{\Omega}_p$	Normalised Characteristic Frequency in Modal Network Theory

Abbreviations

2D	Two-dimensional
3D	Three-dimensional
AC	Alternating Current
ACFM	Alternating Current Field Measurement
ACPD	Alternating Current Potential Difference
CC	Corner Crack
CCMM	Crack-current Modification Method
COD	Crack Tip Opening Displacement
CS(T)	C-shaped Tension
CSMR	Constant Slope Ratio Method in Data Processing

C(T)	Compact Tension
DC	Direct Current
DCB	Double-cantilever Bending
DCPD	Direct Current Potential Difference
DC(T)	Disc-shaped Compact Tension
DEN(T)	Double-edge Notched Tension
EAM	Effective Area Method for Internal Impedance
emf	Electromotive Forces
EN1A	EN1A Mild Steel
error bars I	Error Bars of Potential Difference Covering Uncertainty in Measurement Locations
error bars II	Error Bars of Potential Difference Covering Uncertainty in Measurement Distances
FATT	Fracture Appearance Transition Temperature
FE	Finite Element
FEA	Finite Element Analysis
FFT	Fast Fourier Transform
MNT	Modal Network Theory for Internal Impedance
Mode I	Cracks Propagated under Tension
Mode II	Cracks Propagated under In-plane Shear
Mode III	Cracks Propagated under Out-plane Shear
M(T)	Middle Tension
NDT	Non-destructive Testing
Path-x	Path at x mm to Edge and in 2 mm of Distance on Finite Element Model
Path-Dis-y	Path at 0.8/4.2 mm to Edge and in $2y$ mm of Distance on Finite Element Model
PD	Potential Difference
PS	Partial Symmetrical
R-L	Resistor-Inductor Combined
SEN(B)	Single-edge Notched Bend
SEN(T)	Single-edge Notched Tension
SM	Superposition Method
SSC	Stress Corrosion Cracks
SS304	304 Stainless Steel
SS316	316 Stainless Steel
TMF	Thermo-mechanical Fatigue
WOL	Wedge Opening Loaded

Chapter 1

Introduction

1.1 Background

Technology in several industries, notably power generation, aerospace, and energy storage, is rapidly evolving in response to various societal pressures. Underpinning these developments is a fundamental requirement to understand various aspects of engineering science. Improving the prediction of material failure is critical if component effectiveness is to be maximised and the development of novel testing techniques and component assessment/design procedures is therefore vital if technologies are to remain viable and competitive in the marketplace. In short, there continues to be a necessity for a greater understanding of how components behave and fail in service, in order to achieve the optimal design, and higher mechanical demand on the materials from which they are made (e.g. strength maintenance at increased temperatures), for greater efficiency. There is much technical work to do in order to ensure that these services continue to be available in a sustainable and environmentally and financially viable manner into the future.

Concepts and methodologies, such as fracture mechanics [1], are well established in the lifing of components containing cracks propagating due to loading conditions such as creep, mechanical fatigue, thermal fatigue, corrosion fatigue, erosion damage, etc. Values of stress intensity factors can be used to determine when a crack of known geometry will become critical and cause failure of the component in which it resides. However, as stated, this requires the geometry, which may be developing and coarsely approximated in calculations, to be known. The determination of crack geometry is a complicated task and due to limitations in current capabilities, measurements/predictions are usually associated with considerable levels of uncertainty. As a result, if a component is predicted to be serviceable for a life, it is not inconceivable that a 50% safety factor will be applied to this, in order to compensate for the uncertainty. The capability of accurate, in-situ, non-destructive determination of crack geometry is therefore an important challenge faced by engineers today and is the subject of significant ongoing research activity [2–21].

Non-destructive testing (NDT) is widely performed to detect and size cracks (e.g. without visual access) and assess the remaining service lifetime of structural components without causing additional damage to the components. One of the most favoured techniques developed for NDT are the potential difference (PD) methods, which are divided into alternating current potential difference (ACPD) and direct current potential difference (DCPD) based on the current injected. For decades, ACPD has been widely accepted to detect crack initiation and monitor crack growth due to the advantages of giving continuous measurements and providing the high sensitivity resulting from the skin effect.

1.2 Objectives

The primary aim of the present work was to investigate the capability of the swept frequency ACPD method in detecting the shapes of plain conductors and identifying the features of various geometries and depths. It was achieved by several objectives:

- The application of swept ACPD experiments on various conductors, including the plain and featured samples, by utilising the experimental system developed by Buss et al [2] to inject alternating current (AC) with rapidly varying frequency and measure signals in a wide range of swept frequencies.

- The data processing of experimental signals, converting signals in a time interval into individual periods of signals in the frequency domain. Processed results such as PD and impedance will be presented against the swept frequencies to visually demonstrate the differences in ACPD results between the samples.

- The verification of the ACPD experiments by comparing processed results with theoretical solutions obtained from established theories and numerical approximations based on finite element analysis (FEA).

- The investigation of this capability which will include the sensitivity, limitations, and the principles related to current distributions through experimental, numerical and theoretical methodology.

1.3 Thesis Layout

A literature review is presented in Chapter 2 to provide readers with a comprehensive background of available NDT techniques, especially PD methods, electromagnetic fields within conductors carrying AC, and investigations into the skin effect problem for individual conductors obtained over decades. The first part of the chapter about PD methods has been published as a review [22].

Established theories of the skin effect problem are mainly focused on solving internal impedance (Z_{int}) and AC resistance (R_{ac}) of individual and straight conductors of various shapes. Some of the theories reviewed in Chapter 2 are further demonstrated and applied to calculate Z_{int} for the plain experimental samples in Chapter 3, which offers rudimentary understating of ACPD results for these samples.

Experimental research in the project are divided into two parts, the preliminary and formal stages. Preliminary experiments were applied to simple circuits and conductors whose Z_{int} are known or have available theoretical solutions. Formal experimental samples consisted of four plain samples made from non-magnetic 316 stainless steel (SS316) and five featured samples made from ferromagnetic EN1A mild steel (EN1A), sharing the same gauge dimensions of 55 mm $\times$ 100 mm^2. The SS316 samples are of different cross-sectional shapes of circular, hexagonal, square, and triangular. The EN1A samples were manufactured with different features including a cylindrical drill and rectangular notches with opening widths varying from 1.5 mm to 6 mm. ACPD signals of all preliminary and formal samples were measured by the use of the same equipment and then processed by a MATLAB script to obtain results of PD and Z_{int} in the frequency domain. Chapter 4 introduces experimental methodologies, including the experimental apparatus, the sample information, and the data processing script.

It will be discussed later that ACPD signals measured in experiments can not be used to calculate 'real' Z_{int} of the samples since the current are unevenly distributed on the sample surfaces and localised around edges and features. Therefore, analysis of ACPD results are focused on the processed results of PD rather than Z_{int}. Finite element (FE) models were developed via ANSYS to simulate the current distributions around the formal samples at some frequencies and provide approximations of PD to compare with processed results. In additional, Z_{int} of the formal samples were measured from FE models to compare with theoretical solutions obtained in Chapter 3, and thus to estimate the reliability of several theories and FEA. Chapter 5 discusses approaches of creating models, techniques of reducing model sizes, mesh refinement studies, and methods of post processing. Moreover, FEA was carried out to investigate effects of uncertainties in the welding positions of the current injection wires on ACPD measurements, which is also presented in Chapter 5.

In Chapter 6, processed results of PD and Z_{int} for the preliminary and formal samples are compared with manually measured results and theoretical values (the latter is only available for preliminary samples) to assess the performance of the ACPD experiments and the data processing. Finally, Chapter 7 analyses processed results of PD for all formal (i.e. plain and featured) samples. The sensitivity of the ACPD experiments and the capabilities of the technique in detecting sample cross-sectional shapes and feature geometries are evaluated by comparing processed results with FEA. Furthermore, Chapter 7 discusses the principles of

such capabilities of the ACPD method by relating the differences in ACPD results between the samples to the current distributions approximated by FEA.

Chapter 2

Literature Review

2.1 Introduction

There are several NDT methods available, including optical [23], compliance [24, 25], ultrasonic [26,27], acoustic emission [28–30], eddy current [29–31], alternating current field [32–35], DCPD [35,36], and ACPD [37] methods. All have associated advantages and disadvantages. PD methods possess many benefits as well as much potential for future development and it is for this reason that the current work focusses on the current status and use of such technologies.

Review papers have been produced by leaders in the field which extol the merits and the state-of-the-art of NDT techniques, including PD systems development and usage. An early comparison of DCPD and ACPD was given by Wei and Brazil [38] who described the how electrical signals could be used for monitoring subcritical crack growth and the calibration of the signals generated with crack length. Some benefits and drawbacks of the use of direct current (DC) or AC were also discussed. This was followed by more comprehensive reviews of the use of DCPD and ACPD for monitoring the growth of defects in components [39, 40] and reviews specifically relating to the modelling aspects of NDT, including PD [29, 30]. Later, a further review for the use of specifically ultrasonic and PD techniques for monitoring secondary and tertiary stages of creep damage was given [41]. The latest of these topic specific reviews was published almost a decade ago, highlighting the need for this review. Given in the first part of the chapter is a comprehensive review, including updates since previous reviews, of the use of PD across all loading types (creep, fatigue, for example), including both experimental and modelling aspects. This part have been published as a review paper in [22]. Furthermore, the chapter will discuss the electromagnetic fields generated in conductors carrying time-varying current, as the background for the ACPD experiments. The final section will present a review of the research progress in the field of Z_{int} of conductors in recent decades.

Several laboratory specimen types are referred to throughout this chapter. These specimen types are summarised in Fig. 2.1 and will be referred to in the

subsequent sections of the review.
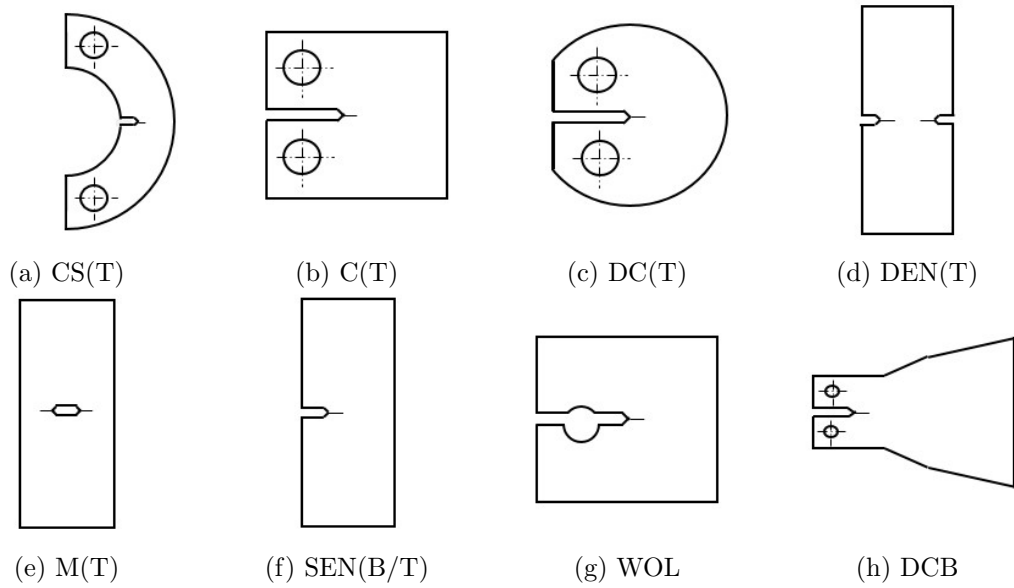
Figure 2.1: Schematics of standard fracture specimens: (a) C-shaped tension. (b) Compact tension. (c) Disc-shaped compact tension. (d) Double-edge notched tension. (e) Middle tension. (f) Single-edge notched bending/tension. (g) Wedge opening loaded. (h) Double-cantilever bending.

2.2 Non-Destructive Testing Techniques for Crack Measurement

Within many industrial sectors (examples include energy generation, aerospace, automotive, etc.), the accurate prediction of lifetime of damaged components has been recognised as an important issue. Modelling efforts require experimental data for calibration/validation and, in this field, this typically requires the detection of crack initiation (in both spatial and temporal dimensions) and measurements of crack growth. Several NDT methods are currently available for crack growth monitoring, including optical observation, compliance methods, sonic methods (involving ultrasonic and acoustic emission), eddy current methods, alternating current field measurement (ACFM) methods, and PD methods. In the interest of completeness, a brief review of several NDT methods are presented as alternatives of PD methods.

2.2.1 Optical

Optical observation methods, in which the fracture surface is marked or the crack tip extension is tracked by a travelling telescope [23], provide accurate predictions

6

of crack lengths but are restricted by visual access [23, 42–48]. Continuous monitoring is infeasible [42–45, 48] and the accuracy is highly dependent on operator skill [16, 23, 44] and image quality [16].

2.2.2 Compliance

Compliance methods, based on the relationship between crack length and the resulting strain, have been widely used for monitoring long cracks but lose sensitivity for small cracks [23–25]. When using compliance methods, periodic unloading at regular crack growth intervals is applied to the specimen and measurements are recorded discretely. For this reason, these methods are not applicable for testing under dynamic or rapid loading [5, 49, 50]. Moreover, the methods are limited for applications of aggressive environments such as creep, corrosion and high temperature (higher than 175 °C according to [49]) [5, 49, 51, 52]. The infeasibility at high temperature is presumably due to the lack of available displacement gauges and the potential influence of stress relaxation at crack tip during unloading [5]. Simultaneous applications of compliance methods and PD methods to crack growth measurement under fatigue have been reported in several studies, with poorer reproducibility and resolution found for compliance methods [12, 25, 53].

2.2.3 Ultrasonic

In ultrasonic testing, an ultrasound wave is transmitted by a transducer placed on the test-piece with part of this wave being reflected due to discontinuities within the material. This part of the wave is collected by a receiver and analysed in order to interpret the flaw [26, 27]. Difficulties in applications of ultrasonic methods arise in high temperature environments [23, 41] (or high temperature transducers must be used [54]), crack curvatures, and certain specimen geometries such as SEN(B) and DCB specimens [23] (schematics of specimens are shown in Fig. 2.1f & 2.1h).

2.2.4 Acoustic Emission

In applications of acoustic emission methods, release of elastic strain energy in the form of sound waves due to crack extension is measured and related to crack growth behaviour [28–30]. The methods are suitable for continuous monitoring such as in manufacturing and in service [29, 30] but disadvantages lie within the difficulties of calibration and interpretation [48], noise rejection and obtaining detectable signals from low strength materials [28].

2.2.5 Eddy Currents

Eddy current methods entail a current-carrying coil being placed on the surface of a conductive specimen, consequently inducing eddy currents in the specimen

beneath the surface that will affect the impedance of the exciting coil. Defects in the specimen are interpreted by measuring variations in this impedance [29–31]. Eddy current methods have received wide acceptance and are well suitable for surface defect detection [31, 48, 55] but are limited to conductive materials and inapplicable to large crack lengths (due to the limited penetrating depth of eddy current, i.e. skin effect, that will be explained in Section 2.3.1) [29, 30]. Moreover, eddy current methods suffer incapability to ferrous metals due to their dependence on magnetic permeability [56].

2.2.6 Alternating Current Field Measurement

In order to overcome some of disadvantages of the ACPD method (e.g. such as stray PD signals due to impedance of the electrical circuit), the ACFM method has been developed. Within ACFM, an AC-field distribution (above the surface of the specimen) containing perturbations due to defects is measured with effectively eliminated spurious voltages by the use of a Crack Microgauge and the crack size is derived by comparing the results to numerical models of the electromagnetic field [32–35]. The together use of physical measurement and filed modelling allows the exclusion of calibration procedure, which minimises possible errors occurring during calibration activities applied by other NDT methods [32–34, 39]. Inverse problems associated with crack profile determination have been solved with numerical iterative procedures [57]. With respect to small crack sizing ability, it has been reported that ACPD was preferred in monitoring long shallow surface cracks but lost accuracy in cases of deep surface cracks that could be accurately predicted by ACFM [32].

2.2.7 Potential Difference

According to [31, 58, 59], Gille [60] has pointed out that the DCPD method was first applied to detect surface cracks by Trost in 1944 [35] but the concept was first mentioned several years earlier by B. M. Thornton and W. M. Thornton in 1938 [61]. Barnett and Troiano [62] first used this technique for laboratory research to measure crack growth kinetics in a study of hydrogen embrittlement in notched tensile specimens. Electrical PD methods, which were also named as electrical resistance methods, have been used with success of detection crack closure in fatigue crack studies [63–72], crack initiation in crack-opening displacement and fatigue tests [25, 49, 50, 73–79], measurement of crack growth under various of loading conditions (including fatigue [10, 23, 58, 80–83], creep [20, 23, 41, 46, 83–87], stress corrosion [23, 88–90], sustained loading [91–93], fretting fatigue [13], hydrogen embrittlement [23, 62]), determination of J curves [49, 50, 74–76, 89], and evaluation of material properties [94–101]. Applications of crack identification by PD methods has been extended to asymmetric cracks [102–104], angled cracks [105, 106], and multiple cracks [107–116]. In additional to the wide application of

PD method on open cracks propagated under tension (Mode I), the method has been used to out-of-plane shear (Mode III) [117], in-plane shear (Mode II) [118], and mixed Mode conditions (tension and in-plane shear) [16].

Several advantages of PD methods enable the wide application of the technique. The relatively cheap instrumentation and simple operation contribute to the preference [44, 46, 48, 55, 119–123]. Moreover, PD methods are believed to provide reliable and accurate predictions [12, 46, 124, 125] yet continuous detection of cracks thereby allows stable automation [46, 48, 55, 119, 120, 122, 124–126]. As reported in an early work by Johnson and Willner in 1965 [88], an increment in crack length of 0.004 in / 0.10 mm is detectable by PD methods. Then according to a work by Soboyejo et al in 1990 [125], the resolution has been improved that a crack increase of 10 μm in a 10 mm thick body was measurable. Because visual accessibility is not required, PD methods are capable to monitor through cracks and other applications in enclosed environmental, which are excluded by optical methods [12, 46, 79, 124, 127]. PD methods are applicable for testing various extreme environments such as corrosive, high pressure, high radiation, elevated and variable temperature conditions [12, 15, 44, 48, 55, 119, 121, 122, 125, 126]. In particular, superior behaviour has been noticed in creep damage monitoring [128] and crack closure detection [77]. On the other hand, some limitations in PD methods have been noted in the literature. Calibration for each test piece geometry and load is required as the accuracy of calibrations seriously affects the capability measurement [46, 129]. PD methods are limited to conductive materials [130] because a conducting path around cracks inside the test piece is necessary. Moreover, there is vulnerability of PD methods to spurious potential signals during measurement (this is discussed in greater detail later in this chapter).

PD methods fundamentally rely on the principle that an electrical potential field will be disturbed by any discontinuity inside a current-carrying body. The location, shape, and size of the discontinuity are detectable by analysing this potential field and comparing it to a 'clean' signal (i.e. a potential field in a discontinuity free body). For this purpose, a constant current is supplied to a cracked or featured conductive body and the PD is measured across the growing feature. An increase in the measured PD is associated with the decreased cross-sectional area caused by crack propagation. The measured PDs are then correlated with crack lengths by using appropriate calibrations curves. Calibration curves and PD measurements are sensitive to several factors which include the crack/notch geometry [3, 4, 47, 58, 131–133], the specimen geometry [4, 47, 51], the arrangement of current injection [3, 4, 51, 58, 132], and the location for potential measurements [4, 47, 51] (the latter two factors will be covered in Section 2.3.5.1). Moreover, in several studies involving multi-frequency ACPD method [24, 126, 134, 135], calibration curves were found to be affected by operating frequency. However, an opposite argument has been reported that a linear slope of calibration established in WOL (see in Fig. 2.1g) specimens was independent of operating frequency [37].

Error signals in calibration measurement may be introduced by plastic deformation [12,37,51,59,62,74,81,82], crack closure [38,52,102,136,137], and temperature fluctuation (which is related to temperature dependent resistivity) [3,78]. With respect to the last point, constant current supply and controlled temperature conditions, such as an immersion in an ice bath [23], is desirable [43].

Depending on the type of operating current, PD methods can be recognized as DCPD and ACPD. PD methods possess some advantages over the other NDT techniques and will be discussed in detail in this chapter.

2.3 Electrical Potential Difference Methods

2.3.1 Comparison between Direct Current Potential Difference & Alternating Current Potential Difference

The DCPD method has been widely accepted due to its easy application and hence relative cheap cost [37,45,133,138]. Because of the nature of DC, DCPD is independent of magnetic permeability of conductive specimens hence the capacitance problem (the capacitance of conductive specimen which is usually ignored actually exerts an effect on measurement of PD) concerned in ACPD is eliminated [14, 56, 123, 133, 138]. The wide use of DCPD offers another advantage, in that previous results and guidance are available for certain specimen geometries [45]. However, in DCPD tests the whole specimen is tested in terms of the current path, and so the specimen geometry itself (rather than just some flaw geometry) influences the calibration [14]. Moreover, a relatively high current level is required in order to achieve measurable potential outputs [45,78,138,139]. According to [37], a DC of 30-50 A is necessary for a steel specimen in normal size. Therefore, it is less suitable for detecting small cracks (due to a small crack extension or electrical resistance) and less applicable in large structures (since a high current input is required to maintain a certain current density in a large range). Furthermore, high current input may lead to undesired localised heating [78,140], which influences the material conductivity and aggravates the effect of thermal electromotive forces (emf) on potential measurements. Another major concern in applying DCPD occurs in the sensitivity to emf that is attributed to temperature differences at connections between the specimen and measurement leads [31,38,45,138,140,141]. It should be noted that ACPD is immune to the DC emf noise [31,38,44,52,127,129,139–141]. Effective actions against emf effects are discussed later. To overcome some of the limitations of DCPD systems, the ACPD method has been developed as an alternate. ACPD takes advantage of skin effect, as illustrated in Fig. 2.2 , which refers to a confined current region beneath the specimen surface caused by interaction of original AC and induced eddy current.

(a) ACPD   (b) DCPD
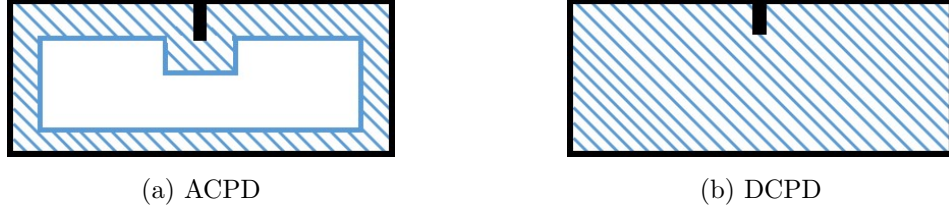
Figure 2.2: Current distributions in ACPD and DCPD. (a) Skin effect in ACPD: AC is forced to flow in a thin layer beneath the specimen surface. (b) In DCPD: the whole cross-section of the specimen is involved.

Compared with the whole body affected in DCPD, in ACPD the current field concentrates in a narrower layer near the material surface, thus a lower excitation current is sufficient to supply easily measurable potentials [11, 14, 31, 44, 45, 76, 78, 86, 98, 126, 127, 129, 133, 138, 140], thereby minimising the risk of localised heating [14, 98, 140]. Hence, ACPD is able to achieve higher sensitivity than DCPD, especially for small crack lengths near the surface of materials [14, 38, 44, 45, 134, 142] and the effect of specimen geometries is reduced [14]. Verpoest et al [134] have applied high frequency ACPD to detect and monitor surface cracks in un-notched steel rods and gave the conclusions that a 40 kHz current frequency would allow detection of cracks in an area of 0.05% of the specimen cross-section, which was unachievable by the other NDT techniques. Proper choice of coating materials, such as nanocomposite coatings which provides adjustable electric conductivity and magnetic permeability [143], could protect components from serve conditions yet enhance the detecting ability of ACPD. Another important advantage of ACPD is that the technique has higher noise rejection capabilities when lock-in amplifiers (which extracts and amplifies signals at certain frequency) are used [11, 31, 38, 126, 141]. ACPD also performs better than DCPD in corrosive environments, since by changing polarity any unwanted electrochemical processes are eliminated [38, 45, 140, 141]. The depth of current penetration, known as the skin depth (δ), is given by [144, 145]

$$\delta = \sqrt{\frac{2}{\omega\mu\sigma}} \qquad (2.1)$$

where μ and σ are of magnetic permeability and electrical conductivity, respectively, and ω is the oscillating frequency. Hence by applying multi-frequency AC in ACPD tests, specific inspection can be conducted in different depths of the specimen [11, 86, 142, 146]. Conversely, in cases of deep cracks and crack tunneling, particular attention should be paid to ensure the AC covers the whole inspection region [21, 44]. Disadvantages of ACPD include higher investment due to the amplification and filtering equipment [52, 78, 138], and disturbance on calibration caused by capacitance effect such as change in permeability and conductivity [21, 33, 34, 133, 138]. In order to minimise spurious effects caused by magnetic properties, low frequency ACPD measurements were proposed in which some of the advantages of ACPD were conserved, yet the noise rejection was improved by

suppressing the skin effect [86, 87, 147–149].

2.3.2 Experimental System Designs

The earliest PD techniques were associated with DC. A typical configuration of a
DCPD system is shown in Fig. 2.3a. The system consists of a stabilized power
supply, a voltmeter to provide high-gain DC amplification and off-set zero control
for initial PD, and recording instruments for automatic control and data acquisi-
tion. Usually the stable DC was supplied by a voltage source and the stability and
desired level of the operating current is achieved by a reference resistor in series
with the specimen [23, 38, 44, 52, 141, 150].

A schematic of an ACPD system is illustrated in Fig. 2.3b and a basic descrip-
tion is given here. A noticeable improvement offered by the ACPD method is the
introduction of phase sensitive detection associated with lock-in amplifiers that
offer excellent noise rejection and improved accuracy and sensitivity for ACPD
measurements [24, 38, 78, 90, 126, 138, 141]. In the excitation circuits a reference
signal provided by a voltage controlled oscillator is fed into a power amplifier for
constant current output [37, 38, 49, 52, 135, 141, 151]. Similar to DCPD system, a
reference resistor connected in series with the test-piece maintains the stability
of current regardless of the specimen resistance [37, 38, 141]. The output signals
from specimen are isolated and pre-amplified at a transformer [38, 44, 141, 150, 151]
and measured with a lock-in amplifier. Only the potential signals at the reference
frequency identical to the current source will be amplified and accepted by the
lock-in amplifier [38, 138, 141] (a signal-to-noise ratio as low as 0.1 is allowed by
lock-in amplifiers [38, 141]).

(a) DCPD

(b) ACPD
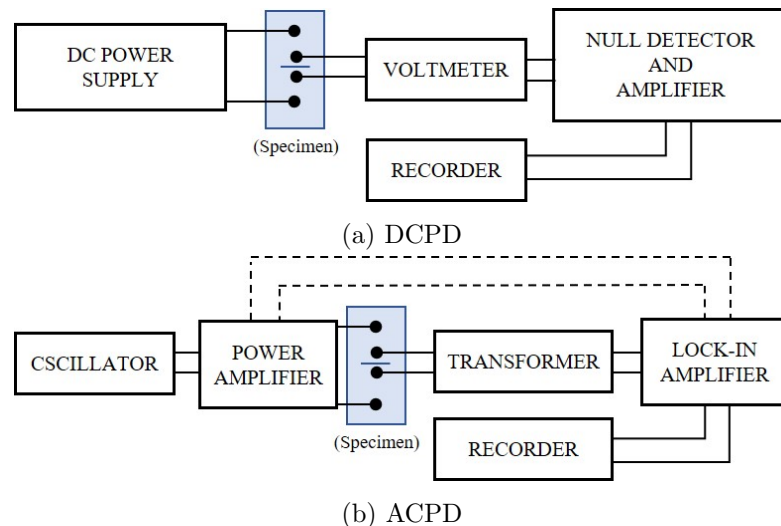
Figure 2.3: Block diagram of PD technique systems.

The current supply leads are usually spot-welded or bolt-screwed on the spec-
imen to minimise contact resistance and in turn to reduce heating effects [38, 43,
140, 150]. By connecting current leads through conductive plates heating effects

due to large dissipation area are avoided, however this strategy causes problems of reproducibility in contact area [43]. In order to minimise thermocouple effects, it has been suggested that potential measuring probes are made of the same, or closely similar materials, as the test-piece [125, 139, 150, 152]. These probes are spot-welded to the specimen [23, 38, 43, 140, 150]. The electric leads should be twisted together to minimise inductive coupling [12, 140, 141, 153] and errors due to movement [12]. It is necessary to exclude any current leakage and ensure that the test-piece establishes the only electrical path for current. Hence electrical insulation should be applied to contact areas between specimen, lead wires and the testing machine, which can be achieved by using, for example, TUFNOL strip [38].

2.3.3 Identification of Crack Lengths - Calibration

2.3.3.1 Introduction

Practically speaking, the length of a growing crack is usually transformed from the PDs measured across it by a calibration curve. Johnson [131] suggested that calibration can be made independent of material composition, material heat treatment, and thickness of test-piece but sensitive to the starter notch geometry. This principle enables a single calibration curve determined for a standard specimen to be applied to practical test-pieces that are similar in geometry but made from different materials. The determination of calibration curves is found to significantly influence the accuracy of the method [59]. Several work have determined calibration curves and obtained linear [23, 24, 37, 38, 78, 141, 154, 155] or non-linear [49, 50, 59, 77, 82, 131, 135, 156–159] relation between PD and crack lengths. The linearity of calibration curves was regarded as an advantage of the PD method over the other NDT methods [45, 78]. Three methods are used to determine the calibration: namely analytical, numerical, and empirical (direct and analogue) methods.

Attempts at analytical solutions consist of finding the solution to Laplace's equation within the boundary conditions of a given specimen geometry, where the steady electrical potential field (V) around a crack in a specimen is given by [58, 59, 119, 129]:

$$\nabla^2 (V) = 0 \tag{2.2}$$

Several analytical solutions to the Laplace's equation are available for simple specimen geometries by using conformal mapping methods [82, 131, 160], which offers a useful guide in experimental work. Analytical methods are difficult to develop for geometries such as C(T) specimens due to the complicated solution domain [6, 46, 58, 59, 79, 154], however it is precisely these type of specimens that are commonly used for crack growth monitoring. When analytical calibration is not possible attention should instead be focused on numerical or experimental methods.

Numerical methods enable precise control of different parameters, such as geometries of crack and specimen, probe position for current injection and potential measurements. Hence these methods are suitable for optimising probe configurations in isolation [4, 19], estimating effects on calibration caused by specimen and crack geometry and plastic deformation [3, 4, 6, 59], and simply determining multiple calibration curves for specimens with different aspect ratios [6]. Numerical techniques are reported to be accurate and fast tools to derive calibration curves at relatively small cost compared with labour-intensive and time-consuming experimental methods [19, 59]. It should be noted, however, that a great deal of work is necessary in order to obtain high confidence in numerical models before calibration curves can be generated [38].

Through the use of experimental data, straightforward calibration curves are accessible for complex specimen geometries under any combined conditions such as thermo-mechanical fatigue (TMF) [6, 38, 46]. Empirical solutions almost always suffer poor accuracy for small crack lengths [58, 59, 161] and measurements are vulnerable to errors likely caused by variations in locations of current leads and potential probes [161]. Moreover, additional tests are required to determine calibration curves for other specimen geometries and probe configurations, which is costly and cumbersome [6, 161]. Alternatively, analogue techniques, in which the cracked specimen is modelled by conductive materials and potential and crack length are measured on the analogue models, has been widely applied to determine empirical calibrations for various specimen types. Available analogue models include graphitised paper, aluminium foil, wax, and rheoelectric tank. In the following sections, progress in calibration curves determined by the three methods are presented separately in more detail.

2.3.3.2 Analytical Solutions

Johnson's Formula

One of the most widely used analytical calibration methods for centre cracked specimens is Johnson's formula [131] in which the potential (V) is measured along the centreline and across the crack, and a uniform current distribution is assumed, as illustrated in the subfigure of Fig. 2.4. By applying the method of conjugate functions with appropriate boundary conditions of a M(T) specimen, Johnson put forward a calibration equation for slit-type centre-cracks for finite-width plate, which was given by the ratio of PD corresponding to the slit length (a) and that to the initial notch length (a_0), i.e. $\frac{V}{V_0}$, as given by

$$\frac{V}{V_0} = \frac{\cosh^{-1}\left(\frac{\cosh\frac{\pi y}{W}}{\cos\frac{\pi a}{W}}\right)}{\cosh^{-1}\left(\frac{\cosh\frac{\pi y}{W}}{\cos\frac{\pi a_0}{W}}\right)} \tag{2.3}$$

where W is the specimen width. (2.3) was then modified for an infinite-width plate by simply changing boundary conditions. As shown in Fig. 2.4, the ana-

logue calibration curve for a razor-shape (or slit-like) centre-crack [129] reasonably located between the curves for finite- and infinite-width plates.
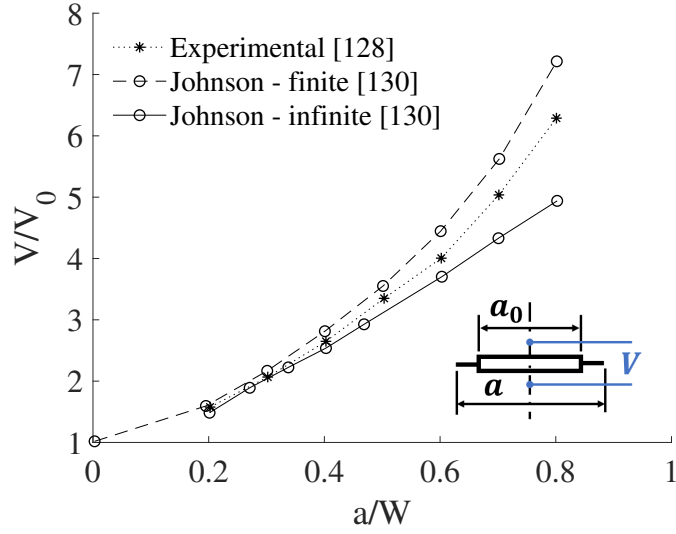
Figure 2.4: Comparisons of calibration curves for M(T) specimens including experimental data for slit-like cracks [129] and theoretical solutions given by Johnson's formula for finite and infinite plates. [131]

(2.3) was further developed for elliptical centre-cracks by modifying the boundary conditions and employing elliptical co-ordinates defined by

$$
\begin{aligned}
x &= c \cosh\left(u\right) \cos\left(v\right) \\
y &= c \sinh\left(u\right) \sin\left(v\right)
\end{aligned}
\tag{2.4}
$$

where c refers to the coordinate proportionality factor, $u > 0$, $0 \leq v \leq 2\pi$. The PD ratio of elliptical centre-cracks is

$$
\frac{V}{V_0} = \frac{c}{c_0} \times \frac{\sinh u_1\left(a\right) + \exp\left[u_0\left(a\right) - u_1\left(a\right)\right] \cosh u_0\left(a\right)}{\sinh u_1\left(a_0\right) + \exp\left[u_0\left(a_0\right) - u_1\left(a_0\right)\right] \cosh u_0\left(a_0\right)}
\tag{2.5}
$$

where $u_1(a)$ and $u_0(a)$ are the elliptic coordinate at the measurement position and slot boundary respectively. The comparison for calibration curves derived by Johnson's formula for slit and elliptical-centre cracks and experimental work for real elliptical cracks is given in Fig. 2.5. (2.5) showed reasonable agreement with experimental results up to $a/a_0 = 1.6$, suggesting that elliptical centre-cracks are more representative of cracks observed in real experimental test-pieces.
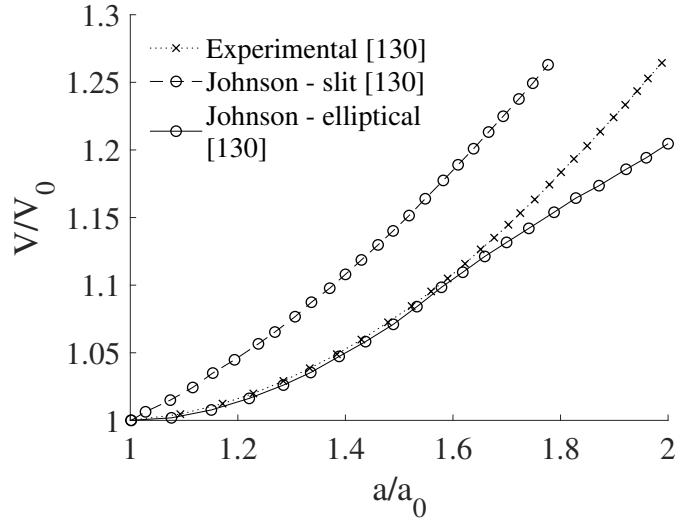
Figure 2.5: Comparisons of calibration curves for elliptical cracks including experimental results and theoretical solutions given by Johnson's formula for slit and elliptical-shaped centre notches. [131]

Johnson's formula has been experimentally validated for slit centre-notched specimens, which by independent studies [162], concluded that by taking a_0 at a position remote from the starter slit rather than half-length of it, the solutions given by Johnson's formula further agreed with experimental results up to $a/a_0 = 3.0$. Additionally, the analytical calibrations presented by Johnson [131] have been successfully applied to SEN(B) and C(T) specimens which benefited from the geometrical similarity between M(T) specimens and SEN(B). C(T) specimens in which a SEN(B) specimen was assumed to be half of a M(T) specimen and a C(T) specimen was regarded as a short SEN(B) specimen [163]. Good agreement with experimental results were achieved for the three types of fracture specimens in a range of $a/W = 1$, as shown in Fig. 2.6.

(a) M(T)

(b) SEN(B)

(c) C(T)
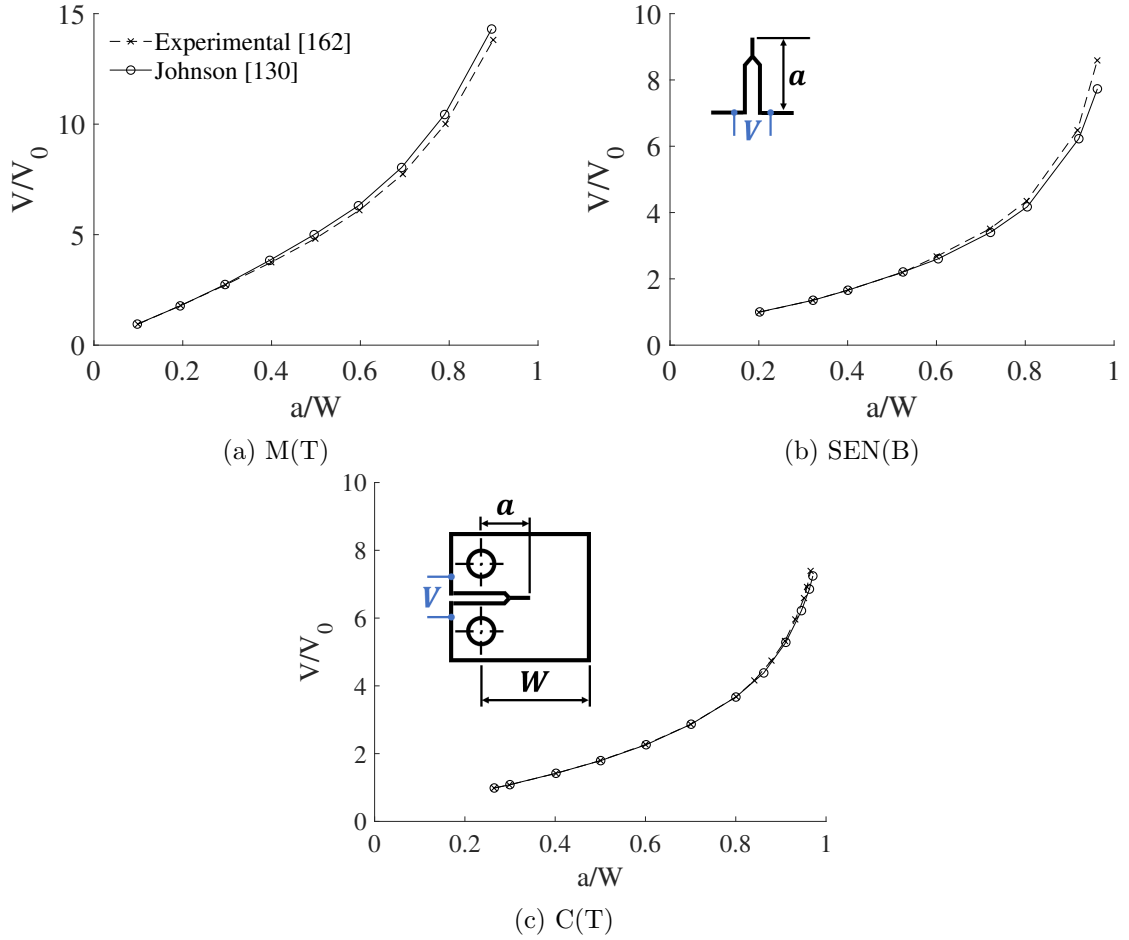
Figure 2.6: Agreement between theoretical calibrations given by Johnson's formula and experimental data for various fracture specimens. [163]

Johnson's formula has also been considered as applicable to SEN and DEN specimens due to the symmetry features proposed by Bakker [75]. In a recent paper [3], the idea of geometric equivalence between specimen types was extended to CS(T), DC(T), and DEN(T) specimens (as shown in Fig. 2.1a, 2.1c, and 2.1d respectively). By the use of two-dimensional (2D) FE models for all the specimen types, Johnson' formula has predicted the crack lengths based on numerically measured PD and gave maximum errors $< 6\%$, suggesting that Johnson's formula could be used as a unified calibration function for all the seven fracture specimen types (M(T), SEN(B), SEN(T), C(T), CS(T), DEN(T) and DC(T)). Moreover, the accuracy of Johnson's formula has been validated by wide applications [21, 25, 46, 51, 104, 137, 164, 165]. In Fig. 2.7, poor correlation between calibrations derived by Johnson's formula and experimental data for C(T) specimens was observed by Vassilaros and Hackett [50], which was likely explained by the change in specimen geometry and electric wire configuration, and variations in what is ideally uniform current field.
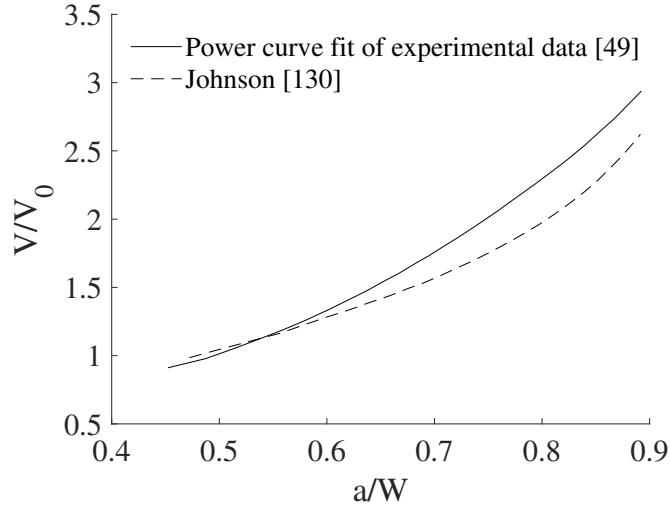
Figure 2.7: Poor comparison of empirical [50] and theoretical (Johnson's formula) [131] calibrations for C(T) specimens. [50]

It has been suggested that Johnson' formula is incapable of predicting open-hole single-crack specimens [6], and instead a series of FEA based calibration polynomials for different centre hole diameters to specimen width ratios should be used. Based on an acceptable error $< \pm 10\%$, Schwalbe et al [25] claimed that Johnson's formula was capable of predicting average lengths of curved front cracks. Nevertheless, Kolitsch [9] noticed that for cases of cracks growing from a semi-elliptical front, Johnson's formula would underestimate the crack depth since a straight through-thickness profile was assumed. In addition, Johnson's solution has been modified by within other works to evaluate the potential field around asymmetric M(T) specimen [103], 2D cracks which is perpendicular to specimen surface and off centre [108], and multiple semi-elliptical surface cracks [112]. A comparison of six calibration methods including several derivational functions of Johnson's formula has been reported by McKeighan and Smith [166] to determine the optimum calibration techniques for M(T) and SEN(B) specimens under fatigue with limited experimental data. The two-point modified Johnson's equation and post-test corrected Johnson's equation have been reported as the optimum calibration equations. The two-point modified Johnson's equation accounted for possible error attributed to probe mislocation by introducing unknown factors α and β into Johnson's formula (2.3) and gave

$$
\frac{V}{V_0} = \frac{\cosh^{-1}\left(\frac{\cosh \frac{\pi \alpha y}{W}}{\cos \frac{\pi a}{W}}\right)}{\cosh^{-1}\left(\frac{\cosh \frac{\pi \beta y}{W}}{\cos \frac{\pi a_0}{W}}\right)} \tag{2.6}
$$

where α and β are solved by a nonlinear equation solver (FORRAN code). In the post-test corrected Johnson's equation, the difference between crack lengths predicted by (2.3) and optical results was assumed to vary linearly from initiation to end, thus a correction was determined from initial and final measurements

(differences in crack lengths and PDs) and added the predicted crack lengths calculated by (2.3).

Conformal Mapping

Conformal mapping techniques, in which the orthogonality in the local geometry of specimens (realised in physical space) are transformed into an alternative simple geometry (that is readily analysed) by considering a complex potential plane, enabling accurate determination of calibration curves for a range simple specimen geometries. More details can be found in studies conducted by Clark and Knott [82, 161]. They have applied the analytical method to several specimens including edge cracks and SEN specimens with semi-elliptical notches and V-notches. The theoretical curve for 45° V-notched specimens showed good agreement with available experimental data [55] and results given by graphitised paper analogue method, in Fig. 2.8. The theoretical analogue solutions for a 45° V-notched SEN specimens were compared with 2D FEA results [59], which is presented in Fig. 2.10 in Section 2.3.3.3. Close agreement was shown especially for short crack lengths with $a/W < 0.5$. The conformal mapping calibrations presented by Clark and Knott [82] has been used to provide comparison to an empirical calibration curve for 60° V-notched cracks under torsion loading [167] (Fig. 2.9) and to an analogue calibration for straight front through thickness crack by use of the electrolytic tank method [168] (Fig. 2.18 in Section 2.3.3.5). Moreover, the conformal mapping technique has been coupled with numerical methods in order to determine calibration curves for C(T) specimens [169, 170], asymmetrical M(T) specimens [102], and inclined edge cracks at any angle to the test-piece face [155].
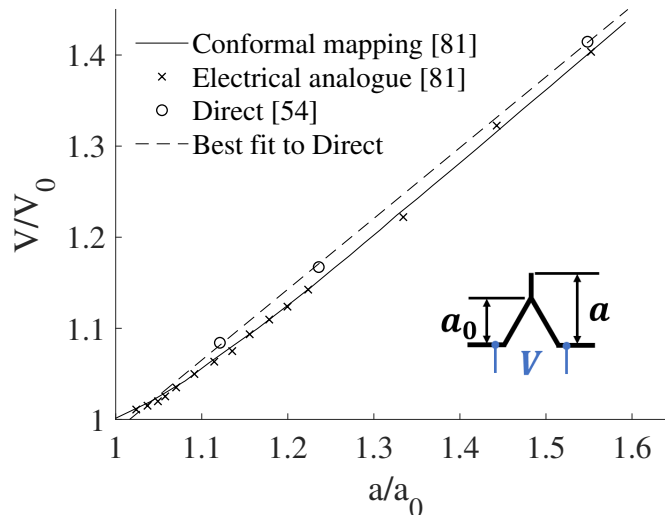
Figure 2.8: Comparison of calibration curves for a 45° V-notched SEN specimen including theoretical solutions given by conformal mapping [82], analogue [82] and direct [55] empirical results. [82]
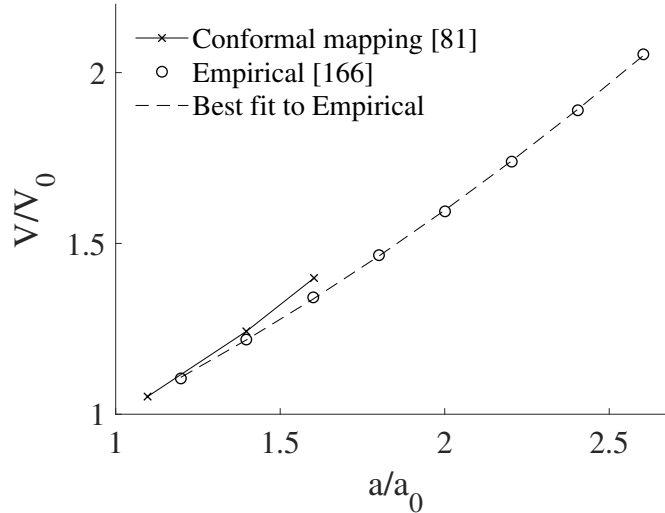
Figure 2.9: Calibrations obtained by theoretical (conformal mapping) [82] and empirical [167] solutions for 60° V-notched cylindrical specimen under torsion loading. [167]

2.3.3.3   Numerical Simulations

Numerical methods have been widely applied in order to establish calibration curves relating crack lengths to measure PDs for complex specimen geometries [3, 4, 6, 44, 46, 58, 59, 104, 107, 110, 111, 113, 124, 140, 169–173] and determine the optimum configuration for measurement leads and probes [19,44,46,58,59,117,173].

In the work conducted by Ritchie and Bathe in 1979 [59], calibration curves for complex geometries, C(T) and SEN with V-notches specimens, were determined by 2D FEA method and then compared with available theoretical methods [82], direct experimental [55,81] and analogue data [82], as shown in Fig. 2.10. The numerical results for SEN specimens showed close agreement at first but deviated slightly at large crack lengths with $a/W > 0.5$, which was explained by the relatively coarse FE mesh away from the notch. Compared to experimental data, the numerical curve for C(T) specimens consistently overestimated the crack lengths. This was possibly because the crack width that was assumed to be infinitesimal in the numerical model but had a finite width in practice.
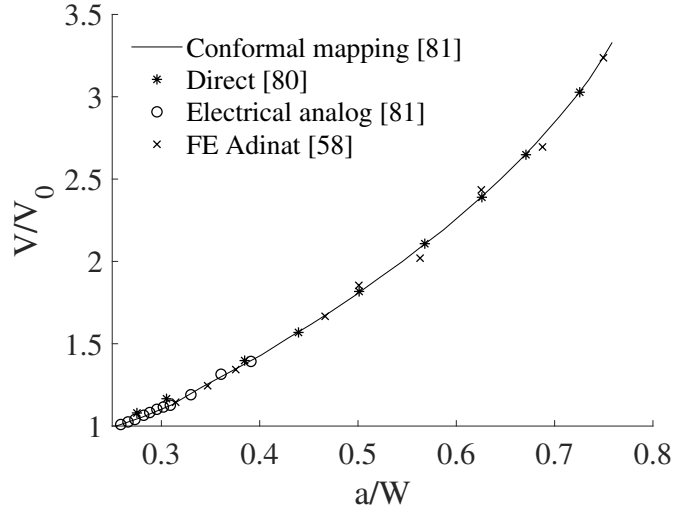
(a) SEN
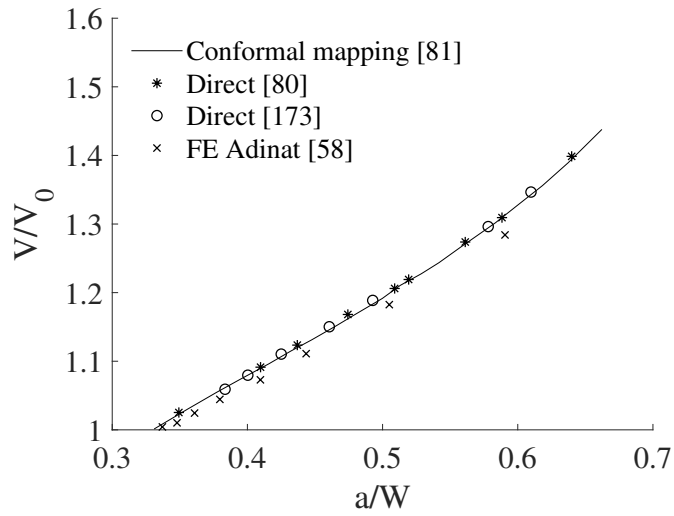
(b) C(T)

Figure 2.10: Comparison of calibrations given by 2D FEA simulation [59], conformal mapping [82], analogue results [82] and direct experimental data [81, 174] for C(T) and SEN specimens. [59]

The 2D FE model developed by Ritchie and Bathe [59] has been used by Aronson and Ritchie [58] to determine the numerical calibration curves and qualitatively evaluate the sensitivity and reproducibility of probe configurations in C(T) specimens. A comparison between 2D FEA and boundary integral equation method, which enabled a reduction of 2D problems into one-dimensional, has been conducted for C(T) and DCB specimens by Klintworth and Webster [44]. It was concluded that both methods are suitable for optimising the measurement leads locations. Good agreement has been achieved between empirical calibrations and numerical calibrations for the C(T) and DCB specimens by the two methods, besides a slightly better accuracy was obtained by boundary integral equation method for C(T) specimens. In order to optimise the location of potential probes of circumferentially-notched cylindrical specimens subjected to torsion, FEA has

been used to obtain numerical calibration curves which suggested the optimum position to be at the notch edge and a second-order polynomial function was given to express the obtained calibration curves for probe location at 12.7 mm chosen in this study [117],

$$a = \left[0.25 \left(\frac{V}{V_0} - 0.715 \right)^{0.5} - 0.133 \right] r \tag{2.7}$$

where r is the specimen radius. A series of numerical calibrations obtained with different potential probe positions are shown in Fig. 2.11.
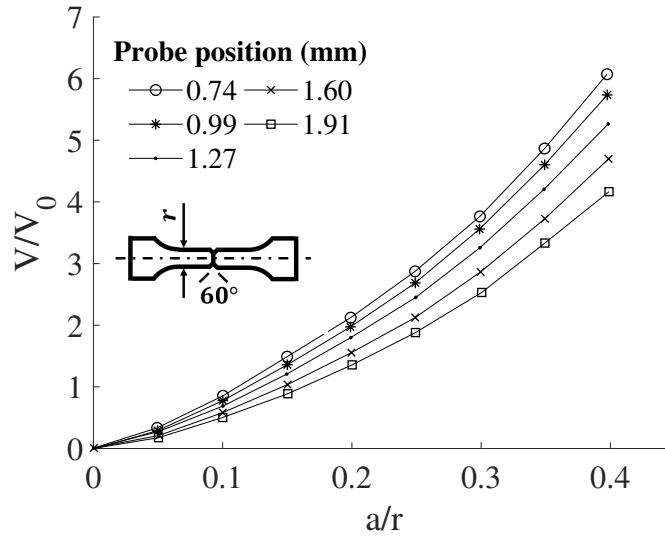
Figure 2.11: Calibrations for circular notched cylindrical specimens under torsion with different potential probe positions. [117]

By using a mathematical analogies between current flow and heat/stress analysis problems [124], 2D C(T) test-pieces were modelled by three available FE programs (MARC-HEAT, S175 and GSS programme) and three-dimensional (3D) corner and surface notches were simulated by one of them (MARC-HEAT). The numerical calibration curves coincided well with aluminium foil analogue results, experimental readings from beach marking and an analytical solution for semi-circular crack. The effect of notch width and height in C(T) specimens and the current application, concentrated or distributed, have been analysed by 2D FEA by Wilson [132]. Moreover, the paper observed insignificant differences in calibration curves by using a fine mesh size (containing 3598 nodes) compared with that obtained by employing a coarse mesh (961 nodes), as shown in Fig. 2.12.
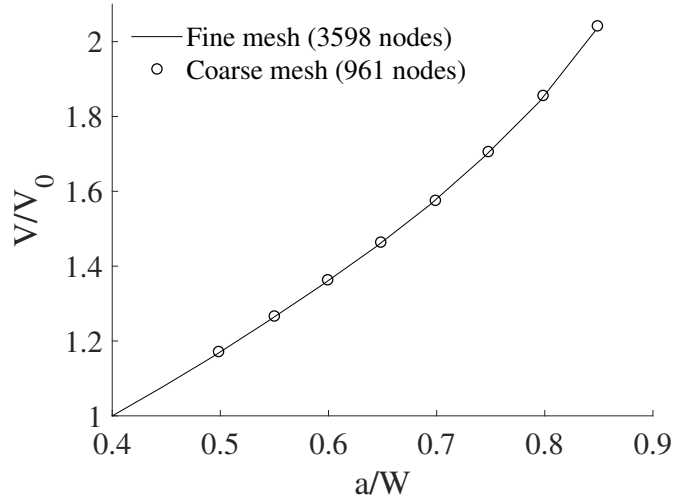
Figure 2.12: Effect of element mesh refinement on numerical calibrations for C(T) specimens. [132]

The use of singular crack tip (collapsed) elements rather than conventional element could improve limited accuracy in calibration curves. A comparison between the behaviour of 2D and 3D FEA in determining the length of a circumferential crack, based on measured DCPD under TMF conditions has been reported by Gandossi et al [46]. By comparing with crack lengths measured before the experiments, it was concluded that 3D FEA gave accurate calibration curves whereas the curve obtained by 2D FEA tended to overestimate the crack lengths. The calibration curves for semi-elliptical and 'ear-shaped' cracks (Fig. 2.13), were numerically determined by 3D FEA analysis by Doremus et al [4]. The author proposed that by inserting experimental beach markings into the numerical calculation, the accuracy of coupled numerical and experimental calibrations would be efficiently improved. In a recent paper [3], the effect of crack geometries and temperature difference on calibration curves were evaluated by employing 3D FE models on circumferential and semi-elliptical surface cracks. Additionally, a comparison between applying 2D axisymmetric models and 3D full model on circumferential cracks was conducted. The use of a DC numerical model with modified geometries to approximate full 3D AC problems has been proposed for the sake of reducing computational expense [17].

(a) Semi-elliptical (b) Ear-shaped
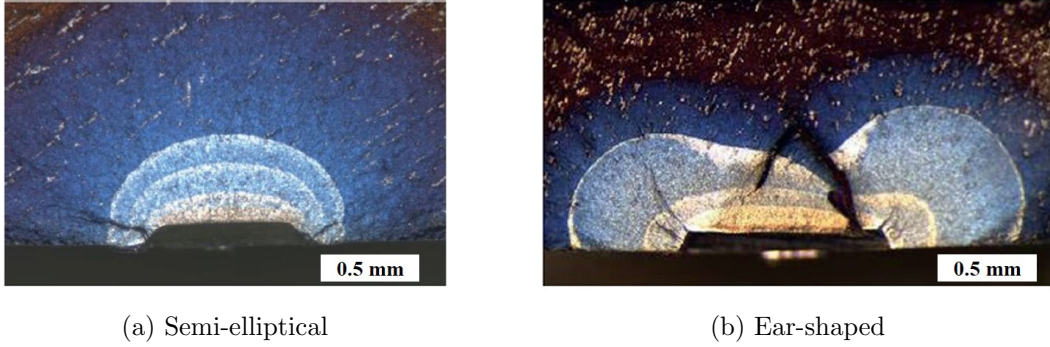
Figure 2.13: Semi-elliptical and ear-shaped cracks. [4]

In a study conducted by Hiroshi et al [171], the boundary element method was used to determine the depth of a semi-elliptical surface crack in ACPD tests and an empirical calibration function was developed based on the numerical results. Due to the insufficient consideration of effects on potential field caused by the AC, and the high-frequency thin-skin mode assumed by the numerical model, the function was suggested to offer a reliable calibration method, although actual coefficient values were not determined with a great deal of confidence. A 3D boundary element method was applied to a pair of coplanar coalescing surface cracks by Harrington et al [172], using two calibration equations which revealed the crack depth and profile. Predicted and estimated crack shapes showed reasonable agreement with beach marking results.

2.3.3.4 Direct Experimental Methods

Empirical calibration determination usually is associated with the use of one of two methods for increasing crack lengths. The first involves increasing crack length by sequentially cutting the sample and measuring the corresponding potential values across the machined cracks. This method has been applied to centre-notched [48], C(T) [23, 37, 50, 55, 59, 117], and SEN [55, 59] specimens. However, empirical calibrations determined from cutting cracks in this way were found to give underestimation in crack length [48, 73, 119]. The second method involves extending the crack by fatigue loading and the increasing crack length measured by optical microscopy and/or the beach marking method.

Optical measurements can be conducted directly. In M(T) specimens, for example, the centre-crack propagates on the specimen surface. Alternatively, specimens may be broken after the test. This depends on the visual accessibility offered by a particular specimen type. Empirical calibration curves based on optical observation are available for DCB [44], C(T) [16], M(T) [102, 131, 162], corner crack (CC) [140], SEN [135], centre-circular hole [83], and circumferential cracked [4, 167] specimens.

When applying the beach marking technique, crack profiles were marked periodically on the fracture surface by changing the loading frequency [51], mean load

[24,51,58,124,125,141,152,154,156,157,164,172], or by heat tinting [4,62,134,158]. The specimens were then broken open after the tests and the crack lengths/depths measured optically. Beach marking enables curvature or irregular growth in crack shapes to be determined, thus necessary corrections can be applied to calibration procures. Empirical calibration curves have been established this way for C(T) [51, 58, 124, 141], DC(T) [157], M(T) [51, 152], SEN [24] and semi-circular crack [4, 125, 151, 156, 164, 172], circular external crack [164], CC [124, 158], and fin notched [124] specimens. Some of the empirical calibration curves have been shown Section 2.3.3.2 and 2.3.3.3 for comparison.

2.3.3.5   Analogue Experimental Methods

Conducting Paper

The conducting paper analogue method is applicable for any 2D problem involving field or flow that obeys the Laplace equation [119]. With respect to the calibration of PD methods, the profile of a specimen is modelled by conducting paper, such as graphitised electrical paper and a sheet of aluminium foil, which benefits from a relatively high resistivity and ease of generating an artificial crack. The conducting paper is cut to conform precisely with the geometry of the test-piece and the accuracy can be improved by scaling up the analogue model (of the specimen) [104, 124]. The crack is manufactured using a razor-blade [44, 119, 129] or scalpel [104, 124]. Current injection is modelled by painting the paper with silver conducting ink [119, 161] and potential distribution is measured by electric wire and a potentiometer.

The graphite electrical paper analogue method has been widely applied to determine calibration curves for various types of cracks and specimens such as V-notched SEN(B) [82, 119, 155], C(T) [44, 119], DCB [44], and centre-notched specimens [48, 119]. Analogue calibrations for V-notched SEN(B), C(T) and centre-notched specimens developed by Smith [119] is shown in Fig. 2.14 as examples. The accuracy of the resulting calibration has been validated by the conformal mapping [82, 119, 155], direct experimental [44] and numerical [44, 59] methods. Beside the determination of calibration, the graphite paper analogue method has been used to reveal the PD distribution on specimens and thus determine the optimum configuration of current and potential probes (the effect of probe positions on PD measurement was indicated by variations of equi-potential lines and the consequent sensitivity was related to potential gradient) [81]. Moreover, the analogue method has been utilised to study the influence of the relative crack closure area, with respect to the crack tip, on the measured PD in C(T) specimens [63].
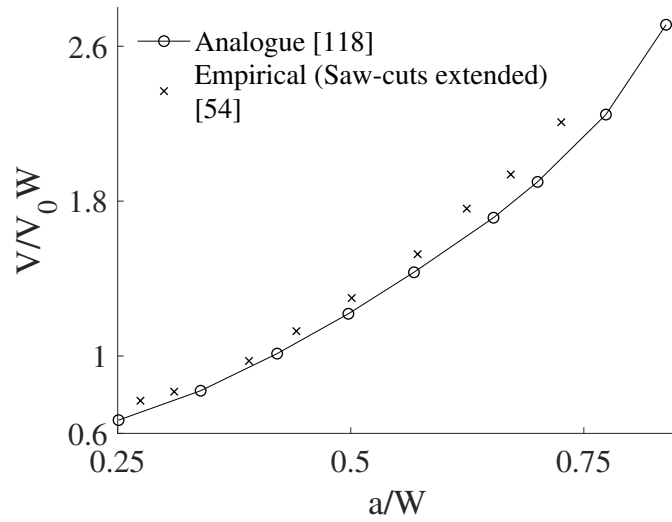
(a) 45° V-notched SEN(B)
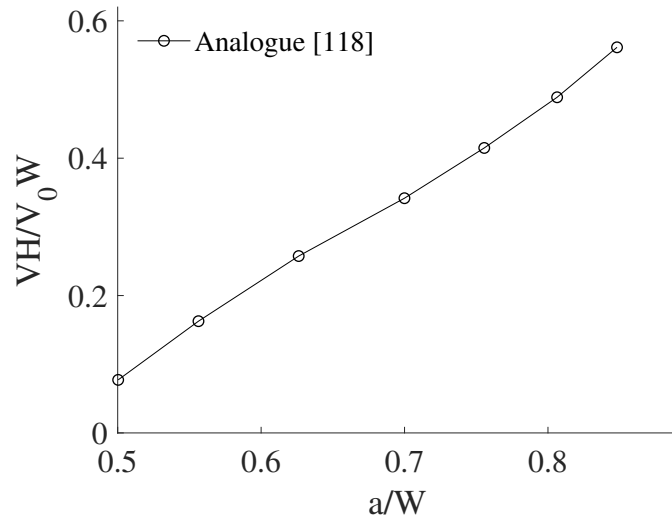
(b) C(T)
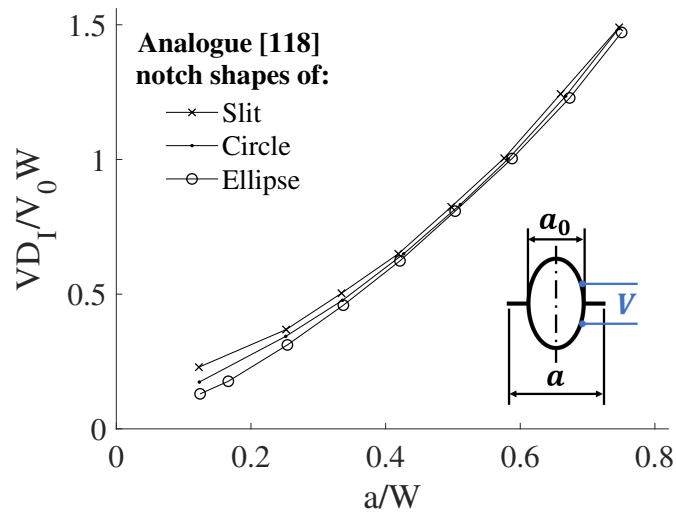
(c) Centre-notched

Figure 2.14: Calibrations of various fracture specimens. D_I represents the distance between the current input and output. [119]

For aluminium foil the analogue method has been applied to M(T) specimen with symmetrical [129] and asymmetrical M(T) [104] specimens, C(T) specimens [124] and specimens with a central hole [79]. Anctil et al [129] claimed that the calibration for M(T) specimen retained its validity for SEN specimens due to the geometrical similarity and for other M(T) specimens with different widths (providing that the positions of lead-wires relative to centre crack were varied in direct portion to the change in width). Anctil et al's paper went on to compare analogue calibration with that produced by experimental specimens. As the actual notch had a finite width, which was different to the razor-generated slit in the analogue specimen, the actual calibration curve was at a position below the analogue curve, as shown in Fig. 2.15. The analogue calibration for C(T) specimen in [124] showed good agreement with the results obtained from FEA and beach marking method. In the study given by Merah et al [79], the empirical calibration equation obtained for centre hole specimen at room temperature was then developed for high temperature application by introducing a correction factor.
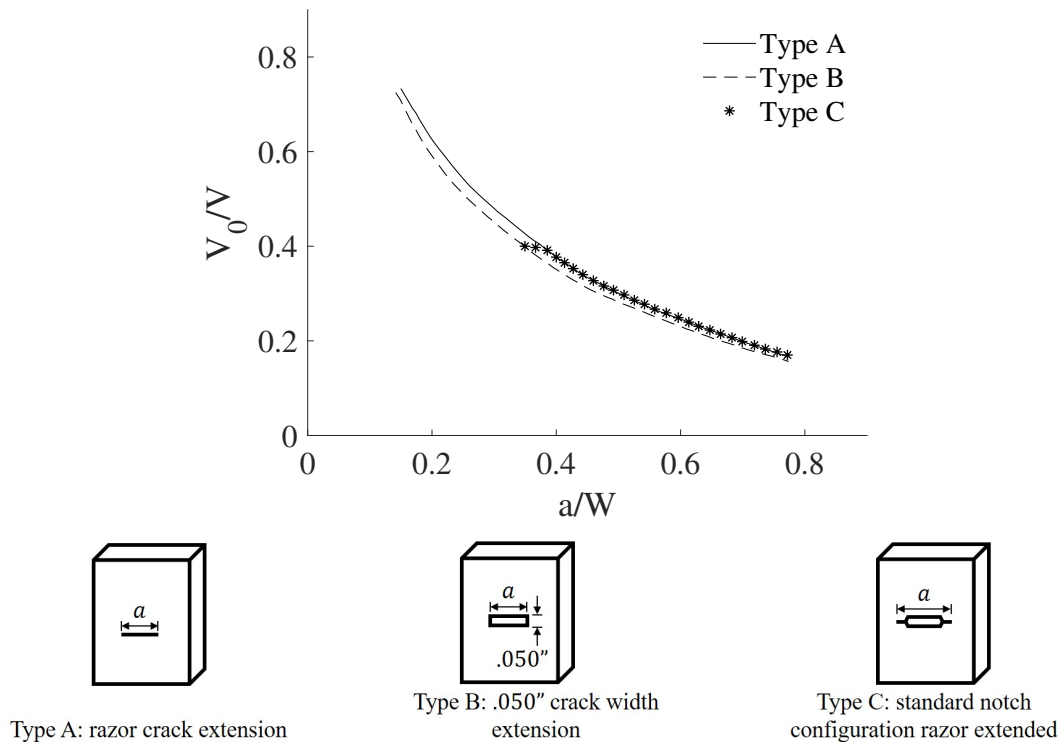
Figure 2.15: Aluminium foil analogue and empirical calibrations for centre-notched specimens. [129]

Three-dimensional Wax Model

A mixing of wax and graphite powder has been used to model the specimen by Smith and Cameron [120]. As illustrated in Fig. 2.16a, the 3D analogue calibration, which developed for through cracks cut by a blade, was shown to coincide to the theoretical calibration [160] for small crack depth up to $a/W =$

0.05 then deviate the theoretical one but approach to an experimental solution [48]. This was considered as a reasonable validation of the wax model by the authors. They also proposed that by applying the wax analogue technique, the size and location of a quarter crack (Fig. 2.16c) could be identified.
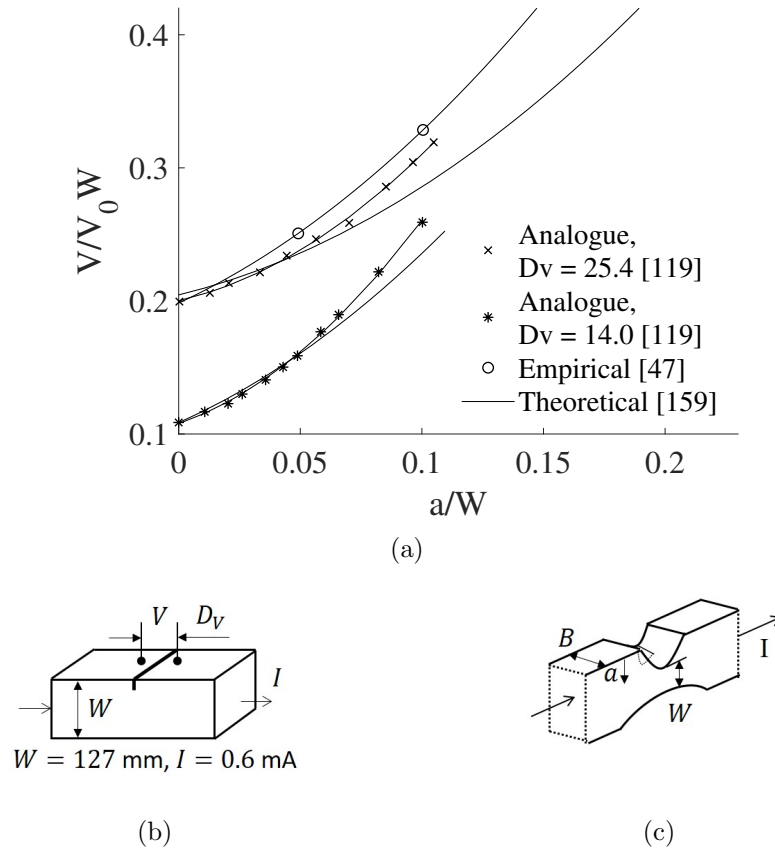
Figure 2.16: (a) Comparison of calibrations obtained by the wax analogue model [120], theoretical [160] and empirical [48] calibrations. (b) The quarter crack. [120]

Three-dimensional Rheoelectric Tank

3D rheoelectric tank technique involves the use of a conductive electrolyte, such as potassium chloride [125, 161, 168], mercury [69] and water [164], to simulate the conductive test-piece (an example is given in Fig. 2.17). Because the insulating insert that represents the crack can be modified to any arbitrary geometry, this method allows the evaluation of any chosen crack profile [164, 168]. The method has been used to generate calibration curves for different crack geometries including straight-fronted cracks [164, 168], semi-circular/thumbnail cracks [125, 164, 168] and circular cracks [164]. The confidence of the rheoelectric tank tests has been confirmed by the reasonable comparison with theoretical results [125, 164, 168], beach marking readings [125, 164], graphitised electrical paper analogue method [168], and FEA results [168]. A comparison given by You and Knott [168] is shown as an example in Fig. 2.18.
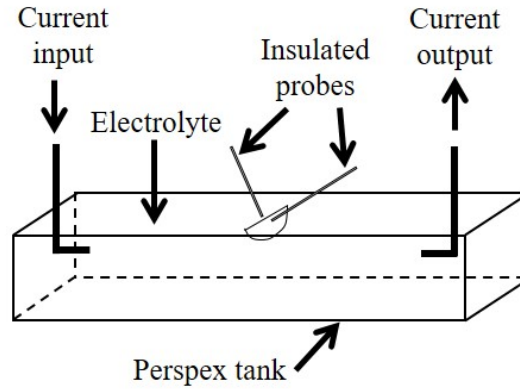
Figure 2.17: Schematic of 3D rheoelectric tanks. [168]
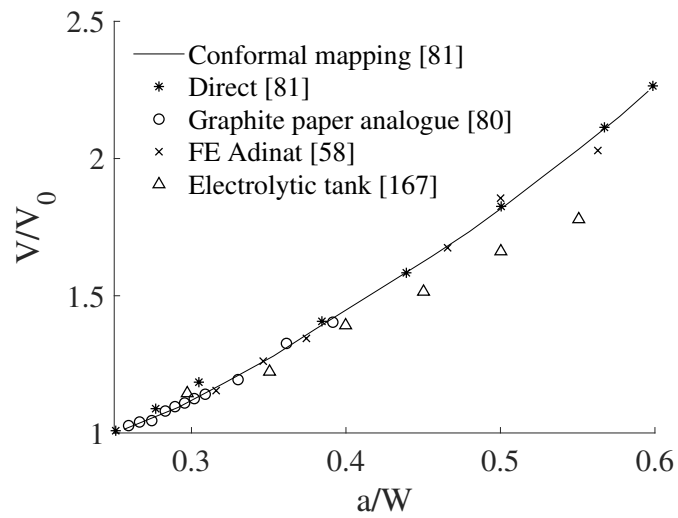
(a) Through-thickness cracks
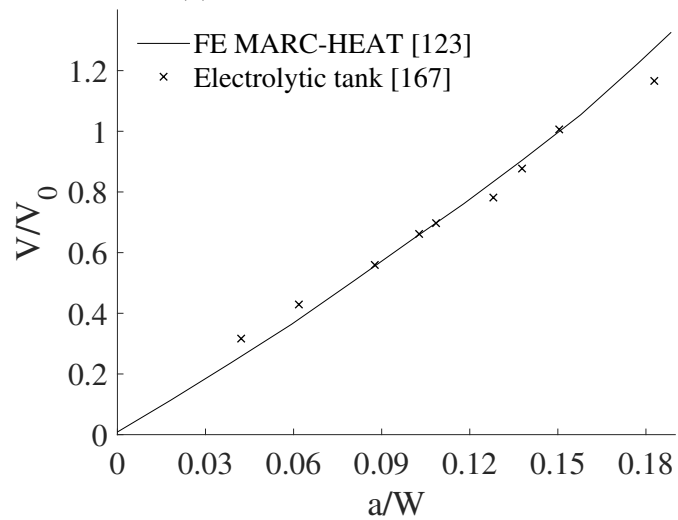
(b) Part-through semi-elliptic cracks

Figure 2.18: Comparison of the analogue calibration curve simulated by electrolytic tank [168] with other calibrations for through-thickness and part-through semi-elliptical cracks.. [168]

Additionally, Ward-Close [69] applied a scaled perspex model to establish a series of calibration curves which indexes the extent of crack closure based on the relation between two PDs measured near and remote the crack in a C(T) specimen.

2.3.3.6   Calibration Curves under Fatigue

Non-linear Calibrations

Several works have determined calibration curves for several specimen geometries by DCPD/ACPD methods and obtained a curved/non-linear relation between PD and crack lengths [49, 50, 59, 77, 82, 131, 135, 156–159]. An empirical calibration curve for C(T) specimens was developed by using DCPD [50] as a precondition for R curve determination, which was approximated by a power fitting function in a range of $0.6 < a/W < 0.8$. The calibration function was given by

$$V_N = \left(1.5 \times \frac{a}{W}\right)^{2.9} + 0.605 \qquad (2.8)$$

where V_N is the normalised PD excluding variations in experimental equipment and in placements of electric leads. Similar forms of calibration have also been reported for circular notched specimens [77]. Empirical calibrations in the form of polynomial functions have been obtained for curved surface cracks [156], disk-shaped C(T) [157] , C(T) [49, 156, 159, 175], SEN [135], corner notched [158] specimens. Gilbert et al [157] reported a fourth order polynomial function for disk-shaped C(T) specimens over the range of $0.3 \leq a/W \leq 0.8$ as

$$\frac{a}{W} = -0.089 + 0.381V_N + 0.053V_N{}^2 - 0.047V_N{}^3 + 0.007V_N{}^4 \qquad (2.9)$$

In a work by Na et al [159] the calibration function for C(T) specimens was as a third order polynomial:

$$\frac{a}{W} = -0.5051 + 0.8857\left(\frac{V}{V_0}\right) - 0.1398\left(\frac{V}{V_0}\right)^2 + 0.0002398\left(\frac{V}{V_0}\right)^3 \qquad (2.10)$$

where V_0 is the reference PD corresponding to $a/W = 0.241$.

With application of multi-frequency ACPD methods [126, 135], empirical calibrations for SEN specimens were expressed by second order polynomials under various frequencies. The polynomial functions given by [126, 135] are shown respectively,

$$\frac{V}{V_0} = 0.4610 + 0.5545\left(\frac{a}{L}\right) + 0.1509\left(\frac{a}{L}\right)^2 \text{ (203 kHz)}$$

$$\frac{V}{V_0} = 0.3443 + 0.6718\left(\frac{a}{L}\right) + 0.1873\left(\frac{a}{L}\right)^2 \text{ (127 kHZ)} \qquad (2.11)$$

$$\frac{V}{V_0} = 0.2335 + 0.7936\left(\frac{a}{L}\right) + 0.2077\left(\frac{a}{L}\right)^2 \text{ (17 kHz)}$$

$$V - V_0 = -5.092 + 25.906a + 7.0a^2 \text{ } (0.2 \leq \text{a} \leq 6 \text{ mm, 30 kHz)}$$

$$V - V_0 = -0.016 - 0.614a + 43.39a^2 \text{ } (0.2 \leq \text{a} \leq 0.43 \text{ mm, 90kHz)} \qquad (2.12)$$

$$V - V_0 = -5.092 + 25.906a + 7.0a^2 \text{ } (0.2 \leq \text{a} \leq 6 \text{ mm, 120 kHz)}$$

where L is the specimen length. Another second order polynomial function for CC specimens (in composites) was given by [158]

$$\frac{a}{W} = -0.074447 + 0.158935\left(\frac{V}{V_0}\right) - 0.007054\left(\frac{V}{V_0}\right)^2 \qquad (2.13)$$

Linear Calibrations

Linear relationships between PD across the crack and the crack length or between the normalised potential and crack length were also obtained in several experimental works [23, 24, 37, 38, 78, 141, 154, 155]. The linearity of calibration curves was regarded as an advantage of the PD methods over the other NDT methods [45, 78]. By applying DCPD methods, McIntyre and Priest [23] obtained empirical calibrations for SEN, C(T) and WOL specimens (schematics are shown in Fig. 2.1g) which displayed linearity up to about $a/W = 0.7$ (note that the current was supplied from notched faces for all the geometries). Austen and Walker [154] established a series of empirical calibration functions for C(T) specimens containing different initial notch depths and in various sizes and materials. A unique linear calibration curve has been derived from all geometrically similar C(T) specimens providing that the current lead distance was remained in constant proportion. Wei and Brazill [38, 141] employed both ACPD and DCPD to monitor crack growth in C(T) specimens where the experimental data could be approximated well be a third order polynomial as:

$$a = 15.9 + 52.0\left(\frac{V - V_0}{V_0}\right) + 26.0\left(\frac{V - V_0}{V_0}\right)^2 - 41.4\left(\frac{V - V_0}{V_0}\right)^3 \qquad (2.14)$$

It was noticed that in an initial range extended to $a = 4.5$ cm (corresponding to $a/W = 0.6$), experimental data presented in [38, 141] exhibited a linear relation between normalised PD and crack lengths. The linearity of calibrations in ACPD methods for SEN specimens has been reported by [24, 37, 78, 155].

2.3.4 Identification of Crack Shapes and Locations

For an arbitrary crack without prescribed information (i.e. without unknown location and shape), the location of the defect can be detected by coarse observation of the electrical potential distribution, followed by fine inspection in the suspected region. Below, a short review is presented which summarises several papers involving various methods for identifying the shapes and locations of cracks.

Identification of defects within structures, such as tube-shaped specimens, has been evaluated by several studies. A boundary element based method was proposed to identify the shape of a surface defect on a tube [176]. Fig. 2.19a shows how Φ and Ψ, the electrical potential and current (stream) functions respectively, may be used to transform coordinates such that Laplace's equation (which Φ and Ψ must satisfy) can be conveniently solved. This technique benefits from constant

potential and stream on a boundary with the transformed domain being rectangular in shape. This enabled the transformed equations to be solved by applying the boundary element method and hence identify the defect shape. The numerical predictions compared well with known shapes of a single crack, multi-cracks, and a V-shaped crack. For the identification of crack length and crack depth of an in-depth elliptical crack, Hashimoto et al [177] presented a procedure that indicated crack length at specimen surface by the distance between a pair of inflection points of PD distribution by using a series of calibration curves for different crack aspect ratios. In a paper given by Chen et al [121], a single crack, an inclined crack and double inclined crack emended on pipe surface were detected and characterised with respect to crack length and inclined angle by observing a contour map of normalised potential on the pipe surface. In the contours, normalised potential values at selected points (distributed throughout the surface at certain horizontal and vertical positions) were computed by FEA and the difference of potential values between neighbour points calculated and compared with a proposed criterion that was determined as 0.01 for the 304 Stainless Steel (SS304) used in this study. Neighbour points satisfying the criterion were marked so that finally the location, size and angle of the crack was visible. A sensor based on the induced current PD method, which was a developed ACPD method and used an induction coil near the specimen surface to supply AC, was developed and applied to measure PDs around circumferential cracks and axial cracks embedded into the pipe wall [178]. A peak of normalised PD measured near a crack (called Representative-V_N) was assumed as the detection of the crack. A linear relation between the peak potential and crack depth that was approximated numerically and used for computing the crack length based on measured Representative-V_N, as illustrated in Fig. 2.20.
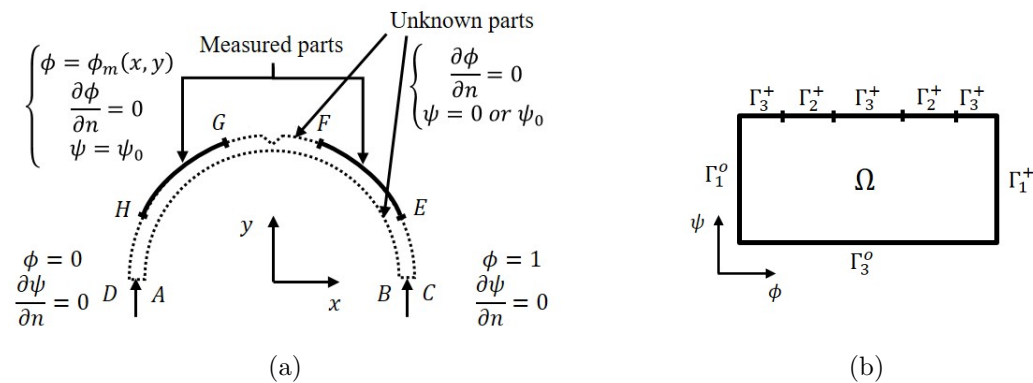
Figure 2.19: (a) Boundary conditions of potential distribution around a 2D surface defect. (b) The transformed domain containing a regular shape. [176]
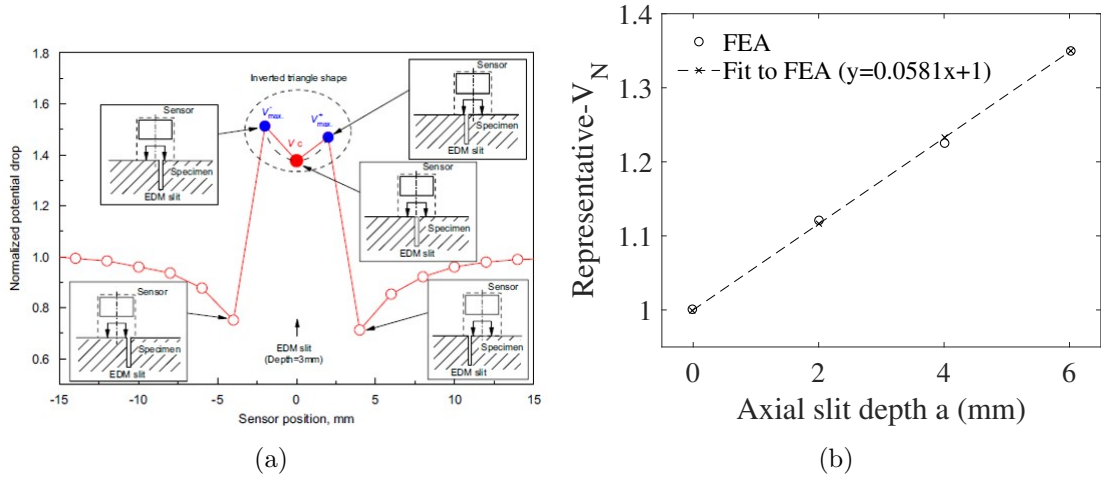
Figure 2.20: (a) Schematics of PD distribution around an surface defect and the Representative-V_N. (b) The linear relation between R-NPD and crack depth. [178]

Abé et al. have proposed techniques to identify plural parameters of 3D surface cracks in homogeneous body [179] and 2D surface cracks in inhomogeneous strips [180]. Saguy and Rittel [146] put forward a method for identifying the location and size of a straight crack (Fig. 2.21a) inside a rectangular specimen using a multi-frequency ACPD approach based on a numerical model. When evaluating a 'bottom crack', as shown in Fig. 2.21a, the author noticed that the V_N remained constant until the skin effect was increased to half of the un-cracked specimen thickness (the drop occurs at $\delta/(T-a) = 0.5$, T is the specimen thickness in Fig. 2.21b), i.e. the potential field was disturbed by the bottom crack at a depth half of the un-crack thickness and deeper. Without an explanation of how a value of 0.5 was determined, this criterion was used to reveal the upper un-cracked depth above the internal crack, then the lower un-cracked depth after flipping the specimen. The multi-frequency ACPD method has also been applied to predict the depth of a bottom crack by Li et al [11], with a particular focus on magnetic materials (steel) in a certain frequency range (5-15 Hz). In the presented method, measured V_N for certain crack depths were found to vary linearly with operating current frequency and a function relating crack depth to the fit gradients were developed by FEA. Experimentally, the bottom crack depths predicted by the slope-depth function showed good agreement with known crack depth (within an error of < 10%). A 3D identification method of semi-elliptical surface cracks was presented and numerically validated by Tada et al [181, 182]. The analysis was based on the electrical PD distribution measured by introducing a multiple-probe DCPD sensor that covered a relatively large specimen surface around the crack. Very recently, limited results have been presented by Buss et al for the determination of crack profiles using frequency sweep impedance signals [2]. The modulus and phase angle of impedance signals were expected to enable identify the geometries of specimen (such as cylindrical or square specimens) and crack features (such as

CC or edge crack).
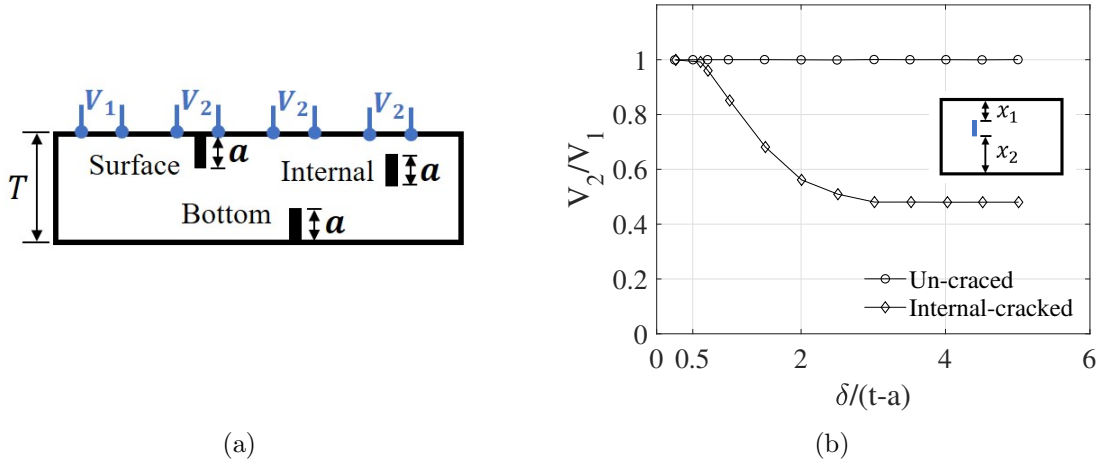
Figure 2.21: (a) The surface and bottom cracks investigated by Saguy and Rittel [146]. (b) The normalised PD ratio when the skin depth equals half of the un-cracked specimen thickness. [146]

2.3.5 Optimisation

2.3.5.1 Probe Configuration

A compromise between sensitivity and reproducibility of measurement should be taken into consideration when choosing the positions for current injection leads and potential measurement probes [81, 117, 140]. In an early study by Ritchie, Garrett and Knott [81], the graphitised electrical analogue paper method was used to determine the optimised positions of electrical probes. As illustrated by equi-potential lines in Fig. 2.22, the uniform current injection introduced from the end surfaces of the specimen was recommended for SEN(B) specimens, while for C(T) specimens the contact area of current injection on the top face was suggested. For C(T) specimens made of aluminium a point contact by screwing was preferred because reproducible area contact, brazing employed in steel, for example, was inapplicable and other area contact methods such as bolts and glues resulted in poor reproducibility. The most suitable positions for potential probes was suggested to be on the top face and close to the notch ends. In the same year, McIntyre and Priest [23] proposed the same arrangement of potential probes as the optimum, but reported that the position of potential probes on opposite sides of the specimen could average the length of curved cracks (also in [49]). The authors recommended current leads to be attached on the notched face and close to the notch for WOL, C(T), SEN(B) specimens with only consideration of sensitivity but without reproducibility.
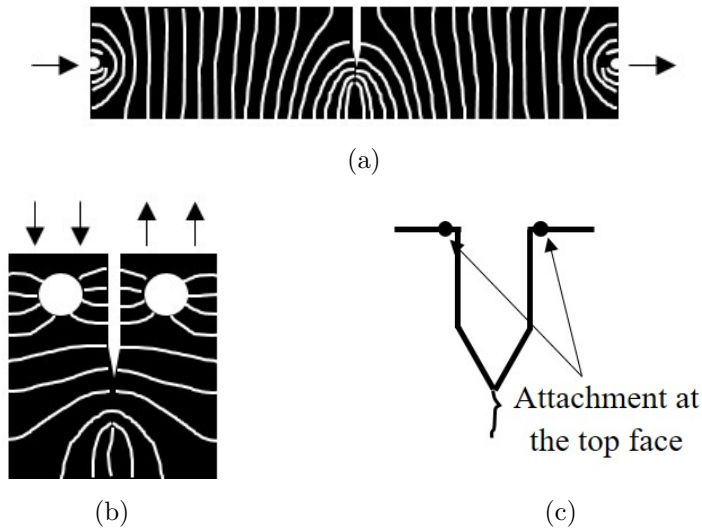
Figure 2.22: The optimum configuration of (a) current leads in SEN(B) specimens, (b) current leads in C(T) specimens, (c) potential probes in SEN(B) and C(T) specimens. [81]

Clark and Knott [82] identified the optimum position of potential probes for SEN specimens by moving the probes along the specimen edge until reaching the notch feature, upon which the probe travels perpendicular to the specimen edge (i.e. along the feature length). A relatively constant sensitivity was observed near the notch end, compared with high sensitivity at the notch tip, indicating a low density of equipotential lines and thus a high reproducibility. The good reproducibility for potential measurement near the notch end was also observed in C(T) specimens by Aronson and Ritchie [58]. They continuously investigated the results given by Ritchie, Garrett and Knott [81] for C(T) specimens based on a FEA program and experimental work. With current applied from the top face, they agreed with the standard configuration presented in [81], that the potential probes attached close to the notch on the top face was optimum. They also presented an alternative configuration for C(T) specimens made of high resistivity materials (note that the magnitude of measurable PD dropped to 40% of that generated by the standard configuration) that could offer a steeper calibration curve and better reproducibility. In this case, current leads were placed on the midpoints of side surfaces and the potential probes were positioned as before, as shown in Fig. 2.23. The same configuration was suggested by Klintworth and Webster [44] from the same considerations of proportional increase in PD with crack length and less vulnerability to probes location. Via FEA simulations, steep calibration curves have also been obtained by moving current injection from the top to the side [132]. But differ to preceding studies in which current was applied by point contact [44, 58], in this paper, a uniform distribution offered by area contact was employed on the side surfaces. The alternative configuration for C(T) specimens with current supplied at the side faces was employed by a
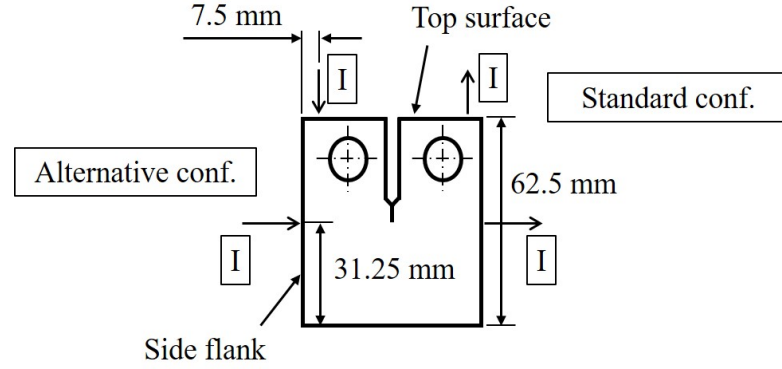
Figure 2.23: The alternative configuration for C(T) specimens with current injected from the midpoints of side surfaces. [58]

number of studies, such as [75, 163, 165, 170]. As for centre-notched specimens, generally, the current is supplied at two ends, away from the centre crack and the potential probes are placed across the crack [48, 51, 102, 129, 131, 152, 162, 163]. The configuration of M(T) used in [131] is given in Fig. 2.3a. When a M(T) specimen contains an asymmetrical crack, as reported by Pulle [102], increasing the proximity of potential probes offers better sensitivity but also results in a vulnerability to asymmetrical crack growth and thereby leads to underestimation in crack length prediction. In a study of monitoring Mode III fatigue cracks under torsion (involving application of FEA) [117], the author determined the optimum potential probes of circumferential notch cylinder specimens to be at the notch edge with both considerations of sensitivity and reproducibility.

In addition to a single pair of potential probes used in conventional configurations, a dual pair of potential probes, which would provide a reference potential signals measured in a crack-free region, is widely used as it allows for the normalisation of the measured potential signals and compensates for variations in current and temperature, in addition to improving reproducibility [21, 104]. Multiple potential probes have been applied to identify multiple crack parameters including curved profile [122, 137, 156, 181, 182], inclined crack angle and location [122, 181, 182], and to detect crack initiation and monitor crack growth in ceramic composites [15]. For the purpose of revealing surface crack profiles, Harrington and Bell [183] developed a mobile probe arrangement in which a moveable single pair of potential probes instead of multiple fixed probes was employed. The sensitivity of crack depth/length identification for small cracks (< 5 mm) has been further improved by a simultaneous application of a standard and a staggered probe configuration. A directional square-electrode sensor has been developed for creep monitoring in which creep behaviour was related to the variation of the ratio of two resistances measured in orthogonal directions [86, 147, 148].

2.3.5.2 Normalisation

Normalising the PD (against a reference potential) and the crack length (against a specimen dimension) helps to compensate the variation of injecting current, test temperature, material properties (including time- or temperature-dependent resistivity changes) and specimen thickness. If this point is taken to its conclusion, calibration becomes a function only dependent on specimen geometry and the probe arrangement, meaning that geometrically similar test-pieces share identical calibrations. There are several methods to determine a reference potential value; measuring across a specified crack length such as the initial notch [7, 44, 46, 58, 119, 141, 154, 156, 170], measuring on the initially un-cracked test-piece [119, 121, 164], measuring on a separate reference specimen placed in the same condition as the test-piece [12, 37, 49, 129] and measuring in a region remote from the crack so that the current field is independent of the crack and remains homogenous (as mentioned for the dual pair potential probes) [4, 52, 55, 78, 79, 83, 84, 104, 184, 185]. Normalisations using a singular reference value allows the elimination of the effects of inherent material properties but excludes sustaining errors due to the variations of temperature and current during testing [152]. These errors can be accounted for by on-line normalisations that involves the measurement of a reference specimen or in an unaffected part of the test-piece. Additional error is likely introduced by using a second specimen (due to slight variations in geometry and properties specimen to specimen). Difficulties in determining the location of a second pair of potential probes arise from limited uniform current regions in some specimens such as C(T) [43], M(T) [152] and through crack [156] specimens.

A normalisation method that accounts for thermal emf and initial crack lengths has been applied to generate empirical calibration curves by Saxena [51]. In this study, the potential increase caused by emf was added into the potential normalisation and the size of the initial crack was covered by the crack length normalisation. The resulting empirical calibration curves were shown to be independent of material and temperature (similar calibration curves were obtained for A470 steel at 538 °C and SS304 at 594 °C) and provided accurate predictions of crack extension with error of less than 10% under creep.

2.3.5.3 Thermoelectric Effect

The emf is generated due to a temperature difference at connections between the test-piece and the electric probes and produces an error in the PDs superposed on measured signals. The effect of emf can be reduced by using electrodes made of the same, or closely similar, material as the test-piece [125, 139, 150, 152] because of similar thermal material parameters. Potential signals can be measured by periodically switching on and off the operating current [4, 51, 52, 79, 83, 102, 104, 128, 152, 184] or altering the current direction [128, 152, 177], then the PD between two readings are calculated as the real output signal caused by crack extension

with a minimised emf effect.

2.3.6 Effects and Errors on Potential Difference Measurements

2.3.6.1 Effects: Specimen, Notch and Crack Geometries

Calibration curves and PD measurements are sensitive to the crack/notch geometry [3,4,47,58,131–133], the specimen geometry [4,47,51], the arrangement of current injection [3,4,51,58,132] and the location for potential measurements [4,47,51] (the latter two factors have been covered in Section 2.3.5.1). In this section, studies relating to the effect of specimen geometries, crack and notch geometries will be reviewed.

Specimen thickness has a significant effect on generated calibration curves, as observed in M(T) specimens by beach marking [152]. It was concluded that the effect of thickness could be minimised by: 1) normalising measured PDs by potential across a reference crack rather than in an unaffected region away from the crack, and 2) decreasing the distance between the voltage probes across the centre notch. The significant effect of specimen thickness on calibration has also been discussed in an independent study [133], in which the influence of three geometrical parameters of a rectangular specimen on the PD measured across a through-width axial crack were studied using a 3D FEA model. The rectangular specimen containing a through-thickness surface crack is shown in Fig. 2.24a. The effect of specimen width and length (W and L in Fig. 2.24a) on calibration was almost negligible for shallow cracks while the effect of thickness (T in Fig. 22a) was noticeable for large crack depths. The variation in calibration curves for through-thickness surface cracks, caused by different specimen thickness, is shown in Fig. 2.24b. For larger specimen thickness, PDs increased as crack extended up to deeper crack depths and at lower increasing rate.

(a)   (b)
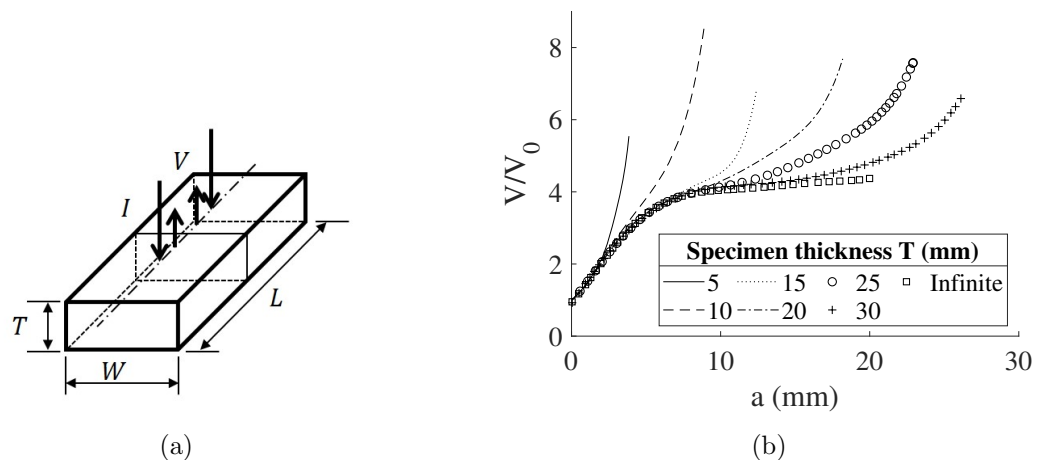
Figure 2.24: (a) Geometries of the rectangular specimen and the through-width axial crack. (b) Effect of specimen thickness T on calibrations. [133]

The electrical conducting paper analogue method has been applied to centre-notched plates to determine empirical calibration curves by Smith [119]. In Fig. 2.14c in Section 2.3.3.5, calibration curves for cracks initiated from centre notches with different elliptical ratios, including notch shapes of slit, circle and ellipse, varied slightly for small crack lengths ($a/W < 0.4$) but were coincident for larger crack lengths. Hence, the effect of the shape of centre notches was suggested to be neglected in practical uses. As for SEN specimens with semi-elliptical notches, Clark and Knott [82] have analytically calculated the calibration curves for of cracks with different elliptical ratios. It was observed that as the calibration related potential ratios to total lengths were summed over lengths of the crack and the varying notch, the effect on potential increased caused by crack growth was ambiguous. A comparison of analytical calibration curves of cracks initiated from V-shaped notches at different angles was also given in [82], as shown in Fig. 2.8 in Section 2.3.3.2. The notch length remained constant as angle was varied, thus the calibration curves effectively showed that the crack length predicted by a certain increase in potential ratio increased substantially as the angle was increased.

By simulating C(T) specimens with FEA [132], it was suggested that the width of the starter notch in C(T) specimens affected calibration curves significantly, in which a potential increase of 25% would result in a difference in crack length prediction of about 30% between the cases of zero-width and infinite-width notches.

With respect to the crack profile, the depth of a curved crack will be underestimated by calibrations developed for straight front cracks [9, 75, 93, 165]. Side groove specimens are less susceptible to tunneling and thus allow better capability of producing calibration curves [25, 75, 123]. Moreover, the introduction of side grooves has been shown to have negligible influence on calibration by experimental studies [50] and numerical schemes [165].

The effect of deflections in the path of an edge crack attributed to surface roughness on calibrations has been evaluated by comparing calibrations for fine and coarse serrated edge cracks [156]. The effect of small crack path deflection was shown to be negligible, thereby the calibration curves for simple straight edge cracks remained feasible, which was the case for commonly used specimen types in most practical studies. Broadly speaking, current paths will flow along all free surfaces belonging to both the specimen and the crack feature. It has been found however that, as a surface crack grows and becomes comparatively deep, current paths will not penetrate to the tip of the crack but flow through the surface along the crack length, meaning that crack depths cannot be correctly resolved [14]. A decrease in crack aspect ratio (the ratio of crack length on surface to crack depth inside material) was considered to introduce a reduction in accuracy of the ACPD method. By way of example, when there is an aspect ratio of less than 5, a difference between predicted and optically measured crack depths of more than 10% can be observed.

2.3.6.2 Effects: Operating Frequency of ACPD

Crack growth in WOL specimens has been monitored by the use of a multi-frequency ACPD method [37], in which a single linear calibration curve, given by different frequencies (150, 1k and 10k Hz), has been found up to a crack lengths as high as $a/W = 0.9$, as shown in Fig. 2.25. This led to the conclusion that the linear slope of calibration was independent of operating frequency.
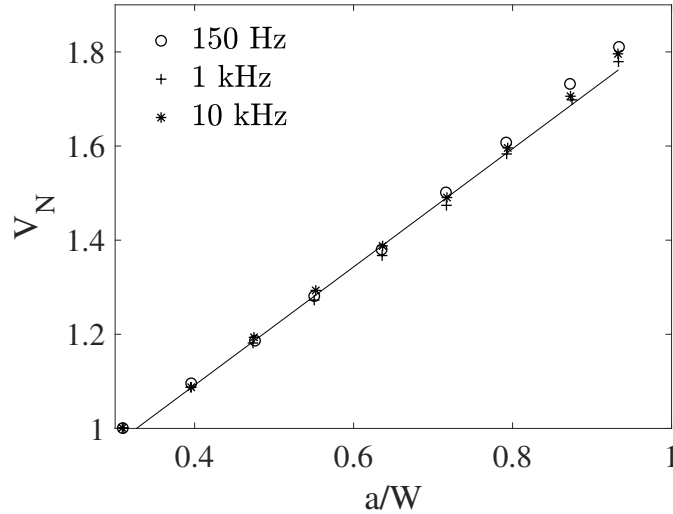
Figure 2.25: A signle ACPD calibration curve obtained by applying various frequencies [37]

Nevertheless, in another study that used a multi-frequency ACPD method with a smaller range of operating frequency (93-940 Hz), it was shown that linear slopes of calibration for SEN specimens [24] decreased noticeably with reducing frequency and the PD across the crack was found to be proportional to the square root of frequency (Fig. 2.26). The same correlation has also been reported by a work monitoring surface crack on un-notched steel rods with high frequency ACPD [134]. Other studies found that non-linear, second order polynomial calibration curves were the result of using multi-frequency ACPD for SEN specimens with frequencies of 17, 127, and 203 kHz [126] ((2.11)) and at 30, 90, and 120 kHz [135] ((2.12)).
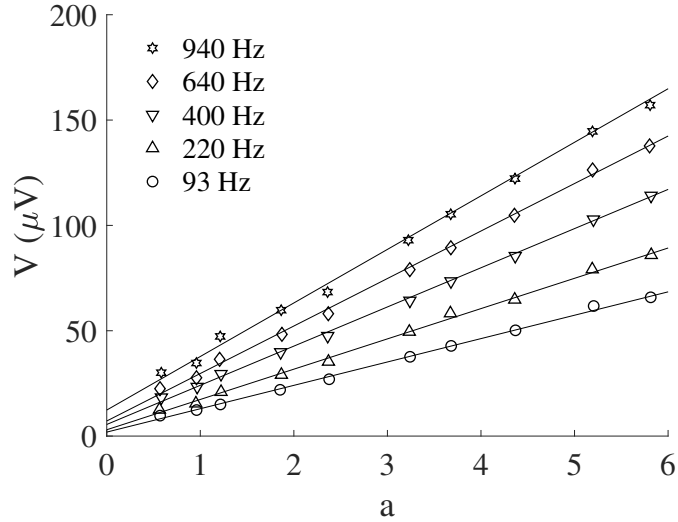
Figure 2.26: ACPD decreases with reducing frequency [24].

2.3.6.3 Error: Plastic Deformation

Plastic deformation that usually occurs under fatigue, creep, sustained/increasing load level conditions affects the material resistivity and specimen geometry around the crack, and in turn produces additional potential variations [37, 62, 74, 82]. Ritchie, Garrett and Knott [81] negated the configuration in which potential probes were attached near the crack tip on C(T) specimen because of the sensitivity to crack tip plasticity (also variations of probe positions). Saxena [51] explained the discrepancies between crack lengths measured optically and those predicted by a previously defined experimental calibration curve by the plastic deformation in the specimen around the crack tip. Ritchie and Bathe [59] presented an hypothesis that by combining experimental measurements on an un-cracked specimen and numerical analysis on fractured specimens, the PD signal caused by crack tip plasticity could be separated from that due to crack extension. The effect of consequent geometry deformation and resistivity change caused by plastic deformation on the calibration curve has been investigated quantitatively by Ljustell [12], which led to the conclusion that the generation of spurious potential signals was dominantly (90%) caused by geometry changes. To improve the accuracy, similar to the suggestion given by Ritchie and Bathe [59], the use of a reference potential measured from a reference test-piece that undergoes the same load level and is in the same deformed state was recommended [12].

2.3.6.4 Error: Crack Closure

Crack closure (the contact between formerly opened fracture surfaces under cyclic load), usually introduces an electrical short across the crack, thereby leading to underestimation of PD. This has been widely observed experimentally [38, 52, 102, 136, 137]. There is no closed solution to eliminate the bridging effect, but the effect can be reduced by measuring the PD at the maximum load (and therefore

maximum crack opening) within each cycle [38, 52].

2.3.6.5 Error: Temperature Variation

Error signals due to thermally induced voltage was discussed in Section 2.3.5.3. Here the inaccuracy introduced by temperature dependent resistivity is discussed.

Temperature fluctuations during PD measurement influences the electrical resistance and magnetic permeability of conductive specimens and in turn affects the PDs. Accordingly, a temperature increase of 3 °C gives rise to a 1% increase in resistivity of aluminium alloys [43]. The temperature variation can be introduced by a few of factors such as material resistivity, current density and input method, environmental temperature and heating/cooling methods used [152]. Noticeably, a dependence of calibration curves on testing temperature was found by Dai et al [78] and Campagnolo et al [3]. Therefore, constant current supply and controlled temperature conditions, such as an immersion in an ice bath [23], is desirable [43]. Generally, normalisation of measured potentials by reference signals has been employed within several studies in order to compensate for this error (as mentioned in Section 2.3.5.2). An experimentally determined temperature coefficient of the test-piece was used to give an additional PD increase due to temperature increase, which would be subtracted from the measured potential [152]. It was noted that long warm-up times of the equipment before use helped to stabilise the temperature (5 hrs was suggested by Sidey [48] and Hosdez et al [7], 24 hrs was suggested by Halliday and Beevers [43]).

2.3.7 Applications

2.3.7.1 Asymmetric Cracks

The effect of asymmetrical crack growth on PD measurements is shown to introduce an underestimation of total crack length [102, 104]. The error increases as the asymmetrical crack grows [103, 104] and as the potential probes approach the crack [102]. Hence a compromise with respect to the determination of the position of potential probes between reading sensitivity and the asymmetric effect is necessary [102]. The advance of an asymmetrical crack which grew from a symmetric crack has been predicted by Read and Rfuff [103]. In this study the direction of the asymmetrical crack (the left or the right half of the crack grew faster) was indicated by the sign of a term denoted as the 'asymmetric' potential. This was measured at two points at equal distances from the centreline, see Fig. 2.27. The asymmetric potential vanished around symmetrical crack and became a positive or negative value around an asymmetrical crack depending on the crack direction. The magnitude of the crack length difference (between the left and right sides of the centre line) was then determined by a solution to the Laplace equation that related the potential field around an asymmetrical crack to the crack length difference. This asymmetric electrical field expression, derived from Johnson's
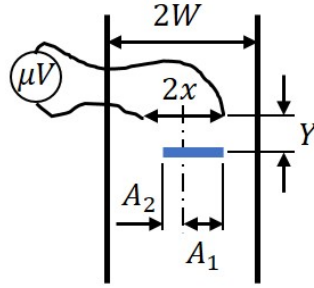
Figure 2.27: Asymmetrical potential measured at (X, Y) and $(-X, Y)$ above an asymmetrical centre crack. [103]

formula [131], replaced the boundary conditions of a symmetrical crack by the asymmetrical equivalent. Polynomial calibration equations for a limited number of crack lengths and asymmetrical extensions were given. An open solution for the expression derived by Read and Rfuff [103] has been provided using a numerical FORTRAN program by Link et al [104]. The numerical solution is capable of the determination of the potential response at any point in the specimen containing either a symmetrical or an asymmetrical crack. A measurement technique was then suggested to take the most robust utilisation of this numerical calibration.

2.3.7.2 Angled Cracks

The electrical-potential computed (EPTC) method (which relies on performing inverse analysis on measured PD fields) [105] was developed for measuring multiple crack characteristics including the location, size and shape of 2D and 3D surface and internal cracks in a number of studies (in Japanese). In a subsequent study [106], a multiple current application method combined with the EPCT method was suspected to be able to provide enough information to quantitatively identify a 2D crack inclined at an unknown angle, as shown in Fig. 2.28. The multiple parameters (crack length, angle and location) of an inclined crack were determined by a least residual method in which potential values were computed by boundary-element analysis based on previously assumed crack parameters, then by comparing the computed potential values and experimentally measured values (by DCPD). The most accurate assumption was then suggested by a minimum residual between the two. The current was injected by 5 pairs of electrical leads alternatively and the resulting potential fields processed simultaneously by the described method. Analytical and empirical calibrations for short surface cracks at angles of 90° and 45° to the specimen edge have been established by using the semi-infinite conformal mapping and graphitised paper analogue technique [155]. The analytical and analogue calibration curves agreed well for small cracks of about $a/W \leq 0.2$ for the two cases of the crack being perpendicular and at an angle of 45° to the specimen edge.

43
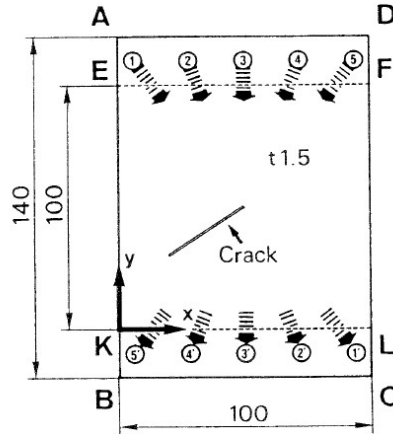
Figure 2.28: Schematics of the multiple current application method and the 2D crack inclined at an unknown angle. [106]

2.3.7.3 Multiple Cracks

Under combined stress loading and aggressive environments, it is likely that multiple cracks will initiate [109,112]. Tada et al have conducted a series of studies on the distribution of electrical PD fields around multiple cracks. First a numerical method namely superposition method (SM) was applied to calculate PDs around a semi-elliptical surface crack that accounts for the effect of back face of the cracked specimen in case the crack size is comparable to the specimen thickness [107]. This technique was then extended to investigate the potential field around multiple through cracks with different lengths and in random positions [110]. A good level of agreement was achieved between potential values calculated by SM and those obtained by the random walk method. The superposition method has also been investigated under the name of the 'crack-current modification method' (CCMM). In particular, it has been used to investigate the potential around multiple internal cracks under creep-fatigue conditions [111]. CCMM has been further developed for evaluating the potential distribution around multiple inner spherical defects at random angles [113,116]. A calibration equation for multiple inner circular cracks with random angles was also presented, which related the PD to several parameters of the defects distribution including volumetric density and mean cubed defect radius.

A DCPD-based iterative procedure has been developed for evaluating the crack depth of 2D multiple cracks perpendicular to the specimen top surface and parallel to each other [108]. In this procedure, the PD at two points across the target crack was measured by DCPD first, then the crack depth was assumed and the PD numerically calculated based on this assumed value. Trial crack lengths were iteratively varied until predicted and measured PD values converged. This method required the generation of a numerical mesh covering the whole specimen, which limited the usage for practical structures containing a wide distribution of cracks [109]. Thus, this method was simplified by introducing a sub-region that only

contained the target crack and its nearest four neighbour cracks at first. The depths of two end cracks of the sub-region were assumed to be fixed, and the depths of the other cracks were assumed. Similarly, the PDs at the two points inside the sub-region were measured and numerically calculated, and this iterative process was repeated until an acceptably small difference was achieved. The assumed depth of end cracks was then changed and the same procedure repeated. If similar results of target crack depth were given by different end crack depths then the process ended otherwise the width of the sub-region was increased to contain more cracks and the iterative process restarted. The effect of crack interaction has been evaluated by using the concept of subregion [114, 115]. As the sub-region size increases to contain more cracks, the PD across the middle crack was successively measured by DCPD. The ratio of two successively measured PDs was proposed to quantitatively express the effect of crack interaction arising from the end cracks on the middle crack, with applicability regardless of crack distances.

Based on an empirical calibration equation given by FEA, a solution has been proposed to predict the PD between two points on both sides of a target crack among a number of 3D semi-elliptical surface cracks perpendicular to the specimen surface, but at random angles to the current flow direction [112]. Starting from a PD without any cracks present, the PD change introduced by the introduction of a crack, the influence of a finite plate, and the interaction between multiple cracks were successively added into the equation. After assuming a value of the depth of the target crack, the PD between two points was measured directly and calculated by the equation, and an iterative process repeated until an acceptably small value was obtained between the two.

2.3.7.4   Mixed Model Fracture

The measurement of open cracks propagated under tension, i.e. Mode I, by the PD method has been widely developed in many studies. It has been shown by Ritter and Ritchie [117] that in Mode III (out-of-plane shear) fatigue under pure cyclic loading, torsional cracks would result in electrical shorting across the crack thereby impeding potential measurement. To minimise this effect, an additional small axial load superposing the cyclic torsion was suggested. In this study PD increase across a finite-width slot was measured in order to avoid electrical shorting. The application of DCPD has been extended to measurements of straight cracks propagated in Mode II (in-plane shear) through the employment of specially designed specimens in which a pure shear stress field can be generated [118]. In a study considering mixed Mode problems (tension and in-plane shear) [16], the length and orientation of inclined cracks developed in mixed Mode conditions has been obtained by introducing a third potential probe in the middle of the shear specimen. An algorithm based on the assumption of a linear relationship between a ligament size measured from the crack tip to the specimen border and the PD signal has been developed in order to automate the experimental determi-

nation of crack growth rate and crack tip position under the same mixed loading conditions [186].

2.3.7.5 Torsion

An empirical calibration formula has been established for circular notched specimens subjected to torsion by Hay and Brown [167]. For small crack depths, the obtained calibration equation showed good agreement with analytical solutions provided by Clark and Knott [82] for 45° V-notched SEN specimens (Fig. 2.9 in Section 2.3.3.2). It was claimed that the calibration was valid up to a depth of 2 mm. A similar study was also conducted by Ritter and Ritchie [117] which computed the potential field at the surface of torsionally loaded circular notched specimen by using FEA. Ritter and Ritchie stated that their numerical calibrations, which were experimentally verified, were consistent with the work of Hay and Brown [167].

2.3.7.6 Stress Corrosion

PD methods have been applied to monitor stress corrosion cracks (SSC) that propagate under a combination of corrosion and fatigue loads [23, 88–90, 119, 175, 178]. In an investigation of the effects of aggressive environmental factors (water and water vapour) on crack growth in high strength steel by Johnson and Willner [88], crack extension was monitored by PD measurements combined with a predefined empirical calibration curve for M(T) specimens. McIntyre and Priest [23] noticed that rough fracture surfaces deformed by corrosion would produce electrical shorting and in turn reduce measurements of PD. To minimize this effect, a correction factor that compared expected potential increase without electrical shorting to actual changes was introduced. A joint use of PD and acoustic emission methods was applied to measure SSC extension by Santos-Leal and López [90], in which correlations of measurements obtained by the two techniques were studied and used to illustrate the acoustic emission magnitudes. For information and comparison with both DCPD and ACPD methods [178], a modified eddy current technique which entails two induction coils located near the surface of a test-piece was proposed to possess higher sensitivity of continuous monitoring of SCC.

2.3.7.7 High Temperature: Fatigue and Creep Loading

The capability of PD methods to detect crack initiation and measure crack propagation at elevated temperatures has been investigated in several studies [8, 51, 77–79, 187]. The greatest challenge for the application of PD methods at high temperature lies in ambiguous potential signals, which mask the potential increase caused by crack extension, attributed to creep deformation, microstructural changes, and bridging between crack surfaces [42]. Errors in crack extensions during creep

(under static loading at 500 °C) obtained between measured values and those predicted by calibrations predefined under fatigue loading were supposed to be due to changes in geometries of the specimen and crack tip caused by high temperature behaviour deformation [51]. Moreover, crack propagation is faster under elevated temperature, which was observed on powder metallurgical nickel-based superalloy by Na et al [159].

PD methods offer reliable tools to detect crack initiation and monitor crack propagation under fatigue loading at elevated temperature. Usually as the cycles of fatigue load accumulate, PD remains constant at first, then begins to increase gradually after the onset of crack initiation or propagation from notch root [77,79]. Note that whether the noticeable increase of PD should be regarded as indication of crack initiation or propagation remains as an open question, which depends on the resolution of the technique applied. Clear transition from seemingly constant to increasing DC potential signal has been observed on circular SS304 notched specimens in both strain and stress controlled fatigue tests at 500 °C [77]. A similar transition in AC signals due to crack initiation and growth has been obtained on SEN specimens of Ti64 in isothermal fatigue test at 400 °C (while in TMF of Ti6246, potential signals increased continuously at increasing growth rates without the initial constant region) [78]. Pure fatigue tests under sustained loading were conducted on SS304 centre-circular notched specimens (Fig. 2.29) at 600 °C by Merah et al [79]. As displayed by Fig. 2.29b, a sudden jump in DC potential signal, due to notch opening and notch induced plastic deformation was followed by a constant period until the end of the crack initiation stage, then a gradual increase and some subsequent step changes indicated crack propagation. In this case, the crack initiation stage was suggested to be determined as a 1% increase in normalised PD. The step changes occurring at elevated temperature in Fig. 2.29 were explained by the contact of multiple cracks and secondary cracks. The behaviour of the same specimen under creep-fatigue tests were investigated in a sequent work given by Merah [83]. Different to pure-fatigue testing reported in [79], during sustained loading the potential starts increase immediately after the initial jump without a stable region (Fig. 2.29c), hence the initiation was suggested to be determined by a deviation from linearity in DCPD-COD curves (crack tip opening displacement, see details in the Section 2.3.7.10).
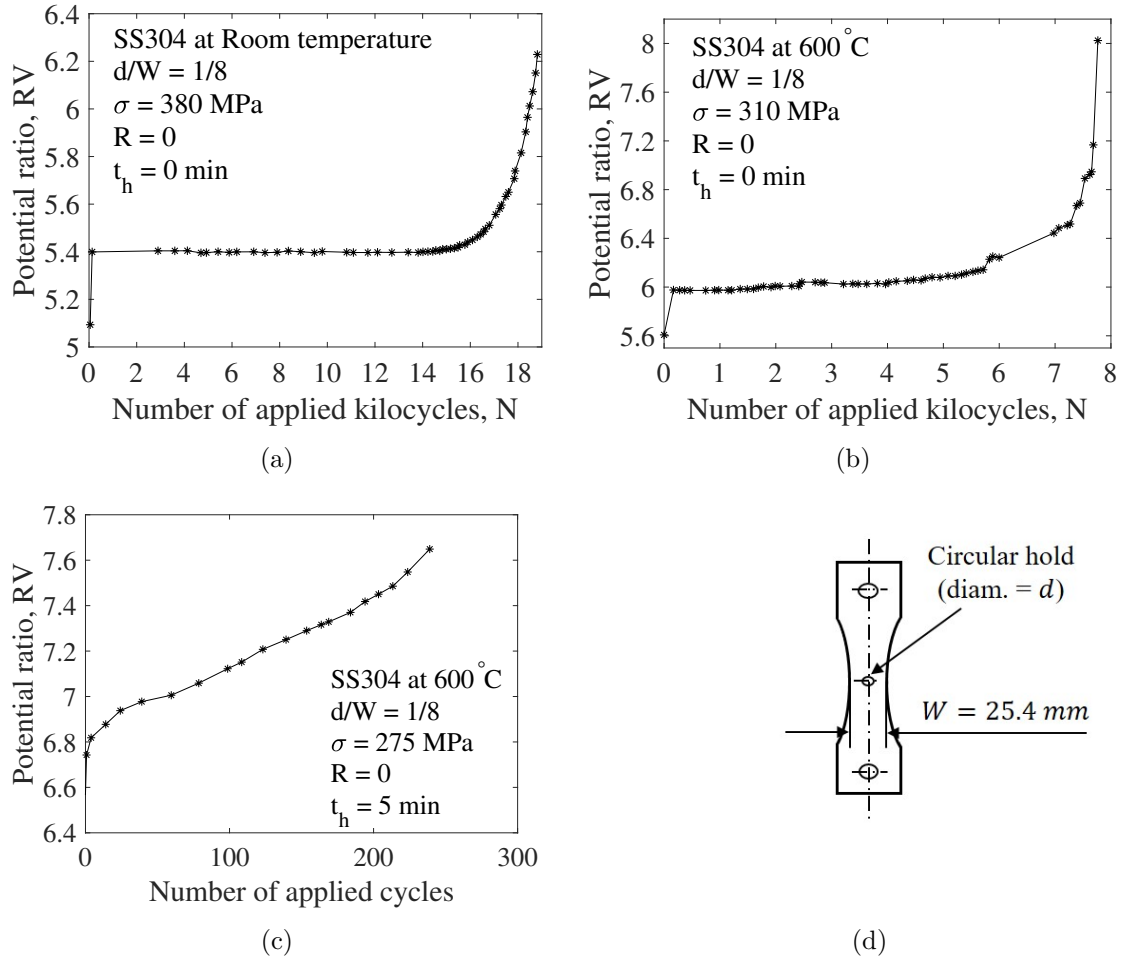
Figure 2.29: PD variations with the number of applied cycles (a) at room temperature, (b) at high temperature (600 °C) and (c) at high temperature (600 °C) with hold hour t_h of 5 min, (d) the SS304 centre-circular specimen. [79, 83]

Empirical calibrations, established under fatigue loading at over 500 °C, for C(T) and CC(T) specimens made of SS304 and A470 steels, have been used to predict crack extensions during creep under static loading with and reasonable accuracy (maximum error of less than 10% compared with results measured by beach marking) by Saxena [51]. Linear empirical calibrations under isothermal and TMF testing conditions have been established by ACPD by Dai et al [78], in which the linear slopes were shown to decrease with increasing temperature and be independent to TMF cycle type, i.e. similar slopes were given by out-of-phase and in-phase conditions. However, it was noticed by Merah et al [79] that higher sensitivity in calibrations was exhibited at 600 °C than at room temperature. This was rationalised by the increase of crack tip plastic zone radius at high tempera-ture. The disagreement in regard to the dependency of calibration sensitivity on temperature is shown in Fig. 2.30. To enable the determination of crack length under high temperature and creep conditions, two corrections were suggested to extend the calibration curve obtained at room temperature ('Prediction 1' in Fig. 2.30b) into a pure-fatigue equivalent at high temperature ('Prediction 2' in Fig.

2.30b) [79] and also then into a creep-fatigue equivalent [83].
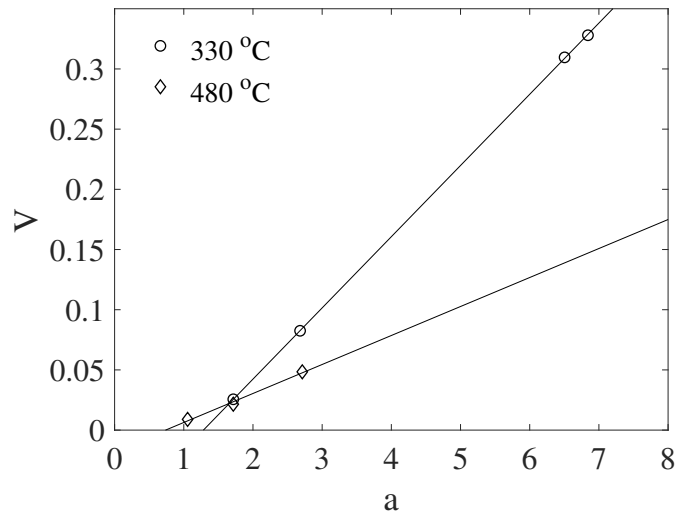
(a)
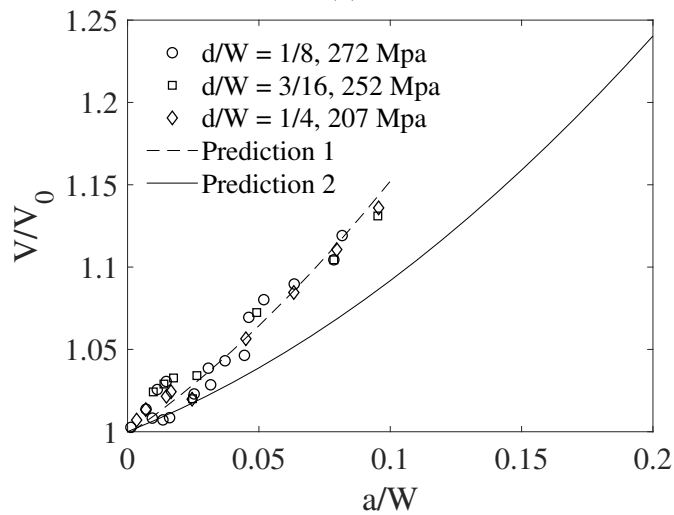
(b)

Figure 2.30: The effect of sensitivity of calibrations (a) ACPD calibration curves at 330 °C and 480 °C for Ti6246 [78], (b) DCPD calibration curves at room temperature and 600 °C for SS304, Prediction 1 – given by a calibration function established at room temperature, Prediction 2 – the calibration function was corrected for high temperature [79].

2.3.7.8 Creep Damage

PD methods have been used to evaluate creep damage, especially at early stages, which benefit from a detectable reduction of electrical resistivity at initial stages, whereas such a small level of creep damage is undetectable by most other methods such as microscopy [41, 128]. A directional quasi-DC (i.e. low frequency AC) ACPD sensor was developed for in-situ monitoring creep damage [86, 147, 148], as shown in Fig. 2.31. Additionally, PD methods have been used for creep damage evaluation with association to distribution of internal cracks [85] and creep strain

[20, 87, 149, 188]. Results of creep damage evaluation derived from PD methods obtained before 2010 can be found in a review by Sposito et al in 2010 [41].
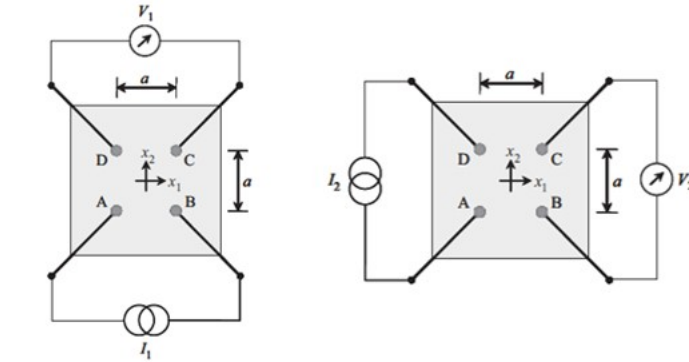
Figure 2.31: Schematics of a directional ACPD sensor for in-situ creep monitoring. [147]

PD methods have been employed to estimate the toughness degradation in 1Cr-1Mo-0.25V steel by Yu et al [128]. As shown in Fig. 2.32, opposite but corresponding variations in electrical resistivity and fracture appearance transition temperature (FATT), which is measured for the remaining life of subjects thus represents the material toughness, with respect to aging times (at 630 °C) have been found in that resistivity decreased substantially while FATT increased substantially as aging time increasing up to 5000 hrs. Such synchronous correlation between material resistivity and toughness enabled PD methods to predict the degradation of toughness.
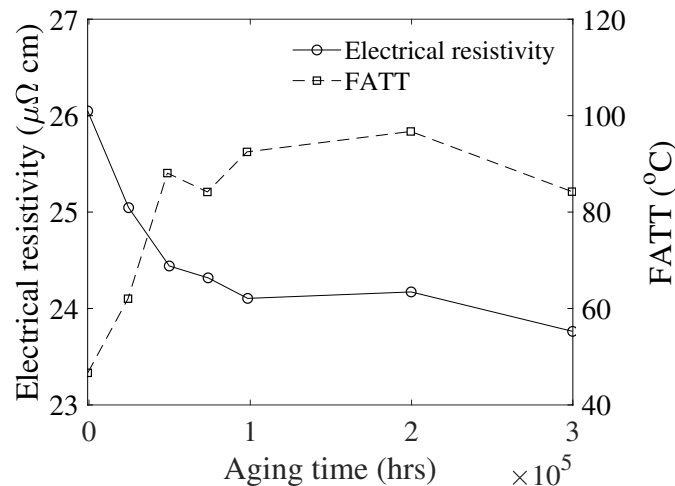
Figure 2.32: Correlation of electrical resistivity and FATT with aging time. [128]

2.3.7.9 Sustained Load

PD methods have been used under dwell time and sustained conditions [18, 84, 91, 92], for example, to monitor subcritical crack growth in AM350 SS with effects of

environmental factors [91], and to study creep crack initiation and propagation in IN-X750 [84]. In a study of fatigue crack growth with an introduction of dwell-time at maximum load [92], DCPD was unable to detect crack growth during a 45 min dwell, due to low crack growth rates (less than 10^{-4} m/cycle). In following sustained load tests for periods of 170 hrs, no crack increase was recorded until the maximum stress intensity factor was increased up to 36.8 MNm$^{-1.5}$, as illustrated in Fig. 2.33. The infeasibility of DCPD has been agreed by Gardiner [93], in which DCPD failed to indicate crack growth that was been clearly revealed by a heat tint. Nevertheless, crack growth rates for sustained load conditions have been successfully obtained by PD methods [18, 84], particularly for high growth rate cases.
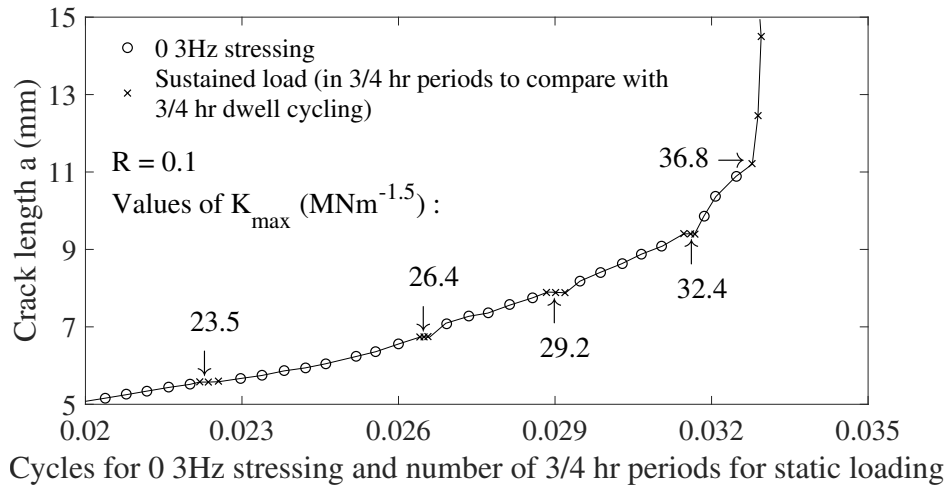
Figure 2.33: Crack growth under sustained load for Ti-6Al-4V bar. No rapid crack growth occurred until at $K_{max} = 36.8$ MNm$^{-1.5}$. [92]

2.3.7.10 In Crack Opening Displacement Tests, R-curves and Crack Initiation Determination

As a further application of monitoring crack growth, PD methods have been widely applied to crack opening testing for the determination of crack initiation and crack growth resistance curves in terms of J-integral or COD, δ [53].

An increase in PD signal has been observed as a response to crack initiation and in turn the feasibility of DCPD in detecting crack extension has been validated [139]. The determination of R-curves by PD methods is achieved in three steps. Firstly, PD signals are measured by DCPD/ACPD while load-line displacements/crack mouth opening displacement can be recorded (e.g. by means of a clip gauge). Next, the measured PDs are transferred into crack length based on an appropriate calibration. Lastly, the J or δ at all data points were calculated using available standard definitions, and hence J or δ resistance curves against crack growth are established. The validity of R-curves resulted from the PD methods has been validated by the agreement between curves obtained from

the regular multi-specimen technique [25, 74–76, 189], the unloading compliance method [25, 49, 50, 73], and other methods, such as the key [49] and normalisation methods [5, 189].

There are several advantages of PD methods in terms of determining R-curves. The determination of R-curves using these techniques can be completed with a single specimen, which liberates the use of multiple specimens as for other methods and thus reduces experimental cost and the influence of material scatter [74, 76]. PD methods can be applied in quasi-static and rapid load rate testing [49, 50, 189], noting that elastic compliance techniques are not readily adaptable to rapid loading because periodic unloading after specific crack growth interval is necessary for measuring the compliance of the specimen. Moreover, unlike the compliance method in which only discrete points could be provided, continuous curves are achievable by PD methods [50].

Based on different arrangements of current leads on C(T) specimens, there are two types of indications of crack initiation that will be exhibited on potential signal to clip gauge displacement curves (PD-U) [25] one with current injected on the top surface containing the crack mouth indicates the initiation by a minimum potential. The other, with current leads positioned on side faces, points out initiation by a deviation from an initially linear relation. With respect to second indication, the linear portion method, the determination of crack initiation by the intersection of the blunting line with J R-curves was preferred since the deviation criterion gives lower J_0 in materials with relatively high ductility [25].

The minimum potential signal indication has been validated in other studies [37, 74, 76]. The initiation point recognised by ACPD by Okumura et al [74] only coincided with actual initiation points obtained from the multi-specimen method at low frequency (150 Hz) but gave earlier predictions at high frequency (4.7 kHz) for high initiation COD (greater than 0.1 mm). The influence of current operating frequency on PD signals was reported by Gibson [76], that J_{min} decreases with increasing frequency, which led to the conclusion that the minimum ACPD signal was not always suitable for detecting crack initiation. It was argued that PD signals should be corrected for the contribution from the effect of stress on the resistance of the specimen and the initiation could be determined by a deviation from linearity of the PD-J relationship. The behavior of the change in a linear slope in PD-U curve has first been observed by Lowes and Fearnehough [73] in using DCPD to determine the initiation of ductile tearing. The linear criterion of ductile crack initiation was later verified by a number of studies [50, 75, 83]. In some rapid loading testing conducted on ferromagnetic materials by Vassilaros and Hackett [50], a pulse of PD occurred in the early part of the loading cycle, which hindered the determination of crack initiation using the linear criterion, which was presumably due to capacitance effect [50] or ferromagnetic properties [189]. The PD pulse that arise in dynamic loading tests of ferromagnetic materials have been investigated by Oh et al [189], which has led to the conclusion that the peak

height and recovering rate of the pulse tent to increase and decrease with increasing loading rates respectively. Due to the abnormal potential pulse that interfered the detection of crack initiation, a backtracking technique in which the crack initiation was tracked back from the measured final crack lengths was recommended.

2.3.7.11   Crack Closure Identification

As mentioned in Section 2.3.6.4, the closed area between two previously opened fractured surfaces would lower the measured PD across the crack. The increase in output potential in the curve of potential and cyclic load is an indication of contact of two crack surfaces.

PD methods have been applied in order to detect crack closure behaviour on fractured specimen surfaces in fatigue tests [63–71]. Crack closure in titanium and titanium alloy specimens has been observed by Irving, Robinson and Beevers [63,65] in vacuum of 1.33 mPa (10^{-5} torr). Closure identification by DCPD failed at pressure higher than 10^{-3} torr, which was considered to be due to the results of geometry deformation at crack tip attributed to the air environment. Dissenting from the findings given by Irving et al [63,65], Bachmann and Munz [67] and Pippan et al [70] suggested that the failure in detection of crack closure in air is due to the deformation of an insulated oxide layer that increases contact resistance and covers the PD caused by closure. This forming of oxides on cracked surfaces is the main objection to the use of PD for crack closure measurements [72]. However, the success of application of PD methods for crack closure measurements in other studies [64,66,71,72] has led to the conclusion that the technique provides reliable results in both vacuum and air environments. By applying the rheoelectric analogue technique, it was claimed that the change in PD caused by crack closure was related to the relative position of closure with respect to the crack tip [68]. A series of calibration curves revealing the extent of assumed planar and square crack closure has been proposed with the use of the perspex analogue method [69].

2.4   Electromagnetic Fields in Conductors

In ACPD experiments, the time-varying fields generated around cracks or features are different to the time-invariant fields which deal with stationary current and charge distribution. Under time-varying conditions, the electric fields and magnetic fields are interdependent, i.e. the electric field intensity ($\mathbf{E}$) (and electric flux density ($\mathbf{D}$)) is coupled with magnetic flux density ($\mathbf{B}$) (and magnetic field intensity ($\mathbf{H}$)). In this section, a brief description of the electromagnetic model will be presented first; then the approximating equation of skin depth δ in cylindrical samples will be derived.

2.4.1 Time-Dependent Fields and Maxwell's Equations

For linear and isotropic medium, the relations between electromagnetic field vectors are specified by the constitutive relations of

$$\mathbf{D} = \epsilon \mathbf{E} \qquad\qquad \mathbf{J} = \sigma \mathbf{E} \qquad\qquad \mathbf{B} = \mu \mathbf{H} \qquad (2.15)$$

where ϵ is the permittivity, σ is the conductivity, and μ is the permeability. In a homogeneous medium, ϵ, μ, and σ are assumed to be constant everywhere within the material. The above constitutive relations will be assumed to hold in this work.

The electrostatic fields can be defined by the two postulates as

$$\nabla \times \mathbf{E} = 0 \qquad (2.16)$$

$$\nabla \cdot \mathbf{D} = \rho \qquad (2.17)$$

where ρ is the volume density of free charge. (2.16)-(2.17) imply that the electrostatic field is generated by a scalar source, e.g. a charge or a charge density, thus the field is irrotational (i.e. conservative) and nonsolenoidal.

Another two basic postulates held for the magnetostatic models are

$$\nabla \cdot \mathbf{B} = 0 \qquad (2.18)$$

$$\nabla \times \mathbf{H} = \mathbf{J} \qquad (2.19)$$

(2.18) represents the fact that a magnetic monopole does not exist. The two equations state that the magnetic field is rotational (i.e. non-conservative) and solenoidal.

These four postulates were experimentally evaluated and have been accepted as fundamental relations for electrostatic and magnetostatic models [144,190–193]. The coupling between the electric and magnetic field has firstly been described by Faraday's law of induction, which can be formulated as

$$\oint_C \mathbf{E} \cdot d\mathbf{l} = -\frac{d\Phi}{dt} = -\frac{d}{dt} \int_S \mathbf{B} \cdot d\mathbf{s} \qquad (2.20)$$

where Φ is the magnetic flux through the surface S, C is the bounding contour of S. Faraday's law states that the induced emf within a conductor (or circuit) is equal to the negative of the time rate of change of flux linking the circuit [144,190–193]. By applying the Stokes' theorem to the left-hand side of (2.20), (2.20) becomes

$$\oint_C \mathbf{E} \cdot d\mathbf{l} = \int_S (\nabla \times \mathbf{E}) \cdot d\mathbf{s} = -\frac{d}{dt} \int_S \mathbf{B} \cdot d\mathbf{s} \qquad (2.21)$$

where the surface integral of the last two terms may be taken off. Thus the derivative form of Faraday's law can be obtained as

$$\nabla \times \mathbf{E} = -\frac{\partial \mathbf{B}}{\partial t} \qquad (2.22)$$

54

(2.22) suggests that in a time-varying field, the two pairs of postulates of time-invariant fields must be modified to show the coupling relation between $\mathbf{E}$ and $\mathbf{B}$.

Magnetic vector potential ($\mathbf{A}$) is defined by

$$\mathbf{B} = \nabla \times \mathbf{A} \tag{2.23}$$

Obviously the differential equation in (2.23) does not completely define $\mathbf{A}$ unless the divergence of $\mathbf{A}$ is specified as well. Arbitrarily, the second definition of

$$\nabla \cdot \mathbf{A} = 0 \tag{2.24}$$

is adopted in this work. By substituting $\mathbf{B}$ in (2.22) by the definition of $\mathbf{A}$, (2.22) becomes

$$\nabla \times \mathbf{E} = \frac{\partial}{\partial t} (\nabla \times \mathbf{A}) \rightarrow \nabla \times \left(\mathbf{E} + \frac{\partial \mathbf{A}}{\partial t} \right) = 0 \tag{2.25}$$

Since the term in the parentheses is curl-free, it can be written as the gradient of a scalar as

$$\mathbf{E} = -\frac{\partial \mathbf{A}}{\partial t} - \nabla V \tag{2.26}$$

where V is the scalar electric potential. In static fields, the time-dependent term in (2.26) vanishes, which is consistent with the definition of V. While for electromagnetic models considered in this work, $\mathbf{E}$ field is non-conservative and must be determined both from the charge distribution through the ∇V term and from time-varying current through the $\frac{\partial \mathbf{A}}{\partial t}$ term [190–193].

2.4.2 Skin Effect in 'Good' Conductors

As stated by Faraday's law, if a good conductor is connected to an AC source, eddy current will be inducted to oppose the original current flow and confine the current to flow within a thin layer beneath the conductor surface (see Section 2.3.1). In this section, a detail derivation of δ in cylindrical samples (i.e. constant angular coordinate) will be presented.

The differential forms of Maxwell's equations are listed below for easy reference,

$$\nabla \times \mathbf{E} = -\frac{\partial \mathbf{B}}{\partial t} \tag{2.27}$$

$$\nabla \times \mathbf{H} = \mathbf{J} + \frac{\partial \mathbf{D}}{\partial t} \tag{2.28}$$

$$\nabla \cdot \mathbf{D} = \rho \tag{2.29}$$

$$\nabla \cdot \mathbf{B} = 0 \tag{2.30}$$

By taking curls of both sides of the Maxwell's equation of Faraday's law (2.27) and applying the constituent relation of $\mathbf{B}$ in (2.15), it can be obtained that

$$\nabla \times \nabla \times \mathbf{E} = -\frac{\partial}{\partial t} (\nabla \times \mathbf{B}) = -\mu \frac{\partial}{\partial t} (\nabla \times \mathbf{H}) \tag{2.31}$$

The expression relating to $\mathbf{H}$ of (2.31) can be eliminated by substituting the Maxwell's equation of Ampère's law (2.28), as

$$\nabla \times \nabla \times \mathbf{E} = -\mu \frac{\partial}{\partial t} \left(\mathbf{J} + \frac{\partial \mathbf{D}}{\partial t} \right) \tag{2.32}$$

In a good conductor (as assumed for the experimental samples in this research), the conduction current $\mathbf{J}$ is generally much larger than the displacement current $\frac{\partial \mathbf{D}}{\partial t}$. Hence (2.32) may be simplified to give

$$\nabla \times \nabla \times \mathbf{E} = -\mu \frac{\partial \mathbf{J}}{\partial t} \tag{2.33}$$

The $\mathbf{E}$ term on the left-hand side may be eliminated by applying the constituent relation of $\mathbf{J}$ in (2.15), there is obtained

$$\nabla \times \nabla \times \mathbf{J} = -\mu \sigma \frac{\partial \mathbf{J}}{\partial t} \tag{2.34}$$

Recalling the vector identity of $\nabla \times (\nabla \times \mathbf{J}) = \nabla (\nabla \cdot \mathbf{J}) - \nabla^2 \mathbf{J}$. With the first term on the right-hand side to be zero, (2.34) becomes

$$\nabla^2 \mathbf{J} = \mu \sigma \frac{\partial \mathbf{J}}{\partial t} \tag{2.35}$$

This equation is known as the diffusion equation for $\mathbf{J}$. Other field quantities like $\mathbf{H}$, $\mathbf{E}$, $\mathbf{B}$, and $\mathbf{D}$ also obey similar equations [193]. For a field oscillating in a sinusoidal wave in z-direction (assuming a polar coordinate), i.e. $\mathbf{J} = \mathbf{J}_z e^{j\omega t}$, (2.35) can be written as

$$\nabla^2 \mathbf{J}_z = j\omega\mu\sigma \mathbf{J}_z \tag{2.36}$$

The general solution for the partial differential equation above is given by

$$\mathbf{J} = Ae^{rz} + Be^{-rz} \tag{2.37}$$

where $r^2 = -j\omega\mu\sigma$, A and B are coefficients. By substituting $\sqrt{j} = (1+j)/\sqrt{2}$, the solution becomes

$$\mathbf{J} = Ae^{\frac{(1+j)z}{\delta}} + Be^{-\frac{(1+j)z}{\delta}} \tag{2.38}$$

where δ is the skin depth or the depth of penetration, which is defined by

$$\delta = \sqrt{\frac{2}{\omega\sigma\mu}} \tag{2.39}$$

The boundary conditions at the center and on the surface of the conductor may be applied to calculate for A and B. Boundary conditions are given as

1. At the center ($z \gg \sigma$): $J = 0$.

2. On the surface ($z = 0$): $J = J_0$ where J_0 is the current density at the surface of the good conductor.

The two coefficients can thus be determined to be

$$A = 0 \qquad\qquad\qquad B = J_0 \qquad\qquad (2.40)$$

AC density in a good conductor decays exponentially from the surface value, as described by

$$\mathbf{J} = J_0 \exp\left[-(1+j)\frac{z}{\delta}\right] \qquad\qquad (2.41)$$

2.5 Internal Impedance of Conductors

The calibration methods for PD methods reviewed above in Section 2.3.3 are 'forward methods' in which the situations of inside cracks are inferred by measured PDs. In the present work, a 'reverse method' is sought to figure out the sizes and shapes of cracks. The reverse approximation is based on measured parameters of frequency-dependent impedance, i.e. R_{ac} and Z_{int} of conductors. The determination of frequency-dependent impedance parameters in skin effect problems has been widely investigated. A short review of the skin effect problem in conductors will be presented in this section.

Kennelly, Laws, and Pierce [194] have published early experimental data of resistance ratio $\frac{R_{ac}}{R_{dc}}$ (R_{dc} is direct current resistance) for an isolated conductor in circular cross-section. The measurements have been further extended to a frequency band up to 100 kHz by Kennelly and Affel [195]. Dwight [196] has proposed a series formula for calculating resistance ratio of an isolated tube and a thin strip but the method for the later case is only applicable for low frequencies. Moreover, these formulas are in the form of infinite series and involve formidable iteration, which restricts the wide application of the formulas. In order to compare results measured under different conductions, i.e. material, dimensions, and frequencies, the author [196, 197] has proposed the 'principle of similitude' in which $\frac{R_{ac}}{R_{dc}}$ were plotted against a parameter of $p_{sim} = \sqrt{\frac{f}{R_0}}$ (R_0 is the R_{dc} in $\Omega/1000$ feet) rather than the frequency f. The principle of similitude has been widely adopted to represent experimental measurements of $\frac{R_{ac}}{R_{dc}}$ for rectangular conductors in various respect ratio, e.g. by Forbes and Gorman [198] and Haefner [199]. Cockcroft [200] has applied an analogy between rectangular conductors and ellipse of large eccentricity, combined with the method of the Schwarz-Christoffel transformation to calculate field distributions. By applying the 'incremental inductance rule', Wheeler [201] has derived a series formulas for computing impedance parameters for several actual cases including isolated and parallel wires, transmission lines, and coils. The concept of 'partial inductance' has been widely used to evaluate frequency-dependent parameters for rectangular conductors [202–204]. A series of papers given by Silvester have derived a modal network theory for predicting skin effect and calculating Z_{int} for isolated non-magnetic rectangular conductors with different aspect ratios [205–207] and then extended to multiple-conductor structures [207, 208]. In the modal method, the total conductor impedance is

represented by a modal network including a large number of individual modal branches; the conductance of each network branch is measured by eigenfunctions of a distance matrix which relates only to the sectional shape of the conductor (see more detail in Section 3.5). Waldow and Wolff [209, 210] have presented a numerical method, in which R_{ac} and Z_{int} of rectangular conductors are solved from integral equations of **A**, and verified Haefner's measurements [199]. A 2D FEA method has been applied to solve the skin effect and proximity effect problems for strip transmission line by Costache [211]. Tsuk and Kong [212] have calculated the frequency-dependent parameters at low and high frequency by two different methods thereby developed a hybrid technique to solve the skin effect problem for transmission lines with arbitrary cross-section.

Now the solution of frequency-dependent parameters for an isolated conductor of circular cross-section is available and well know [213–215]. More detailed introduction of the closed problem will be presented in Section 3.2. The solution suggests that, for well-developed skin effect, the real and imaginary part of Z_{int} for cylindrical conductors are equal, which agrees with Wheeler's incremental inductance rule [201, 216, 217]. However, Antonini, Orlandi, and Paul [218] have argued that the equality between high-frequency internal reactants and high-frequency resistance was invalid for rectangular conductors. They have stated the importance of a separated determination of Z_{int} and developed a numerical method which derived from a 2D integral equation of current distribution over the cross-section [193, 219] for computing both the two parameters. The above numerical method has been developed for better performance by other investigators [220, 221].

More recently, Rong and Cangellaris [222] have derived an expression for calculating Z_{int} of a conductor with arbitrary cross-section by applying the Thévenin theorem. Then the method has been extended to inhomogeneous conductors by Demeester and Zutter [223]. Zhilichev [224] has proposed an analytical solution which based on the Grinberg's method for computing current distribution and Z_{int} of cylindrical conductors. Additionally, Zhilichev [224] has also presented a detailed investigation of the effect on field distribution arose from the finite length of the conductor and the sizes and locations of current electrodes. Payne [225, 226] has presented a semi-empirical equation which approximates the current crowding by the proximity loss in parallel wires for computing frequency-dependent R_{ac} of rectangular conductors.

In the next Chapter, several of the aforementioned theories will be expounded upon in greater detail and applied to calculate Z_{int} for some of the experimental samples (i.e. the plain samples of different cross-sectional shapes).

2.6   Conclusions

- An overview of many common NDT methods, currently proposed for the detection and measurement of cracks, is given. The techniques discussed are optical, compliance, ultrasonic, acoustic emission, eddy current, ACFM, and PD methods.

- PD methods have been widely applied to the detection of crack initiation and the subsequent monitoring of crack growth as discussed in this review. Also presented is the use of PD in identifying crack closure/opening.

- These methods have received wide acceptance in various applications as reliable NDT tools, due to a number of advantages offered by the methods. Such advantages include the fact that these technologies are capable of providing accurate and continuous measurements with low cost and simple installation. Moreover, PD methods exclude the requirement of visual access and are feasible in extreme service conditions such as high temperatures and other harsh conditions.

- Basic experimental systems of DCPD and ACPD have been presented and explained. In excitation circuits of the systems, DC/AC is produced by a stable power supply and injected to the specimen. The output signals, i.e. the PDs, are then measured, amplified and recorded in measuring circuits.

- Compared with DCPD, ACPD takes advantage of the skin effect, in which AC are governed to flow within a thin layer beneath the specimen surface. Hence, ACPD requires lower current input yet offers higher sensitivity (due to the reduced dilution of the flowing current due to a lower area in which this current flows). ACPD also offers better noise rejection via the use of lock-in amplifiers and is immune to DC-induced emf. However, measurements are sensitive to the capacitance effect and the installation is more expensive than for DCPD.

- Calibration curves (for crack length v.s. PD measurement) can be determined analytically, numerically or by direct or analogue experimental measurements. Such calibration curves/functions have been established for various types of specimens in many studies reported in the literature. However, calibration is not the unique technique to evaluate cracks using PD methods. Crack shape, size and location have also been achieved by non-calibration methods.

- With consideration of sensitivity and reproducibility of test results, close proximity of the measurement probes with the notch has been recommended as optimum for both C(T) and SEN(B) specimen types. The optimum attachment of current injection leads is suggested to be on the top-faces with

area contact for C(T) specimens and on side-faces with uniform application for SEN(B) specimens (see Fig. 2.30b). Additionally, the placement of current leads at mid-points of side-faces of the C(T) specimen geometry (see Fig. 2.33) has been shown to be capable of obtaining steeper calibration curves but at the cost of the magnitude of the generated PD.

- Normalisation of PD measurements and crack lengths enables the elimination of errors caused by variables such as unstable temperature and material properties. Several methods of determining the reference PD have been introduced and compared. A reduction in errors caused by thermally induced emf, for example, can be achieved by choosing similar materials of specimen and measuring probes, and by periodically changing the direction of current.

- The shape of a calibration curve is influenced by geometry of the specimen and the crack being measured (and the frequency of the AC, in ACPD). Errors in measurement arise from many factors including plastic deformation, crack closure and temperature variations. There is no closed answer to eliminate such errors, however, precautions have been suggested in order to weaken these errors.

- PD methods have been applied with success to the monitoring of many crack geometries, including asymmetric centre cracks, angled cracks, multiple cracks and cracks extended under mixed mode fracture. Performance of the methods under aggressive conditions such as corrosion, high temperature, creep and cycled loading have been discussed in detail.

- In addition to the error sources possibly faced during the application of potential drop methods, which have been discussed, disadvantages of this technique include the effect of the determination of calibration on the sensitivity and the limitations to conductive materials. The confidence in generated calibration will ultimately affect the measured results unless PD methods which dispense with the need for calibration are applied. In order to extend the application of such technologies to electrical-insulated materials, application of conductive layers covering the material surface are considered as a feasible method.

- Although PD methods have been accepted as a reliable tool to identify crack lengths, other crack parameters such as shape and location are currently beyond this technology (for curved/tunnelled cracks, such as thumb-like cracks), a single crack length is insufficient for representing the whole crack and for supporting subsequent crack growth modelling activities. Therefore, the determination of crack shape is recommended as a significant area for future research.

- The coupled electro-magnetic fields generated within and around the conductors in ACPD experiments were discussed in detail, following the derivations of the equation for skin depth in good conductors.

- The solutions of Z_{int} for isolated straight conductors have been widely investigated in the few decades with use of various theoretical and numerical approaches.

Chapter 3

Theoretical Methodology: Computing Internal Impedance of Non-magnetic Conductors of Various Cross-sectional Shapes

3.1   Introduction

Effort has been put on seeking available theoretical methods to solve the skin effect problem for the ACPD samples and provide comparisons with the experimental results. To the author's knowledge, there is no general method to predict PDs from arbitrary positions on conductors of any cross-sectional shapes with or without features. Fortunately, several theoretical methods are available to calculate Z_{int} or R_{ac} (i.e. $Re\left(Z_{int}\right)$) per unit length of infinitely-long conductors, as reviewed in Section 2.5. It will be discussed later that these two parameters can not be obtained from the ACPD experiments, since AC is consistently unevenly distributed on the conductor surfaces due to the exist of edges and features. On plain samples of polygonal cross-sections, current are concentrated around edges and corners at high frequencies, which is referred as current crowding. While on cracked/featured samples, current are more interfered by the feature, leading to a more uneven distribution. Thereby, PDs that are measured from certain positions on the samples can not represent the whole electric/current field or be used to calculate Z_{int} of the conductive body between measurement points. However, this may be easily achieved through FEA via ANSYS. FEA can be used to measure Z_{int} of arbitrary parts from models even including features.

This chapter will focus on employing several established theoretical framework (reviewed in Section 2.5) to calculate Z_{int} of the samples and comparing theoretical solutions of Z_{int} to FEA, rather than validating experimental results of PD through theoretical methodology. The samples that will be analysed in the chapter are the plain SS316 samples of four cross-sectional shapes, circular, hexagonal, square,

and triangular. The end effect caused by current injections (applied on the end surfaces) to the experimental measurements will be investigated and then excluded through FEA in Section 5.4. The present chapter will use the conclusion so that the plain samples will be considered as infinitely-long, which conforms to the general assumption of impedance analysis in literature.

In this chapter, the Bessel Function Method [144, 215, 227–230] that is well-accepted as the solution of Z_{int} for cylindrical conductors will be presented first. Then, a straightforward method called Effective Area Method (EAM) will be developed for the four cross-sectional shapes. EAM will be further improved for the square shape by combining an approximation of current crowding developed exclusively for rectangular cross-sections by Payne [225]. Payne's full theory [225, 226] of calculating Z_{int} will also be introduced, however, which is limited to rectangular conductors. Next, another two theories that solve the impedance problem for rectangular conductors based on discretisation of the cross-section will be demonstrated and then extended to arbitrary cross-sectional shapes. The first discretisation-based theory relies on solving an integral equation of current over the cross-section through matrix operations [193, 218]. The second theory, which is named as Modal Network Theory (MNT), simulates the total current by a current modal network. In MNT, individual impedance of each modes are obtained by solving an eigenvalue problem of a distance matrix which contains spatial distributions of modes [205–208].

3.2   Bessel Function Method

Bessel functions of a differential equation describing the electromagnetic fields of a circular cross-section has been widely accepted as the solution of Z_{int} for cylindrical conductors [144, 215, 227–230]. The present section will demonstrate the derivation of the final solution of Z_{int} based on Bessel functions. Z_{int} refers to the sum of the resistance and the reactance contributed by the magnetic field induced within the conducting medium [229]. For an infinitely-long cylindrical conductor with radius of r_0 carrying a total current of I, $\mathbf{E}$ may be assumed as a longitudinal scalar of E_z. Thus Z_{int} is given by [144, 229, 230]

$$Z_{int} = \frac{E_z\left(r_0\right)}{I} \tag{3.1}$$

To solve the above equation for Z_{int}, a Bessel equation of the $\mathbf{J}$ will be derived first; both the two quantities on the right will then be replaced by $\mathbf{J}$ to construct a new equation of Z_{int} which is only dependent on $\mathbf{J}$; eventually Bessel functions of the new equation will be employed to obtain individual solutions of impedance at low and high frequencies.

Recalling the Maxwell's equations given in (2.27)-(2.28), the electromagnetic

fields generated inside the conductor may be described as [144, 229, 230]

$$\nabla \times \mathbf{E} = -\frac{\partial \mathbf{B}}{\partial t} \tag{2.27}$$

$$\nabla \times \mathbf{H} = \mathbf{J} + \frac{\partial \mathbf{D}}{\partial t} \tag{2.28}$$

In addition, relations between characteristics of fields and quantities of the material are defined by constitutive relations given in (2.15) as

$$\mathbf{D} = \epsilon \mathbf{E} \qquad\qquad \mathbf{J} = \sigma \mathbf{E} \qquad\qquad \mathbf{B} = \mu \mathbf{H} \tag{2.15}$$

Again for a good conductor, displacement current $\frac{\partial \mathbf{D}}{\partial t}$ is negligible by comparing to the current. Hence (2.28) becomes

$$\nabla \times \mathbf{H} = \mathbf{J} \tag{3.2}$$

By assuming a sinusoidal form of $\mathbf{H}$ (i.e. $\mathbf{H} = H_0 e^{j\omega t}$), (2.27) can be written as

$$\nabla \times \mathbf{E} = -j\omega\mu\mathbf{H} \tag{3.3}$$

Taking curl to both sides of (3.3) to get

$$\nabla \times \nabla \times \mathbf{E} = -j\omega\mu\nabla \times \mathbf{H} \tag{3.4}$$

Then to replace $\mathbf{E}$ and $\mathbf{H}$ by $\mathbf{J}$ through substituting the constitutive relation of $\mathbf{J}$ in (2.15) and (3.2) into (3.4), the equation only relates to $\mathbf{J}$ is obtained as

$$\nabla \times \nabla \times \mathbf{J} = -j\omega\mu\sigma\mathbf{J} \tag{3.5}$$

Recalling that $\nabla \times \nabla \times \mathbf{J} = \nabla (\nabla \cdot \mathbf{J}) - \nabla^2 \mathbf{J}$. The first term on the right side relating to the charge density can be easily proven to vanish by the following process. Taking divergence to both sides of (3.2), which gives

$$\nabla \cdot (\nabla \times \mathbf{H}) = \sigma \mathbf{J} = \sigma (\nabla \cdot \mathbf{E}) = 0 \tag{3.6}$$

Since the divergence of the curl of any vector on the left side of (3.6) is zero, it has been proved that

$$\nabla \cdot \mathbf{E} = 0 \tag{3.7}$$

Similar conclusions can be obtained for $\mathbf{J}$ and $\mathbf{D}$ based on other Maxwell's equations OF

$$\nabla \cdot \mathbf{J} = 0 \qquad\qquad\qquad \nabla \cdot \mathbf{D} = 0 \tag{3.8}$$

Hence (3.5) may be written into a Laplace equation of current density as

$$\nabla^2 \mathbf{J} = j\omega\mu\sigma\mathbf{J} \tag{3.9}$$

By assuming only a radial variation in $z-$direction of the current density, the expression of (3.9) in cylindrical co-ordinates becomes

$$\frac{d^2 J_z}{dr^2} + \frac{1}{r}\frac{dJ_z}{dr} + Q^2 J_z = 0 \qquad (3.10)$$

where $Q^2 = -j\omega\mu\sigma$. Then by dividing Q^2 throughout (3.10), it becomes

$$\frac{d^2 J_z}{d(Qr)^2} + \frac{1}{Qr}\frac{dJ_z}{d(Qr)} + J_z = 0 \qquad (3.11)$$

This is a Bessel equation of the independent variable Qr, order zero. The solution of (3.11) is the linear combination of zero-order Bessel and Neumann functions [231, 232]

$$J_z = A\mathcal{J}_0(Qr) + B\mathcal{N}_0(Qr) \qquad (3.12)$$

Because $\mathcal{N}_0$ contains logarithmic terms, it is discontinuous at $r = 0$. Hence, B must be zero in order to remain infinity of J_z. The solution to current density is then obtained as

$$J_z = A\mathcal{J}_0(Qr) \qquad (3.13)$$

Reviewing the formula of Z_{int} in (3.1), E_z may be easily replaced by J_z through applying the constitute relation (2.15). More efforts are required in the substitution of I, which may be conducted by two methods:

(1) I can be calculated by integrating the current density over the circular area as [229, 230]

$$I = \int_0^{r_0} J_z(r_0)\,2\pi r dr = \frac{2\pi A}{Q^2}\int_0^{r_0} \mathcal{J}_0(Qr)\cdot(Qr)\,d(Qr) \qquad (3.14)$$

Recalling the derivatives of Bessel function $Z_v(z)$: $\frac{d}{dz}[z^v Z_v(z)] = z^v Z_{v-1}(z)$ [231, 232], the solution of the integral term in (3.14) can be obtained as

$$(Qr)^1 \mathcal{J}_1(Qr) = \int (Qr)^1 \mathcal{J}_0(Qr)\,d(Qr) \qquad (3.15)$$

Then by substituting (3.15), the equation of I in (3.14) becomes

$$I = \frac{2\pi r_0 A}{Q}\mathcal{J}_1(Qr_0) \qquad (3.16)$$

(2) I can be computed as the line integral of magnetic field around the outside [144, 229]

$$I = 2\pi r_0 H_\phi(r_0) \qquad (3.17)$$

Again assuming no variation with ϕ or z, expressions of (2.28)-(2.27) in cylindrical co-ordinate are

$$\frac{d(rH_\phi)}{rdr} = (\sigma + j\omega\epsilon)E_z \qquad\qquad \frac{dE_z}{dr} = j\omega\mu H_\phi \qquad (3.18)$$

65

$$\frac{d(rH_z)}{rdr} = (\sigma + j\omega\epsilon) E_\phi \qquad \frac{dE_\phi}{dr} = j\omega\mu H_z \qquad (3.19)$$

The case of (3.18) that contains components of H_ϕ and E_z would be generated by an infinitely long wire, i.e. the case of interested. While the case of (3.19) would be produced by an infinitely long line of closely spaced coaxial loops carrying currents. (3.18) is considered here. The expression of E_z can be obtained from the second equation of (3.18) as

$$H_\phi = \frac{1}{j\omega\mu} \frac{dE_z}{dr} \qquad (3.20)$$

By substituting the constitutive relations in (2.15) for H_ϕ and E_z and (3.13) for J_z, (3.17) becomes

$$I = \frac{2\pi r_0 A}{j\omega\mu\sigma}[-\mathcal{J}_1(Qr)] = \frac{2\pi r_0 A}{Q}\mathcal{J}_1(Qr) \qquad (3.21)$$

(Recalling $\frac{d\mathcal{J}_0(Qr)}{d(Qr)} = -\mathcal{J}_1(Qr)$ [231, 232].)

Both two methods give the same solution of I, i.e. (3.21) is identical to (3.16). Therefore, (3.1) can be rewritten to given the theoretical solution of Z_{int} in cylindrical conductors as

$$Z_{int,Bes} = \frac{J_z(r_0)/\sigma}{I} = \frac{Q}{2\pi r_0 \sigma} \frac{\mathcal{J}_0(Qr_0)}{\mathcal{J}_1(Qr_0)} \qquad (3.22)$$

This solution is difficult to be used for all frequencies due to the exist of Bessel functions. Thus, approximations of Bessel functions at low and high frequency are usually applied to simply the result and calculate $Z_{int,Bes}$ for these two situations separately. Expressions of separated $Z_{int,Bes}$ can be derived by following steps.

(1) For thin wires at low frequencies.

The series expansion of the ratio of Bessel function of fist kind order 0 to order 1 is [227]

$$\frac{\mathcal{J}_0(x)}{\mathcal{J}_1(x)} = \frac{1}{x}\left(2 - \frac{x^2}{4} - \frac{x^4}{96} - \frac{6}{1536} - \frac{x^8}{23040} - \frac{x^{10}}{4423680} - \cdots\right) \qquad (3.23)$$

Substituting only the first three terms of (3.23) into (3.22), the expression of $Z_{int,Bes}$ for low frequencies can be obtained as

$$Z_{int,Bes-dc} = \frac{1}{\pi r_0{}^2\sigma}\left[1 + \frac{1}{j}\left(\frac{r_0}{\delta}\right)^2 + \frac{1}{48}\left(\frac{r_0}{\delta}\right)^4\right] \qquad (3.24)$$

The term before bracket is the steady state resistance per unit length of the conductor. Low frequency resistance and inductance can be determined from real and imaginary parts of (3.24) as

$$R_{dc,Bes} = Re(Z_{int,Bes-dc}) = \frac{1}{\pi r_0{}^2\sigma}\left[1 + \frac{1}{48}\left(\frac{r_0}{\delta}\right)^4\right] \qquad (3.25)$$

$$L_{dc,Bes} = \frac{Im(Z_{int,Bes-dc})}{\omega} = \frac{1}{\pi r_0{}^2\sigma\omega}\left[\frac{1}{j}\left(\frac{r_0}{\delta}\right)^2\right] = \frac{\mu}{8\pi} \qquad (3.26)$$

66

(2) For thin wires at high frequencies.

By using the asymptotic term of Bessel function for large argument, i.e. $\frac{\mathcal{J}_0(x)}{\mathcal{J}_1(x)} = -j$, (3.22) becomes,

$$Z_{int,Bes-ac} = \frac{1}{2\pi r_0 \sigma \delta} (1 + j) \tag{3.27}$$

Similarly this leads to

$$R_{ac,Bes} = Re\left(Z_{int,Bes-ac}\right) = \frac{1}{2\pi r_0 \sigma \delta} \tag{3.28}$$

$$L_{ac,Bes} = \frac{Im\left(Z_{int,Bes-ac}\right)}{\omega} = \frac{1}{2\pi r_0 \sigma \delta \omega} \tag{3.29}$$

Equations in (3.24)-(3.29) were applied to the SS316 sample of circular cross-sectional shape. Calculated impedance were compared to FE results, as displayed in Fig. 3.1. For frequencies lower than 20 kHz, $R_{dc,Bes}$ and FE results show good agreement, giving differences smaller than 1%. While for higher frequencies upto 300 kHz, $R_{ac,Bes}$ are consistently lower than FE results for about 0.002 Ω. However, it can be seen that $R_{dc,Bes}$ and $R_{ac,Bes}$ are incoherent around the transitional region at 20 kHz, which demonstrates the imperfection of this theory at least in the application in the SS316 sample. It is necessary to consider other theoretical methods and re-calculate for the circular sample.
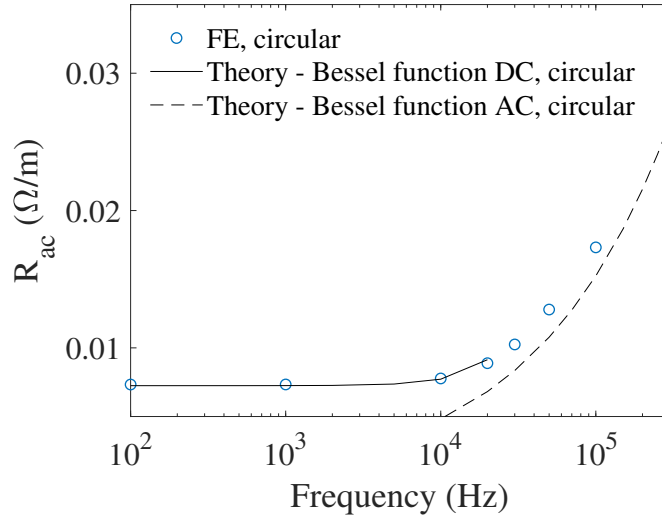
Figure 3.1: Resistance per unit length of the plain SS316 sample of circular cross-sectional shape obtained by FEA and theoretical method based on Bessel function given by (3.24)-(3.27).

3.3 Effective Area Method and Current Crowding

As the above theory based on Bessel functions is limited to circular samples, analysis for hexagonal, square, and triangular cross-sections will rely on other theoretical

methods. This section will start with the development of Effective Area Method (EAM), then introduce two other theoretical frameworks based on distinct principles, finally improve EAM by combining the effect of current crowding provided by the former introduced method.

In EAM, R_{ac} of the conductor is calculated by using the effective area with current flowing through $(S_{ac,EAM})$, i.e. confined by the skin depth on the cross-section of the conductor. Fig. 3.2 shows an example of $S_{ac,EAM}$ on a hexagonal cross-section. $S_{ac,EAM}$ is easily calculated by adding up all the rectangular areas on sides, and then subtracting the overlapping triangular areas at corners, as illustrated in Fig. 3.2b. The general equation of $S_{ac,EAM}$ of polygons in arbitrary shapes is given by

$$S_{ac,EAM} = n\delta \left(a_0 - \delta \tan \frac{\theta}{2} \right) \tag{3.30}$$

where n is the number of corners, a_0 is the side length, and the interior angle $\theta = \frac{2\pi}{n}$. a_0 of the cross-section with a constant area of S_0 is

$$a_0 = 2\sqrt{\frac{S_0}{n} \tan \frac{\theta}{2}} \tag{3.31}$$

By using the resistance formula of R_{dc} and substituting $S_{ac,EAM}$ for the area, $R_{ac,EAM}$ per unit length can be calculated by

$$R_{ac,EAM} = Re\left(Z_{int,EAM} \right) = \frac{1}{\sigma S_{ac,EAM}} \tag{3.32}$$
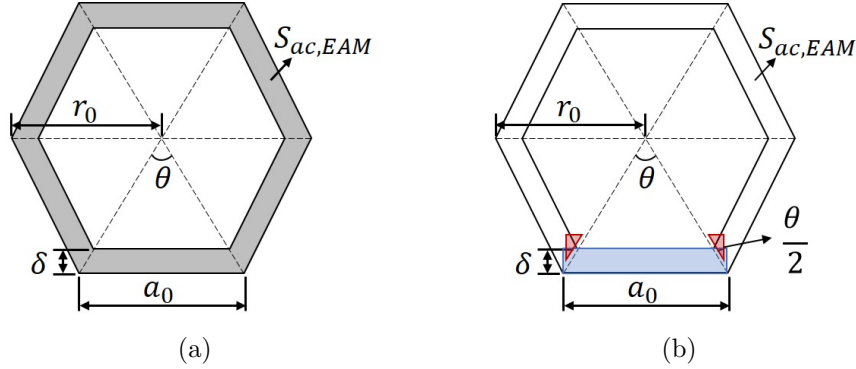
Figure 3.2: Schematic of $S_{ac,EAM}$ of a polygonal cross-section with a number of corners $n = 6$.

EAM assumes a uniform current distribution within the area of $S_{ac,EAM}$ and ignores any current beyond the skin depth, as shown in Fig. 3.3a. However, the definition of skin depth indicates that AC exponentially decays from the surface into the center rather than uniformly distributes over $S_{ac,EAM}$, see in Fig. 3.3b. Additionally, AC reduces to $\frac{1}{e}$ of the surface current density at the skin depth but does not vanish to 0. These two basic assumptions of EAM violate the facts. Moreover, EAM only considers the skin effect but excludes the other significant

influence due to AC with high frequencies — the current crowding near edges of the sample. The current crowding refers to the current concentration at corners occurs at high frequencies in conductors [226]. This phenomenon was widely observed in FEA and will be shown in later sections (e.g. Fig. 5.3c in Section 5.3). Therefore, this method is only capable of providing rough approximations of R_{ac} with limited precisions.

(a) EAM
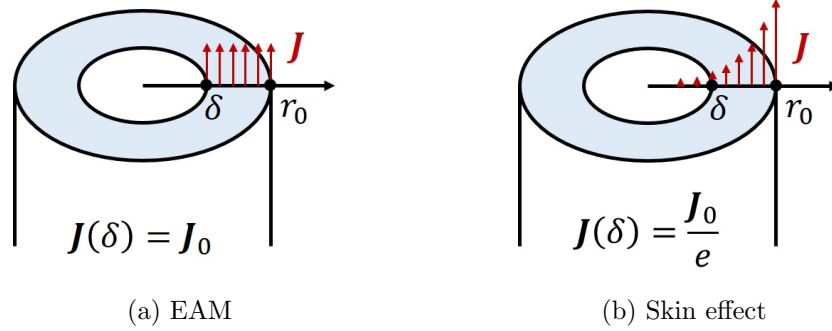
(b) Skin effect

Figure 3.3: Schematics of the uniform current distributions assumed in EAM and the exponential decay of current in skin effect.

Theoretical impedance calculated from (3.32) are compared to FE results for the four SS316 samples, as shown in Fig. 3.4. At 300 kHz, FE results of the circular, hexagonal, square, and triangular cross-sections reach 0.0284, 0.0290, 0.0301, and 0.0315 Ω/m, respectively. By contrasting between $R_{ac,EAM}$ for the four samples, the triangular sample has the lowest results, which is opposite to the order approximated by FEA. For the circular sample without current crowding (due to the absence of edges on the sample surface), theoretical and FE results are similar for the whole frequency range with an average difference of 1.7%. Whereas for the other three shapes, the differences between two types of results rise as the frequency increasing, reaching a maximum of 7% for the hexagonal, 16% for the square, and 29% for the triangular respectively at 300 kHz.
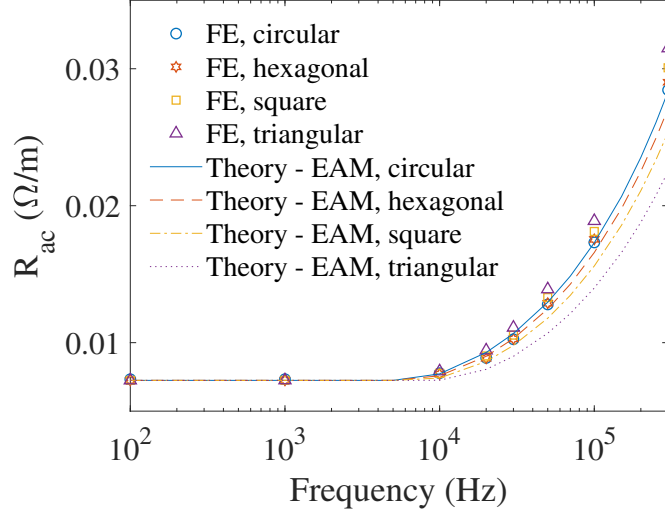
Figure 3.4: Resistance per unit length of plain SS316 samples of various cross-sectional shapes obtained by FEA and the theoretical method of EAM.

Rong and Cangellaris [222] have put forward a definition of Z_{int} of rectangular conductors based on the Thévenin theorem in which the circuit inside the conductor is analogised to a circuit composed of a voltage source and a series of impedance. Two boundary conditions of electromagnetic problem inside the conductor are provided by the analogue, giving

$$(Z_{int,Thev})^{-1} = \frac{64\sigma}{w_1 w_2} \sum_{m=1}^{\infty} \sum_{n=1}^{\infty} \frac{G_1 + G_2}{G_1 G_2 \left(G_1 + G_2 + j\omega\mu\sigma\right)} \tag{3.33}$$

in which constants G_1 and G_2 are given as

$$G_1 = \left(\frac{\left(m - \frac{1}{2}\right)\pi}{\frac{1}{2}w_1}\right)^2 \qquad\qquad G_2 = \left(\frac{\left(n - \frac{1}{2}\right)\pi}{\frac{1}{2}w_2}\right)^2 \tag{3.34}$$

where m and n refer to discretisation of the rectangular cross-section, w_1 and w_2 represent the side lengths of the conductor along the direction of m and n. $R_{ac,Thev}$ calculated based on (3.33)-(3.34) show good agreement to $R_{ac,EAM}$ for the square sample, as displayed in Fig. 3.5. Two theoretical results are similar for the whole frequency range with an average difference smaller than 1.4%.
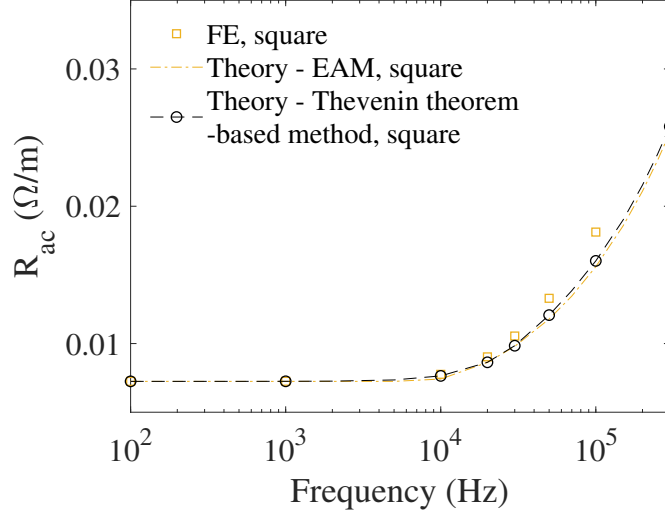
Figure 3.5: Resistance per unit length of the plain SS316 sample of square cross-sectional shape obtained by FEA and theoretical method of EAM and the Thévenin theorem-based method [222].

The poor performance of EAM for polygonal cross-sections containing edges in Fig. 3.4 suggests the necessity of including the current crowding in calculations. Payne [225, 226] has proposed a semi-empirical equation to compute R_{ac} of rectangular conductors in which the two factors, skin effect and current crowding, were expressed explicitly. Payne's full theory will be introduced in detail first, then the analysis of current crowding will be separated out and employed to EAM. As Payne's full equation is only applicable to rectangular bars, calculations here will be focused on the square sample.

Payne [226] described the problem of Z_{int} for rectangular conductors in terms of the two factors explicitly:

$$R_{ac,Pay} = \frac{1}{\sigma S_{ac,Pay}} K_{cc} \tag{3.35}$$

$S_{ac,Pay}$ is the effective area confined by δ with current flowing over, covering the impact of skin effect. K_{cc} represents the increase in resistance due to current crowding. The method of calculating $S_{ac,Pay}$ is different to $S_{ac,EAM}$ in EAM. For a rectangular conductor with the length of w_1 and the thickness of w_2, Payne introduced a frequency-dependent dimension w_2' (called 'apparent conductor dimension due to diffusion') to define $S_{ac,Pay}$, giving

$$S_{ac,Pay} = w_1 w_2' \tag{3.36}$$

w_2' is then solved by considering two boundary conditions at low and high frequencies:

(1) At low frequencies, the effective area equals the cross-sectional area of $w_1 w_2$, thereby

$$w_2' \to w_2 \text{ as } \delta \to \infty \tag{3.37}$$

71

(2) At high frequencies, $S_{ac,Pay}$ is simplified to be the area of the long strip with the length of the perimeter of the conductor and the width of δ:

$$S_{ac,Pay} = 2\delta\left(w_1 + w_2\right) \tag{3.38}$$

$w_2{}'$ is thus given by

$$w_2{}' = 2\delta\left(1 + \frac{w_2}{w_1}\right) \text{ as } \delta \to 0 \tag{3.39}$$

After assuming an exponential decay of $w_2{}'$ with the increasing frequency, the expression of $w_2{}'$ is determined to be

$$w_2{}' = w_2\left(1 - e^{-x_{se}}\right) \tag{3.40}$$

with

$$x_{se} = \frac{2\delta}{w_2}\left(1 + \frac{w_2}{w_1}\right) \tag{3.41}$$

which satisfies the boundary conditions in (3.39)-(3.40). However, Payne noticed that resistances calculated from above solutions showed poor fitness with experimental measurements for conductors with small and large aspect ratios, i.e. for square bars and thin strips. (3.41) was thus modified by including two extra terms obtained from empirical methods to rectify calculations for the two situations, which gives

$$x_{se} = \left[\frac{2\delta}{w_2}\left(1 + \frac{w_2}{w_1}\right) + 8\left(\frac{\delta}{w_2}\right)^3 \Big/ \left(\frac{w_1}{w_2}\right)\right] \Big/ \left[\left(\frac{w_1}{w_2}\right)^{0.33} e^{\frac{-3.5w_2}{\delta}} + 1\right] \tag{3.42}$$

Then to quantify the effect of current crowding, Payne [225] extended a theory, which describes the proximity effect between two parallel wires, to multiple wires, finally to rectangular conductors. The rectangular cross-section is decomposed into a finite set of subsections, hence the effect of current crowding within the conductor is approximated by the total proximity loss in series of the subsections. The approximation of current crowding was based on the theoretical method for computing the resistance increase due to proximity effect between two wires, which was proposed by Butterworth [233, 234]. To avoid complex calculations in Butterworth's theory, Payne constructed an empirical equation by fitting curves of theoretical results given by Butterworth [234]. This empirical equation is give as

$$K_{cc} = 1 + 1.2\left(e^{\frac{-2.1w_2}{w_1}} + e^{\frac{-2.1w_1}{w_2}}\right) \tag{3.43}$$

which represents the portion of increase in resistance due to the current crowding. However, (3.43) only contains geometrical information of the conductor and is independent of frequency, which disagrees with the fact that current crowding only occurs at high frequencies. The frequency-related term was determined by

solving (3.43) under boundary conductions with DC and high-frequency AC. (3.43) is modified to be

$$K_{cc} = 1 + 1.2F\left(f\right)\left(e^{\frac{-2.1w_2}{w_1}} + e^{\frac{-2.1w_1}{w_2}}\right) \tag{3.44}$$

where

$$F\left(f\right) = 1 - e^{-0.026p_{sim}} \tag{3.45}$$

Frequency is included in the parameter p_{sim} which was proposed based on the principle of similitude by Dwight [196], as mentioned in Section 2.5. p_{sim} is defined as

$$p_{sim} = \frac{\sqrt{S_0}}{1.2533\delta} \tag{3.46}$$

The final equation of $R_{ac,Pay}$ is then obtained by combing the skin effect in (3.36) & (3.42) and the current crowding in (3.44)-(3.46):

$$R_{ac,Pay} = R_{dc}\frac{K_{cc}}{1 - e^{-x_{se}}} \tag{3.47}$$

Furthermore, K_{cc} in (3.44) is combined with $R_{ac,EAM}$ to produce Improved EAM:

$$R_{ac,IEAM} = \frac{K_{cc}}{\sigma S_{ac,EAM}} \tag{3.48}$$

Impedance of the square sample calculated based on EAM, Improved EAM, and Payne's full equation are compared with FE results, as shown in Fig. 3.6. The participation of K_{cc} in Improved EAM slightly increases the results of R_{ac}. At 300 kHz, the maximum difference between $R_{ac,EAM}$ and FE results is reduced from 16% to 10% by introducing K_{cc} into Improved EAM. $R_{ac,Pay}$ increase much earlier at about 4 kHz than other three results. The maximum difference between $R_{ac,Pay}$ and FE results occurs around 20 kHz and is about 8%. Overall, theoretical results given by Improved EAM fit well with FE results from quasi-DC to about 20 kHz but start to diverge at higher frequencies; while the results based on Payne's full theory only show good agreement to the FE results at quasi-DC and high frequencies (i.e. < 1 kHz & > 30 kHz). For both the two methods, the mean discrepancies averaged from differences to FE results at all frequencies are similar to be 7%.
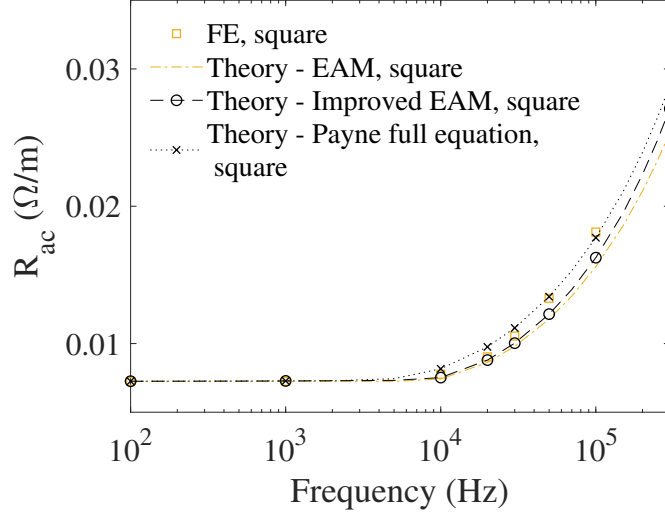
Figure 3.6: Resistance per unit length of the plain SS316 sample of square cross-sectional shape obtained by FEA and theoretical methods of EAM, Improved EAM containing K_{cc} in (3.44) [226], and Payne's full equation in (3.47) [225, 226].

3.4 Integral Equation for Current Distribution

Silvester [193] and Antonini [218] have proposed a theory which based on an integral equation of current density over the cross-section of a current-carrying body to calculate Z_{int} and R_{ac} of the long straight conductor surrounded by a time-varying field. In this method, a conductor with a constant cross-section along the vertical z-direction is divided into many parallel subsections (or filaments) which are in areas small enough (may be unequal) so that the current distribution and resistance of subsections are assumed to be uniform. Since each filament contains a small portion of the total varying current, mutual and self induction occurring around all individual subsections contribute to the uneven distribution of total current density over the conductor cross-section. Such induction is related to the current density through the introduce of $\mathbf{A}$ which was defined in (2.23). The derivation procedure to obtain the integral equation of current density and the subsequent computing process to solve the integral equation via MATLAB will be presented in detail in this section. It will be demonstrated by FEA later in Section 5.4 that AC injection points on end faces of the experimental sample are far enough to the the measurement region at the center. Hence, the measuring parts of the samples was unaffected by end effects and can be considered as infinitely-long, i.e. R_{ac} per unit length (or at least for the measurement distance) of experimental samples without features could be calculated by the present theory. Field quantities such as $\mathbf{A}$ and $\mathbf{J}$ can be expressed as scalar, i.e. by z-directed components.

For an individual circular wire containing a total current of I with radius of r_0,

A outside the wire at a distance of d to the circular center is calculated by [193]

$$A = \frac{\mu I}{2\pi}\left(\frac{1}{2} + \log\frac{d}{r_0}\right) \tag{3.49}$$

Since divided subsections are imagined to be in tiny area of dS, subsections can be assumed as cylindrical wires. Hence, the fractional current carried by a subsection can be given by

$$i = dI = J \cdot dS \tag{3.50}$$

(3.49) is applied to the subsection, which gives

$$dA = \frac{\mu dI}{2\pi}\left(\frac{1}{2} + \log\frac{d}{r_0}\right) = \frac{\mu J}{2\pi}\log(d)\,dS + \frac{\mu J \cdot dS}{2\pi}\left(\frac{1}{2} - \log r_0\right) \tag{3.51}$$

The last term irrelevant to d can be temperately eliminated by choosing an appropriate reference of A. Then A outside the subsection is obtained by integrating (3.51), as

$$A(x,y) = \frac{\mu}{2\pi}\int\int J\log(d)d\xi d\eta + A_0 \tag{3.52}$$

where A_0 is the arbitrary addictive term which is included to complete the integration. d becomes the distance between the measurement point at (x,y) (the observation subsection) to the induction generation points at (ξ, η) (other subsections for mutual induction and the observation one for self induction). d is given by

$$d = \sqrt{(x-\xi)^2 + (y-\eta)^2} \tag{3.53}$$

Then recalling the electric distribution over a cross-section of a sample governed by a time-dependent field, as given in (2.26):

$$E = -\frac{\partial A}{\partial t} - \nabla V \tag{2.26}$$

By substituting the constitutive relation of J in (2.15), (2.26) is written as

$$J = -\sigma\frac{\partial A}{\partial t} - \sigma\nabla V \tag{3.54}$$

The last term that contributed by the applied V can be replaced by the impressed current density J_{imp} as

$$J_{imp} = -\sigma\nabla V \tag{3.55}$$

(3.52) and (3.55) are substituted into (3.54) to build up an equation only related to J as

$$J = -\frac{\mu\sigma}{2\pi}\int\int \frac{\partial J}{\partial t}\log\sqrt{(x-\xi)^2 + (y-\eta)^2}d\xi d\eta + J_{imp} \tag{3.56}$$

Because sinusoidal waves were applied in the ACPD experiments, the above equation can be simplified by inserting a phasor form of J to be

$$J(x,y) = -\frac{j\omega\mu\sigma}{2\pi}\int\int J(\xi,\eta)\log\sqrt{(x-\xi)^2 + (y-\eta)^2}d\xi d\eta + J_{imp} \tag{3.57}$$

The above integration equation of current density over the cross-section of the sample is then approximated by the method of moments in which the surface of integration is divided into subsections. As stated before, a constant distribution is assumed over each subsections. Thus, (3.57) can be written to roughly calculate the current density over a single subsection (e.g. the subsection p) as

$$J_p\left(x_p, y_p\right) = -\frac{j\omega\mu\sigma}{2\pi} \sum_q^N J_q\left(\xi_q, \eta_q\right) \int\int \log\sqrt{\left(x_p - \xi\right)^2 + \left(y_p - \eta\right)^2}d\xi d\eta + J_{imp} \tag{3.58}$$

where subscripts p and q refer to different subsections, $p = 1, \cdots, N$ and $q = 1, \cdots, N$. If all subsections are produced to be square in an area of ${a_s}^2$, the above equation can be further simplified to be

$$J_p = -\frac{j\omega\mu\sigma}{2\pi}{a_s}^2 \sum_q^N J_q \log D_{pq} + J_{imp} \tag{3.59}$$

Thus geometric mean distances between subsections were be simplified to be distances between centres of subsections, D_{pq} can be written as

$$D_{pq} = \sqrt{\left(x_p - \xi_q\right)^2 + \left(y_p - \eta_q\right)^2} \tag{3.60}$$

Complex equations in (3.59) is written to a matrix equation in a dimension of N as

$$(\mathbf{U} + j\mathbf{G})\mathbf{J} = \mathbf{K} \tag{3.61}$$

where $\mathbf{U}$ is a unit matrix, $\mathbf{J}$ is a column matrix of current densities, $\mathbf{K}$ represents a constant matrix with all elements equalling J_{imp}, and $\mathbf{G}$ is given by

$$\mathbf{G} = \frac{\omega\mu\sigma}{2\pi}{a_s}^2 \log D_{pq} \tag{3.62}$$

Eventually the matrix equation in (3.62) is solved by MATLAB, which based on the conservation of dissipated power in subsections and in the sample, i.e.

$$\sum^N i^2 r = I^2 R_{ac,IntJ} \tag{3.63}$$

where $R_{ac,IntJ}$ is the R_{ac} per unit length of the sample, r is the resistance per unit length of each subsection. Again subsections are so small that σ of the sample material can be used to compute r. Thereby, for example in the subsection p, i_p and r_p are calculated by

$$i_p = \int_{\Delta S_p} J_p dS = J_p {a_s}^2 \tag{3.64}$$

$$r_p = \frac{1}{\Delta S_p \sigma} = \frac{1}{\sigma {a_s}^2} \tag{3.65}$$

A MATLAB script was developed to construct the integral equation in (3.59) and the matrix equation in (3.62) and finally to solve for $R_{ac,IntJ}$ of plain samples in various shapes by using (3.64)-(3.65), see in Appendix A.1. This theory

was devised exclusively for rectangular conductors. By the use of the script, the application of the theory is extended to the four cross-sections involved in Case 1 by creating a general geometric matrix $\mathbf{G}$ that is adapted for arbitrary polygonal cross-sections. The illustration in Fig. 3.2 is used as an example again here. The effective radius of a polygonal cross-section (r_0), i.e. the distance between the center to the corners, is given by

$$r_0 = \frac{a_0}{2 \sin \frac{\theta}{2}} \tag{3.66}$$

By taking the center as the origin of the Cartesian coordinates, the coordinates of the n corners ((x_{ci}, y_{ci})) can be calculated by

$$\begin{aligned} x_{ci} &= r_0 \sin \left[\frac{\theta}{2} + \theta \, (i-1) \right] \\ y_{ci} &= r_0 \cos \left[\frac{\theta}{2} + \theta \, (i-1) \right] \end{aligned} \tag{3.67}$$

where $i = 1, ..., n$. The general matrix $\mathbf{G}$ can be obtained by following the two steps. A square with the side length of $2r_0$ is first defined and divided into finite square subsections with a side length of a_s, as illustrated in Fig. 3.7. Then the subsections confined within the periphery, which connects the n corners (with known coordinates), are found out to approximate the polygonal cross-section. The coordinates of these subsection located within the periphery are used to construct the matrix $\mathbf{G}$.
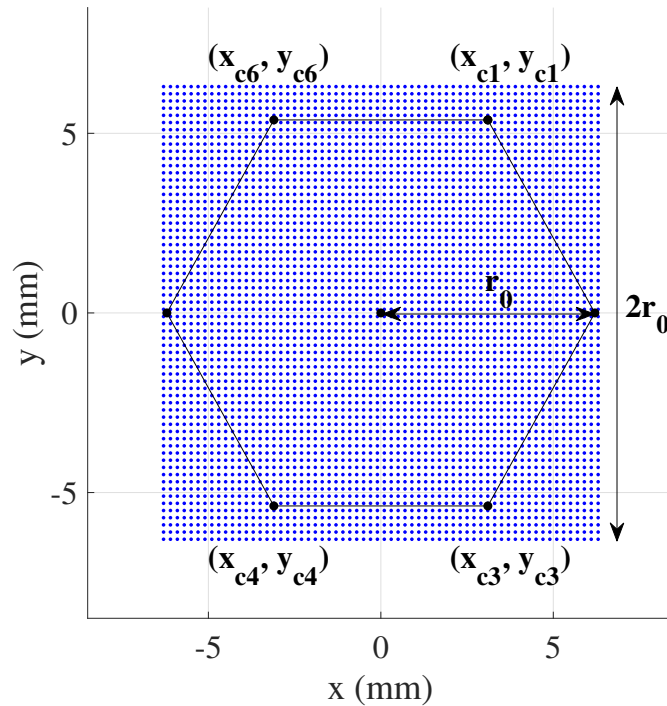
Figure 3.7: Process of discreting the polygonal cross-section with finite subsections.

A refinement study was conducted to determine appropriate values of a_s and N which produce converged theoretical results of $R_{ac,IntJ}$. As a result, the uniform dicretisation containing about 10000 subsections with $a_s = 0.1$ mm was used in the subsequent calculations. The distributions of subsections with $a_s = 0.1$ mm are shown in Fig. 3.8. The four cross-sectional shapes are precisely approximated by the uniform discretisation.

(a) Circular   (b) Hexagonal

(c) Square   (d) Triangular
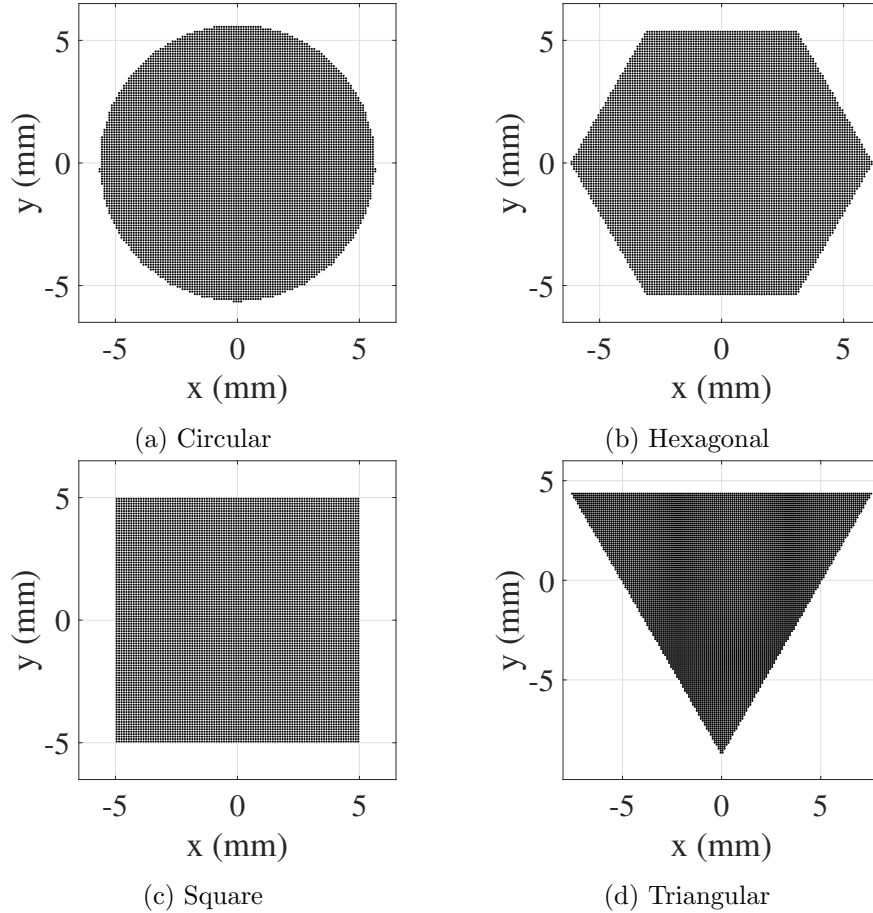
Figure 3.8: Discretisation of the four cross-sectional shapes with subsections with the size of $a_s = 0.1$ mm and in a total number of $N = 10000$ approximately.

Theoretical solutions of $R_{ac,IntJ}$ computed by the script are compared with FE approximations, which is given in Fig. 3.9. Both the theoretical and FE results show distinct order of R_{ac} which is attributed to different cross-sections shapes of samples. The triangular sample possesses the highest R_{ac} at all frequencies whereas the circular sample has the lowest results. Difference between two types of results for all sample shapes in the whole frequency range is smaller than 1%. This validates the reliability of the FE models for the plain samples and the precisions of FEA in measuring Z_{int}.
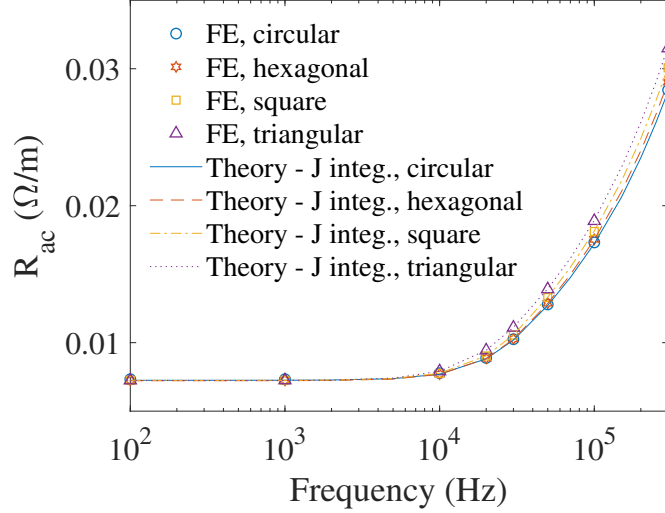
Figure 3.9: Resistance per unit length of plain SS316 samples of various cross-sectional shapes obtained by FEA and theoretical methods of integral equation of current distribution [193, 218].

3.5 Modal Network Theory

Another method called Modal Network Theory (MNT) has been developed by Silvester [205–208] to predict Z_{int} and R_{ac} of non-magnetic linear conductors through disassembling the total current into a modal network which represented spatial current distributions. In this section, the theory will be briefly introduced then applied to calculate impedance of plain SS316 samples in four cross-sectional shapes. Finally, theoretical solutions of impedance will be compared with the same FE results given above in Fig. 3.9.

In the first step of discretisation, the current flowing in the long straight conductor is disintegrated into an infinite number of modal distributions which are individual and independent of other distributions. Distributions of current modes are only related to the cross-sectional shape but independent of material properties or oscillating frequencies. The modal problem with infinite distributions is approximated by dividing the sample into a large number N of square subsections with the same side length of a_s, which is similar to the process in obtaining the integral equation of current in Section 3.4. By choosing a_s to be very small, uniform current distributions can be assumed over the cross-section of subsections. Therefore, each subsection possesses the same resistance and inductance as

$$r_p = R_{dc}N \qquad\qquad l_p = \frac{\mu}{2\pi} \log \frac{a_s}{d_p} \qquad\qquad (3.68)$$

where d_p refers to self and mutual geometric mean distances between subsections but is simplified here to be the distance from center to center due to the equal-area and square shape of subsections, as given in (3.60). r_p and l_p of all subsections

are assembled to give matrices of

$$\mathbf{R} = R_{dc}N\mathbf{U} \qquad\qquad \mathbf{L} = \frac{\mu}{2\pi}\mathbf{G} \qquad (3.69)$$

where $\mathbf{U}$ is the unit matrix, $\mathbf{G}$ represents the geometric matrix that only depends on the cross-sectional shape of the sample.

Then in the second step of 'relaxation', the current modal network is solved by conducting a thought-experiment. Imaging a sample carrying a DC is encased by a thin cylindrical sheath that contains the return path of the DC. If the conductor is suddenly connected to the sheath at two points far apart, i.e. short-circuited, the system relaxes and the current declines. This relaxation behaviour can be represented by the network to be

$$\left(\mathbf{R} + \mathbf{L}\frac{d}{dt}\right)\mathbf{i} = \mathbf{0} \qquad (3.70)$$

which has N solutions in the form of [205–208]

$$\mathbf{i}_p = \mathbf{I}_p e^{m_p t} \qquad (3.71)$$

where the time constant m_p is defined as

$$m_p = \frac{r_p}{l_p} \qquad (3.72)$$

By substituting matrices of $\mathbf{R}$ and $\mathbf{L}$ and the solution of $\mathbf{i}$ into (3.71), it can be obtained that

$$\left(\frac{N}{\sigma S_0}\mathbf{U} + \frac{\mu}{2\pi}\mathbf{G}m_p\right)\mathbf{I}_p = \mathbf{0} \qquad (3.73)$$

The above equation can be further rearranged to separate geometrical and electromagnetic term, as

$$\left(\mathbf{G} + \frac{2\pi N}{\mu\sigma S_0 m_p}\mathbf{U}\right)\mathbf{I}_p = \mathbf{0} \qquad (3.74)$$

It is an ordinary eigenvalue problem of the geometric matrix $\mathbf{G}$, which can be conveniently solved to obtain several eigenvectors $\mathbf{I}_p$ and eigenvalues of

$$\gamma = -\frac{2\pi N}{\mu\sigma S_0 m_p} \qquad (3.75)$$

The conductance and inductance of each network mode were presented by two quantities defined from corresponding eigenvector and eigenvalue, the average component value $\boldsymbol{\alpha}_p$ and the normalised characteristic frequency $\boldsymbol{\Omega}_p$, which are defined by

$$\boldsymbol{\alpha}_p = \sqrt{\frac{\sum_p^N I_p^2}{N}} \qquad (3.76)$$

$$\boldsymbol{\Omega}_p = \frac{-2N}{\gamma} = \frac{\mu\sigma S_0 m_p}{\pi} \qquad (3.77)$$

Eventually, Z_{int} of the sample is calculated by applying the parallel rule to modal impedance as

$$Z_{int,MNT} = \frac{1}{\sum_{p=1}^{N} 1/(r_p + j\omega l_p)} \tag{3.78}$$

By substituting expressions of parameters of $\boldsymbol{\alpha}_p$ and $\boldsymbol{\Omega}_p$ obtained above, this equation can be written to

$$Z_{int,MNT} = \frac{R_{dc}}{\sum_{p=1}^{N} \boldsymbol{\alpha}_p{}^2 / \left(1 + j\frac{\Omega}{\boldsymbol{\Omega}_p}\right)} \tag{3.79}$$

where the frequency-dependent term Ω is introduced to exclude effects of sample sizes, material properties, and oscillating frequencies on skin effect. It is related to the frequency parameter p_{sim} [196] as

$$\Omega = \sqrt{p_{sim}} = \frac{\mu\omega}{\pi R_{dc}} \tag{3.80}$$

This theoretical method was employed to calculate impedance for plain SS316 samples via MATLAB (see in Appendix A.2). During the application of the theory, above process may be simplified to three steps:

1. Establishing the specific geometric matrix $\mathbf{G}$ for the sample;

2. Computing eigenvalues and eigenvectors of $\mathbf{G}$ with enough number to converge, then calculating $\boldsymbol{\alpha}_p$ and $\boldsymbol{\Omega}_p$;

3. Substituting $\boldsymbol{\alpha}_p$ and $\boldsymbol{\Omega}_p$ into (3.79) to calculate Z_{int} and hence R_{ac}.

It is suggested in the literature that 7 to 15 eigenvectors are sufficient to accomplish the approximation with high accuracy [206], however, such requirement was found to be inadequate for the SS316 samples at related frequencies. The influence of the number of eigenvectors on the convergence of the impedance results are shown in Fig. 3.10. Situations of convergence are slightly different between the circular and triangular samples, but obviously 15 eigenvectors are not enough to reach convergences. For clearer observation, theoretical results of the circular sample at some frequencies in Fig. 3.10a are demonstrated against the number of eigenvectors in Fig. 3.11. It is shown that situations of convergence vary at different frequencies. Calculations for high frequencies require much more eigenvectors to reach a desired precision. At least 50 eigenvectors are required for the SS316 samples with a highest frequency of 300 kHz.

| (a) Circular | (b) Triangular |
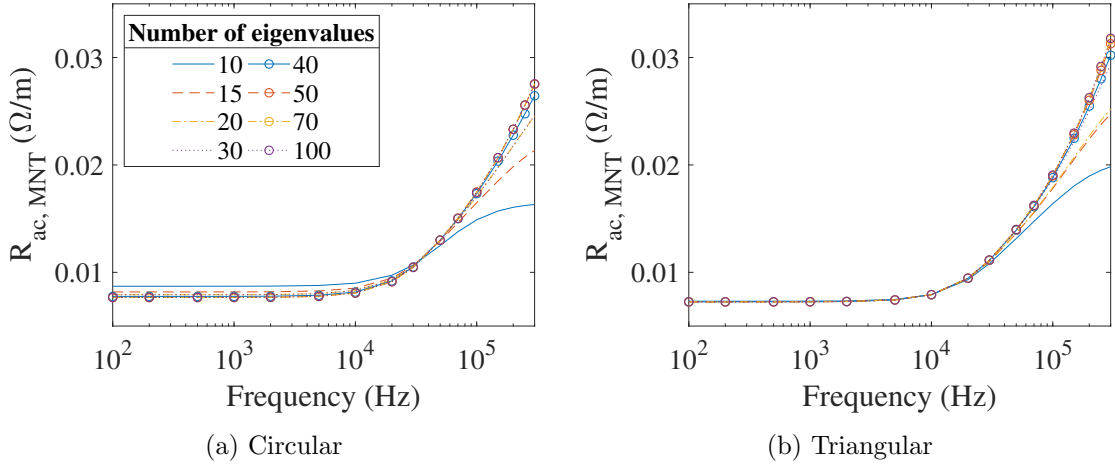
Figure 3.10: The effect of the number of eigenvectors on theoretical MNT results of impedance for the circular and triangular samples.
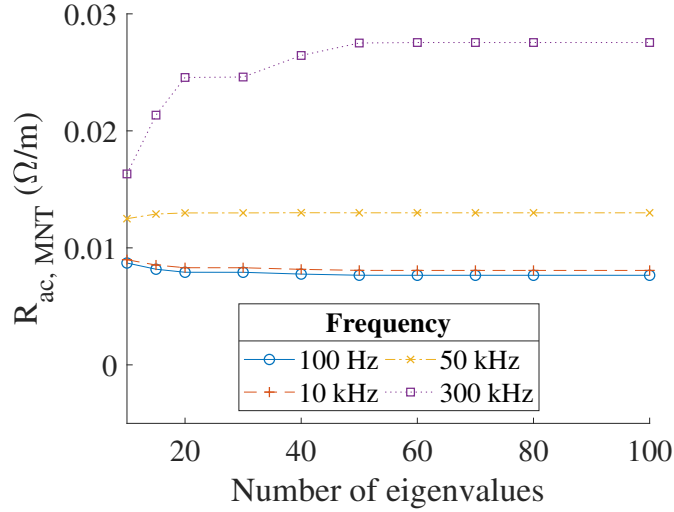
Figure 3.11: The effect of the number of eigenvectors on theoretical MNT results of impedance for the circular sample at different frequencies.

In Fig. 3.12, $R_{ac,MNT}$ based on 100 eigenvectors are compared with FE results for four samples. $R_{ac,MNT}$ of the circular sample at quasi-DC frequencies are higher than the FE results for 4%. While for the other samples, mean differences (averaged from all frequencies) between $R_{ac,MNT}$ and FE results are within 1% and decrease as the cross-sectional shape varying from circular to triangular. The mean difference of the triangular sample is only 0.05%. Divergence between theoretical and FE results increase as the frequency rises up (except for the circular one). At the highest frequency of 300 kHz, the maximum difference between MNT and FE results of R_{ac} is 3% for the hexagonal sample (as well as the circular) and within 1% for the square and triangular samples. Such agreement between FE results and solutions calculated by MNT is slightly lower than the comparison based on the former theoretical method as presented in Fig. 3.9. But it is sufficient to provide confidence of FEA at least in measuring Z_{int} for the SS316 samples.
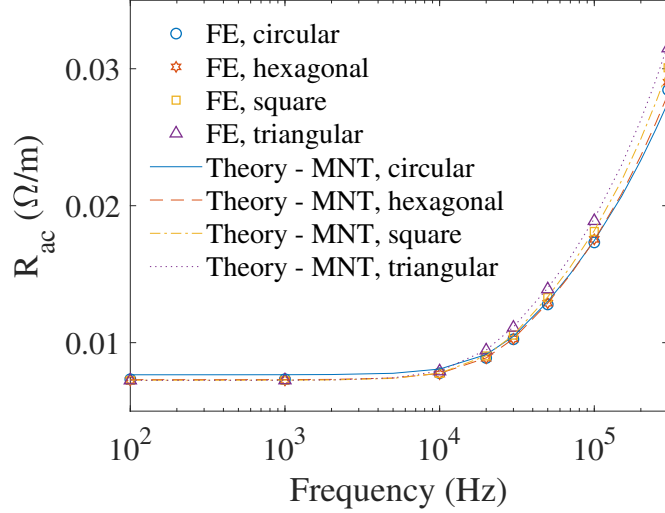
Figure 3.12: Resistance per unit length of plain SS316 samples of various cross-sectional shapes obtained by FEA and theoretical methods of MNT [205–208].

3.6 Conclusions

Several available theories of calculating Z_{int} of straight and individual conductors have been demonstrated and employed to the plain SS316 samples in various cross-sectional shapes of circular, hexagonal, square, and triangular. Based on FEA, Z_{int} of the samples in the same cross-sectional area of 100 mm^2 increases as the cross-sectional shape varies from circular to triangular, reaching 0.0284, 0.0290, 0.0301, and 0.0315 Ω/m, respectively, at 300 kHz.

The Bessel Function Method, which is well-known as the solution to Z_{int} of cylindrical conductors, was derived from Maxwell's equations. In this method, a Bessel equation of current density describing a time-varying field is firstly established; then the equation is solved under low and high frequencies separately by inserting approximated solutions of Bessel functions to figure out solutions of $Z_{int,Bes}$. However, $R_{dc,Bes}$ and $R_{ac,Bes}$ for the circular cross-section do not encountered at intermediate frequencies around 20 kHz. $R_{dc,Bes}$ show good agreement with FE results in which the maximum difference is within 1%; whereas $R_{ac,Bes}$ are constantly lower then FE results for about 0.002 Ω.

The second theory, EAM, calculates $R_{ac,EAM}$ based on effective areas confined by skin depth on the rim of cross-sections. The main advantage of EAM is the general applicability for any cross-sectional shapes. $R_{ac,EAM}$ for the four SS316 samples are lower than FE results and show an opposite order in magnitudes to FE results, which is caused by the absence of current crowding in this method. $R_{ac,EAM}$ is compared to another theoretical solution, $R_{ac,Thev}$, which is devised for rectangular conductors and based on Thévenin assumption [222]. Two types of theoretical solutions agree well for the square SS316 sample, giving mean differences for the whole frequency range smaller than 1.4%.

There is a half-empirical definition of $R_{ac,Pay}$ for rectangular conductors which expresses resistance increases due to skin effect and current crowding separately [225, 226]. In this method, the analysis of skin effect is different to EAM that the effective area is simplified to be the area of a strip beneath the conductor surface with a width of the skin depth. On the other side, the current crowding is estimated by the proximity effect between imaginary cylindrical subsections within the conductor. The approximation of current crowding in $R_{ac,Pay}$ is employed to $R_{ac,EAM}$ to improve the performance of EAM for rectangular cross-sections. The half-empirical solution and Improved EAM provide similar R_{ac} for the square sample and show limited agreement to FE results with average differences for all frequencies within 7% (both the two types of theoretical solutions). However, Improved EAM is suggested as preference at least in predicting the increase in resistance due to skin effect since EAM computes the effective area more precisely without simplification.

The last two theories involve discretisation which refers to dividing the conductor into a finite number of subsections. In the first method [193, 218], subsections are assumed as individual subsections whose self and mutual inductance are related to the distribution of A, and hence J. The double integral equations of J over the cross-section is thus produced. Current distribution is then roughly solved by converting the integral equation into the matrix form and calculating the inversion. The second method of MNT [205–208] assumes each subsection as a resistor-inductor (R-L) modal branch, i.e. a spatial part of the total current. The modal resistance and inductance are related to corresponding eigenvector and eigenvalue of a distance matrix which represents spatial distribution of current modes. These two methods were devised for rectangular conductors in literature but are extended to other geometries in this section. The procedures of the extension, i.e. constructing the general geometric matrix adapting for arbitrary cross-sectional shapes, were presented in detail. Expect for $R_{dc,MNT}$ of the circular sample which are higher to FE results for 4% at quasi-DC frequencies (< 10 kHz), R_{ac} predicted by the two methods for all cross-sectional shapes fit well to FE results with average differences smaller than 1%. Thereby, these two discretisation-involved methods are assumed as the optimum theoretical solutions of Z_{int} for straight individual non-magnetic conductors of arbitrary cross-sectional shapes. Furthermore, numerical methodology of simulating the SS316 models including the modelling procedures and post-processing are validated.

Chapter 4

Experimental Methodology: Preliminary and Formal Experiments and Data Processing

4.1 Introduction

This chapter introduces the experimental methods that were utilised in this work. To study the capability of the ACPD method in identifying various features on (and in) conductive components, several samples were manufactured to be in the same dimension of 55 mm $\times$ 100 mm^2 and contain different features such as a cylindrical drill and a wide notch (or remain flawless for plain samples) for measuring. Experimental researches were consisted of two phases — a preliminary stage for verifying experimental methodology and a formal stage of conducting ACPD experiments on the manufactured samples (i.e. the plain and featured samples of the same size). In the preliminary stage, ACPD signals were measured from some conductors and circuits with available theoretic solutions of impedance to validate the measuring procedures and the data processing. In formal experiments, the plain and featured samples are divided into three cases. Cases 1-3 are designed to investigate the detection ability of the ACPD method in distinguishing sample geometries, features with dissimilar opening shapes, and features with similar opening and in the same cross-sectional area step by step.

In this chapter, experimental apparatus and procedures from inputting AC signals to recording ACPD data will be demonstrated first. Then all experimental samples and relevant configurations of shielding from electromagnetic interference and connecting to the rest circuits will be introduced, which includes four preliminary samples and nine formal samples with/without features in materials of SS316/EN1A.

The final section focuses on the data processing. As will be presented in the first section of this chapter, AC and PD signals were recorded simultaneously in the ACPD experiments. Measured signals in the time domain are indistinct to

detect sample shapes or feature geometries. It is necessary to process and convert measured data into the frequency domain so that frequency-related quantities such as amplitudes and phase angles of impedance can be used to identify the sample shapes and the features. Since the swept oscillating frequency continually increases even within a single period, a MATLAB script has been developed to identify and interpret ACPD measurements for a frequency range from 10 Hz to 300 kHz. The ideas and considerations behind each processes of the script will be introduced first. Then, challenges due to the varying frequency and error signals that were encountered during the development will be described. This will demonstrate the advantages of the script over other available methods that it adapts to swept signals for a wide range of frequency (from 10 Hz to 300 kHz).

4.2   Experimental Set-up and Procedures

The ACPD experiments were applied to several preliminary and formal samples in the research. Preliminary samples include simple conductors and circuits with known or calculable impedance, such as an isolated resistor and R-L combined circuits. Experimental results processed after the data processing were then contrasted with the known and calculated results to verify the experimental methodology. Formal experiments involve the plain samples in non-magnetic SS316 of various cross-sectional shapes and the featured samples in ferromagnetic EN1A of square.

All the preliminary and formal experiments followed the same procedure that AC was injected into the conductor (or circuit) then induced PD and real AC outputted from the conductor were measured. A swept sinusoidal wave of AC that sampled frequencies from 10 Hz to 300 kHz in 2 secs intervals with a constant amplitude of 3 A was supplied in all experiments. This input AC was connected to the conductor through screw blocks, which can be seen on the left hand side of Fig. 4.1a. Fig. 4.1a shows an example of a plain square sample, two silver steel wires were bended and welded onto the sample at one ends and screwed to the current lead at the other ends. To eliminate electromagnetic disturbance on measurements, the measuring part was shielded by a die-cast aluminium box, see on the right hand side of Fig. 4.1a. Moreover, contact areas between the box and the sample was insulated by using a polymer tape, as shown in Fig. 4.1b.
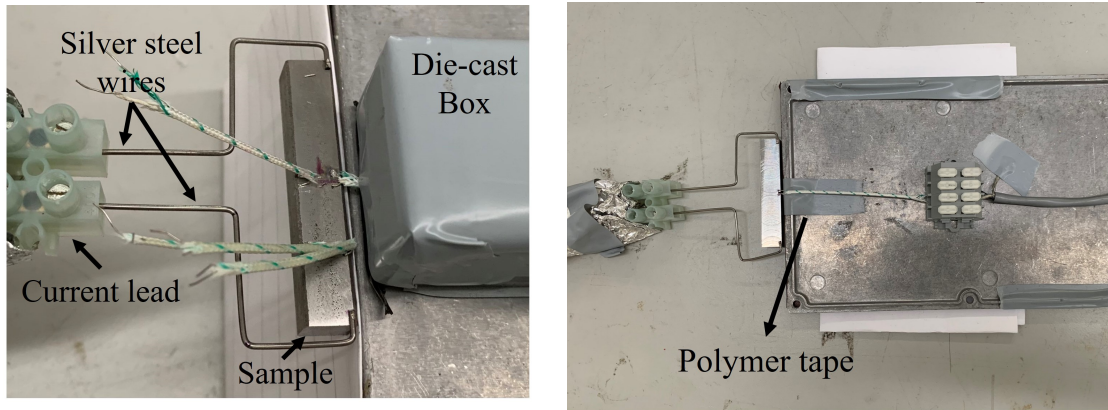
(a) The die-cast box for shielding.

(b) Insulations around and inside the box.

Figure 4.1: Strategies for shielding and insulation for measurements from electromagnetic interference in the ACPD experiments.

Fig. 4.2 shows the schematic of equipment and procedures of the ACPD experiments developed by Buss [2]. Expect for the sample and connections around the sample inside the dash circle that were disconnected and replaced in different experiments, the rest of set-up was shared by all experiments. The swept sinusoidal signal of 3 A was generated through a LabVIEW program. The generated signal was outputted by an NI-PXIe-6124 input/output module, then amplified by a bespoke amplifier (which was supplied by Fylde Electronics), finally injected into the sample. Induced PDs were measured from areas with interested in on the sample surface. Taking the square sample in Fig. 4.1 as an example, PDs were measured with a distance of 2 mm across the center and close to the edge. Since PDs obtained in formal experiments were at magnitudes smaller than 0.05 mV at quasi-DC, signals of PD were amplified 1000 times by a Fylde FE-H793-TA before feeding back into the same PXI unit. Smaller factors were used to amplify measurements for samples that outputted greater PDs, e.g. the combined circuits and long rod in preliminary experiments. Output signals of AC and PD were captured at a constant sampling frequency (f_s) of 4 MHz.
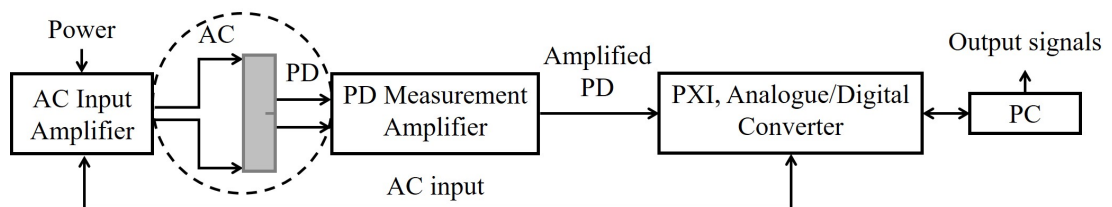
Figure 4.2: A Schematic of equipment and process of ACPD experiments.

Measured signals of AC and PD in the time domain were then processed by a MATLAB script to calculate results of impedance and PD in the frequency domain. As an example, Fig. 4.3 presents raw and processed results obtained for the circular SS316 sample. In Fig. 4.3b, processed results of impedance with

87

respect to modulus and phase angles are compared to manual measurements with good agreement. A detailed review of the MATLAB problem will be given in Section 4.5.

(a) Raw signals of AC and PD.

(b) Processed results of impedance.
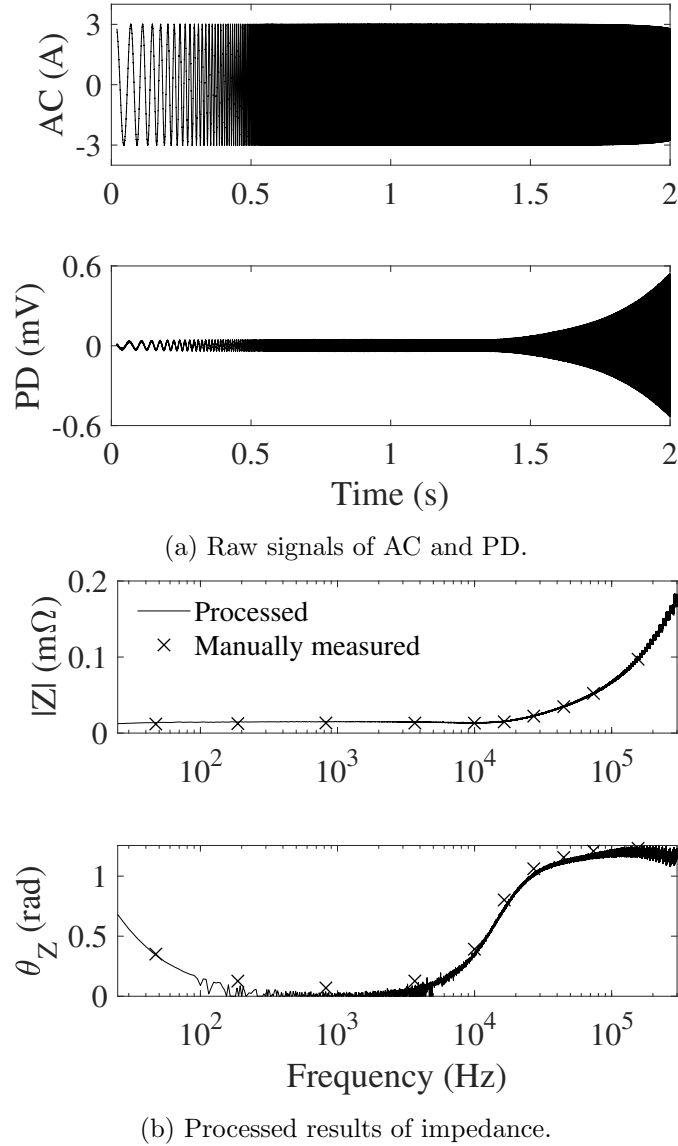
Figure 4.3: Raw and processed results of ACPD measurements of the circular SS316 sample.

4.3 Circuits and Conductors in Preliminary Experiments

To test and evaluate experimental methodology of the ACPD method, the same measurement procedures and the data processing as in formal ACPD experiments were applied to a series of preliminary experiments. Preliminary experiments were designed to form a progressive investigation, starting from measuring R_{dc}

of an individual resistor then to determine inductive quantities such as R_{ac} and Z_{int} of simple circuits. Preliminary samples include an individual resistor, R-L combined circuits in series and parallel connections, and a long copper rod. For all the preliminary samples, a current excitation of quasi-DC was firstly applied to simply measure R_{dc}. After obtained desired R_{dc}, another current excitation of AC with stepped frequencies was injected to determine R_{ac} and Z_{int} at some constant frequencies. Finally the swept sinusoidal wave of AC varying from 10 Hz to 300 kHz was used for inputting, which was the same as formal experiments. Three cases of the preliminary samples and relevant connections to the measuring part will be introduced in this section. Results of experiments sampled with swept-frequency AC, which was considered as the most representative, will be presented in Chapter 6.

The first sample was an individual resistor with a known resistance (R_{res}) of 0.22 Ω. It was placed on a breadboard and connected to the rest of equipment by two pairs of wires. The same resistor was then combined with an inductor with a known inductance (L_{ind}) of 1.8 μH to form a series and a parallel circuit for the second part of preliminary experiments, see in Fig. 4.4. As mentioned before, the die-cast box was used to shield measuring parts, which can be seen on the right hand side of Fig. 4.4b. Moreover, an insulated clapboard was inserted between the resistor and the inductor in the parallel circuit to avoid contact between two units thus eliminate interference. Equivalent impedance of combined circuits processed from measured signals were then compared with theoretical solutions based on the series and parallel rule to evaluate the precision of the ACPD method.

(a) The series circuit.   (b) The parallel circuit and insulations.
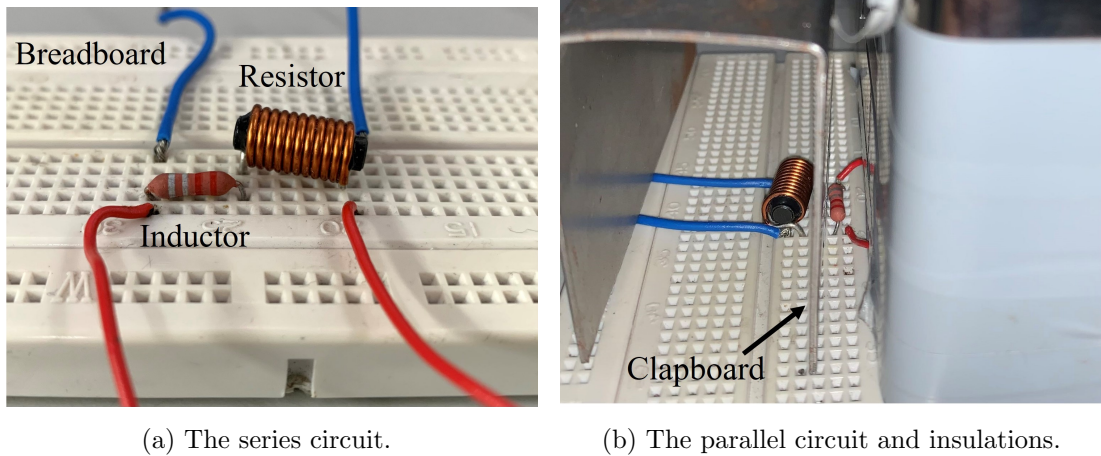
Figure 4.4: Configurations of the R-L combined series and parallel circuit involved in preliminary experiments.

In formal experiments, ACPD signals were directly measured from isolated conductors, which was different to measurements from a breadboard in these preliminary experiments. Thereby, it is necessary to contain a single conductor in the validation stage. Considering that the Bessel Function Method introduced in Section 3.2 is widely used to calculate Z_{int} for an infinitely long conductor, a long

copper rod with an aspect ratio of 250 (assumed to be infinitely long) was chosen for the last preliminary sample. The copper rod is 1 m in length and 4 mm in diameter. Since the rod is in a finite length, the proximity effect of two ends is negligible but remains effective. The rod was hence formed into a U-shape with a separation between two halves of the wire (i.e. the forward and return paths of current) to be 3 cm, which reduced the proximity effect smaller than 2% [215,228]. As the rod was too long to be covered by the shielding box, measuring parts at two ends of the rod were sealed by foil paper to reduce error signals. Raven has measured impedance of a copper rod in the same dimension of 1 m × 4 mm [215]. Impedance obtained in this preliminary experiment will be compared with solutions given by the Bessel Function Method and experimental results provided by Raven in a later section.
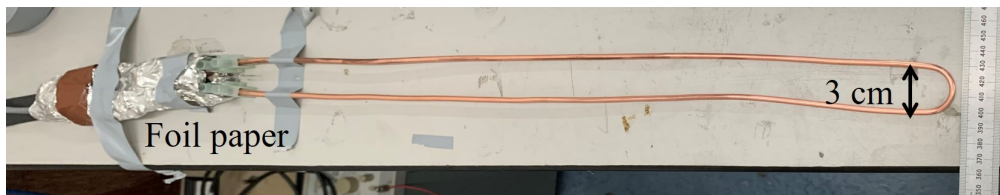
Figure 4.5: The U-shaped copper rod involved in preliminary experiments.

4.4 Plain and Featured Samples in Formal Experiments

Formal experiments involved several plain and featured samples which are in the same dimension of 100 mm^2 in cross-sectional areas and 55 mm in lengths. Samples were divided into three cases according to three research purposes in order to sequentially investigate the ACPD method in detecting sample geometries and feature shapes.

To study the ability of ACPD methdos in identifying the shape of a conductor, Case 1 was designed to include four plain samples made of the non-magnetic material of SS316 and in the same cross-sectional area but different shapes of circular, hexagonal, square, and triangular, as shown in Fig. 4.6. Since four samples are in the same material and dimensions, samples possess the same R_{dc}, which suggests the incapability of DCPD methods in distinguishing between these samples. It was expected to observe different R_{ac} at high frequencies through the ACPD method as a result of various cross-sectional shapes.
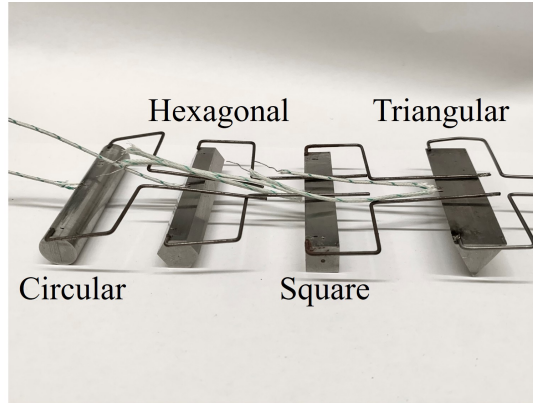
Figure 4.6: Plain SS316 samples in Case 1: four samples are in the same cross-sectional area of 100 mm^2 but with different shapes of circular, hexagonal, square, and triangular.

In the next stage of the formal experiments, several featured samples including various features were measured in Cases 2 & 3. To highlight the ability of ACPD in approximating internal features, a strong skin effect is preferred thus the ferromagnetic material of EN1A was chosen for samples in feature detection experiments (see more details in Section 7.2.1). All the featured samples are in the square shape. Features were manufactured at the middle of the edges and towards the center of the conductors. Three featured samples in Case 3 are shown in Fig. 4.7 as an illustration, however, internal geometries of features are invisible in these pictures. Drawing of features on samples in Cases 2 & 3 are given in Fig. 4.8-4.9 for better presentation.
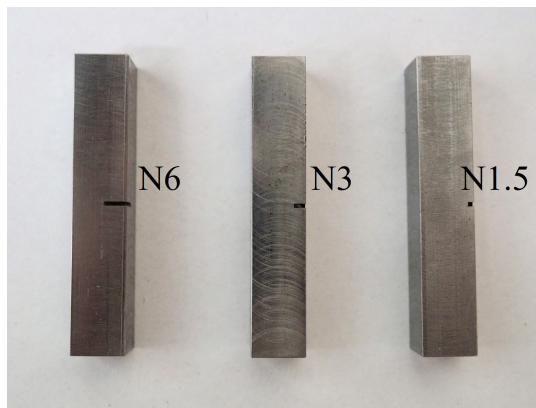
Figure 4.7: Featured EN1A samples in Case 3: three features (N6, N3, and N1.5) have the same cross-sectional area of 9 mm^2.
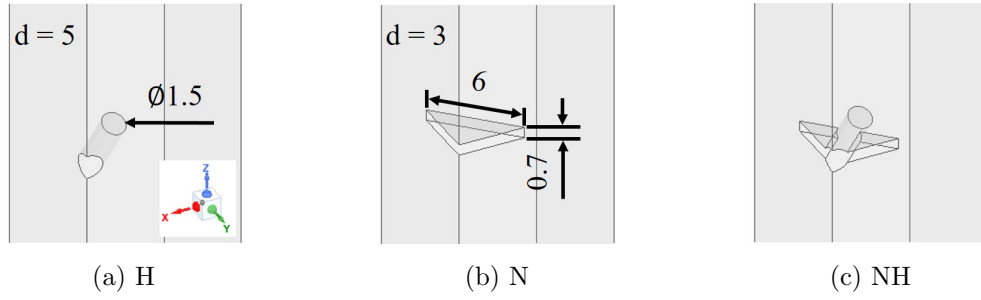
Figure 4.8: Drawings of features in Case 2 (H, N, and NH). d refers to the depth into the conductor (all dimensions are in mm).
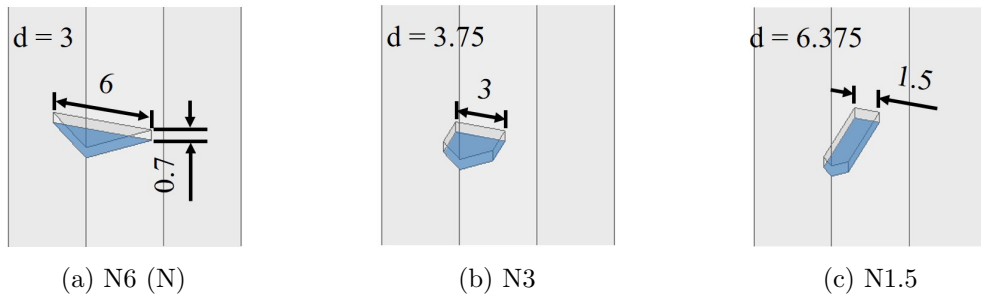
Figure 4.9: Drawings of features in Case 3 (N6 (N), N3, and N1.5). d refers to the depth into the conductor (all dimensions in mm).

As shown in Fig. 4.8, Case 2 includes a cylindrical hole, a wide notch, and a hybrid feature combining the drill and the notch, which were named as the H, N, and NH feature respectively. The research of Case 2 focuses on investigating the ability of the ACPD method in identifying features with dissimilar opening shapes. In the next stage of Case 3, two notches similar to the N feature were introduced in to further study the detection capability. Three notches in Case 3, as displayed in Fig. 4.9, were manufactured with the same cross-sectional area of 9 mm^2 by controlling the lengths and depths of the notches. The N feature was also named as N6 in Case 3, referring to the opening length of 6 mm. Similarly, the other two notches were named based on opening lengths as N3 and N1.5.

Same connections of AC injection and PD measurement were applied to all formal samples, see in Fig. 4.10. For each sample, a pair of silver steel wires in a diameter of 1.13 mm were bended to connect the sample with the current lead. Silver steel wires for AC inputting were welded at positions close to the edge with the feature located on. Another pair of thin electric wires for PD measurement were welded close to the same edge and at the middle of the sample length with a distance of 2 mm in between. More specific, the measurement probes were located on the plain surfaces of the plain samples in Case 1 and across features in Cases 2 & 3.
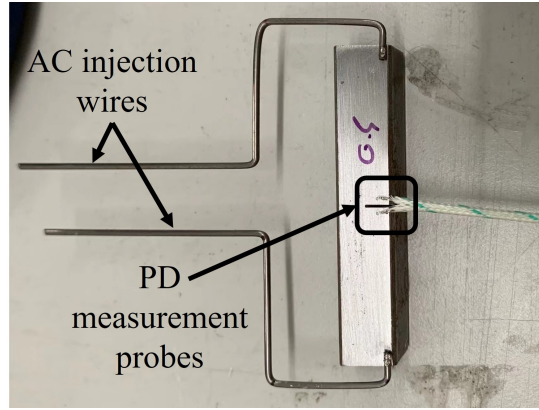
Figure 4.10: The configuration of AC injection and PD measurement consistently applied to all formal samples in Cases 2 & 3.

However, uncertainties in manual work of welding were inevitable and had to be considered in analysis. Welding errors of current injection wires and PD measuring probes will be taken into consideration through FEA, which will be presented in Section 5.4 & 5.6 respectively. Processed results obtained in Cases 1-3 will be compared with manual measurements in Chapter 6 for the purpose of validation as preliminary experiments. Such experimental results will be further analysed with FE results to reach comprehensive conclusions of the detection ability of the ACPD method in Chapter 7.

4.5 Experimental Data Processing

4.5.1 Challenges in Data Processing

In ACPD experiments conducted in the project, the frequency of input AC was designed to increase from 10 Hz to 300 kHz in 2 secs. The output AC, which was the real current supplied by the amplifier and injected to the sample, and PD signals were recoded together at a constant f_s of 4 MHz. Raw data of AC and PD signals measured from the SS316 circular sample are shown in Fig. 4.11 as an example. As the time grows, the swept frequency of signals increases and the time period of signals becomes narrower. AC and PD signals measured in the time domain are incapable to indicate obvious differences between different samples, while frequency-related quantities, such as the frequency, amplitude, and phase shift between AC and PD signals, are more convenient and distinct to compare between various experiments. It is thereby necessary to translate raw data in the time domain to the frequency domain, i.e. continuous signals were separated into individual periods. Then quantities obtained from the frequency domain may be used to analyse PDs across different features or further interpreted to calculate impedance with respect to modulus and phase angles of the conductor.
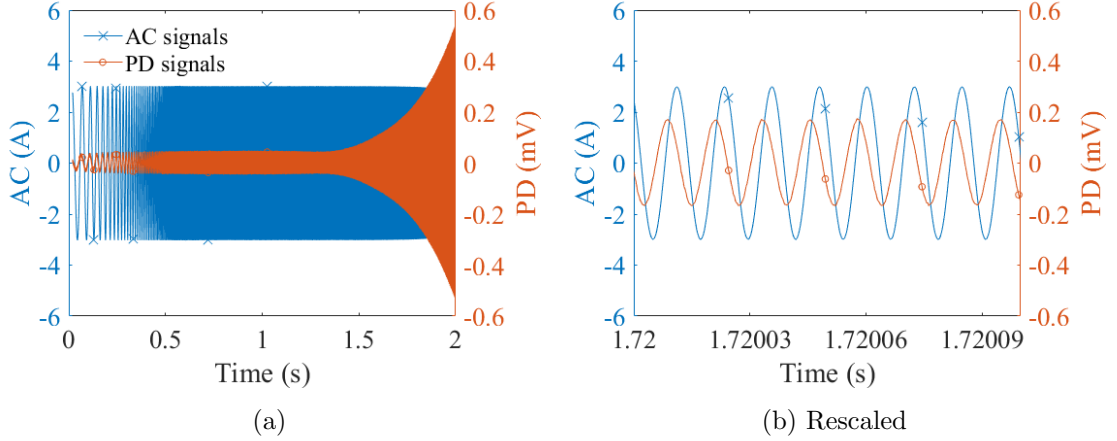
Figure 4.11: Raw signals of AC and PD measured from the SS316 circular sample with 2 mm in distance.

The data processing of interpreting signals into frequency domain encountered two main challenges. The first problem was due to the swept frequency sampled for signals in experiments. Available interpreting methods including Fast Fourier Transform (FFT) are inapplicable here, since ACPD signals belonging to periods at various frequencies are continuously distributed in the time interval of 2 secs. Components such as the amplitude, frequency, and phase angle of each signal period are desired in the data processing. It is necessary to develop a script to interpret signals with continuously increasing frequencies. The second problem was caused by inevitable error signals recorded in experiments. Moreover, since f_s remained constant, ACPD signals had very different performance at extremely low and high frequencies. For $f \ll f_s$, many error signals were recorded, which caused difficulties in identifying and separating data; while for $f \gg f_s$, few signals were recorded for each period so that the accuracy of data interpretation was limited. The development of the script focused on overcoming the two challenges and achieving high precisions of the interpretation.

4.5.2 Development of Data Processing Script and Constant Slope Ratio Method

The data processing script developed in MATLAB (see in Appendix B) consists of three steps. Fig. 4.12 shows a piece synchronous AC and PD of signals at a frequency of f_i to help illustrate. At first, positions of two zero-crossings of AC signals in time domain are figured out as t_1 and t_2 by the script. Then in the second step, the identification of PD signals is started from positions of t_1 and t_2 and moved forward to find out the two zero-crossings of PD signals at t_3 and t_4. The four zero-crossing are then used to calculate f_i and the time shift between

AC and PD periods Δt as,

$$ f_i = \frac{1}{t_2 - t_1} = \frac{1}{t_4 - t_3} \qquad\qquad \Delta t_i = t_1 - t_3 = t_2 - t_4 \qquad (4.1) $$

The equal signs in (4.1) only hold for ideal conditions that all zero-crossings of signals were exactly recorded. For real signals measured in the ACPD experiments, several 'zero-crossings' including error signals were recorded and fluctuated around zero, the real zero-crossing (e.g. t_1) was almost impossible to be precisely captured. So the script takes averages of the later two terms in (4.1) for f_i and Δt_i. Amplitudes of AC and PD ($|I_i|$ & $|V_i|$) are then determined conveniently from signals confined by t_1 to t_2 and t_3 to t_4, as

$$ f_i = \frac{1}{2}\left(\frac{1}{t_2 - t_1} + \frac{1}{t_4 - t_3}\right) \qquad\qquad \Delta t_i = \frac{1}{2}\left[(t_1 - t_3) + (t_2 - t_4)\right] \qquad (4.2) $$

If impedance results are required for analysing, the third step will be conducted to calculate the modulus ($|Z_i|$) and phase angle (θ_{Zi}) at the certain frequency of f_i by equations of

$$ |Z_i| = \frac{|V_i|}{|I_i|} \qquad\qquad \theta_{Zi} = 2\pi f_i \Delta t_i \qquad (4.3) $$
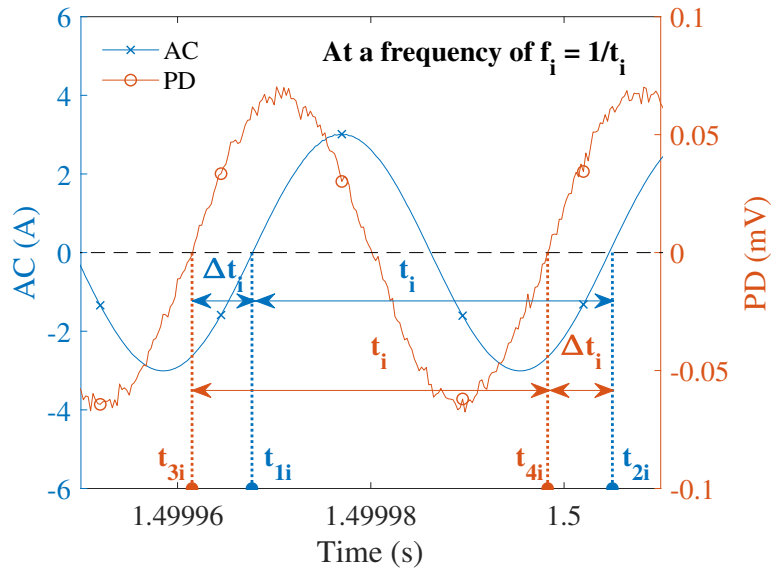
Figure 4.12: Schematic of a corresponding pair of AC and PD signals at a certain frequency of f_i.

The first two steps in the script will be introduced in detail below. The main task in the first step of current identification is to identify zero-crossings from all measured signals then separate signals into individual periods. To reduce the computing time, only the part of signals near to the zero are involved in identification while signals far from the zero are excluded. This is achieved by applying

a positive and negative tolerance (I_{tol}), see in Fig. 4.13a. $\pm I_{tol}$ is determined to cover all possible 'zero-crossings' of measured data, i.e. AC signals beyond $\pm I_{tol}$ could be definitely eliminated from the data processing. AC signals within $\pm I_{tol}$ are divided into many 'bands', for example in Fig. 4.13a, the band AB in the 1st period contains the zero-crossing at t_{AB} and the band CD in the 3rd period contains the zero-crossing at t_{CD}. Now the problem are converted from separating all signals into individual frequencies to simply separate the bands. A Constant Slope Ratio Method (CSRM) has been devised to solve the problem, relative schematics are displayed in Fig. 4.13b.
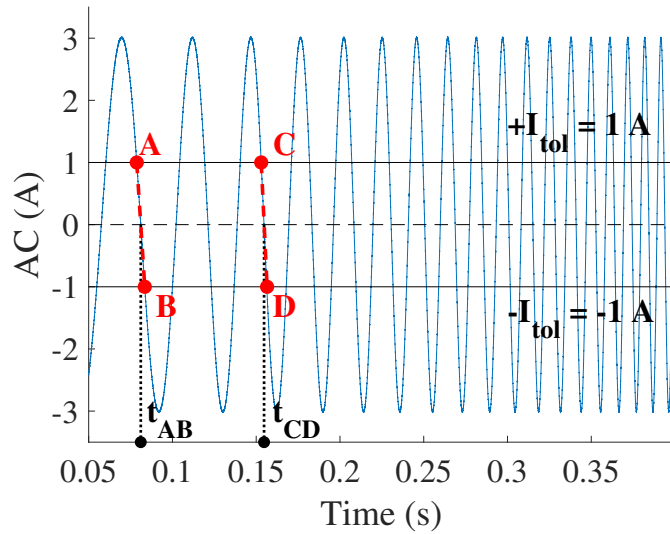
(a) Concepts of $\pm I_{tol}$ and bands.

(b) CSMR
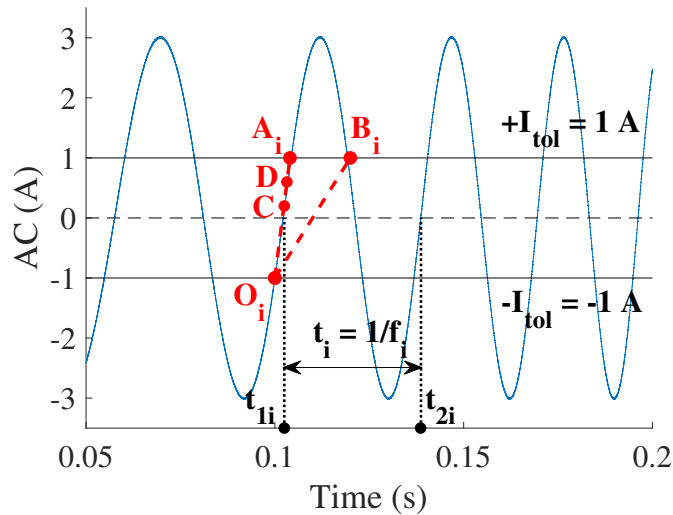
Figure 4.13: Schematic of the AC identification procedure in the MATLAB script.

AC signals belonging to the period at f_i and with a phase angle of θ_i is expressed by

$$I_i(t) = |I| \sin\left(2\pi f_i + \theta_i\right) \qquad (4.4)$$

where $|I|$ is the amplitude of the current injection. The positions of zero-crossing of the 1st band (t_{1i}), the ending point of the 1st band (t_{A_i}), and the starting point of the 2nd band (t_{B_i}) can be calculated based on (4.4) as

$$t_{1i} = \frac{-\theta_i}{2\pi f_i} \tag{4.5}$$

$$t_{Ai} = \frac{\sin^{-1}\left(\frac{I_{tol}}{|I|}\right) - \theta_i}{2\pi f_i} \tag{4.6}$$

$$t_{Bi} = \frac{\pi - \theta_i - \sin^{-1}\left(\frac{I_{tol}}{|I|}\right)}{2\pi f_i} \tag{4.7}$$

Slopes of the segment $O_i A_i$ and $O_i B_i$ are given by

$$k_{O_i A_i} = \frac{I_{tol}}{t_{Ai} - t_{1i}} \tag{4.8}$$

$$k_{O_i B_i} = \frac{I_{tol}}{t_{Ai} + t_{Bi} - 2t_{1i}} \tag{4.9}$$

By substituting (4.5)-(4.7) into (4.8)-(4.9), the ratio between $k_{O_i A_i}$ and $k_{O_i B_i}$ can be obtained as

$$R_{ki} = \frac{k_{O_i A_i}}{k_{O_i B_i}} = \frac{\pi}{2\sin^{-1}\left(\frac{I_{tol}}{|I|}\right)} \tag{4.10}$$

It can be seen that R_{ki} is only dependent on I_{tol} and $|I|$ but independent of f_i and θ_i of any specific period. It suggests that a constant slope ratio (R_k) is applicable to the whole frequency range, i.e. can be used as the criterion to continuously identify bands for all frequencies. This is the principle of CSMR.

CSRM is applied to the MATLAB script through following processes. For example to find out the experimentally measured (or interpreted) zero-crossing of the band $O_i A_i$ in Fig. 4.13b, firstly the signal at O_i is recognised as the first signal of the band (based on identification results for the preceding band); then all signals behind O_i are detected by calculating slopes of signals with O_i. Slopes between O_i and all signals belonging to the band $O_i A_i$ are almost equal to $k_{O_i A_i}$. Until the signal at B_i which is the first signal of the next band is encountered, slopes between B_i and O_i is much smaller than $k_{O_i A_i}$. Ratios between two slopes calculated from two adjacent signals are used as the indication. As examples, for the signal at C and its next signal at D, the slope ratio of $R_{kCD} = \frac{k_{O_i D}}{k_{O_i C}}$ is about to be 1; whereas for signals at A_i and B_i, the slope ratio of R_{kAB} is much larger than 1. The noticeable rise in R_k is a clear sign that all data before B_i belong to the band $O_i A_i$ and the signal B_i is the first data of the next band. After identifying all current bands, theoretical zero-crossings are calculated by intersecting bands and the axis. Signals that are closest to theoretical zero-crossings are determined as processed zero-crossings of AC signals at each frequency.

One of the advantage of CSRM is the reduction of negative effects due to error signals. Since the uncertainties in AC signals caused by error signals is negligible

by comparing with the scale of band lengths, the method enables the script to complete the current identification with high precisions. Additionally, the value of I_{tol} is adjusted to adapt different situations of signal numbers at low and high frequencies, see quantified evaluation in Chapter 6. For low frequencies, excess signals were captured hence a small I_{tol} was used to reduce the computing time; while at high frequencies too less signals were recorded, a greater I_{tol} was applied to cover enough data and assure the precisions. The value of I_{tol} is adjusted automatically based on numbers of signals contained in bands. As long as a band is detected to cover too few signals (at least 4 data is required in the script), a greater value of I_{tol} will be used for subsequent identifications. Values of I_{tol} and corresponding R_k used in the script are given in Tab. 4.1.

I_{tol}	R_k
$\frac{1}{3}|I|$	4.62
$\frac{2}{3}|I|$	2.15
$|I|$	1.00

Table 4.1: Values of I_{tol} and corresponding R_k used in the MATLAB script.

After determining all zero-crossings of AC signals, the next step is to identify zero-crossings of PD signals. The method of convolution is incapable of processing data with high precisions at low frequencies since results of convolution are strongly affected by error signals. Thereby, the PD identification are completed by a simpler method based on the symmetry of the sinusoidal curve of signals, as demonstrated in Fig. 4.14. At first, the PD signal nearest to the identified AC zero-crossing that located at t_{1i} is marked as $V(t_{1i})$. Then signals before $V(t_{1i})$ are detected one by one until the signal $V(t_{xi})$, which has an opposite sign to $V(t_{1i})$ and in a magnitude closet to $|V(t_{1i})|$, is identified. The zero-crossing of the fitting line of $V(t_{1i})V(t_{xi})$ is computed as the theoretical zero-crossing of PD, the PD signal nearest to the theoretical result is picked out as the processed zero-crossing of PD that located at t_{3i}.
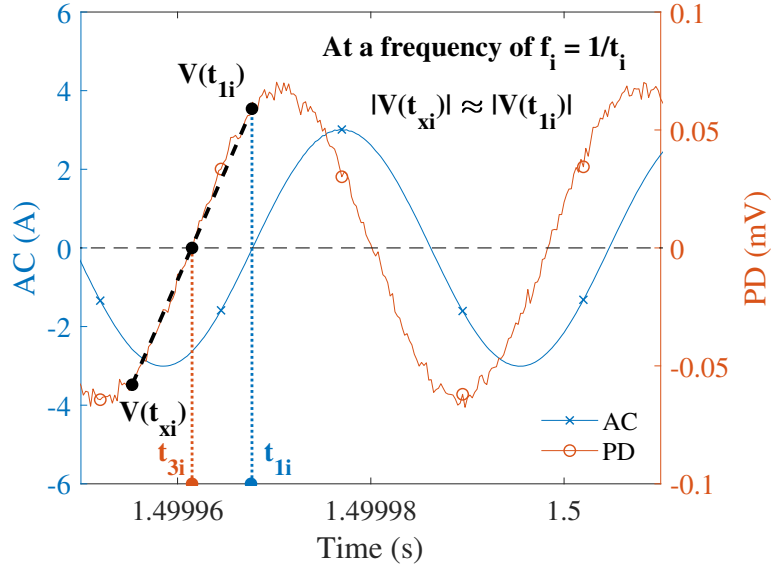
Figure 4.14: Schematic of the PD identification process in the MATLAB script.

By following the two steps, the script identifies zero-crossings of AC and PD signals for all frequencies, thus oscillating f_i, $|V_i|$ & $|I_i|$, and Δt_i can be easily obtained. Impedance parameters of $|Z_i|$ and θ_{Zi} can then be calculated against frequencies based on (4.3).

The Matlab script overcomes deficiencies of FFT and the method of convolution in identifying AC and PD periods and reduces interference caused by error signals. To validate the precision of the data processing, processed results processed by the script will be compared with manual measurements for all preliminary and formal samples in Chapter 6.

4.6   Conclusions

In the first section of the chapter, equipment and process of ACPD experiments have been demonstrated, including the injection, amplification, and measurements. Attention was paid to protect measurements from electromagnetic interference, such as shielding all measuring parts by a die-cast box and sealing exposed area of samples and wires by insulated materials.

Then in the next section, the experimental samples for all preliminary and formal experiments were introduced with detailed information. Preliminary samples include the isolated resistor, R-L circuits constructed by a breadboard, and the long cylindrical wire. Impedance of these samples are known or may be calculated based on available theories, which provides contrasts with experimental results to verify experimental methodologies before conducting formal experiments. Formal experiments are consisted of three cases that respectively contain four plain samples in different shapes, three featured samples with dissimilar feature openings (H, N, and NH), and another three featured samples with notches in the same

cross-sectional area (N6, N3, and N1.5). These cases enable progressive investigations of the ACPD method from detecting sample shapes to identifying feature geometries. Processed results obtained from all experiments will be presented in Chapter 6.

Finally, the MATLAB script has been created to interpret measured ACPD signals into PDs and impedance in the frequency domain with a wide frequency range from 10 Hz to 300 kHz. In the first step of the data processing, CSRM is applied to identify and separate AC signals into individual periods, which adapts to a wide range of swept frequencies. Moreover, through using different values of I_{tol} and R_k at different frequencies, the script properly eliminates interference of abundant error signals at low frequencies and utilises sufficient signals at high frequencies for identification to remain high precisions. Then in the second step of PD interpretation, straightforward judgement statements are used to precisely find out corresponding PD periods for identified AC periods. The script has been successively applied to process PD signals with high precisions especially for low frequencies from 10 Hz, which was unattainable by other available methods such as the method of convolution. The precision of the data processing will be evaluated in Chapter 6 in which processed results of PD and impedance will be compared with manual measurements that directly read in NI DIAdem (for all samples) and available theoretical solutions (for the preliminary samples).

Chapter 5

Numerical Methodology: Finite Element Analysis of Alternating Current Potential Difference Samples

5.1 Introduction

This chapter focuses on simulating the formal samples by FEA. Several theoretical solutions of solving Z_{int} and current fields for finite long conductors were presented in Chapter 3. However, applications of these theories are variously restricted to different situations, e.g. some solutions are limited to weak magnetic materials or plain conductors without features. Analytical solutions are incapable of providing comprehensive comparisons to experimental results, especially to contrast with PDs which are the primary data directed measured from ACPD experiments. For this reason, FEA have been employed to approximate the electric/current fields generated within and around the samples in ACPD experiments.

In the first section, the approaches of creating FE models for the formal samples will be presented in detail. Then the techniques of partial and symmetrical modelling designed for reducing model sizes will be introduced and verified. Next, FEA will be applied to investigate the impact of welding uncertainties of current injection wires on the experimental measurements, i.e. the end effect due to current injections. Then mesh refinement study will be conducted and presented separately for the plain SS316 models and featured EN1A models to evaluate the mesh statistics. The optimum parameters of convergence and meshes will be determined for the models based on the compromise between model precisions and simulation cost. Finally, post processing procedures of outputting field solutions, PDs, and error bars of PD (which represent possible ranges of results due to welding errors) will be reported.

5.2 General Approaches for Finite Element models

In this research, FE models were developed using the Eddy Current solver in Maxwell 3D from ANSYS Electronics Desktop. At first, a complete model comprising of a conducting bar and a pair of current injection wires was built to simulate the full field induced within and around the experimental sample. Then based on results of further study (see in the next section), the complete model was replaced by a partial model that only consists of a small part at the center of the sample. These two types of models are shown in Fig. 5.1. According to the ANSYS manual [235], all FE models were created by following a sequence of modelling steps: drawing the geometry, assigning material properties, specifying excitations and boundary conditions, applying mesh operations, defining global parameters, and specifying solution options. The application of these procedures in creating models of the formal samples will be introduced in this section. Post processing including generating reports of desired quantities will be presented in Section 5.6.

(a) A complete model.   (b) A partial model.
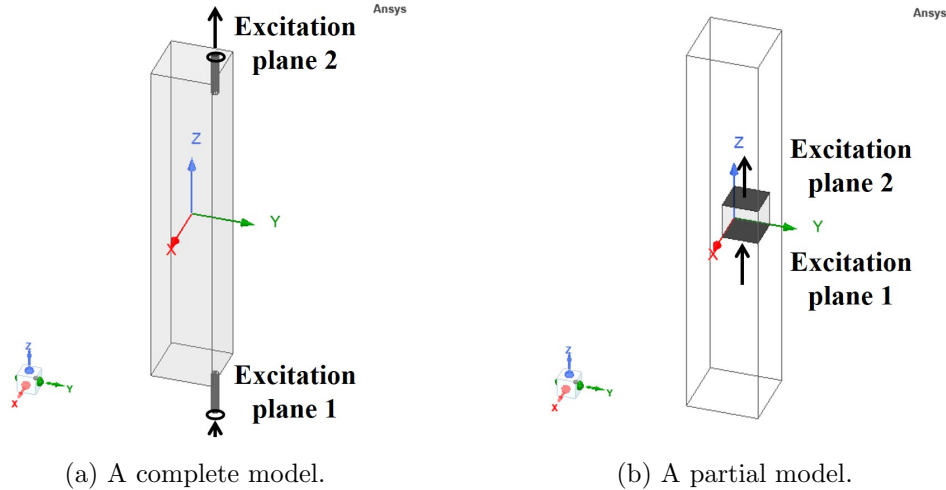
Figure 5.1: Two types of FE models.

Since the objective of FEA is to solve the skin effect problems for various samples with current injections at different frequencies, the Eddy Current solver is determined as the solution type of the analysis. Then the geometry of the model is defined to be a bar of a certain shape and in the dimension of 55 mm $\times$ 100 mm^2. To circumvent difficulties in generating meshes on curved surfaces, a polygon with 24 faces rather than a cylinder is used for modelling the circular SS316 sample. In the complete model, the pair of current wires are modelled by two small polygons with 24 faces located at ends of the bar. These two small polygons are assembled with the bar by a boolean operation of subtraction in which the overlapped volume (i.e. welded material) of about 0.4 mm in depth is removed from the bar. It will be demonstrated later in Section 5.4 that the modelling of current wires hardly

affect measurements at the center of the model. Thereby, details of modelling such as the size of subtracted volume, the meshing of two wires, and even the material of current wires are of negligible importance.

Properties of two sample materials, i.e. SS316 and EN1A, were measured in experiments by Buss [2]. However, these measurements were conducted at the initial stage of the project when the importance of shielding the measuring region had not been realised. As a result, the measured permeability of SS316 is questionable and a literature value [236] is used for FEA and theoretical calculations. Due to the ferromagnetic property of EN1A, measurements of EN1A are assumed to be valid. Properties of the wire material, i.e. silver steels, were not measured and a literature data of high carbon steel is used in modelling. Tab. 5.1 presents measured and literature data used for defining these materials in FEA.

Material	Relative μ	σ (MS/m)
SS316	1.02 [236]	1.38
EN1A	4002.75	54.90
High carbon steel	100 [237]	4.60 [236]

Table 5.1: Material properties of samples and current wires used in FEA.

The next step is to apply current excitations and create an air box surrounding the model as the analysis region. In ANSYS Maxwell 3D, the current excitation of a conducting body can only be applied on two opposing and external faces of the environmental region. It suggests that two outer boundaries of the air region must coincide with current injection surfaces of the model so that current excitations can be assigned on. According to the guidance, the input and output current with a peak value of 3 A are assigned on the top and bottom surfaces of wires on the complete model, see in Fig. 5.1a. While for a partial model in Fig. 5.1b, current excitations are imposed on two cross-sections of the remaining part of the sample. The equivalence between two methods of applying excitations will be discussed in detail later. A too small region may cause interference in simulation, e.g. producing an asymmetric electric field for a model in a symmetric geometry and carrying a uniform excitation. To consider this point and also avoid excessive meshing of the region, the padding of air regions for the SS316 models were determined to be 500% of the model dimension by trial and error, while that for the EN1A models were decided to be 100% of the model size. Fig. 5.2 shows air regions of the complete and the partial SS316 model. In Fig. 5.2a, the padding of the region for the complete model is defined on $\pm X$ & $\pm Y$-directions. The default boundary condition on vertical surfaces of the air region is the Neumann boundary in which $\mathbf{H}$ field is tangential to the surface and no flux cross it. While on the partial model, the region extends along $+X$ & $+Y$-directions and coincide with the symmetry planes on which the model is split, which can be seen in Fig. 5.2b. Even symmetry boundary conduction, which defines $\mathbf{H}$ to be normal

to the surface, is applied to the symmetry planes to assure magnetic symmetry. As mentioned before, horizontal surfaces of air regions are defined to overlap with current injection surfaces of the model for applying current excitations as boundary conditions.

(a) Region of the complete model.   (b) Region of the partial model.
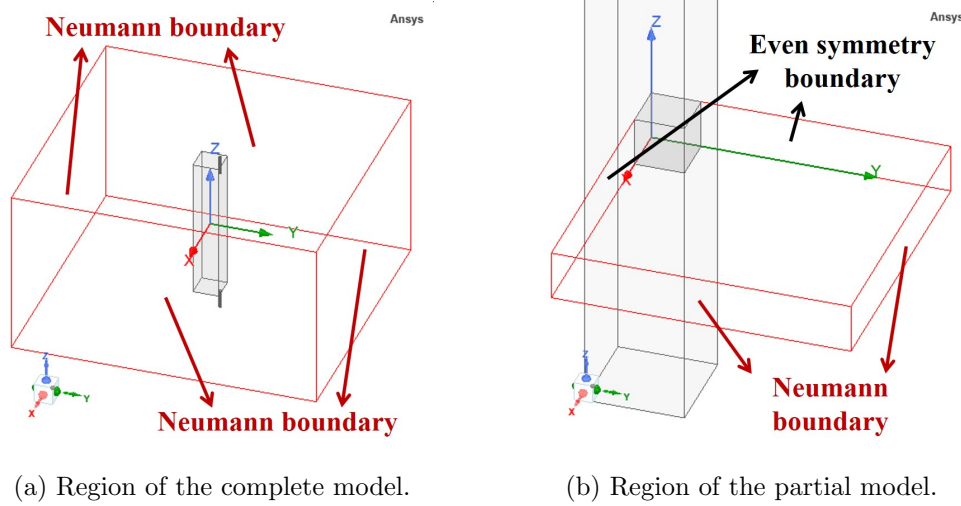
Figure 5.2: Regions and boundaries defined for two types of FE models.

Then all vertical surfaces of the sample are selected to apply a skin-depth based mesh. Two mesh parameters, i.e. 'maximum element size' and 'number of layers with skin depth', are determined based on the mesh refinement study. In the complete model, objects of two wires are selected to define a length-based mesh with the maximum element size of 2 mm. Inductance matrix is assigned as a global parameter to calculate impedance of the whole model, which is significant to analysis for the plain samples in Case 1.

The last step before submitting the job is to specify solution options including the adaptive frequency and suggestions of convergence. Default values of the 'minimum and maximum number of passes' are 2 and 50 respectively, and of the 'refinement of the number of elements per pass' is 20%. These value are used for the SS316 and EN1A models. The significant parameter of percent error, which refers to the final requirement of convergence (see detailed definitions in Section 5.5), is decided with mesh statistics in the mesh refinement study.

By way of example, Fig. 5.3 shows FE results of current fields predicted by the complete model that simulates the skin effect within a square SS316 sample at 10 kHz and 100 kHz. In Fig. 5.3a & 5.3c, current fields are concentrated near injection points thus skin effect are interrupted near two end surfaces. The disturbance due to current injection recedes with distances from the end surface towards the center plane, which can be observed more clearly through current fields and skin depths on internal sections at different distances from the end, as shown in Fig. 5.3b & 5.3d.

(a) The complete model, 10 kHz.

(b) Internal sections, 10 kHz.

(c) The complete model, 100 kHz.

(d) Internal sections, 100 kHz.
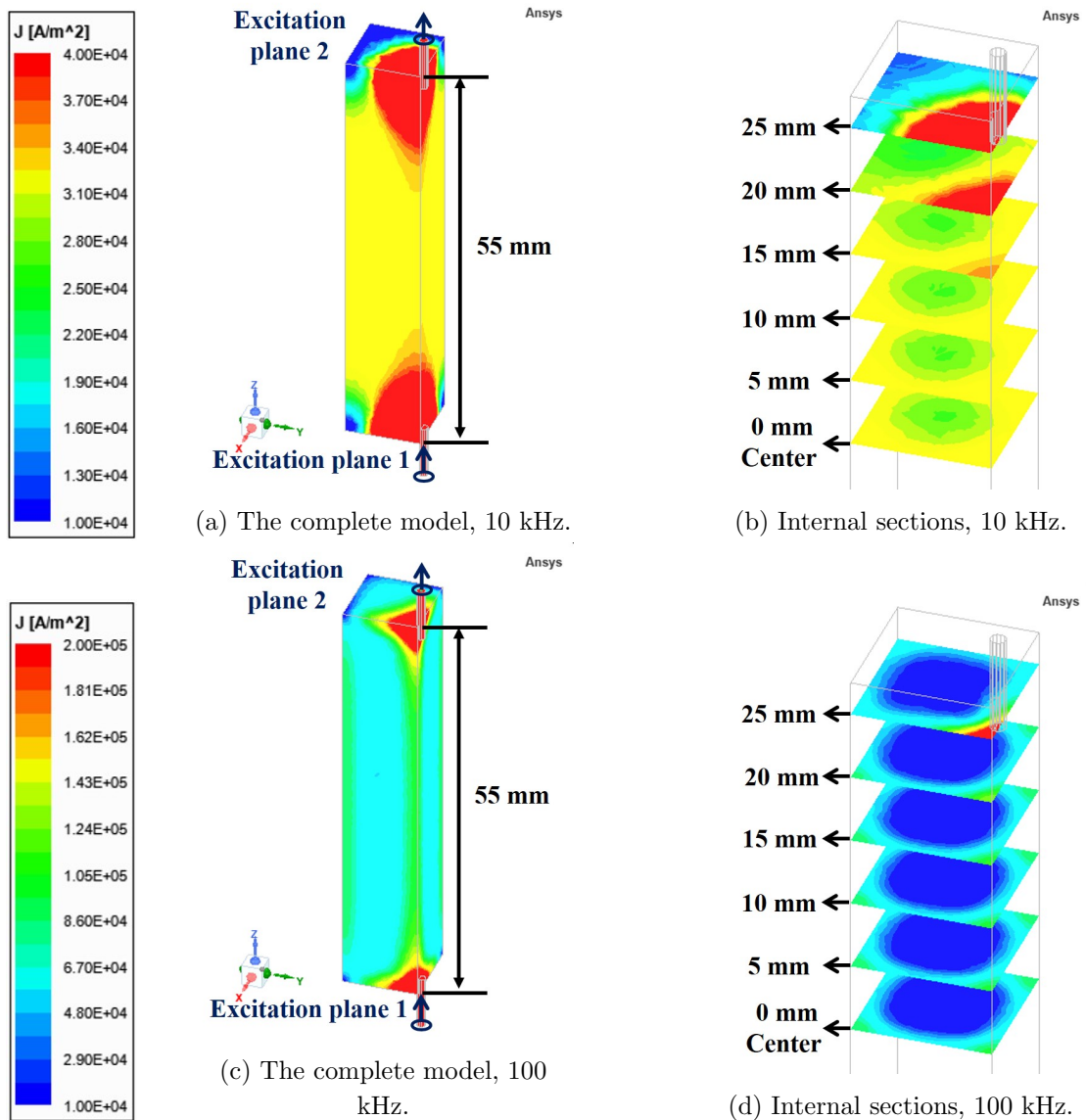
Figure 5.3: Current fields generated by the complete model of the square SS316 sample at 10 kHz and 100 kHz.

5.3 Partial Symmetrical Modelling

The complete model requires numerous elements in modelling current wires, which greatly increases the simulation time or reduces the precision of field solutions. Fig. 5.4 shows a mesh plot of the complete SS316 model simulated at 30 kHz. The mesh applied to the sample part is skin-depth based with the maximum element size of 0.5 mm and 4 layers of elements within the skin depth ($\delta = 2.45$ mm). While the length based mesh assigned to the wire part is much coarser with the maximum element size of 2 mm. However, due to the stronger magnetism of high carbon steel than that of SS316, ANSYS automatically refines the mesh that the mesh around the current wire is much finer than that within the skin depth region. It is beneficial to build partial models that simulates the significant part

near the center of the sample and excludes current wires. Due to the mechanism of excitation application in ANSYS Maxwell 3D, the total current remains constant through all sections normal to the current flowing direction inside the conducting body, i.e. current injection through two current wires in the complete model is equivalent to the assignments through two internal sections of the samples in partial models. Moreover, by taking the advantage of the geometrical symmetry of the samples and the uniformity of surface current excitations, the sizes of partial models can be further reduced by applying even symmetry boundary conditions on two symmetry planes.
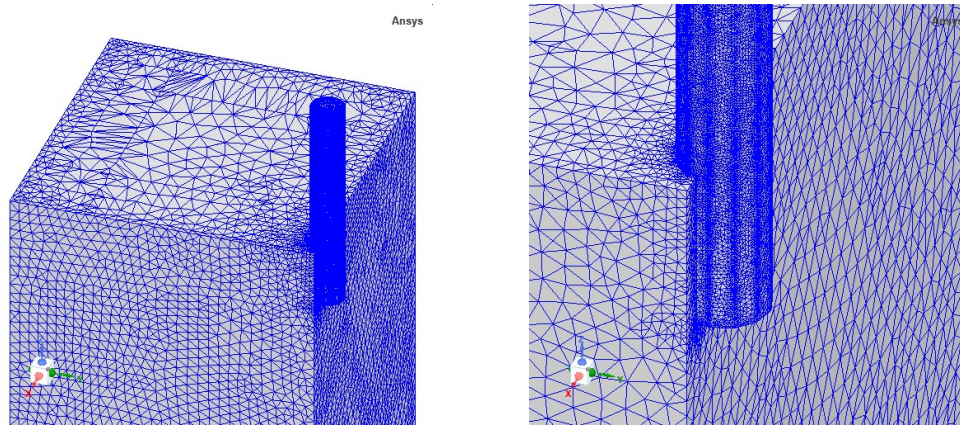
Figure 5.4: The mesh plot around current wires in the complete SS316 model at 30 kHz with skin depth of 2.45 mm.

The processes of developing a partial symmetrical (PS) model are demonstrated in Fig. 5.5. Firstly in Fig. 5.5a-5.5b, a volume in 10 mm long (with or without a feature) around the center of the sample is cut out as a partial model. Then in Fig. 5.5c, even symmetry boundary conductions are assigned to two symmetry planes A and B in which the plane A is horizontal and across the center plane and the plane B is vertical and across the diagonal. For the plain samples without features, the models were not split by the diagonal plane B but by vertical planes on the X & Y-axis, as shown in Fig. 5.2b. Finally in Fig. 5.5d, a conductive path highlighted in pink which is parallel to the symmetry diagonal plane B and follows the feature edge is defined to simulate the real conductive path measured in the ACPD experiments. PDs integrated along such conductive paths are then use to analyse and evaluate the precision of the model. The definition of conductive paths and methods in calculating field outputs will be presented in Section 5.6.

(a) A complete model of 55 mm.

(b) A partial model of 10 mm.

(c) Two symmetry planes.
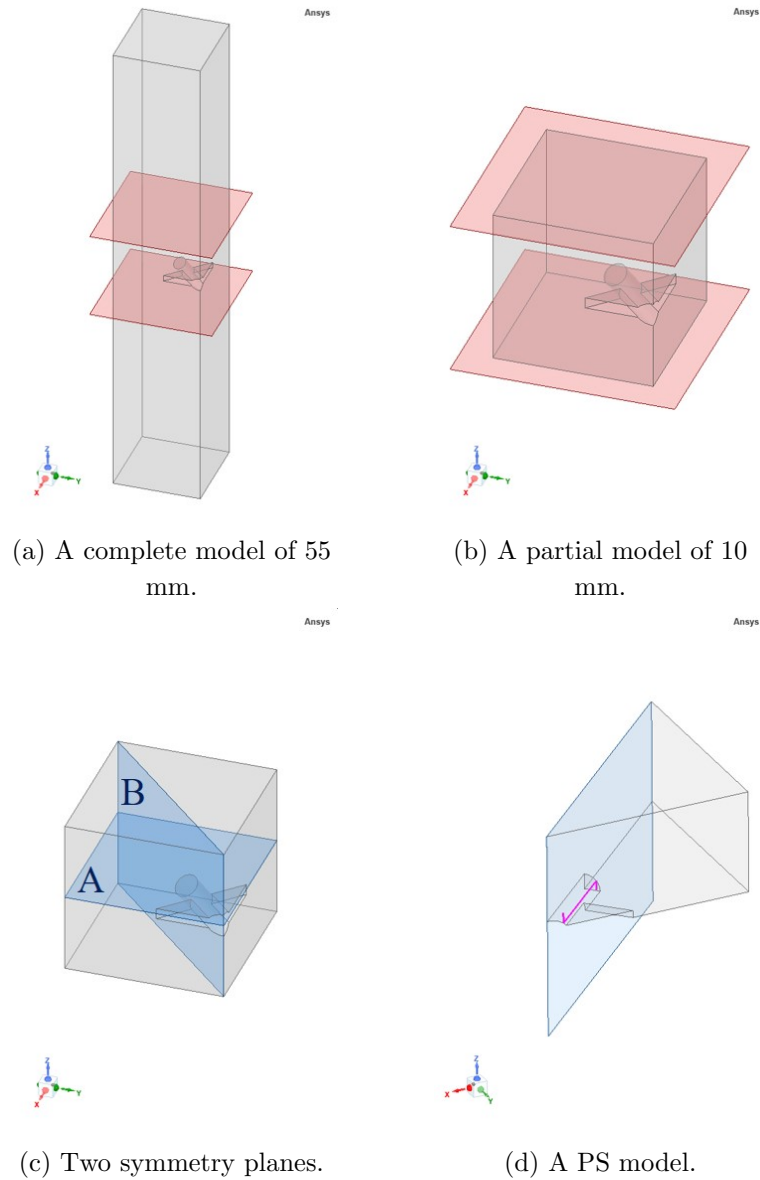
(d) A PS model.

Figure 5.5: The processes of developing a partial symmetrical (PS) model.

To evaluate the feasibility of PS modelling, the current field approximated by a PS model simulating the square SS316 sample at 10 kHz were compared with the results computed from the complete model, comparisons are given in Fig. 5.6. Current fields along two conductive paths called 'Path-0.8' and 'Path-4.2' were measured to quantify the difference in field solutions given by two models. Two paths are highlighted in black in Fig. 5.6, Path-0.8 is at a position of 0.8 mm to the edge with current wire welded on and Path-4.2 refers to a position at 4.2 mm to the edge. Path-0.8 simulates the paths on samples that were most likely to be measured in experiments, which will be introduced in more detail in Section 5.6. Since Path-0.8 is close to the edges and current injections, another paths far from the edges are desired for contrast, e.g. Path-4.2 was chosen here.

(a) The complete model, 10 kHz.   (b) The PS model, 10 kHz.

(c) The complete model, 100 kHz.   (d) The PS model, 100 kHz.
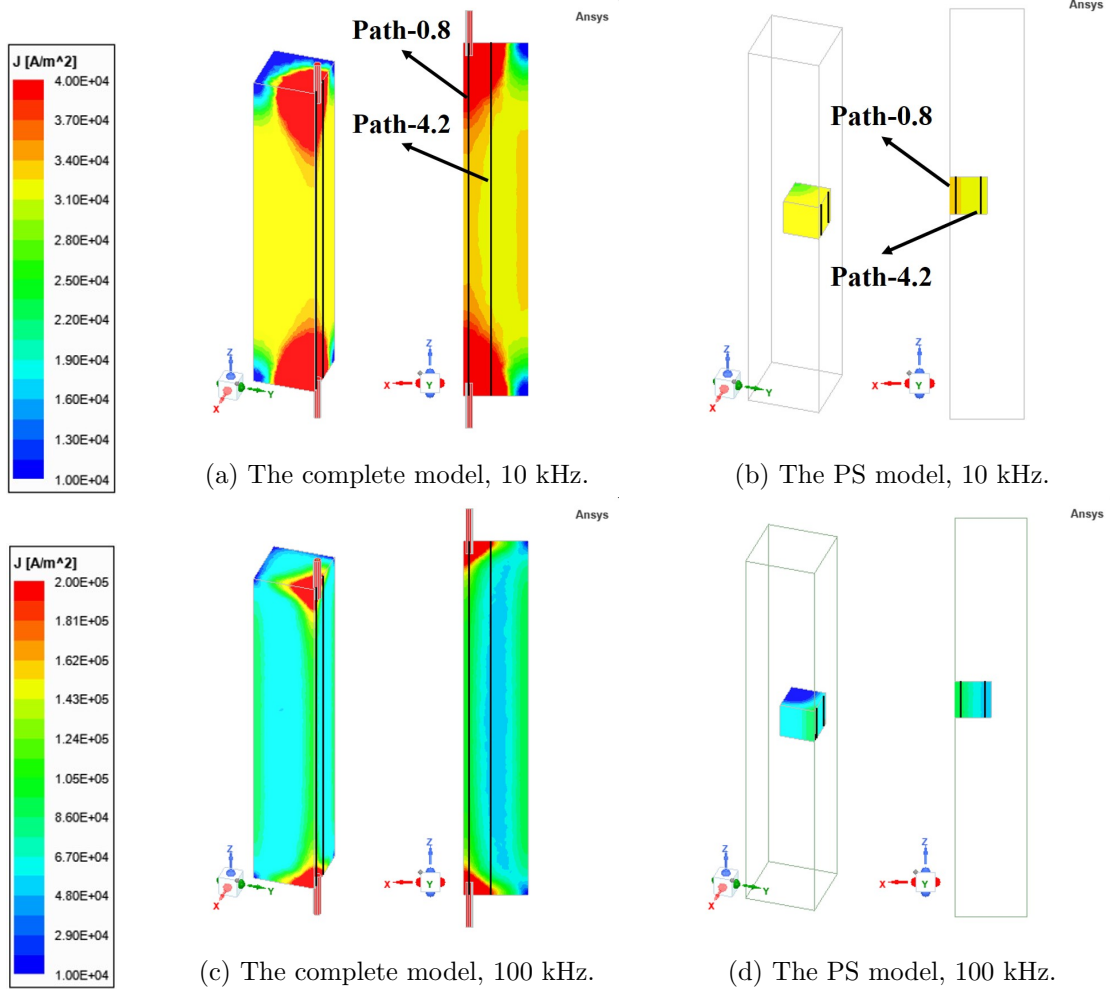
Figure 5.6: Current fields approximated by the complete model and PS model of the square SS316 sample at 10 kHz and 100 kHz. (In the complete model: the maximum element length on surface = 1 mm, the number of layers of elements within skin depth = 2, convergence = 0.05%. In the PS models the maximum element length on surface = 0.5 mm, the number of layers of elements within skin depth = 4, convergence = 0.001%.)

Current fields on these paths given by two models at 10, 30, and 100 kHz are presented against the distance in Fig. 5.7. It can be seen that in the complete model, end effect due to current injections causes greater impact on current fields along Path-0.8 than those along Path-4.2, which is because Path-0.8 is closer to the current injection area. The end effect on current fields attenuates along the distance and vanishes beyond 15 mm on both two paths. Results of current fields near the center at 0 given by two models show good agreement, the detailed comparison of results near the center is given in Fig. 5.7b. The maximum discrepancy of average values of current field excluding end effects approximated by two models is about 4% at 100 kHz. The agreement between the complete and PS model is reasonable since a coarse mesh and a lower requirement of convergence are defined for the complete model. For example at 30 kHz, the PS model comprises of about

170k elements and takes 11 mins to reach a convergent requirement of 0.001%, whereas the complete model contains 1.4M elements and requires a much longer simulation time of 2 hrs to achieve a lower precision of 0.05%.
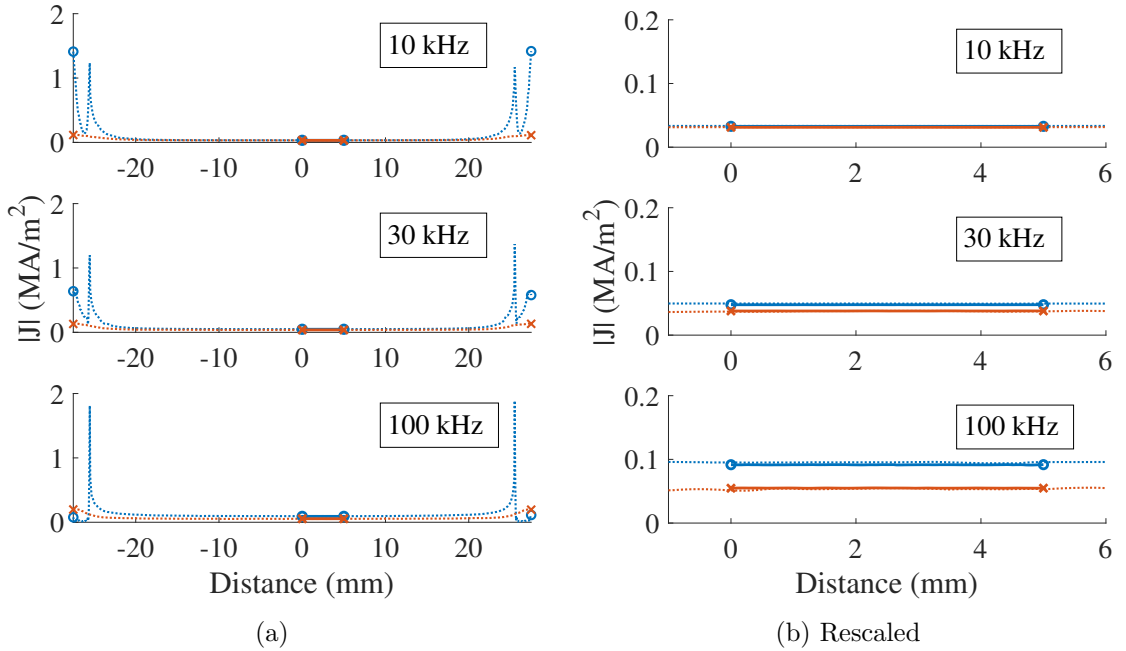
Figure 5.7: Current fields along Path-0.8 and Path-4.2 on the two models in Fig. 5.6 at various frequencies. Dotted line: the complete model; solid line: the PS model; blue line with circles: Path-0.8; orange line with crosses: Path-4.2.

Consequently, in terms of FEA, laborious simulation of current injection wires can be avoided by developing partial models that only focus on segmented volumes of the samples near the center. It has been shown that the two approaches in reducing the model size, i.e. partial modelling and symmetrical modelling, are capable of providing similar field solutions as the complete model with less simulation time, thus further increasing the precision of FEA.

5.4 End Effects due to Current Injections in Experiments

In the last section, the end effect due to current injections on the electric fields has been shown to be inconsequential from the viewpoint of FEA. Nevertheless in experiments, current injection configurations were different from sample to sample due to inevitable uncertainties in welding of current wires. Such different situations of current injections resulted in different impact on practical electric fields. It was unknown whether all various effects vanished around the center of the samples and conformed to former FE conclusions or not. Thus several FE models were built to approximate influences of different welding situations of current wires on field results.

The SS316 sample of circular cross-sectional shape is shown in Fig. 5.8 to demonstrate the welding configuration of current wires. Two wires in silver steel were welded near to end faces of the sample with a welding length of 2 mm. For the samples of other cross-sectional shapes containing edges like the square samples, current wires were welded as close to the edge as possible, only leaving a distance of about 0.3 mm. The expectant configuration of welding was simulated by the complete model presented in the previous section. Three additional half models were developed to cover possible uncertainties in welding work, including $\pm 75\%$ of error in welding length and an error in welding position much greater than the wire diameter of 1.13 mm. Details of welding configurations simulated by models are given in Tab. 5.2.
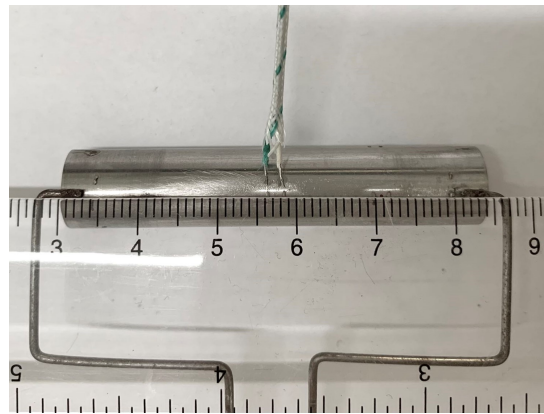
Figure 5.8: Uniform configurations of current injection wires welded on ends of the formal samples.

Model type	Welding length (mm)	Welding position (mm)
Complete (expectant)	2	0.3
Half 1	0.5	0.3
Half 2	3.5	0.3
Half 3	2	2

Table 5.2: Four welding situations of current injection wires simulated by the complete model and three half models.

Fig. 5.9 shows current fields predicted by four models at 10 kHz. The welding situations listed in Tab. 5.2 are also marked out. Magnitudes of current fields along Path-0.8 and Path-4.2 were measured from the field plots in Fig. 5.9 and compared for clearer contrast, see in Fig. 5.10. Similar to results in Fig. 5.7a, the current localisation due to current injections has greater impact on fields along Path-0.8 than Path-4.2 as the former path is closer to current wires. Various end effects due to different welding situations cause different influence on fields near to ends, but all impact decrease along the distance and become negligible beyond 10 mm. The measurement region at the center is almost unaffected by the

disturbances. The difference of current magnitudes within the region from 0 to 5 mm given by four models is within 1% at 100 kHz.
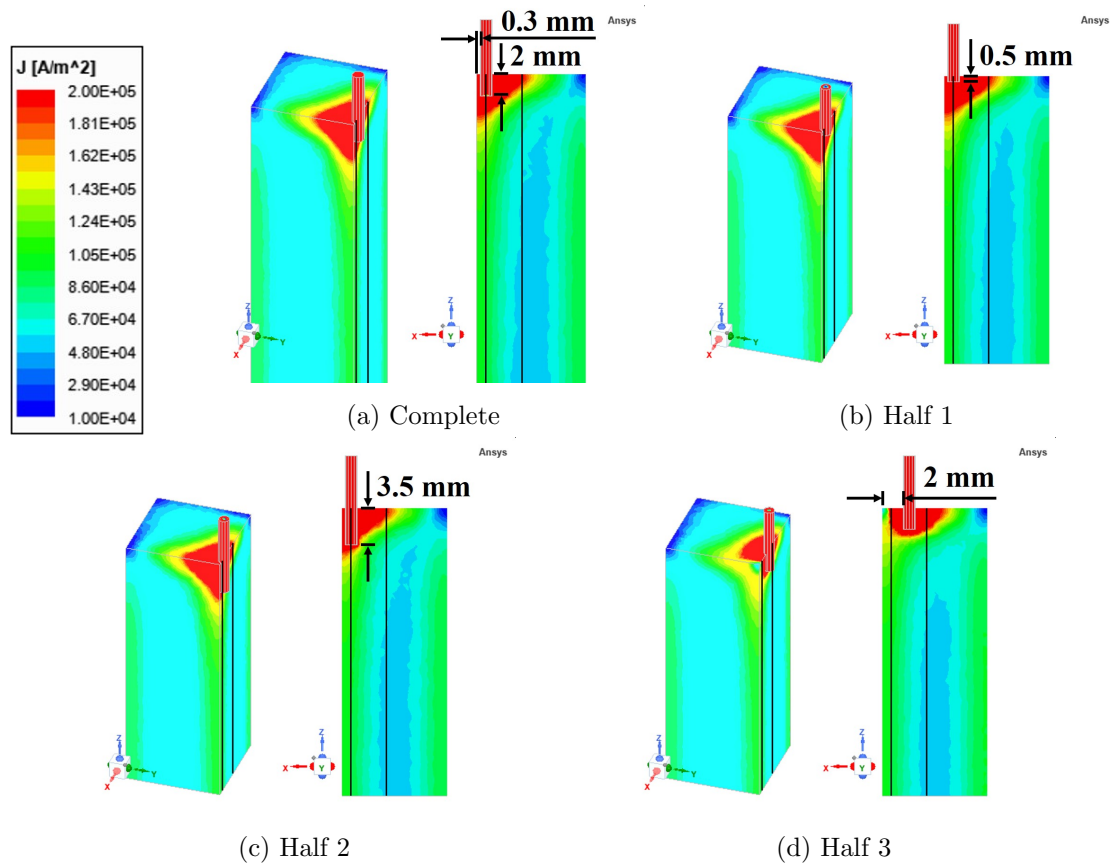
Figure 5.9: End effect in current fields caused by different welding configuration of current injection wires at 100 kHz. All models simulate the square SS316 sample. (In half models: the maximum element length on surface = 1 mm, the number of layers of elements within skin depth = 2, convergence = 0.05%.)
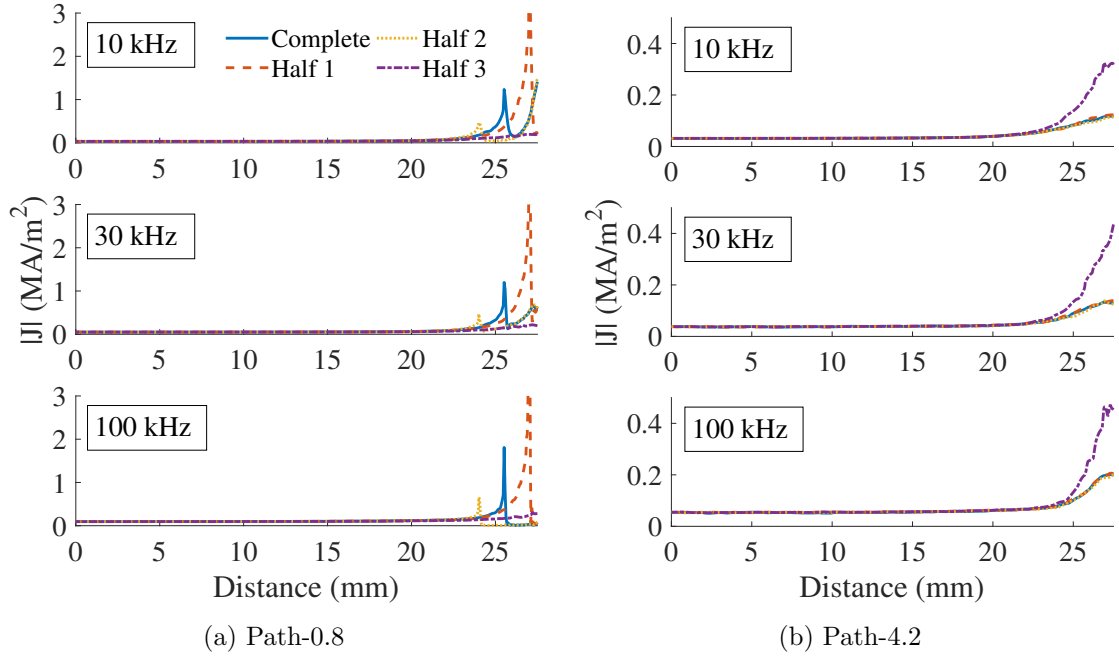
Figure 5.10: End effect along Path-0.8 and Path-4.2 on the four models in Fig. 5.9.

End effect caused by possible uncertainties in welding work of current injection wires have been investigated by developing additional models. It was suggested by FEA that for the SS316 models, inaccuracies in welding work would cause various impact on current fields, however, which is restricted to a short distance near ends and produce negligible influence on the measurement region at the center of the samples.

To investigate impact of PS modelling and absence of current wires on FE results of the other type of model — EN1A, similar analysis of comparing between complete and PS models were also desired. However, due to strong skin effect occurring inside the EN1A samples, EN1A models are too large to be simulated in the full size of 55 mm by the computer equipment accessible to the author. With the limitation of computing devices, analysis of PS modelling for EN1A models were constrained to the half size of the samples (i.e. 27.5 mm) at 10 Hz. At 10 Hz, the skin depth of EN1A is only 0.33 mm. The half EN1A model generates about 2.5M elements and requires 9 hrs to reach a convergence of 1%. While in the above analysis of the SS316 models, the skin depth at the highest frequency of 100 kHz is 1.34 mm. The complete SS316 model produces about 0.66M elements and only takes 1.5 hrs to obtain a much lower convergence of 0.005%.

Fig. 5.11 demonstrates three types of EN1A models to investigate the PS modelling and end effects: a half model, a partial model containing the part of 5 mm long at the bottom of the half model, and a PS model symmetrically split along the diagonal plane of the partial model. Path-0.8 across the N feature and Path-5 on the plain surface are marked out on the models in Fig. 5.11. Results

of current fields on these two paths were extracted from the plotting in Fig. 5.11
and presented in Fig. 5.12 for distinct contrasts.

(a) Half

(b) Partial

(c) PS
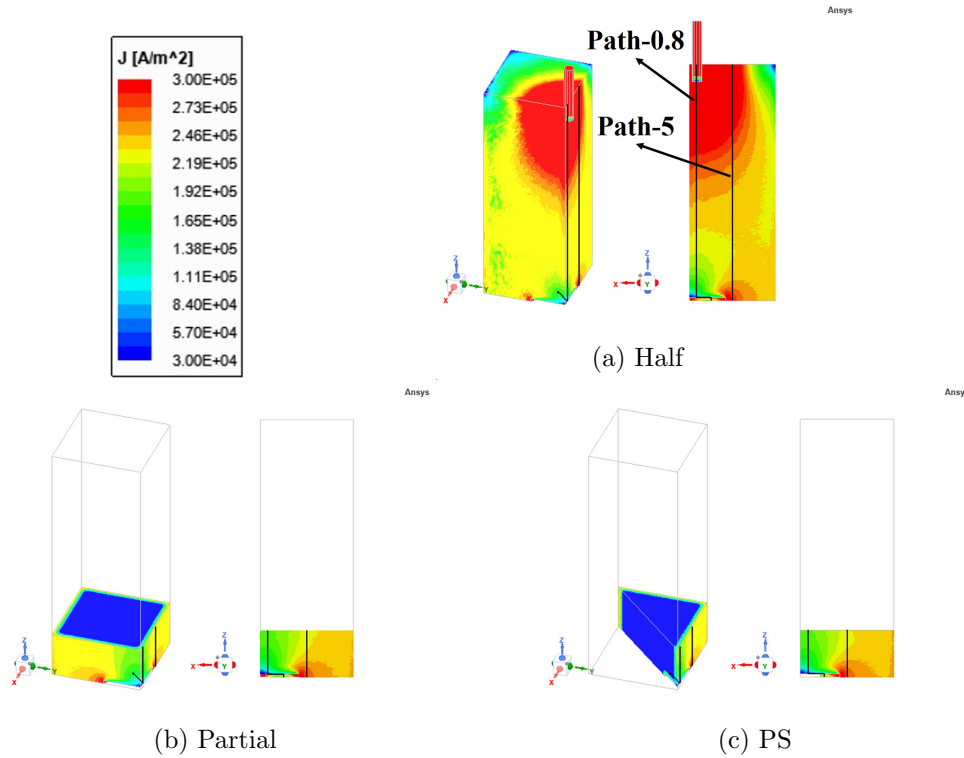
Figure 5.11: Current fields approximated by the half model, the partial model,
and the PS model of the N-featured EN1A sample at 10 Hz. (In all models: the
maximum element length on surface = 0.25 mm, the number of layers of
elements within skin depth = 4, convergence = 1%.)

(a)

(b) Rescaled
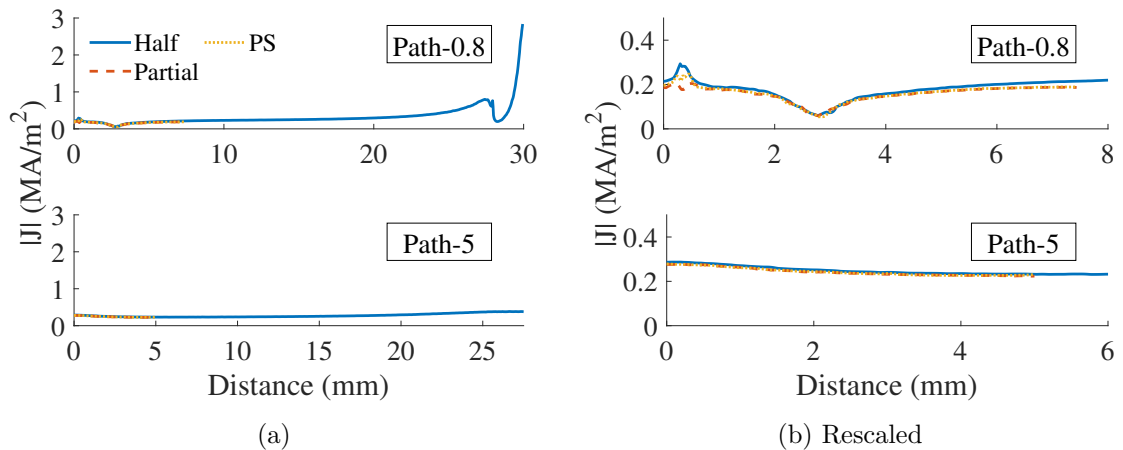
Figure 5.12: Current fields along Path-0.8 (across the feature) and Path-5 (on
the plain surfaces) on the three models in Fig. 5.11.

The effect of symmetrical modelling can be evaluated by comparing field so-
lutions given by the partial model and the PS model. It can be see in Fig. 5.11
that current distributions approximated by the two models are similar. Average

113

differences between results of the partial and PS model in Fig. 5.12 is 2.8% for Path-0.8 and 0.5% for Path-5. Such minor differences indicate the feasibility of applying symmetrical modelling for EN1A models. Nevertheless, by comparing with the half model, current results given by the PS model are lower for 7.73% along Path-0.8 and 3.11% along Path-5. It suggests that the end effect of current injections through wires (or impact of partial modelling) on the EN1A models is more significant than those on SS316 models. For the EN1A models, uniform surface injection of current on the internal sections is unable to completely replace current excitations through wires. Nonetheless, considering the limitation in simulating half models at higher frequencies, such defect of PS models are accepted and PS models are still used for further FEA in this work.

5.5 Mesh Refinement Study

In order to simulate the experimental samples by achieving acceptable accuracies with minimum computing resources, the study of mesh refinement has been conducted to determine optimum mesh definitions of FE models involved in this research. In ANSYS Electronics Desktop, the precisions of field solutions approximated by FE models are evaluated by analysing the convergence of two energy quantities, which are called 'energy error' and 'delta energy'. The energy error describes the precision of the model with the present mesh by comparing the energy value based on residual error and the total energy calculated with original sources. The delta energy reveals the stability of the model by calculating the change in total energy of the model in the present and previous pass. Because of different magnetic behaviour of SS316 and EN1A, simulations for two types of the samples are very different — SS316 models usually require much less elements and converge faster with significantly higher precisions.

5.5.1 Partial Symmetrical Models of Plain Samples in 316 Stainless Steel

The mesh refinement study of the SS316 models will be presented first. The SS316 models produce relatively small error quantities for both the energy error and delta energy, which quickly converge within 0.2% at the beginning of simulations. Curves of a convergence of PS SS316 model at different frequencies are displayed against the number of passes in Fig. 5.13. Meshes of the models involved in Fig. 5.13 were defined according to general guidance in the ANSYS manual [235], specific refinement of mesh will be conducted after determining the optimum convergent value. In Fig. 5.13a, the energy error decreases continuously as the pass increasing. Whereas, the delta energy fluctuates before declining steady for all frequencies, as shown in Fig. 5.13b. It can be seen that rebound of delta energy appear in earlier passes for low frequencies and in later passes for

high frequencies. However, the delta energy with all frequencies terminate the fluctuation before the Pass 10 and start to converge from 0.005%.

(a) Convergence of energy error.

(b) Convergence of delta energy.
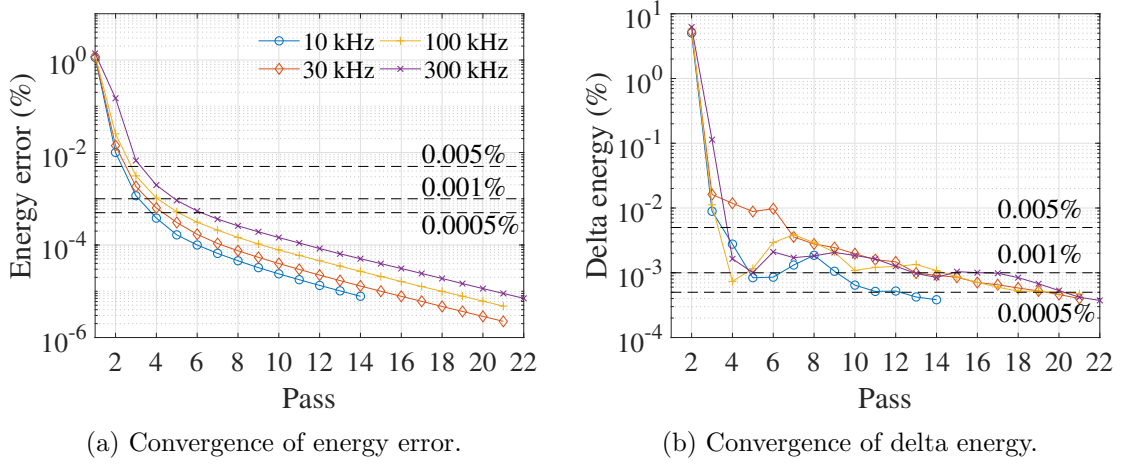
Figure 5.13: Convergence of the PS models simulating the square SS316 sample at various frequencies with a consistent mesh definition: the maximum element length on surface = 0.5 mm, the number of layers of elements within skin depth = 4.

To determine an appropriate requirement of convergence without fluctuations, field solutions approximated by models with different convergent requirements of 0.005%, 0.001%, and 0.0005% were compared with respect of the inductance matrix (including $Re(Z)$ & $Im(Z)$) of the whole models and PDs on conductive paths defined on the model surfaces, the comparison are shown in Fig. 5.14. Similar to former analysis, Path-0.8 and Path-5 were chosen here because the former one simulates the most likely measured paths in experiments and close to the edges, while the latter one is far from the edges and on surfaces. $Re(Z)$ and $Im(Z)$ obtained with three convergent requirements are almost coincided with a maximum difference of 0.01% at 300 kHz. PDs given by the model with the highest precision, i.e. 0.0005% of convergence, show a maximum discrepancy of 1.0% and 1.3% to results from models with lower precisions of 0.001% and 0.005% in convergences receptively.

(a) Z	(b) PDs of paths in 1 mm
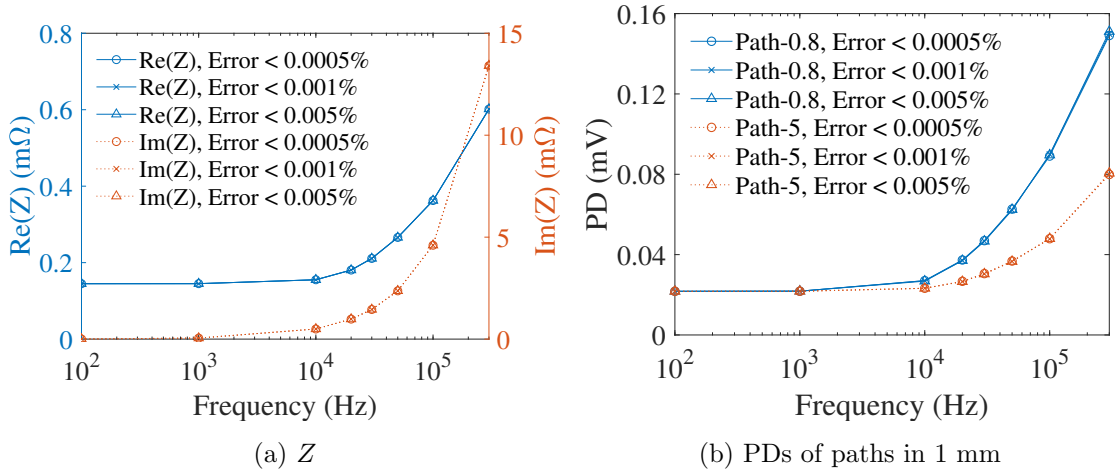
Figure 5.14: The effect of convergent requirements on field results of the PS
models simulating the square SS316 sample.

Computing costs to achieve different precisions of models are presented in Fig.
5.15. Considering the significant increase in number of elements and computing
time of the '0.0005%-model', a compromise is made between the precision and
simulation resources that the convergent requirement of 0.0005% is not adopted.
For the least precise '0.005%-model', it is noticed that models at different frequen-
cies require similar amount of elements and simulation time. This is because the
convergent requirement of 0.005% is too high to cover rebound during simulation
at high frequencies, which can also be seen in Fig. 5.13b. Therefore, the conver-
gent requirement of 0.001% has been determined as the optimum for the PS SS316
models.
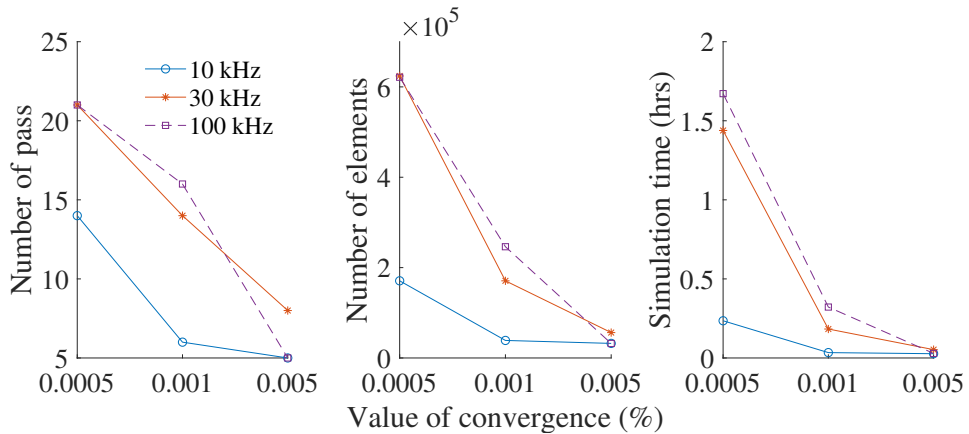
Figure 5.15: The effect of convergent requirements on mesh statistics and
simulation time of the PS models simulating the square SS316 sample.

Due to the skin effect generated within the samples in the ACPD experiments,
a skin-depth based mesh was applied to the surfaces of all models. This type
of mesh is created by defining two quantities, which are called 'the maximum
element length on surface' and 'the number of layers of elements within the skin

depth'. With respect to the first quantity, three different sizes of 1, 0.5, and 0.25 mm (i.e. $\frac{1}{5}$, $\frac{1}{10}$, and $\frac{1}{20}$ of the model dimension) were investigated in the mesh refinement study. As illustrated in Fig. 5.16, solutions of Z and PDs based on different surface element lengths show small differences within 0.06% and 1.5% respectively for the whole frequency range, indicating ignorable impact of this parameter on the precision of the SS316 models.

(a) Z (b) PDs of paths in 1 mm
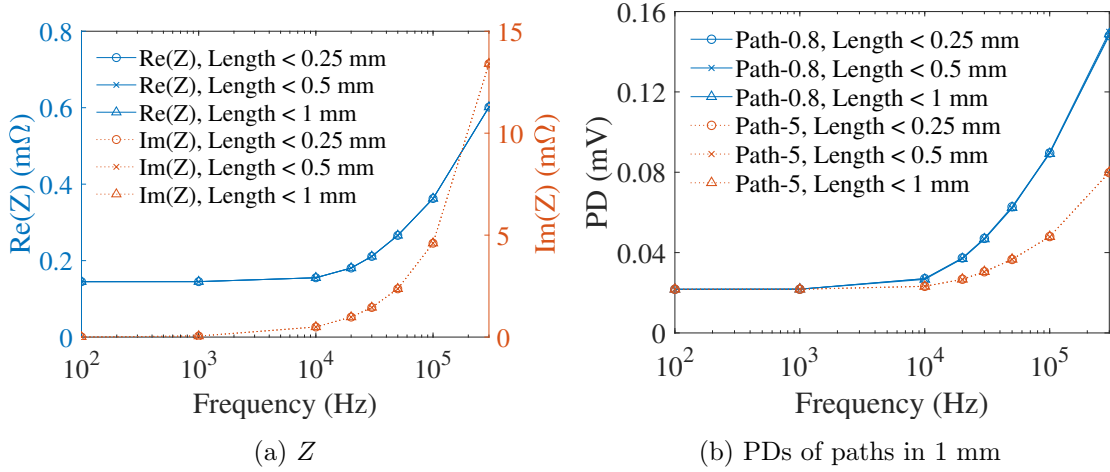
Figure 5.16: The effect of the surface element length on field results of the PS models simulating the square SS316 sample.

According to simulation resources displayed in Fig. 5.17, the effect of element size on resources is non-linear. This is because that the model with element sizes within 0.25 mm generates overfull elements at beginning so takes excessive computing time, whereas, the model with maximum element length of 1 mm involves a coarse initial mesh and has to spend more passes to reach the same convergence. As a result, models with the maximum element length of 0.5 mm that involves moderate amount of elements and consumes shorter simulation time has been applied to all SS316 models.
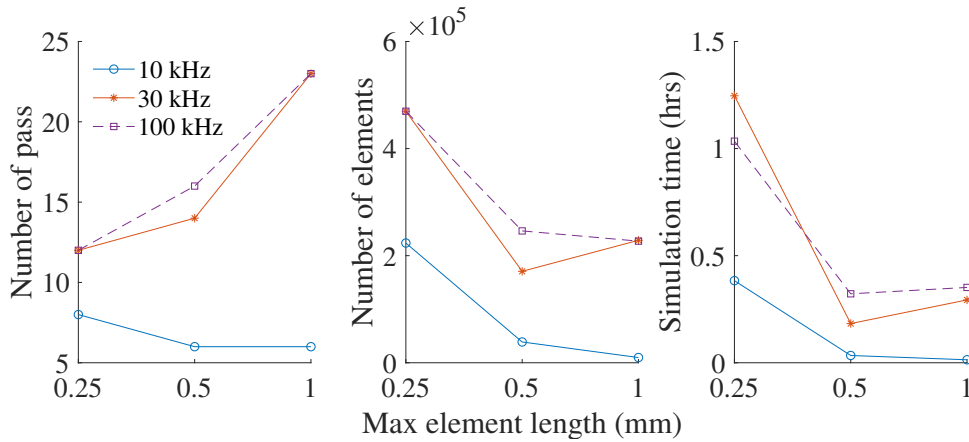
Figure 5.17: The effect of the surface element length on mesh statistics and simulation time of the PS models simulating the square SS316 sample.

The second parameter of the element layers inside skin depth is more important in simulating field solutions especially on PDs along paths at high frequencies, see in Fig. 5.18. To better demonstrate the discrepancy of curves in Fig. 5.18b, PDs are plotted against the number of layers in Fig. 5.19. It is clear that at high frequencies, PDs calculated based on 2 layers of elements inside skin depth are lower than 6-layers results for about 5%, whereas, PDs from a 4-layers mesh decrease the difference to 3%.

(a) Z (b) PDs of paths in 1 mm
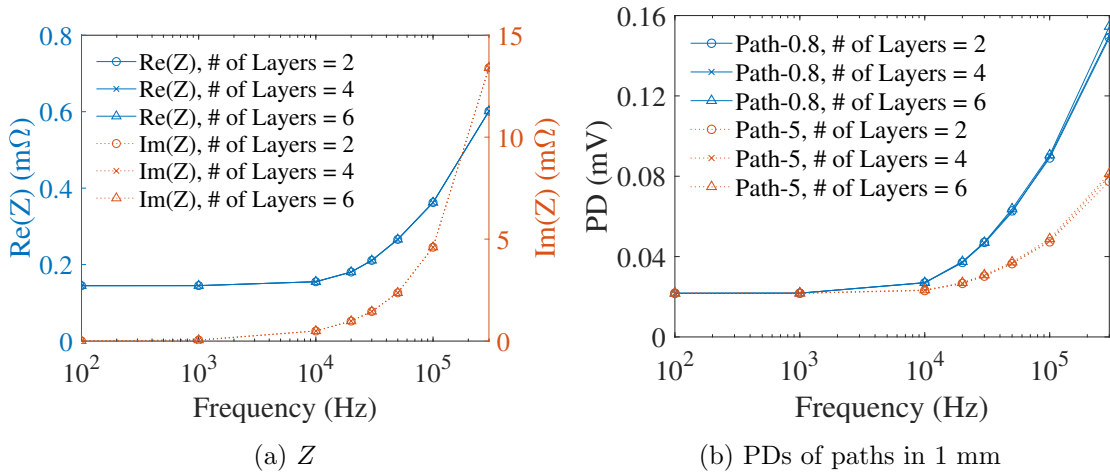
Figure 5.18: The effect of the number of layers of elements within the skin depth on field results of the PS models simulating the square SS316 sample.
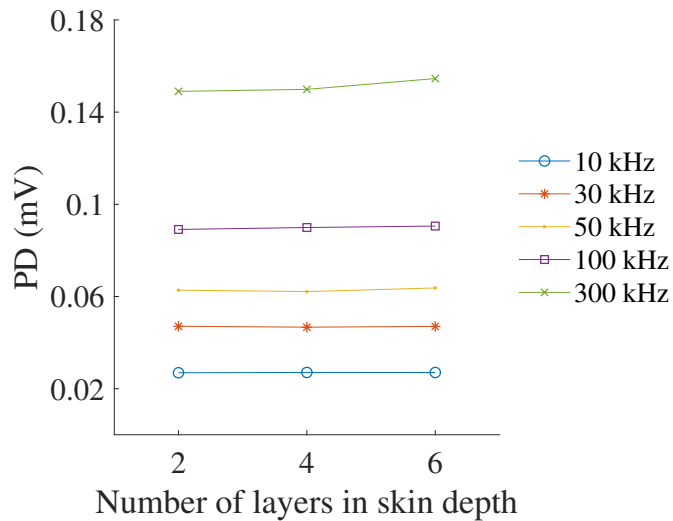
Figure 5.19: The effect of the number of layers of elements within the skin depth on PDs of Path-0.8 approximated by the PS models simulating the square SS316 sample.

The mesh statistics and simulation time of the models with different number of layers inside skin depth are given in Fig. 5.20. Similar to the former parameter, simulation resources have non-linear dependency on the number of element layers. Meshes containing 2 layers of elements within skin depth produce too less elements

118

at initial, and thus spend more passes and time to reach the convergence. On the other side of 6-layers meshes, the model sampled by different frequencies from 30 kHz to 300 kHz contain similar mesh statistics of element number and passes, suggesting the redundancy of 6-layers mesh for the SS316 models. The mesh with 4 layers of elements inside skin depth region, which is capable to achieve a similarly high precision with the 6-layer based mesh at a cost of shorter simulation time, has been decided as the optimum for SS316.
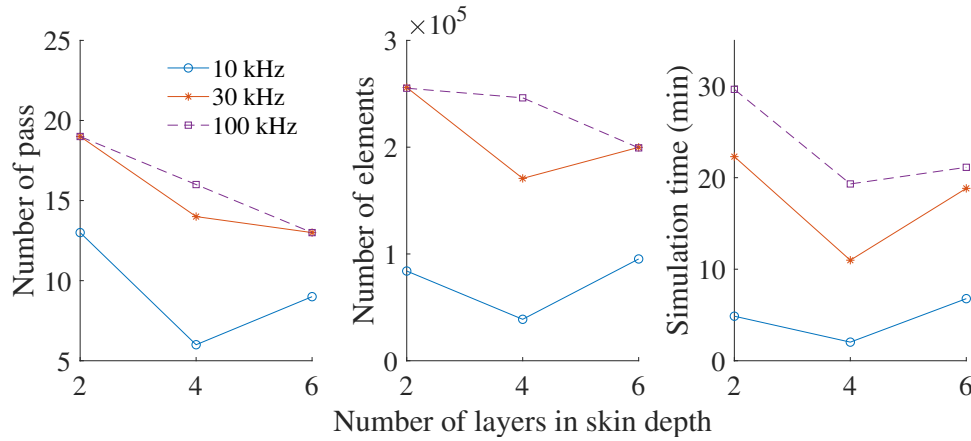
Figure 5.20: The effect of the number of layers of elements within the skin depth on mesh statistics and simulation time of the PS models simulating the square SS316 sample.

Based on the mesh refinement study, all the PS SS316 models were developed based on a consistent convergence requirement and mesh definitions as: 0.001% of convergence, 0.5 mm of the maximum element length on surface, and 4 layers of elements inside skin depth.

5.5.2 Partial Symmetrical Models of Featured Samples in EN1A Mild Steel

The above decisions for SS316 models are inapplicable to EN1A due to the strong magnetic behaviour of the material. For example, the skin depth in EN1A at 10 Hz is 0.34 mm that is only half of the minimum depth achieved by SS316 at the highest frequency of 300 kHz. The EN1A models require numerous elements to simulate thin regions of skin depth hence are difficult to reach convergence of high precisions. As shown in Fig. 5.21, energy error and delta energy produced during simulations of the EN1A models give slower convergence speed and lower precisions by contrasting with convergences of SS316 models in Fig. 5.13.

(a) Convergence of energy error.   (b) Convergence of delta energy.
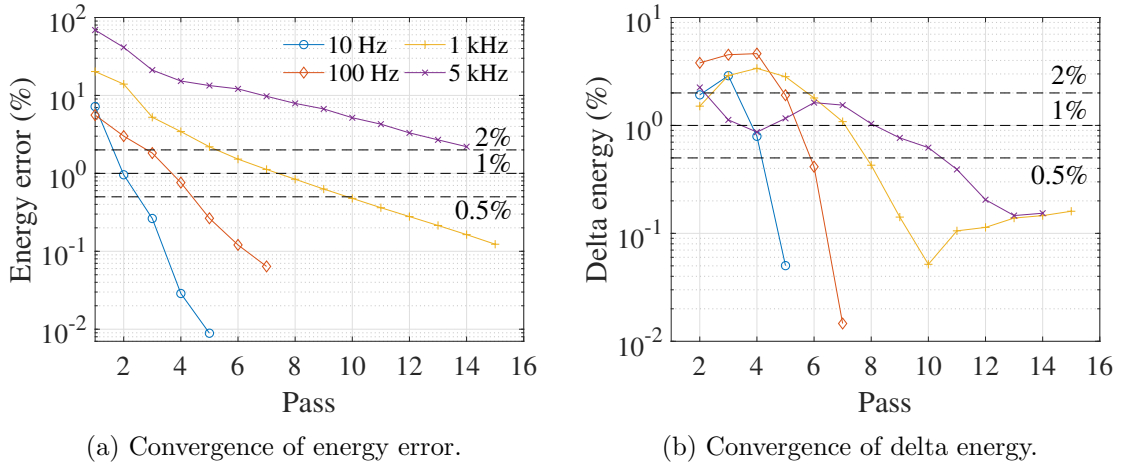
Figure 5.21: Convergence of the PS models simulating the square N-featured
EN1A sample at various frequencies with a consistent mesh definition (the
maximum element length on surface = 0.25 mm, the number of layers of
elements within skin depth = 4).

Three convergent requirements of 2%, 1%, and 0.5% were investigated to de-
termine the optimum value for EN1A, comparisons of inductance matrix and PDs
along conductive paths are displayed in Fig. 5.22. The EN1A models with dif-
ferent convergence export similar $Im(Z)$. For $Re(Z)$ at 1 kHz, results computed
based on 1% and 2% convergence are lower to that based on the highest precision
of 0.5% convergence for 1.6% and 4.4% respectively. Results of PD presented in
Fig. 5.22b were measured from two conductive paths, Path-0.8 across the feature
and Path-5 on the plain surface. Different convergent requirements result in slight
effect on PDs of Path-5 in which results of 1% and 2% convergence are higher
to that of 0.5% convergence of 1.4% and 2.5% at 1 kHz respectively. Whereas,
PDs of Path-0.8 increase as the simulation converging, PD computed from the
0.5%-converged model at 1 kHz are higher than the 1% and 2% result for 9.4%
and 15.3%.

(a) Z (b) PDs of paths in 1 mm
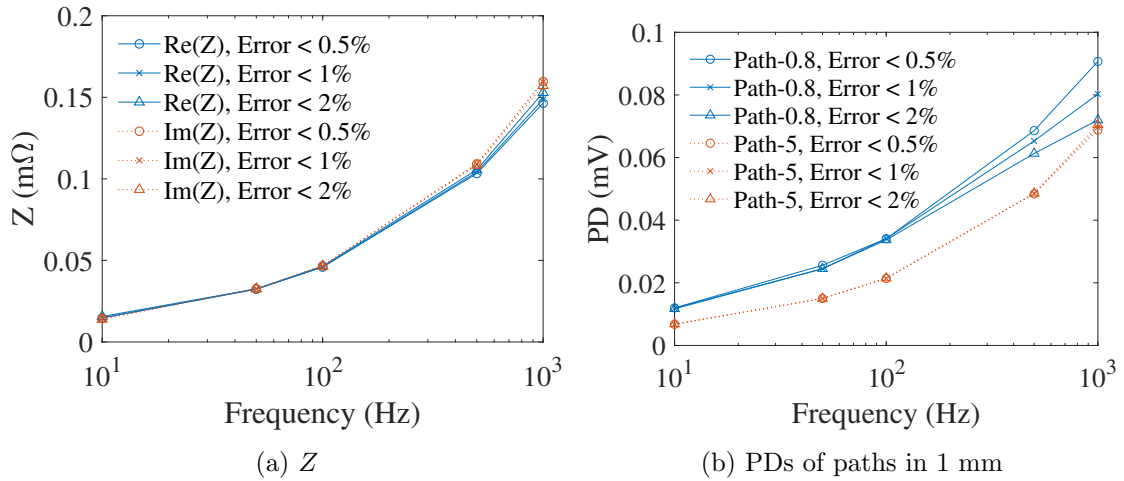
Figure 5.22: The effect of convergent requirements on field results of the PS models simulating the square N-featured EN1A sample.

Meshes of models are automatically adjusted by ANSYS during the process of simulation to contain more elements and approach to higher precisions. This automatic refinement is prior to manual definitions such as the maximum number of additional elements per pass. As a result, elements along the radial direction (e.g. elements on Path-0.8 on the featured surface) are particularly affected and shrink in dimensions. As shown in Fig. 5.23, meshes on the featured surface containing Path-0.8 from bottom views significantly construct in size as the model converging from 2% to 0.5% (by comparing between Fig. 5.23a & 5.23c). While elements on the plain surface containing Path-5 from side views remain roughly constant dimensions (in Fig. 5.23b & 5.23d).

(a) Convergence of 2%, bottom view

(b) Convergence of 2%, side view

(c) Convergence of 0.5%, bottom view

(d) Convergence of 0.5%, side view
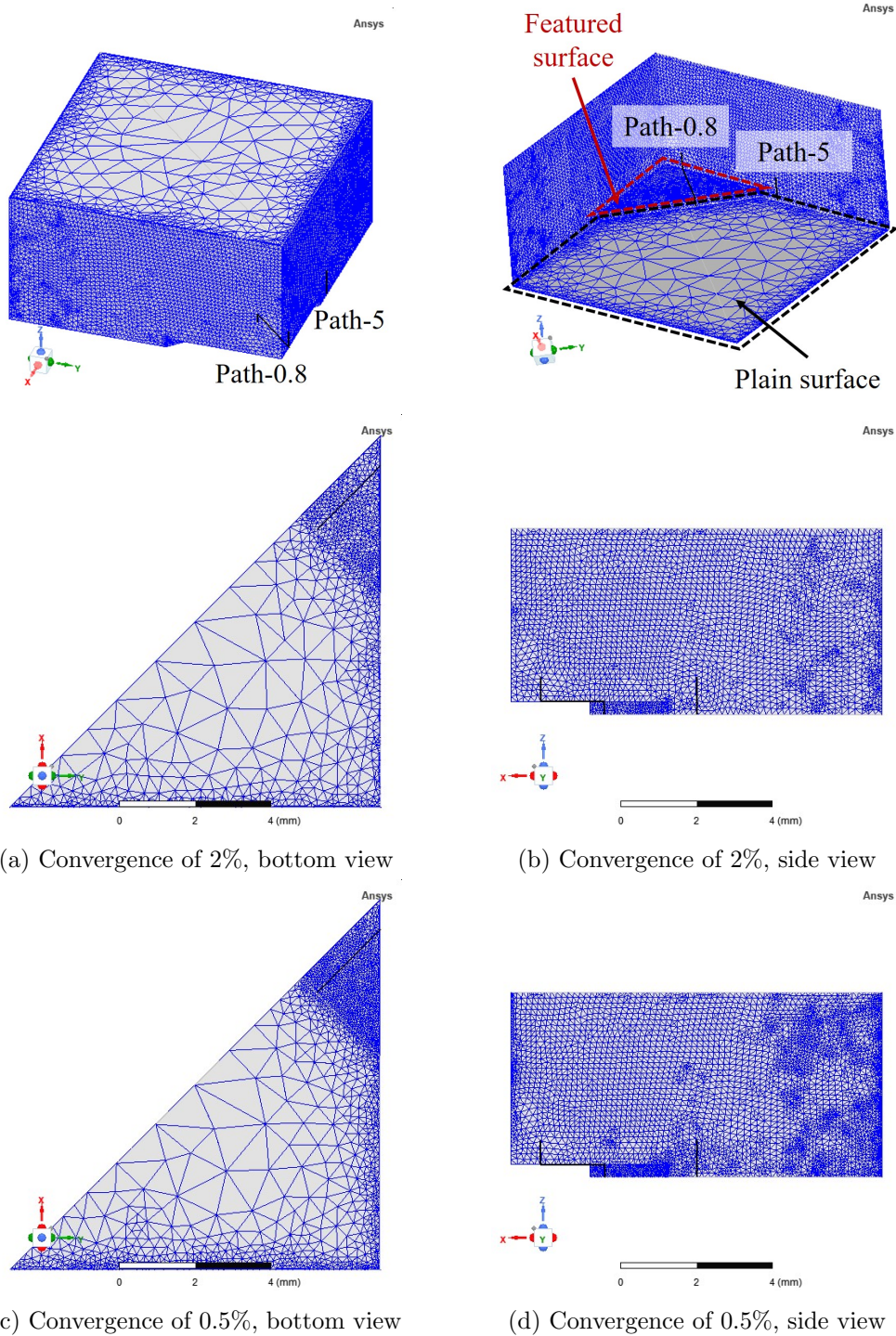
Figure 5.23: The effect of convergent requirements on mesh sizes developed on featured and plain surfaces of the PS models simulating the square N-featured EN1A sample at 1 kHz.

Considering simulating consumptions of models with different requirements, as shown in Fig. 5.24, a compromise has been made that 1% of convergence was determined as the optimum precision for the PS EN1A models.
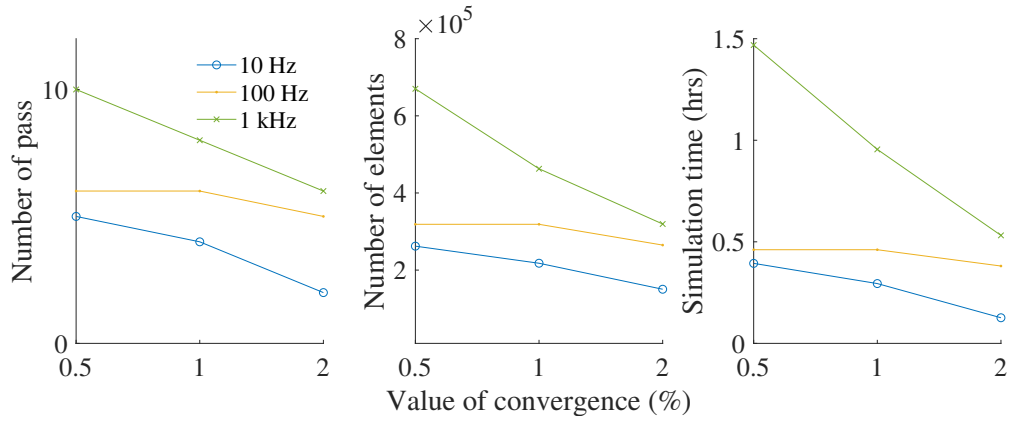
Figure 5.24: The effect of the convergent requirements on mesh statistics and simulation time of the PS models simulating the square N-featured EN1A sample.

Then to decide the maximum element length on surface, the EN1A models developed with elements with the maximum sizes of 1, 0.5, and 0.25 mm were simulated and compared, results against frequencies and surface element lengths are given in Fig. 5.25-5.26. The maximum element length on surface results in minor differences in Z and PDs of Path-5. However, this parameter causes significant effect on PDs of Path-0.8 across the feature. In Fig. 5.26, dash curves of Path-5 remain almost constant regardless of the maximum element length, however, solid curves of Path-0.8 fluctuate at high frequencies. Comparing to the finest mesh with the maximum element length of 0.1 mm, PDs calculated from models with the maximum length of 0.5 mm demonstrate clear deviation for all frequencies while results based on 0.25 mm meshes show good agreement with differences smaller than 3.8% at 1 kHz. The dependency between simulation recourse and the maximum element length shows evident non-linearity, see in Fig. 5.27. For the sake of reducing model sizes and simulation time, the maximum element length on surface of EN1A models has been decided as 0.25 mm.

(a) Z (b) PDs of paths in 1 mm
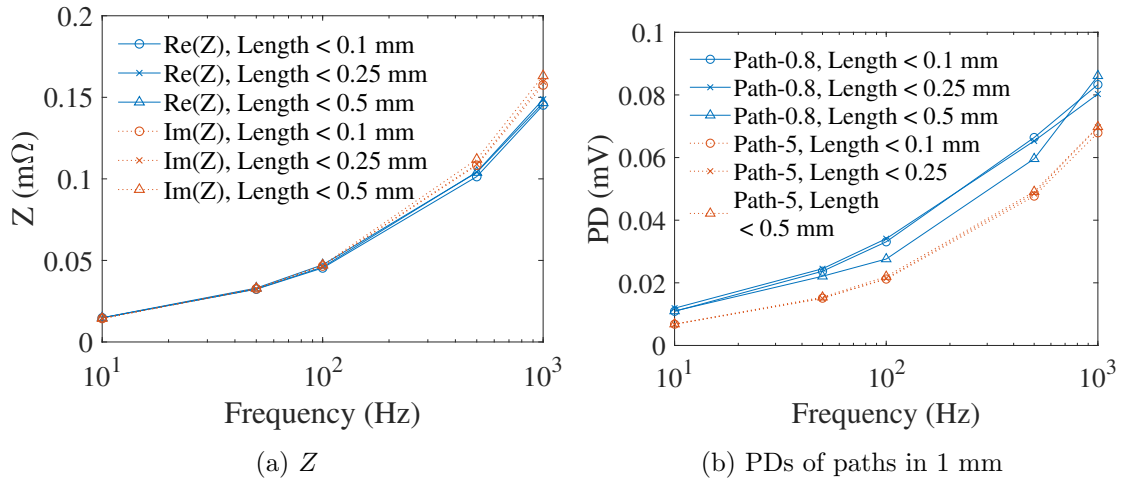
Figure 5.25: The effect of the surface element length on field results of the PS models simulating the square N-featured EN1A sample.
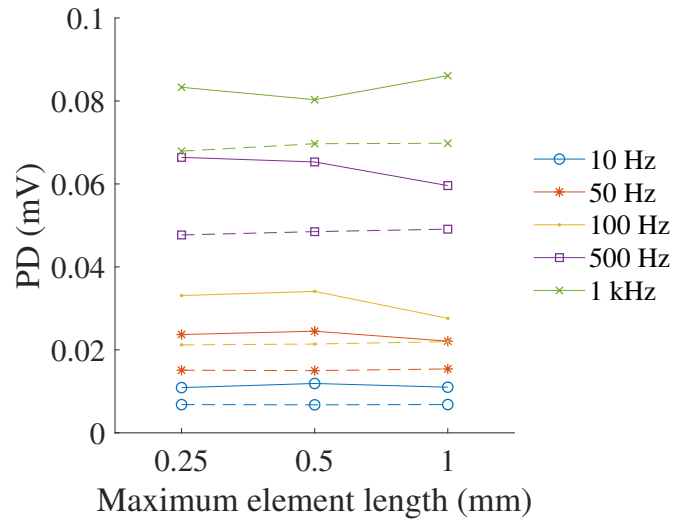
Figure 5.26: The effect of the surface element length on PDs of Path-0.8 (in solid lines) and Path-5 (in dash lines) approximated by the PS models simulating the square N-featured EN1A sample.
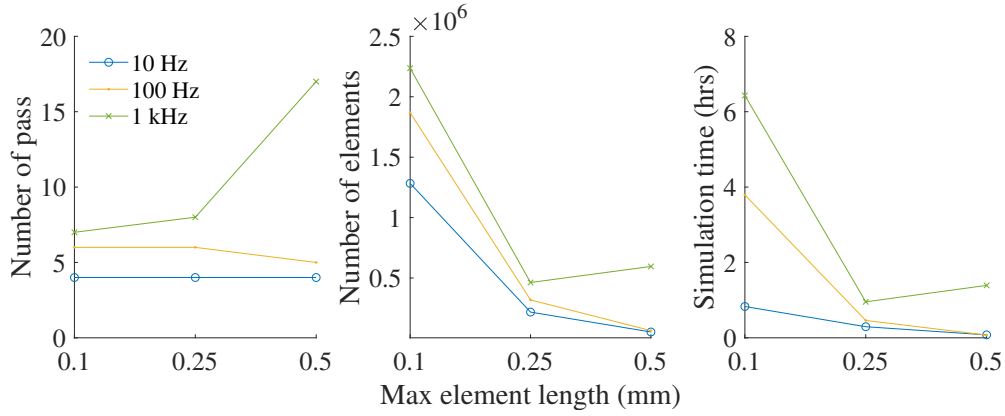
Figure 5.27: The effect of the surface element length on mesh statistics and simulation time of the PS models simulating the square N-featured EN1A sample.

For the third parameter of the number of element layers within the skin depth, comparison of Z and PDs on the same two paths are displayed in Fig. 5.28-5.29. Visible differences can be observed in PDs of Path-5, indicating that the final parameter is more significant than the other two. PDs of Path-5 that obtained from models with 2 layers of elements within the skin depth remain consistently well below results given by the 6-layers model, thereby the definition of 2-layers elements in skin depth is excluded. Nevertheless, comparison of PDs of Path-0.8 is very different that results based on 2-layers and 4-layers meshes diverge to 6-layers results to varying degrees, leading to differences of 7.2% and 5.6% at 1 kHz respectively. However, available computing equipment is incapable of simulating the EN1A models with 6-layers of elements in skin depth for all frequencies, meshes of the EN1A models have to be defined with less layers of elements.

(a) Z

(b) PDs of paths in 1 mm
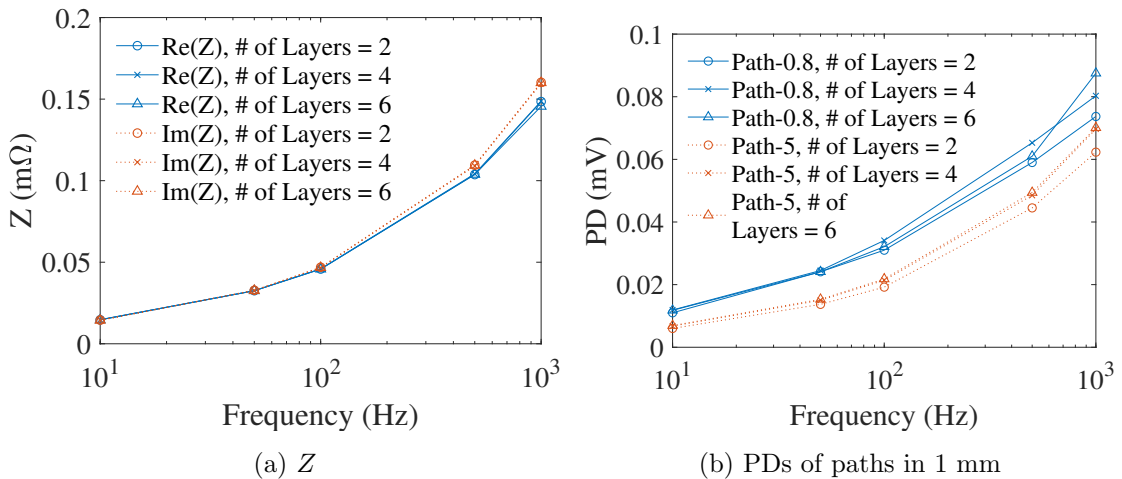
Figure 5.28: The effect of the number of layers of elements within the skin depth on field results of the PS models simulating the square N-featured EN1A sample.

Similar non-linear dependency is observed between the number of element layers within the skin depth and simulation resources, as given in Fig. 5.30. Models

with 4-layers meshes present quicker convergence (i.e. require less passes and time) but involve more elements than 2-layers models. Hence for models at frequencies lower than 1 kHz, 4-layers meshes were applied to shorten simulation time; for models at higher frequencies up to 10 kHz, 2-layers meshes were defined to reduce the number of elements otherwise simulations would aborted due to excessive sizes of models.
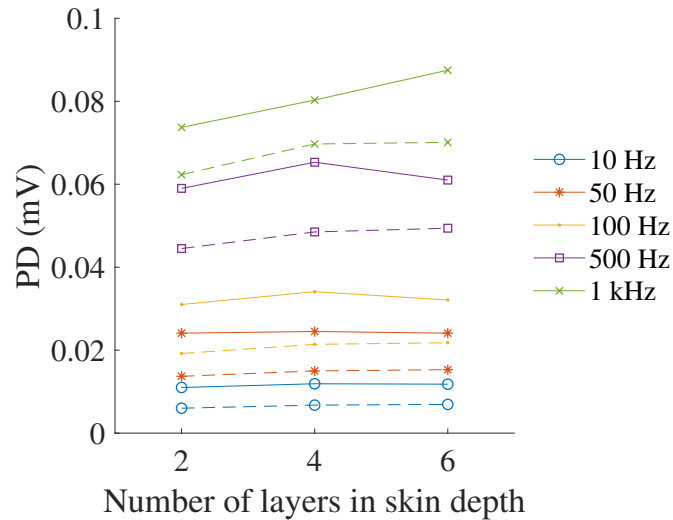
Figure 5.29: The effect of the number of layers of elements within the skin depth on PDs of Path-0.8 (in solid lines) and Path-5 (in dash lines) approximated by the PS models simulating the square N-featured EN1A sample.
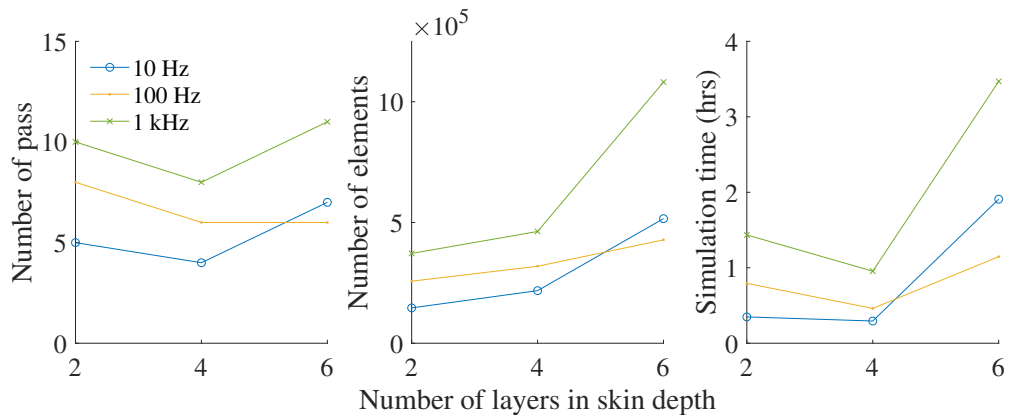
Figure 5.30: The effect of the number of layers of elements within the skin depth on mesh statistics and simulation time of the PS models simulating the square N-featured EN1A sample.

In summary, all the PS EN1A models were produced with a consistent convergent requirement of 1% and the same maximum element length on surface of 0.25 mm. The number of element layers inside skin depth was depended on the oscillating frequency that 4 layers of elements was defined for frequencies lower than 1 kHz and only 2 layers was used for higher frequencies.

5.6 Post Processing of Exporting Field Solutions

After establishing reliable FE models for the formal samples, the next step was to output field solutions from models and compared with experimental results. In the ACPD experiments, PDs across the features on featured samples (or across the plain surfaces with same distance on the flawless samples) were directly measured as outputs. It is necessary to export the same quantity of PDs from FE models for comparison.

For a converged model, the Eddy Current solver in ANSYS Electronics first computes $\mathbf{H}$ by [235]

$$\nabla \times \left(\frac{1}{\sigma + j\omega\epsilon} \nabla \times \mathbf{H} \right) = -j\omega\mu\mathbf{H} \tag{5.1}$$

Then the solver calculates $\mathbf{B}$ and $\mathbf{D}$ from solutions of $\mathbf{H}$, the full solution of Maxwell's equations including $\mathbf{E}$ and $\mathbf{J}$ can thus be solved for the whole region. Related quantities of interest such as inductance matrix and ohmic loss may be solved from these fundamental field solutions and exported directly. Results of PD along a conductive path defined by two points is calculated as the integral of tangential components of $\mathbf{E}$ along the path. Thereby, the critical process in exporting PDs is the definition of the conductive path. On the plain SS316 models, the conductive paths are simply defined as the 2 mm-long path across the welding positions on the plain surfaces of the samples, as highlighted in pink in Fig. 5.31a (the pink path is in 1 mm long due to symmetrical modelling). Whereas, on the featured EN1A models, the definitions are more complex. As shown in Fig. 5.31b, a plane T that is parallel to the diagonal symmetry plane is moved to the welding position and cut the sample, the tangent contour following the feature shape and in a total distance of 2 mm in vertical z-axis are defined as the conductive path for this type of feature (again the total length of path in vertical direction is 1 mm in the symmetrical model).

(a) Plain   (b) NH-featured
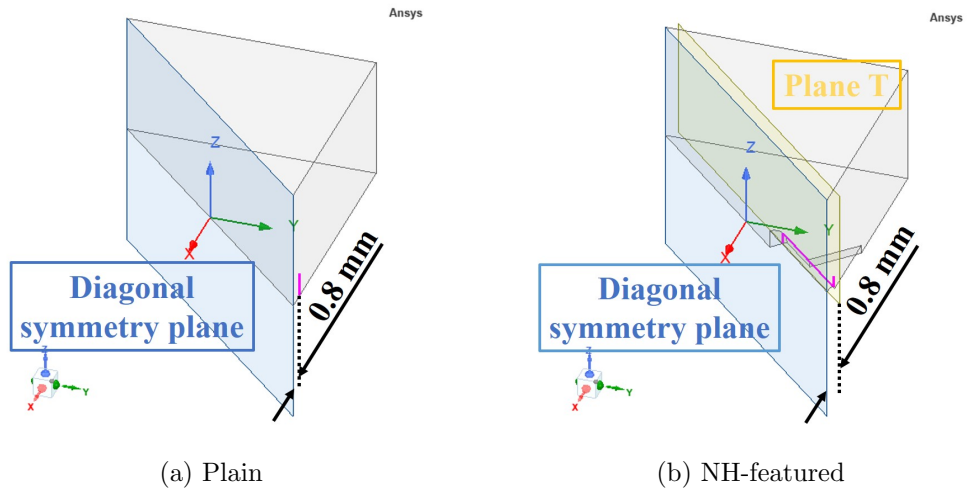
Figure 5.31: Schematic of the definitions of conductive paths in PS models for calculating PDs. The position of path at 0.8 mm to the edge is the expectant welding position of PD probes in experiments.

The above definitions of conductive path suggests the ability of FEA in outputting PDs from arbitrary locations. Since it was hardly possible to apply an ideal 'point welding' on the experimental samples, the precise position of the conductive path measured in experiments remained unknown. Fig. 5.32 shows the configuration of experimental measurements on the N sample as an example. The pair of electrical probes were welded on the sample at positions of ±1 mm to the center. Moreover, the probes were expected to be welded as close to the edges as possible, leaving small distances of about 0.3 mm. About 1 mm of the wire were welded to ensure robust connection during measuring, suggesting that PDs could be possibly measured from any conductive path within the regions from 0.3 mm to 1.3 mm to the edges. Therefore, the paths at the middle of the regions (0.8 mm to the edges) were assumed as the paths that were most likely to be measured in experiments.
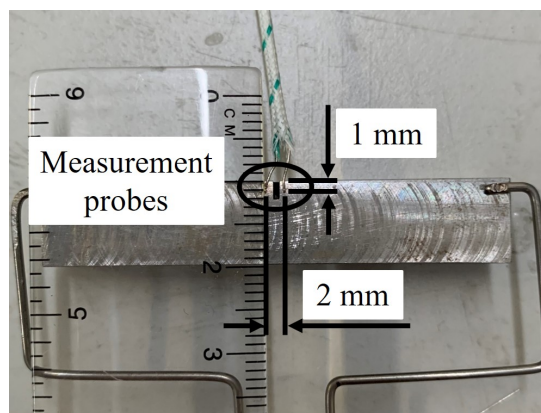
Figure 5.32: Configurations of PD measurement wires welded near the center of the EN1A N-sample.

In order to contain all possible measuring paths, multiple conductive paths covering the whole welding region were defined on the models to produce 'error bars' of PD. Fig. 5.33 shows several conductives paths defined on models. The numbers in the names refer to the distances to the edge. Path-0.8 is created to export the results that were most likely to be obtained in experiments, thereby Path-0.8 is assumed as the 'optimum simulation path'. The other two auxiliary paths are defined to simulate the maximum offsets of welding positions possibly occurred in lab work. In later sections, PDs measured from Path-0.8 will be compared to experimental results and PDs of two auxiliary paths will be displayed as error bars.
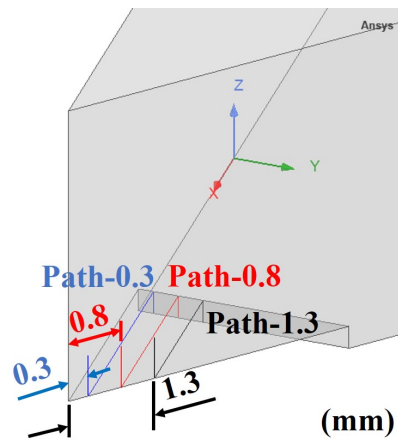
Figure 5.33: Multiple conductive paths created to provide the optimum approximation of PD and error bars.

Although the maximum uncertainties in welding distances were recognised as the region of 0.3-1.3 mm, a narrower region of 0.5-1.1 mm was used in modelling. Since it will be presented later that PDs measured across the H feature are significantly sensitive to measurement positions, the offset of ± 0.5 mm introduces wide error bars, which is insignificant to compare with experimental results. PDs from the narrower region of 0.5-1.1 mm are adequate to demonstrate the sensitivity of PDs across the H feature and hardly affect comparisons of other samples. Hence, error bars of measurement locations for all models presented in this work were calculated from Path-0.5 and Path-1.1.

In additional to welding positions, possible uncertainties of the measurement distances in welding work were considered in FEA by measuring PDs from several paths with different lengths. PDs read from a path in 2 mm long will be compared with the experimental results as the optimum approximations, results with a shorter (1.5 mm) and a longer (3 mm) distance will be shown as error bars.

In summary, Fig. 5.34 illustrates four auxiliary paths related to Path-0.8 that are uniformly defined on all the plain and featured models to generate error bars. In Fig. 5.34a, PDs integrated from Path-0.5 and Path-1.1 are used to produce 'error bars I' which consider effects in PDs caused by ± 0.3 mm offset in

measurement locations. In Fig. 5.34b, Path-Dis-1.5 and Path-Dis-3 are used to measure PDs from different measurement distances and thus create error bars II.

(a) For error bars I
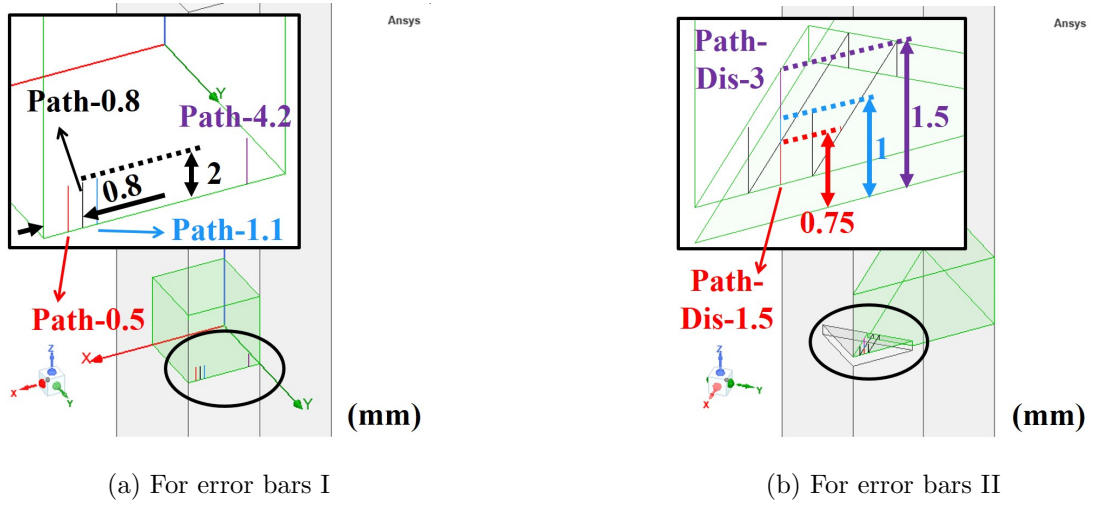
(b) For error bars II

Figure 5.34: Multiple conductive paths uniformly defined on all PS models to produce error bars I & II.

5.7 Conclusions

FEA have been conducted via ANSYS Maxwell 3D to simulate the formal samples and approximate results of PD and impedance at various frequencies. The sequence of modelling steps to create models for the samples were presented in this chapter. Definitions of materials, current excitations, and boundary conditions specifically assigned for the models were displayed in detail.

By taking the advantage of the mechanism of excitation injection in ANSYS, the partial modelling referring to simulate the part of 10 mm at the sample center can be applied to reduce model sizes and shorten simulation time. Moreover, since the sample geometries are symmetrical and the current excitations (i.e. surface current) on the partial models are uniform, the partial models can be further simplified by applying symmetry boundary conductions on the symmetry planes, i.e. by employing the symmetrical modelling. Good agreement was observed between field solutions approximated by PS models and the complete model containing the sample in full size and two current injection wires. It suggests the feasibility of replacing the complete model with smaller PS models.

Additional PS models were created to study effects of possible welding errors of current wires on electric fields and ACPD measurements. It was demonstrated that different welding situations of current wires variously disturb current fields near the end faces but are unable to influence measurements around the center of samples. Hence, end effects of welding uncertainties of current wires can be excluded through FEA.

130

Furthermore, mesh refinement study has been conducted for SS316 and EN1A models based on the principle of compromising between model precisions with simulation cost. The optimum parameters of developing the SS316 PS models were determined to be 0.001% of convergent requirement, 0.5 mm of the maximum element size on surface, and 4 layers of elements within skin depth. Whereas due to the ferro magnetism of EN1A, the EN1A PS models require a large number of elements to simulate extremely thin skin depths hence is unable to achieve precisions as high as SS316 models. The first two parameters were decided to be consistent of 1% and 0.25 mm for all EN1A models. However, the last parameter was determined to vary with the frequency, 4 layers of elements inside skin depth was defined in models with frequencies lower than 1 kHz while 2-layers meshes were created in models with higher frequencies.

Eventually, post processing procedures especially the method of exporting PDs on specifically defined paths were presented. Path-0.8 were defined on the models as the optimum simulation path for the path actually measured in experiments. Furthermore, several auxiliary paths around Path-0.8 were created to cover the measurement uncertainties (i.e. welding uncertainties of PD measurement probes) and produce error bars. Error bars I & II represent the effect on PDs caused by uncertainties in horizontal measurement locations and those in vertical measurement distances respectively. In Chapter 7, FE approximations of PD on the optimum simulation path and the two types of error bars will be compared by experimental results to investigate the detection capability of the ACPD method. Additionally, approximated electric fields/current distributions will be relied on to comprehend differences between the samples caused by different sample shapes and features.

Chapter 6

Experimental Data Verification and Data Processing Validation

6.1 Introduction

ACPD results obtained in preliminary and formal experiments were processed by the MATLAB script introduced in Section 4.5 to compute results of PD and impedance against frequencies. In the present chapter, processed results will be displayed with another type of experimental results — manually measured results. About ten periods at distinct frequencies were manually measured via NI DIAdem for each experiment. To obtain the manual measurements, precise positions in time of zero-crossings and positive and negative amplitudes of AC and PD signals were recorded for each period. Such results were then used to calculate impedance for each period based on the same method applied to the MATLAB script. Fitness between these two types of experimental results were used to evaluate the performance of the data processing, i.e. whether the script operated as expected. In addition to validating the data processing, experimental results in Case 1 were contrasted with the known values or theoretical solutions to verify the procedure of the ACPD experiments. Raw data were averaged from three sets of measurements for all experiments.

6.2 Results of Preliminary Experiments

6.2.1 Resistance of an Individual Resistor

The resistance of the individual resistor is known as 0.22 Ω. The resistor was pushed hard into the breadboard for measuring in experiment. Experimental results of $|Z|$ (or R_{res}) obtained by two methods, i.e. processed and manually measured, are compared in Fig. 6.1. Processed results show good agreement to manual measurements for the whole range of frequency in which the average difference between the two is 0.4%. It indicates the high precision of the data

processing in computing $|Z|$ in this preliminary experiment.
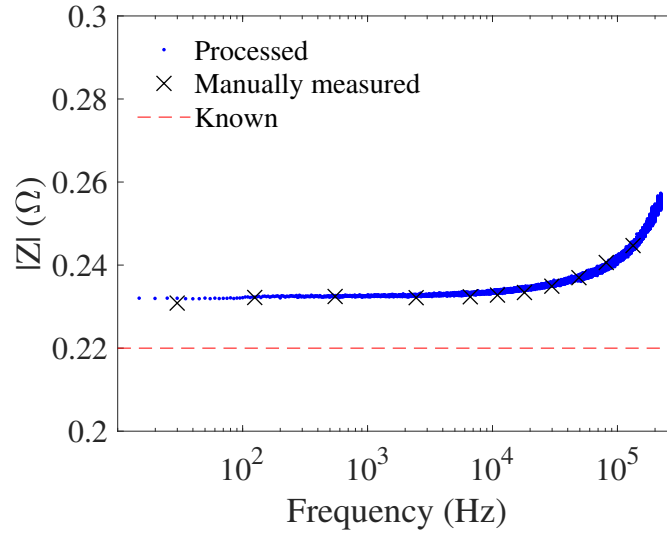
Figure 6.1: Comparison of the impedance (i.e. resistance) of the individual resistor.

However, Fig. 6.1 shows that experimental results of $|Z|$ increases at frequencies higher than 10 kHz. The average of experimental results before 10 kHz is 0.233 Ω, which is 5.9% higher than the known value of 0.22 Ω. Considering the built-in resistances of the breadboard and connections in the circuit, it is reasonable that measured values are higher than the pure resistance of the resistor. As the frequency rises, experimental resistances increases and finally reaches 0.253 Ω at 220 kHz. This is because that ACPD signals vary at high frequencies rather than remaining constant as expected for the pure resistor, which can be seen in Fig. 6.2. Processed amplitudes of AC and PD signals before 10 kHz were almost constant with average values of 1.002 A and 0.2335 V. In Fig. 6.2, the amplitudes of AC and PD are divided by these two averages to demonstrate variations in magnitudes of signals against frequencies. It can be seen that PD signals rise for 3% and AC signals drop for 7% at the highest 220 kHz. The increase in PD signals is possibly because that AC generated heat in experiments, which raised the resistance. Whereas AC signals do not follow the specified constant amplitude but decrease, which is considered as a defect of the original current input file. The drop in AC input signals was then reduced from 7% in this case to 2% in later experiments by improving the current input file. Such decreases in signal amplitudes (both for AC and PD) could not be eliminated since real amplitudes at high frequencies were possibly missed during measuring due to the constant f_s.
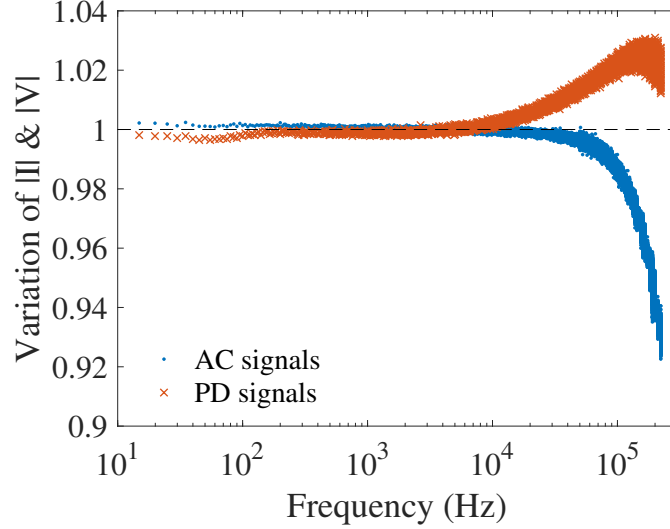
Figure 6.2: Variation in processed signals at high frequencies. Differences were
calculated by dividing processed amplitudes of AC and PD by average values
calculated from signals lower than 10 kHz.

6.2.2 Combined Series and Parallel Circuit

Total impedance of combined circuits can be theoretically calculated by the well-known rules for combining impedances in series and parallel as

$$Z_{ser} = R_{res} + Z_{ind} \tag{6.1}$$

$$Z_{par} = \frac{1}{\frac{1}{R_{res}} + \frac{1}{Z_{ind}}} \tag{6.2}$$

where Z_{ser} and Z_{par} represent the total impedance of a series and a parallel circuit. Noting that the inductor measured in experiments is not an ideal component but possesses an intrinsic resistance R_{ind} which was measured to be 0.007 Ω. Thus Z_{ind} is given by

$$Z_{ind} = R_{ind} + j\omega L_{ind} \tag{6.3}$$

Theoretical impedance were calculated by substituting known quantities (i.e. $R_{res} = 0.22$ Ω and $L_{ind} = 1.8$ μH) into (6.1)-(6.2).

Fig. 6.3-6.4 demonstrate comparisons of experimental and theoretical results of Z_{ser} and Z_{par}. In Fig. 6.3b & 6.4b, processed results of θ_Z become scattered at frequencies higher than 10 kHz. It is because that the measuring method with a constant f_s is incapable of capturing all zero-crossings of signal periods at high frequencies, which is the same reason of drops in signal amplitudes at high frequencies as mentioned in the above section. For example, Fig. 6.5 shows a piece of raw data at about 150 kHz, 'real zero-crossings' are absent thus 'measured zero-crossings' marked with square boxes are found out and used to calculate impedance during the data processing. These 'measured zero-crossings' are slightly lead to or lag behind 'real zero-crossings', leading to errors in processed θ_Z.

134

Processed results show good agreement to manually measured results in $|Z|$ and θ_Z, which can be seen in Fig. 6.3-6.4. For both the two circuits, the absolute average difference between two types of experimental $|Z|$ is smaller than 2.5%. Such differences are mainly attributed to low-frequency comparisons due to small magnitudes in $|Z|$ at the beginning. For the same reason, the absolute mean difference between two results of θ_Z in the series case was calculated by excluding low-frequency comparisons, otherwise θ_Z that approaches to zero at the beginning would significantly increase the difference. The absolute average difference in θ_Z is 5.5% for the series circuit and 3.6% for the parallel. Therefore, the data processing has been shown to convert ACPD signals into $|Z|$ and θ_Z with high precisions for all frequencies in these two preliminary cases.
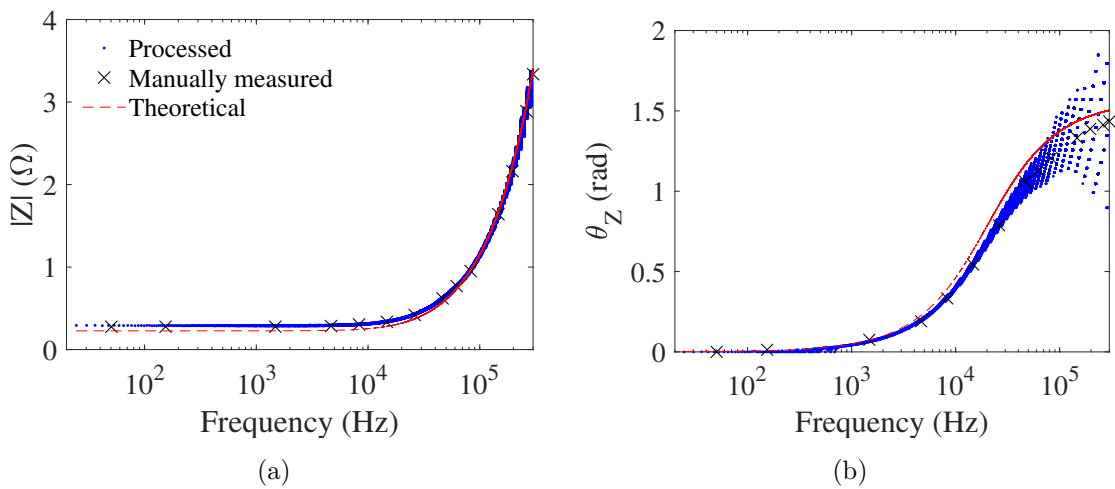
Figure 6.3: Comparison of the total impedance of the series circuit (Z_{ser}).
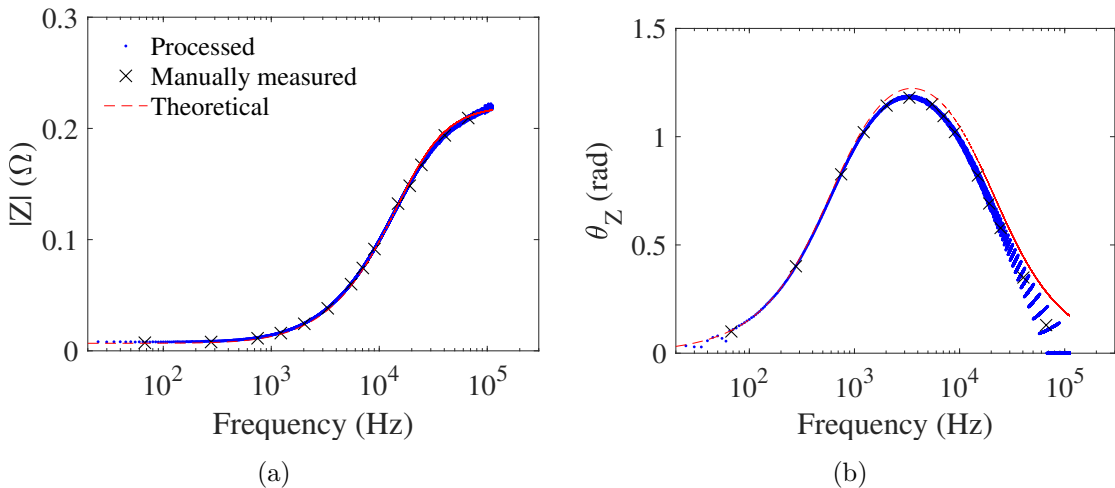
Figure 6.4: Comparison of the total impedance of the parallel circuit (Z_{par}).
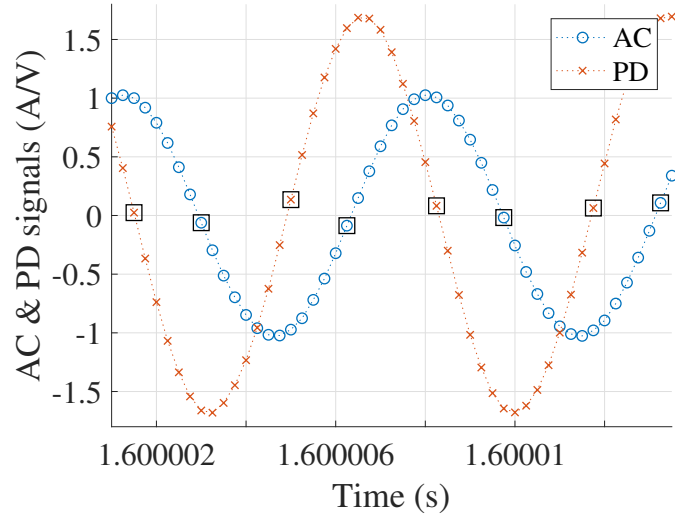
Figure 6.5: Measured zero-crossings of AC and PD signals at high frequencies.

Then to compare between processed results with theoretical solutions calculated from (6.1)-(6.2), average differences between two types of results are insufficient to present comparisons. Since theoretical solutions were computed for all processed frequencies, features in signal results such as small magnitudes at low frequencies and the scattered distribution of θ_Z at high frequencies greatly affected average differences. Thereby, comparisons are demonstrated through normal distributions of differences, which are shown in Fig. 6.6-6.7.

(a) $\mu = 0.0157$, $\sigma = 0.0756$

(b) $\mu = -0.0785$, $\sigma = 0.0898$
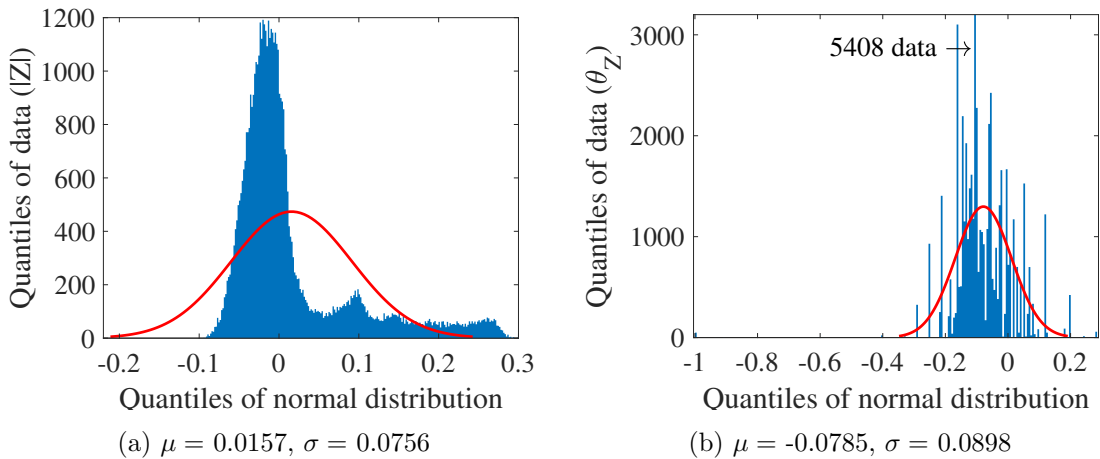
Figure 6.6: Normal distribution of differences between processed and theoretical results of Z_{ser}. μ is the mean and σ is the standard deviation. Total number of data is 52107.

(a) $\mu = 9.86 \times 10^{-4}$, $\sigma = 0.0213$ (b) $\mu = -0.4867$, $\sigma = 0.3768$
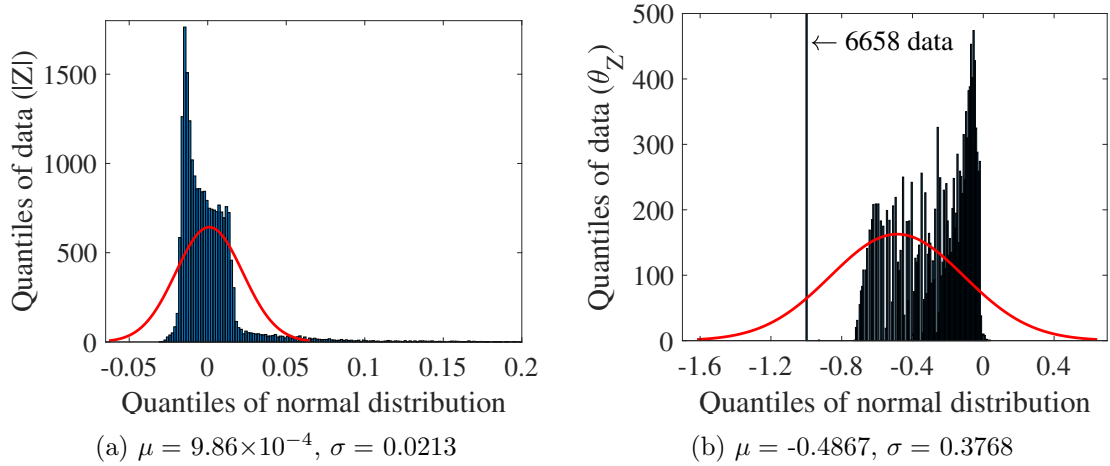
Figure 6.7: Normal distribution of differences between processed and theoretical results of Z_{par}. μ is the mean and σ is the standard deviation. Total number of data is 22001.

For the series circuit, the absolute average differences between processed and theoretical results of $|Z|$ and θ_Z are 4.6% and 9.8% respectively. It can be seen in Fig. 6.3a that at low frequencies, processed $|Z|$ are consistently higher than theoretical results, which is considered due to built-in resistances of the breadboard and connections. This corresponds to the part of positive differences from 0 to 0.3 in Fig. 6.6a. In Fig. 6.3b, processed θ_Z fluctuate widely at high frequencies especially higher than 100 kHz. As a result, differences of θ_Z in Fig. 6.6b basically follow in the normal way but give uneven distributions in densities hence the absolute average difference is relatively large as 9.8%.

In the parallel case, the built-in resistance of the circuit causes less effect in the total impedance, thus processed $|Z|$ agree well to theoretical results from low frequencies, see in Fig. 6.4a. Difference calculated between two types of $|Z|$ follow the normal distribution in Fig. 6.7a, which gives an absolute average difference of 1.3%. However, the distribution in Fig. 6.7b indicates that for about one third (i.e. 6658 of 22001) of signal periods, theoretical results of θ_Z are twice (i.e. about 100%) as large as processed values. It is attributed to results at frequencies higher than 20 kHz, see in Fig. 6.4b. θ_Z at such high frequencies are approaching to zero, which magnifies slight discrepancies between two types of results. The absolute average difference is calculated to be 6.1% by excluding this part of comparisons.

In summary, it is necessary to take account of features of signal results at different frequencies in analysing processed results and comparing to theoretical solutions. After considering such features, the comparison between experimental and theoretical results of impedance was acceptable hence the capability of the data processing has been validated.

6.2.3 Infinitely Long Conductor

Raven has measured impedance of several long copper wires in different dimensions including the diameter of 4 mm [215] that is the same as the present sample. In this section, experimental results of impedance of the copper rod will be presented with theoretical solutions given by the Bessel Function Method in (3.24)-(3.29) and experimental measurements published by Raven [215]. Since Raven presented results with respect to resistance and inductance rather than impedance, same quantities separated from experimental results of impedance will be displayed first, as shown in Fig. 6.8.
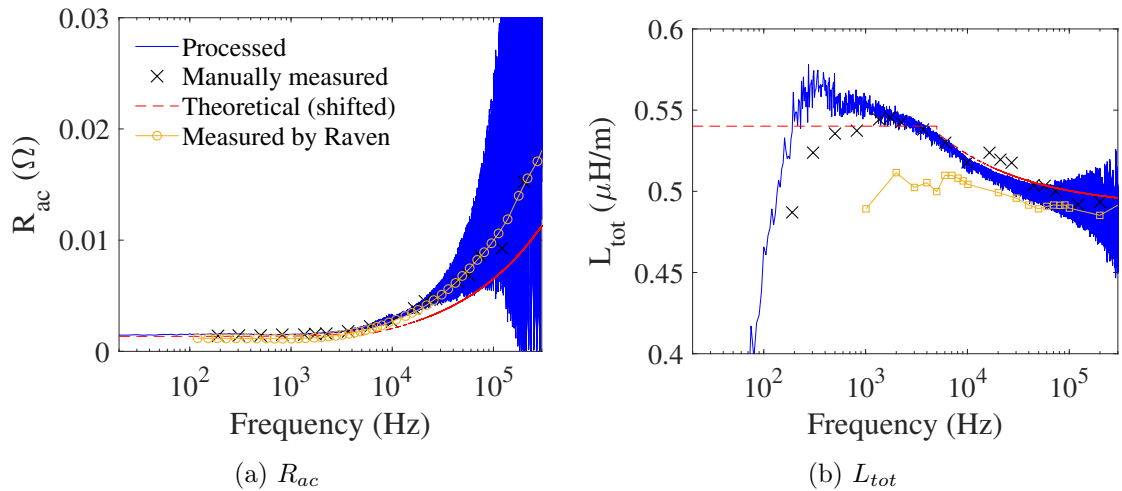
Figure 6.8: Comparison of the resistance (R_{ac}) and total inductance (L_{tot}) of the long copper rod.

The experimental measurements obtained by Raven and also in this project are all of total impedance rather than Z_{int}. Thereby, total inductance (L_{tot}) were calculated from experimental results, including internal inductance (L_{int}) within the sample and external inductance (L_{ext}) around the measuring circuit. Whereas, Bessel Function Method calculates theoretical solutions of L_{int}. By comparing calculated $L_{int,Bes}$ with experimental L_{tot}, it has been noticed that $L_{int,Bes}$ was constantly lower than all experimental L_{tot} for about 0.49 μH/m for the whole frequency range. L_{ext} around the copper rod was thus assumed as 0.49 μH/m. The theoretical curve in Fig. 6.8b is shifted up to include L_{ext} and compare with experimental results of L_{tot}. Moreover, theoretical results in Fig. 6.8 combine two approximations for low and high frequencies (as given by (3.24) and (3.27) respectively), which are sectioned at about 5 kHz.

In Fig. 6.8a, processed and manually measured results of R_{ac} obtained in this project show good fitness with the literature data (i.e. measured by Raven). However, all experimental R_{ac} are higher than theoretical results at high frequencies. Fig. 6.8b shows that experimental results of L_{tot} measured in this project give better contrast with theoretical results at high frequencies than the literature measurements. Nevertheless, experimental L_{tot} disagree with low-frequency

theoretical results, which indicates that L_{ext} was excluded from measuring in the ACPD experiments until about 100 Hz. processed results of R_{ac} are noisy especially at high frequencies. It is because calculations of resistance involve cosine of θ_Z, as

$$R_{ac} = |Z| \cos(\theta_Z) \tag{6.4}$$

It will be demonstrated later that θ_Z approach to $\frac{\pi}{2}$ as frequency rising, hence R_{ac} fluctuate widely from negative to positive.

Impedance results with respect to $|Z|$ and θ_Z are shown in Fig. 6.9. Similarly, theoretical solutions were processed to include L_{ext}. processed results of impedance are clearer than former results and agree well to manual measurements and theoretical solutions. The average difference between two experimental results of $|Z|$ is 3.0% and that of θ_Z is 0.7%. Differences between processed and theoretical results of impedance obey normal distributions, see in Fig. 6.10. The absolute average differences are of 1.8% in $|Z|$ and 2.1% in θ_Z.
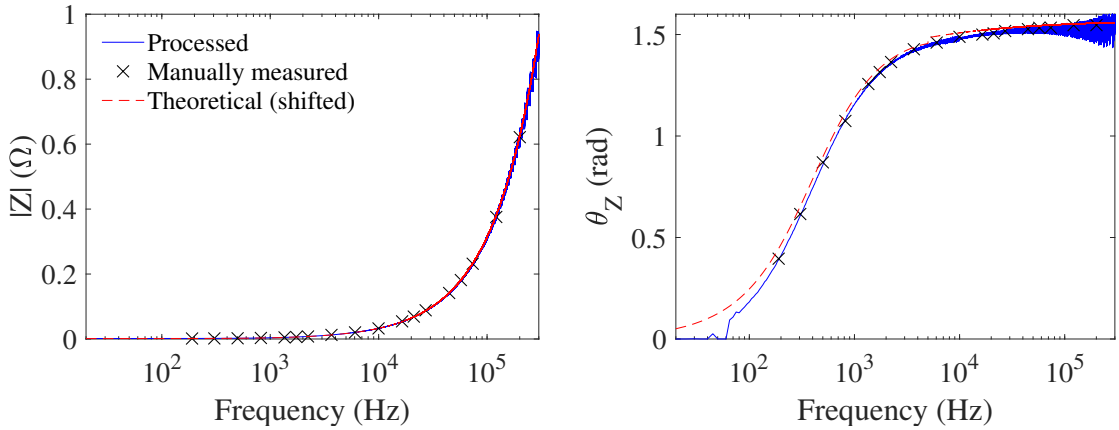
Figure 6.9: Comparison of the total impedance (L_{tot}) of the long copper rod.

(a) μ = -0.0123, σ = 0.0213   (b) μ = -0.0158, σ = 0.0235
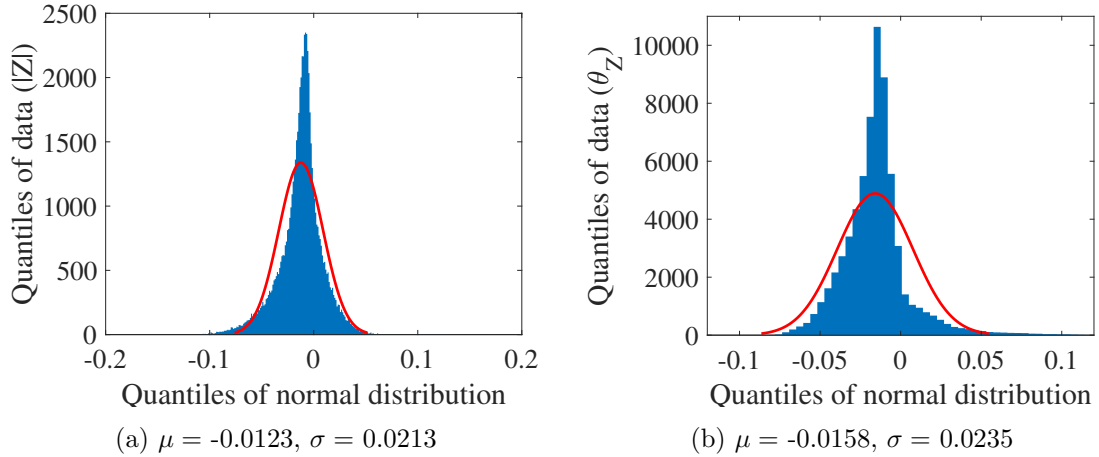
Figure 6.10: Normal distribution of differences between processed and theoretical results of Z_{tot}. μ is the mean and σ is the standard deviation. Total number of data is 66006.

In the preliminary experiment of the long copper rod, processed results of R_{ac} and L_{tot} show limited agreement with theoretical solutions. Experimental measurements from literature [215] are close to processed results but also diverge to theoretical solutions. Nevertheless, experimental results of Z_{tot} coincide closely with theoretical solutions, which is assumed as verification of experimental methodology in this preliminary case.

6.3   Results of Formal Experiments

As discussed in Chapter 3, there is no available theories that could provide theoretical comparisons to ACPD results measured from certain locations on the formal samples. Thereby, this section focuses on evaluating precisions of the data processing by comparing processed results to manually measured values without verification by contrasting with expected solutions. Experimental (or processed) results of PD measured in three formal cases will be compared with FE approximations to reach a comprehensive conclusion in Chapter 7.

6.3.1   Case 1: Polygonal Cross-sectional Shapes of Plain Non-magnetic Samples

Four plain samples in Case 1 were measured twice by different investigators. Experimental results of PD and impedance of eight sets of ACPD measurements are displayed in Fig. 6.11-6.14.

(a) Circular

(b) Hexagonal

(c) Square

(d) Triangular
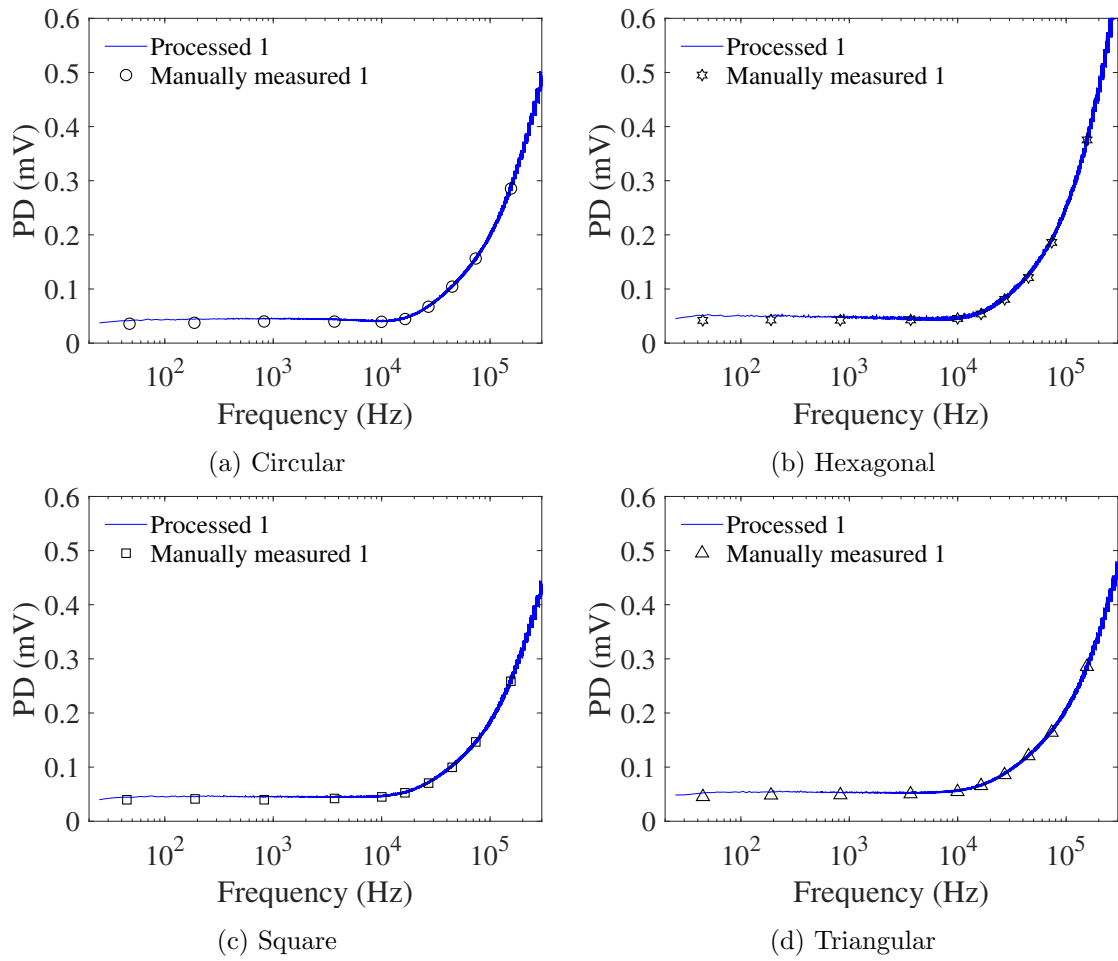
Figure 6.11: Comparisons of PDs obtained from the first measurements of the four SS316 samples in Case 1.
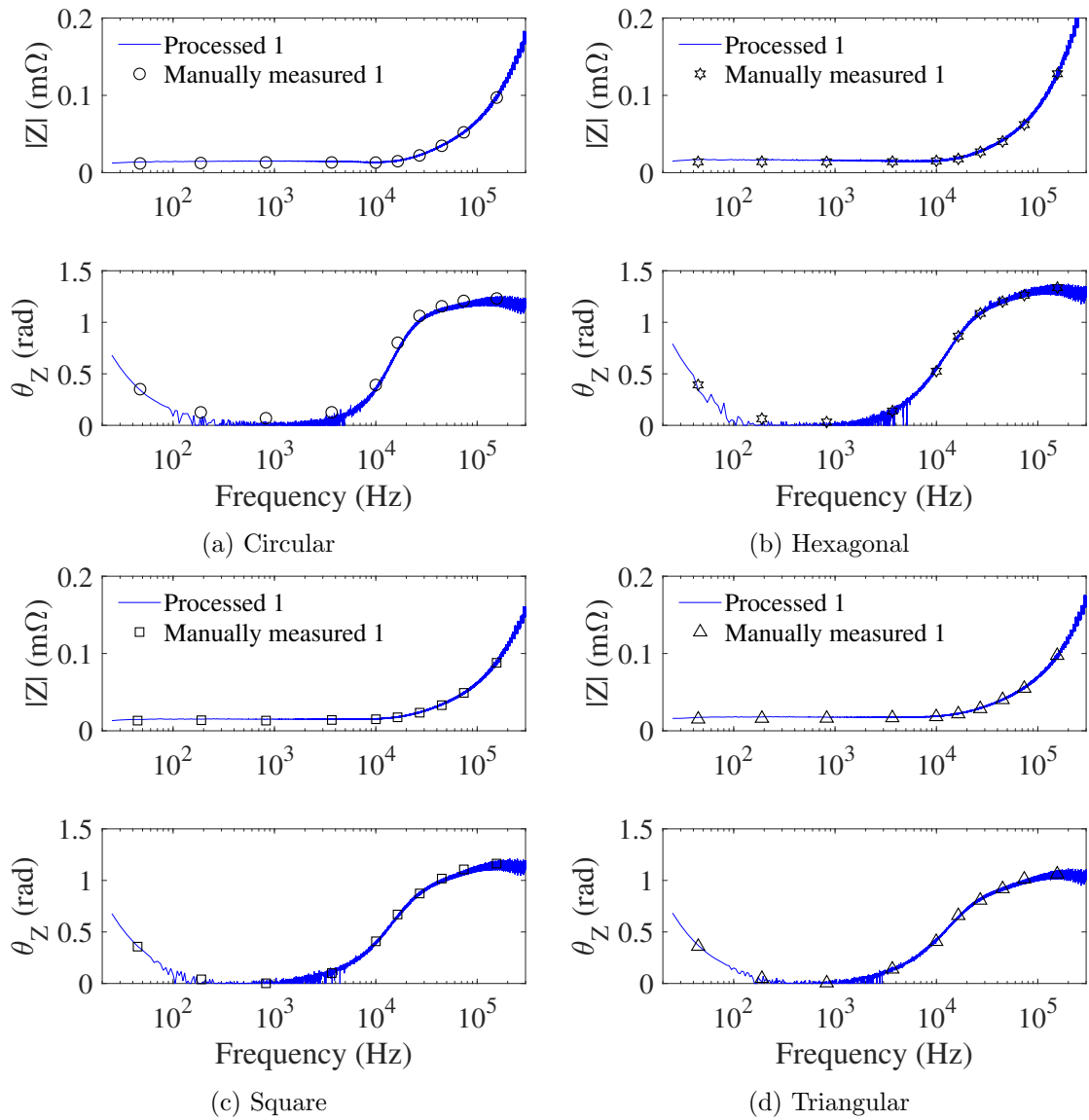
Figure 6.12: Comparisons of impedance obtained from the first measurements of the four SS316 samples in Case 1.

(a) Circular

(b) Hexagonal

(c) Square

(d) Triangular
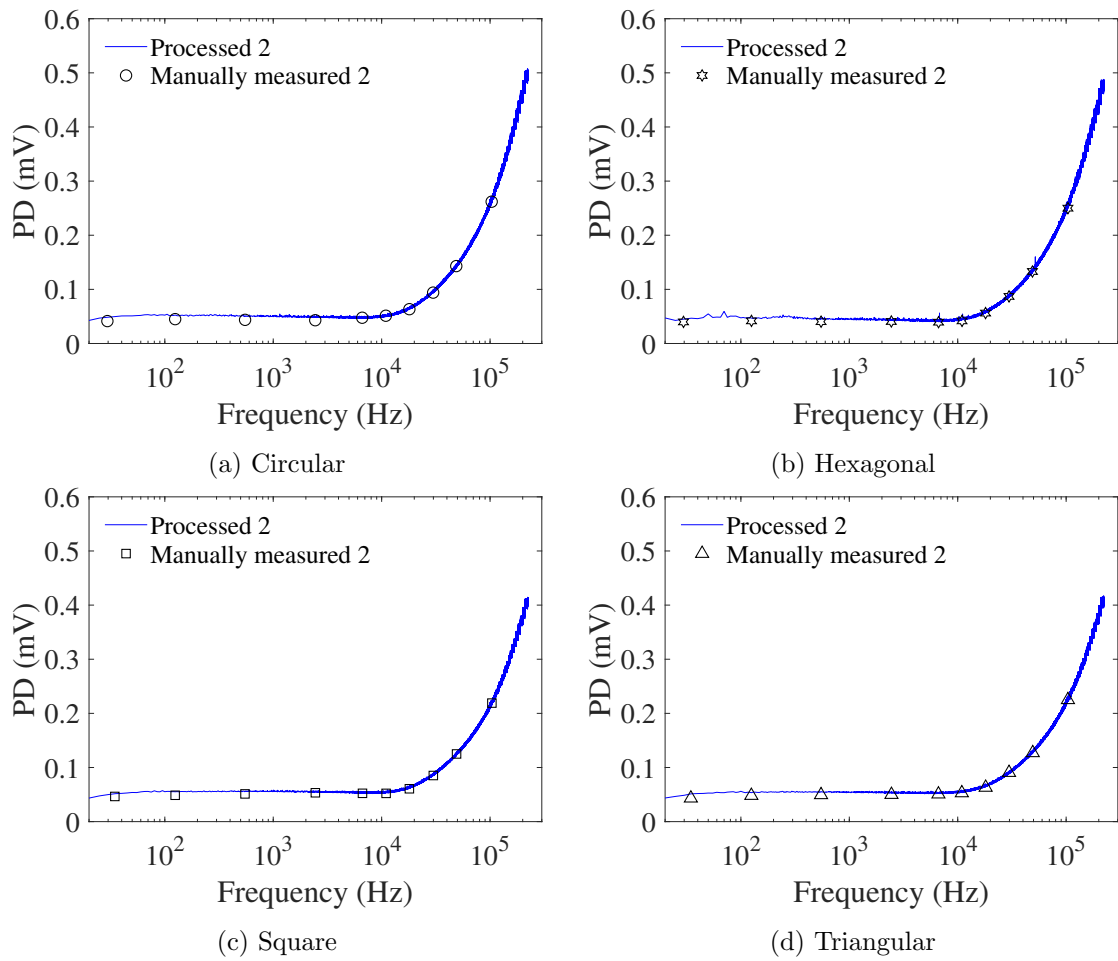
Figure 6.13: Comparisons of PDs obtained from the second measurements of of the four SS316 samples in Case 1.
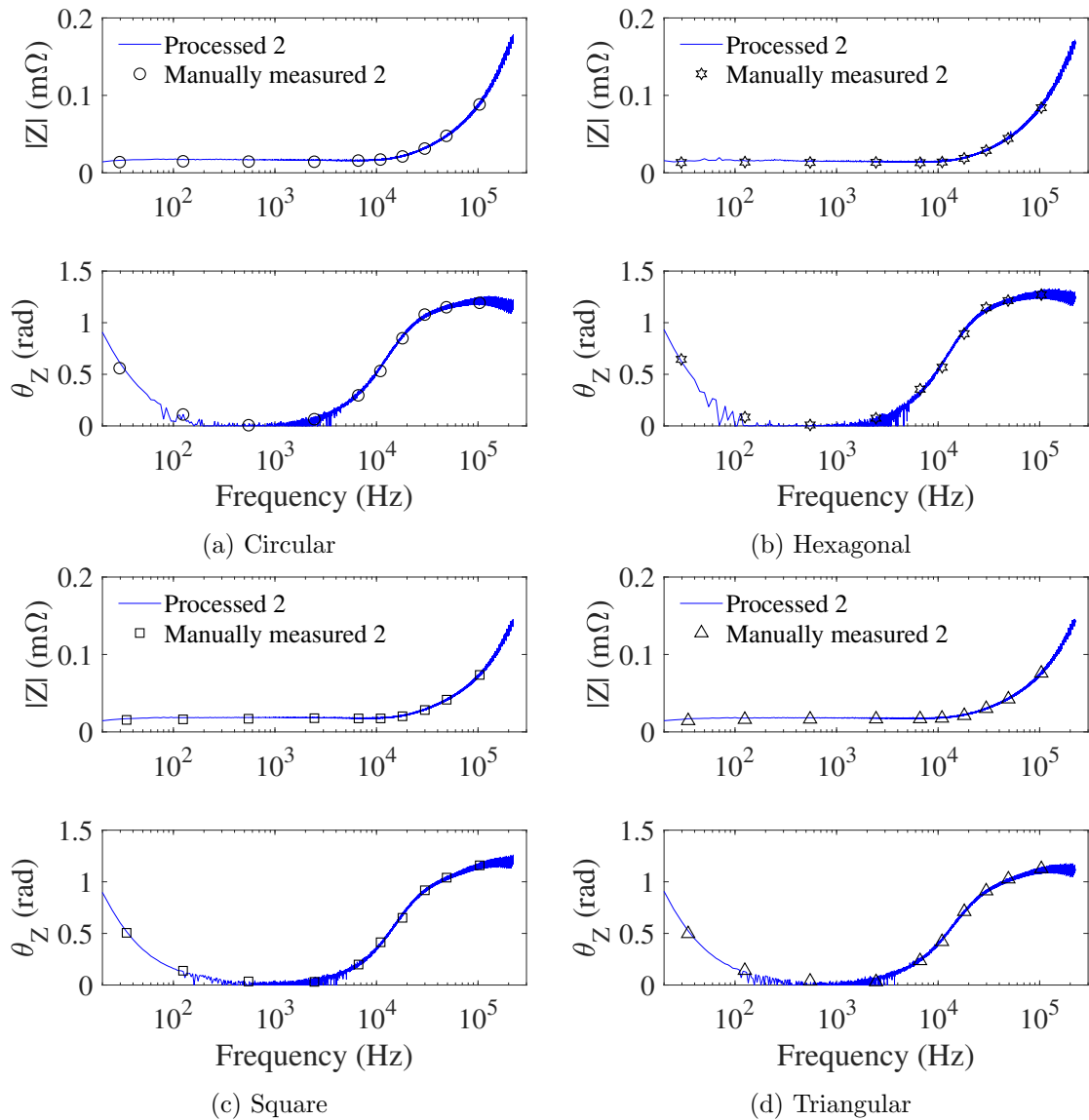
Figure 6.14: Comparisons of impedance obtained from the second measurements of the four SS316 samples in Case 1.

Two types of experimental results agree well to each other for the eight sets of measurements. However, manually measured PDs and $|Z|$ are slightly lower than processed results at frequencies lower than 40 kHz in all cases. This is because raw data are not smoothed before the data processing, since experimental measurements of Case 1 are relatively clean and data smoothing is not required. processed amplitudes of signals are calculated by averaging the maximum and the minimum data within each period. Whereas during manual measuring, noisy signals are smoothed artificially by choosing median values around peaks as amplitudes. Fig. 6.15 illustrates these different chooses in determining amplitudes during the data processing and manual measurements for a piece of noisy signals at about 50 Hz. Such differences may be reduced by smoothing the raw data before interpretation.
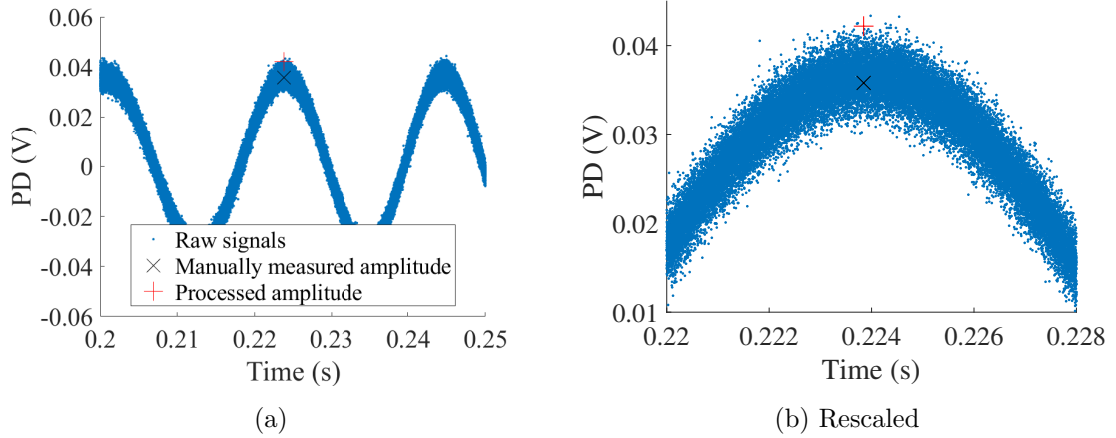
Figure 6.15: Processed and manual measured amplitude of PD signals from the first measurements of the cylindrical sample at 50 Hz.

Differences between two types of experimental results are calculated for PDs and impedance, as displayed in Fig. 6.16-6.17. For the aforementioned reason, differences of PDs and $|Z|$ are quite large for about 15% at low frequencies and decrease to under 5% after about 40 kHz. For eight sets of measurements, absolute average differences between two types of results of PD and $|Z|$ for the whole frequency range are within 8%. To contrast between processed and manual measured θ_Z, differences within the range of 100 Hz to 40 kHz are very large since θ_Z approach to zero at such frequencies thus small magnitudes in discrepancies still give huge differences in percent. These differences are futile to demonstrate comparisons between two types of results hence are not shown in Fig. 6.16-6.17 and excluded from calculating average differences. Absolute average differences of θ_Z at frequencies higher than 40 kHz, for eight sets of measures, are all smaller than 4%.

(a) Circular

(b) Hexagonal

(c) Square

(d) Triangular
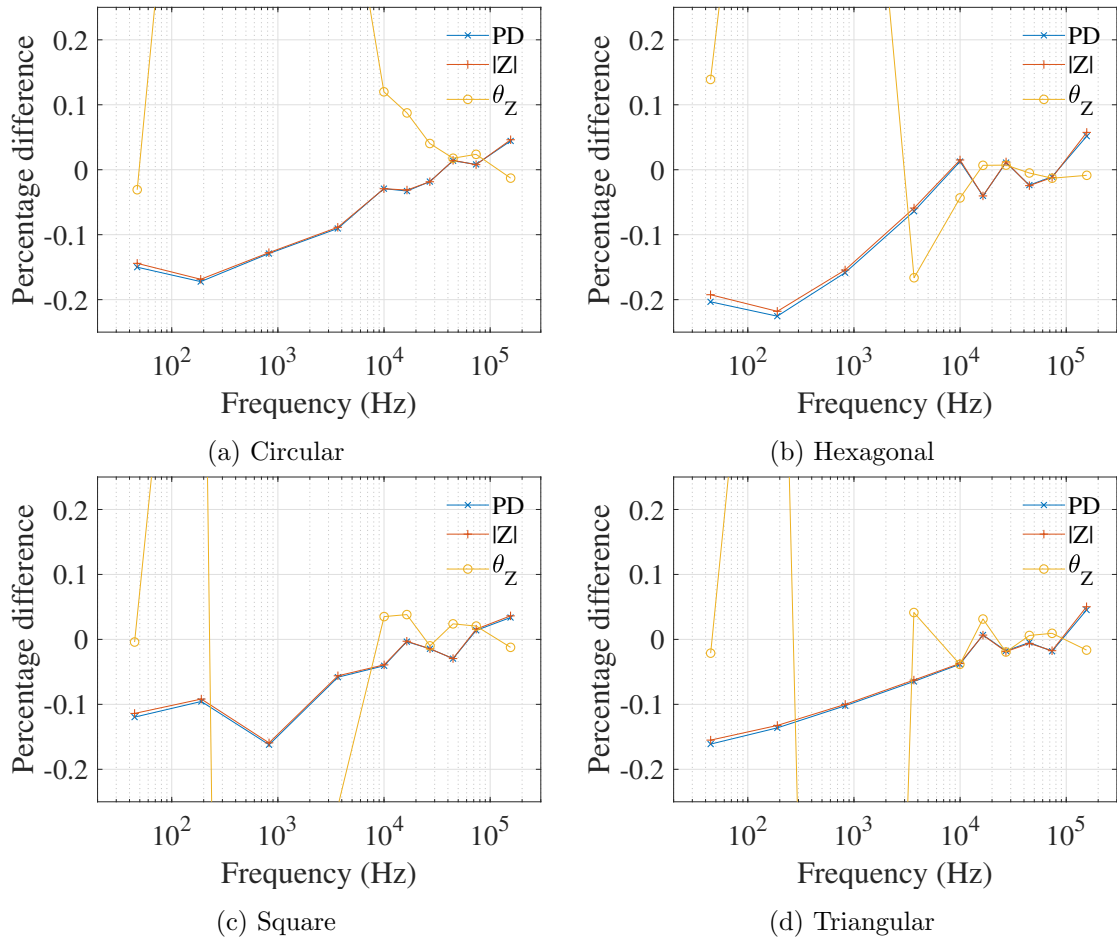
Figure 6.16: Differences between processed and manual measured results obtained from the first measurements of the four SS316 samples in Case 1.
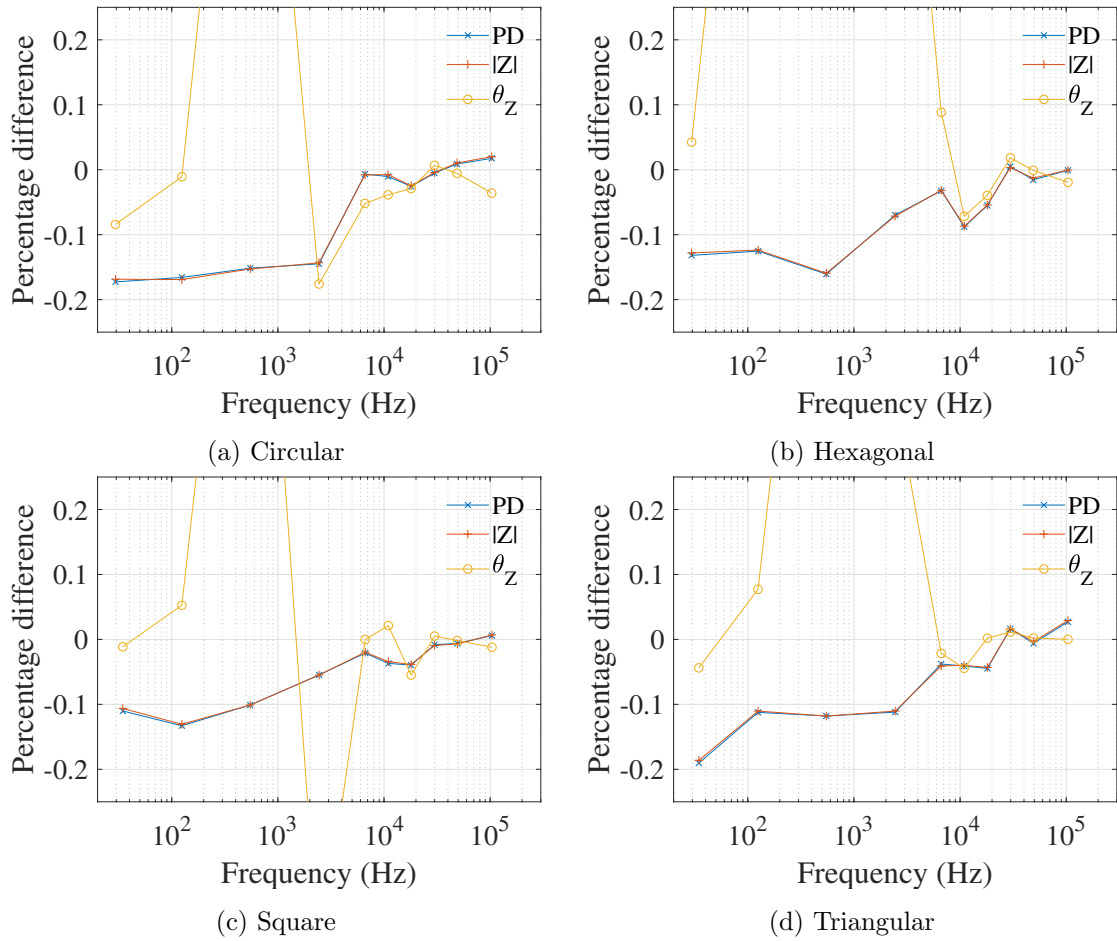
Figure 6.17: Differences between processed and manual measured results obtained from the second measurements of the four SS316 samples in Case 1.

6.3.2 Case 2: Various Features with Dissimilar Opening Shapes Contained in Featured Magnetic Samples

In Cases 2 & 3, 'impedance' calculated based on ACPD data measured across the features is not real impedance of the measuring part, as discussed in Chapter 3. Since the electric field produced around a featured sample is uneven and tends to concentrate near the feature edges, PDs measured from certain locations are not representative of the whole field. Results of 'impedance' of featured samples will only be presented in this sections for validating the data processing but excluded from further analysis.

Fig. 6.18 & 6.19 show comparisons of processed and manual measured PDs and impedance of the featured samples in Case 2. Differences between these two types of results are given in Fig. 6.20.

(a) H

(b) N

(c) NH
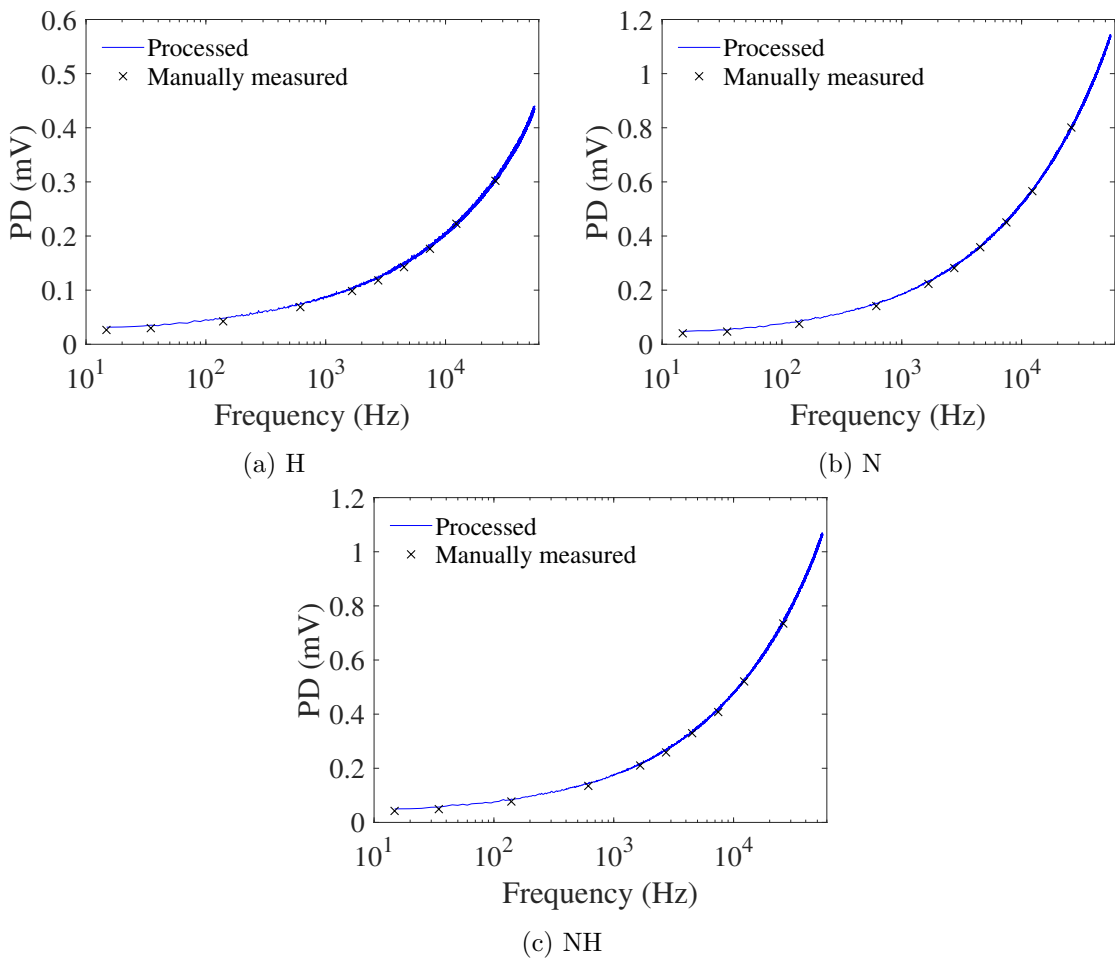
Figure 6.18: Comparisons of PDs obtained from the three featured EN1A samples in Case 2.
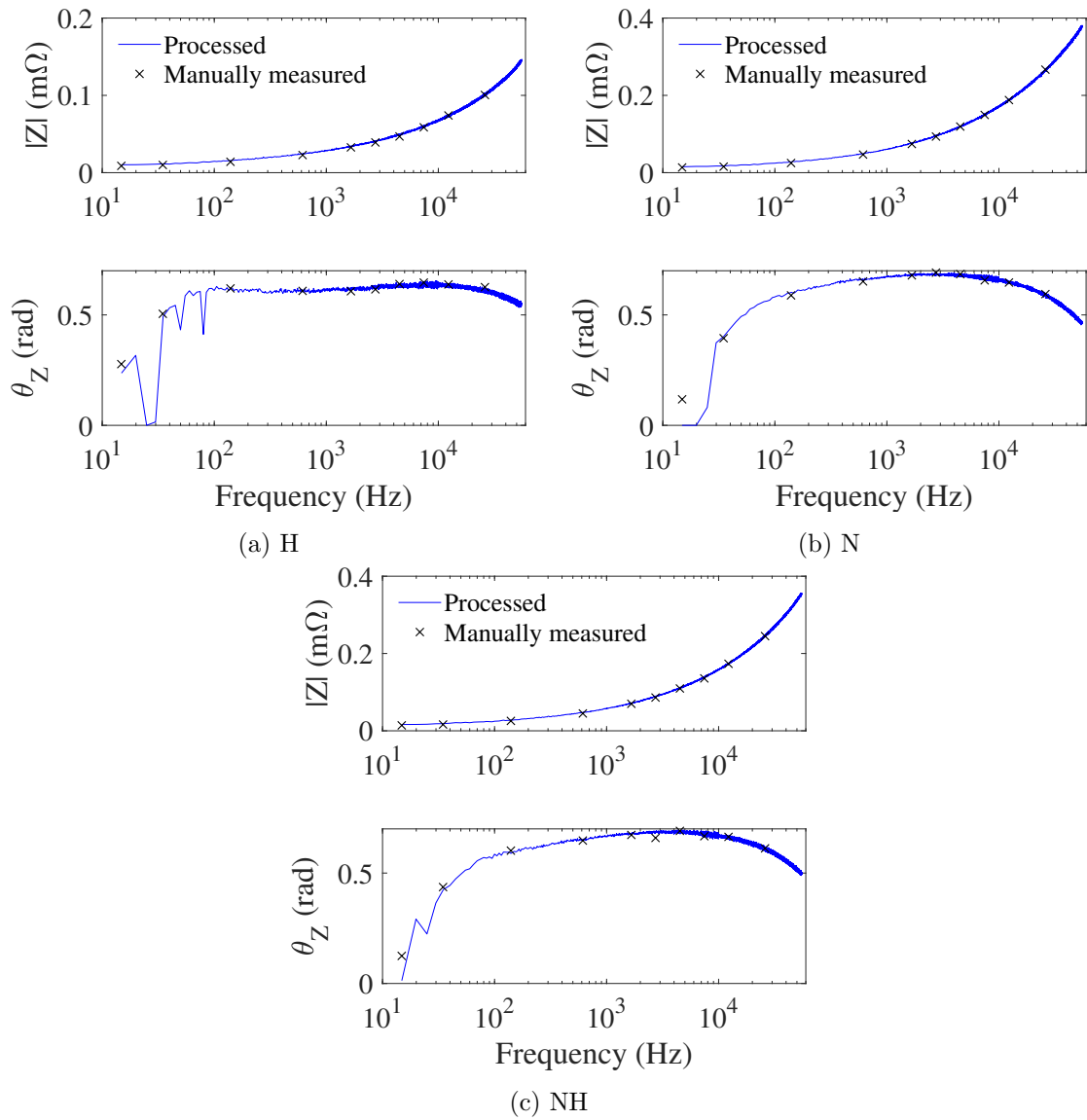
Figure 6.19: Comparisons of impedance obtained from the three featured EN1A samples in Case 2.
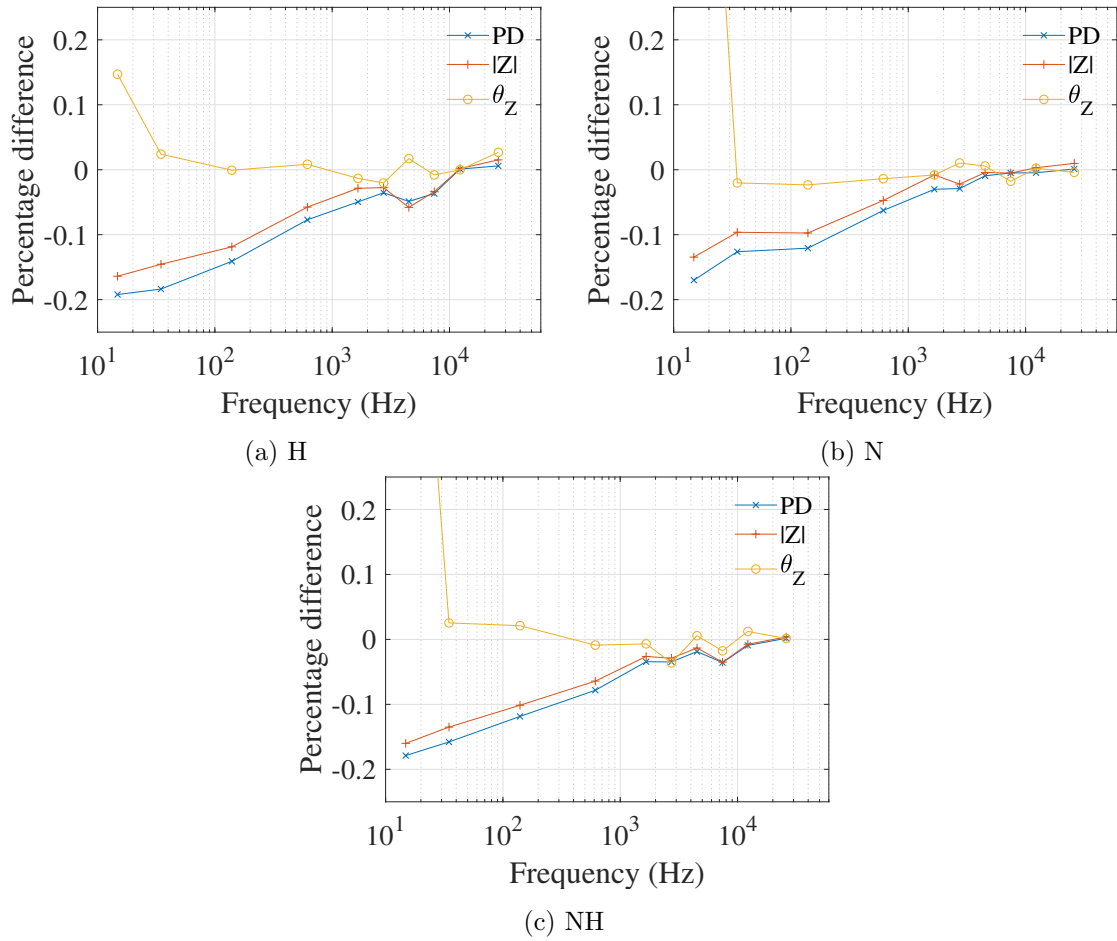
Figure 6.20: Differences between processed and manual measured results obtained from the three featured EN1A samples in Case 2.

Since EN1A is ferromagnetic, lower frequencies in the ACPD experiments were sufficient to generate strong skin effect inside these featured samples. AC oscillated with a lower frequency range of 10 Hz to 50 kHz were applied in Cases 2 & 3. Comparing to measurements in Case 1 with higher frequencies from 10 Hz to 300 kHz, signals captured in Cases 2 & 3 are much more noisy at the beginning, however on the other side, possess more plentiful data at the end. Therefore, processed results of Cases 2 & 3 are less desired at low frequencies but more precise at high frequencies (upto 50 kHz). For example in Fig. 6.19a, processed θ_Z of the H sample are not smooth at frequencies lower than 100 Hz. For three sets of measurements in Case 2, absolute average difference between two types of $|Z|$ are within 8%, while these average differences of θ_Z that exclude results lower than 100 Hz are smaller than 2%.

6.3.3   Case 3: Various Features of the Same Cross-Sectional Area Contained in Featured Magnetic Samples

Comparisons of results measured from the N3 and N1.5 samples in Case 3 are displayed in Fig. 6.21-6.23. In these two cases, absolute average differences of $|Z|$ and Z_θ are within 7% and 2% respectively.

(a) N3   (b) N1.5
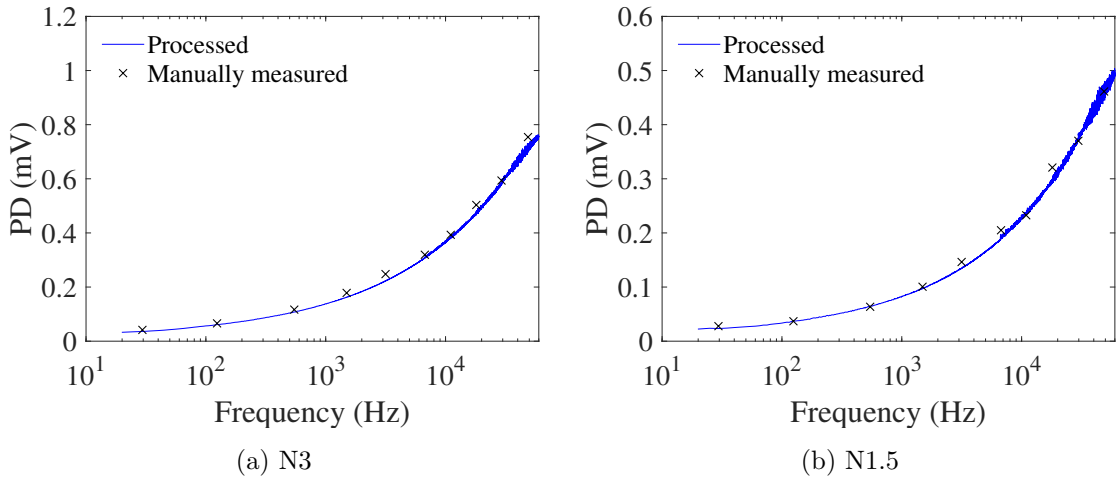
Figure 6.21: Comparisons of PD obtained from the two featured EN1A samples in Case 3.
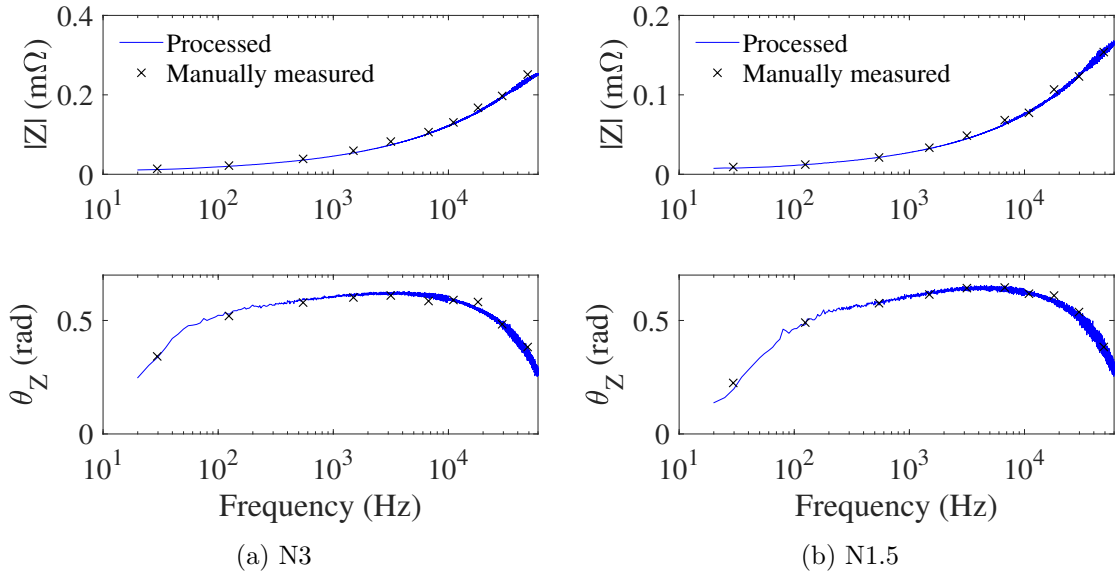
Figure 6.22: Comparisons of impedance obtained from the two featured EN1A samples in Case 3.
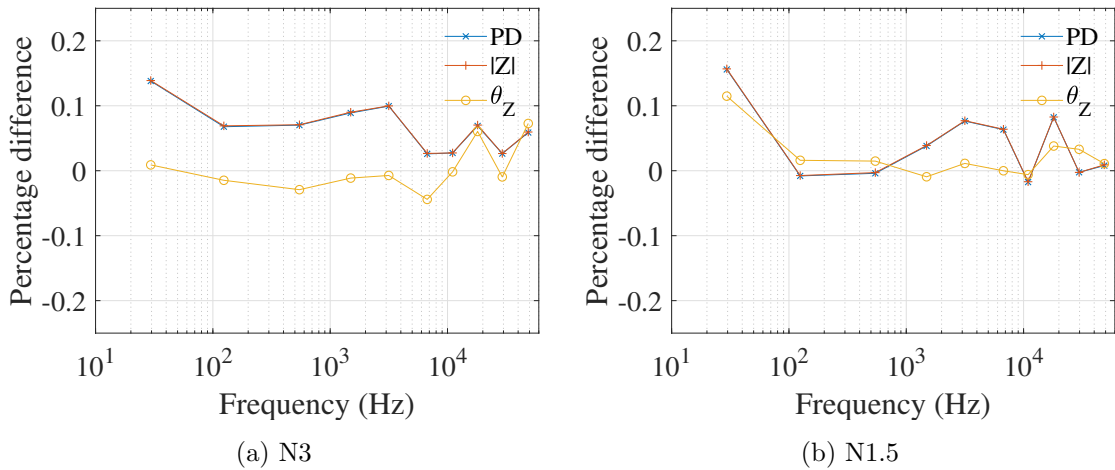
Figure 6.23: Differences between processed and manual measured results obtained from the two featured EN1A samples in Case 3.

6.4 Conclusions

Experimental results of the preliminary and formal experiments processed by the MATLAB script were presented with manually measured results and some theoretical solutions. In the first preliminary experiment about the individual resistor, the average difference between processed and manual measured results of resistance is within 0.4%. Experimental results are consistently higher than the known value of 0.22 Ω for 5.9% from the beginning of 10 Hz to 10 kHz due to intrinsic resistance of other part of the circuit. These results start to increase at frequencies higher than 10 kHz, which indicates the fault of the current input file in remaining constant

amplitudes of AC input. The problem was solved in later experiments.

In the second preliminary experiment involving two R-L circuits, processed results of impedance were compared with manual measurements and theoretical solutions based on rules for combining impedances. Processed results show good fitness with manual measurements with average differences smaller than 2.5% in $|Z|$ and those smaller than 5.5% in θ_Z, for both two circuits. Comparisons between processed and theoretical results were displayed through normal distributions, in which average differences are within 5% in $|Z|$ and 10% in θ_Z in two experiments. Discrepancies between processed and theoretical $|Z|$ are largely attributed to low-frequency results because of intrinsic resistance from the rest of circuits. Relatively high differences in Z_θ are mainly caused by scattered processed results at high frequencies. This is because that the measuring method with a constant f_s in experiments is unable to accurately capture zero-crossings (and amplitudes) for all the periods especially at high frequencies. Measured signals closest to real zero-crossings were used in the data processing, which decreases the performance of the interpretation given by the MATLAB script at high frequencies.

Then with regard to the final preliminary sample of the long copper wire, comparisons were made between results from interpretation, manual measurements, Bessel Function solutions, and experimental measurements published in literature. In comparisons of R_{ac} and L_{tot}, experiments results obtained in this research agree well with the literature data but only shown limited fitness with theoretical solutions. However, processed impedance are more distinct and fit well with manual measurements and theoretical results with average differences within 3% in comparisons of both $|Z|$ and θ_Z.

ACPD measurements of the formal experiments were processed by the script and presented with manual measured results, which including eight measurements of the four plain samples in Case 1 and five measurements of the five featured samples in Cases 2 & 3. For these thirteen sets of results, average differences between two types of $|Z|$ are within 8%. These differences are primarily caused by low-frequency comparisons, in which processed amplitudes of signals are determined from absolute maximums and minimums of raw data while manual measured amplitudes are always chosen as medians of noisy signals due to artificial smoothing. With respect to contrasts of θ_Z, average differences between two types of results of eight measurements in Case 1 are smaller than 4% and those of five measurements in Cases 2 & 3 are within 2%.

Based on above analysis, comparisons between processed results to other types of results in all experiments were accepted. Thereby, the procedure of the ACPD experiments was verified and the performance of the data processing was validated.

Chapter 7

Results and Discussions of Alternating Current Potential Difference Results for Formal Samples

7.1 Introduction

Experimental methodology of obtaining ACPD results from the formal samples and numerical methodology to provide comparison with experimental results were fully introduced in previous chapters. In Section 6.3, processed results of the formal samples were compared with manually measured results to validate the data processing. This chapter will continue the analysis to compare the ACPD results between different sample shapes and features, and then to comprehend the principles of such differences (or the detection capability) through electric fields/current distributions approximated in FEA.

In the following analysis, the emphasis will be placed on comparing experimental (i.e. processed) results of PD between various samples in each case to study, firstly the sensitivity in detecting the cross-sectional shape of the sample (Case 1); then the capability in distinguishing between the features with dissimilar shapes of openings on the surfaces, like a deep drill and a shallow notch (Case 2); finally the ability and limitation in discriminating the features with similar opening shapes of rectangular and of the same cross-sectional area (Case 3). Additionally, the analysis will focus on contrasting between experimental and FE results. On one hand, FE results of PD measured from the optimum simulative path, which approximates the expectant welding positions of PD measurement probes on the samples, will be compared with experimental PDs to testify the sensitivity of the ACPD method. On the other hand, FE results of PD obtained from several auxiliary paths around the optimum path will be used to produce error bars to present the differences in PDs caused by welding uncertainties of measurement

probes possibly occurred in experiments. To concisely cite two different types of error bars, the bars indicating effects of different measurement locations are referred to as 'error bars I', whereas those consisting of PDs obtained with different measurement distances are named as 'error bars II'.

This chapter is consisted of two parts, the results and discussions. The sections of results will include the contrasts of experimental PDs between various samples in each case and the agreement between experimental and FE results for each sample. Error bars I & II will be compared in magnitudes between samples to demonstrate differences in the measuring sensitivities due to different sample shapes and feature geometries. The ACPD method involved in this project measured signals from a single position (or path) on the sample surfaces, which actually reflects a small part of the electric fields in the vicinity of this position. In the discussions, the complete electric fields (and the current distributions) approximated by FEA will be introduced to conveniently illustrate these results, e.g. variations in electric fields on auxiliary paths can be directly related to the differences in magnitudes of error bars. In addition to help comprehend ACPD results, the electric fields will be utilised to provide practical guidance in applying the ACPD experiments on plain and featured conductors similar to the formal samples.

7.2 Alternating Current Potential Difference Results of Experimental Measurements and Finite Element Analysis Approximations

7.2.1 Case 1: Polygonal Cross-sectional Shapes of Plain Non-magnetic Samples

Experimental Results

In Case 1, the ACPD method was applied to four plain samples of cross-sectional shapes twice by two investigators at different times, i.e. Experiments 1 & 2. Experimental results of PD processed from two sets of experimental measurements are presented in Fig. 7.1. Eight sets of PDs are similar in remaining constant at about 0.05 mV for the quasi-DC frequencies lower than 10 kHz then increasing with the frequencies rising, eventually reaching about 0.5 mV at 200 kHz.
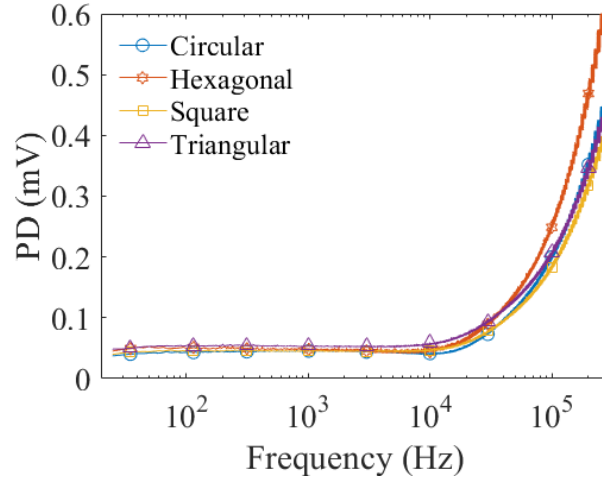
(a) Experiments 1
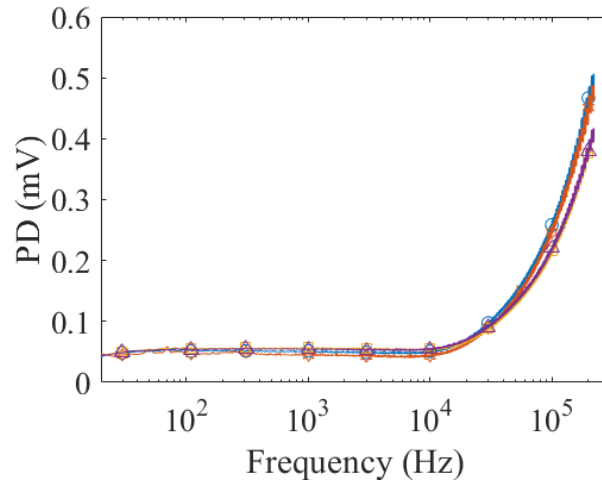
(b) Experiments 2

Figure 7.1: Experimental results of PD measured from the uniform positions in 2 mm on the plain geometry SS316 samples in Case 1.

To clear demonstrate the repeatability between Experiments 1 & 2, eight sets of results presented in Fig. 7.1 are grouped by the samples or the cross-sectional shapes, as shown in Fig. 7.2. The repeatability are numerically analysed by calculating the differences of PD magnitudes (from about 44k periods) for each sample between Experiments 1 & 2. It can be seen in Fig. 7.2b & 7.2d that two sets of measurements for the hexagonal and triangular samples are close for the whole frequency range. For both the two samples, the average differences of PD amplitudes (averaged from the 44k periods) obtained in Experiments 1 & 2 are smaller than 5%. However, the repeatability of the circular and square samples are less desirable in which results of Experiments 2 are consistently higher than those of Experiments 1. Moreover, gaps between two sets of results rise as the frequency increases. The maximum difference of PD amplitudes obtained in Experiments 1 & 2 for the circular sample at 200 kHz is about 0.1 mV (i.e. 22.8%), that for the

square sample is about 0.06 mV (i.e. 16.3%).
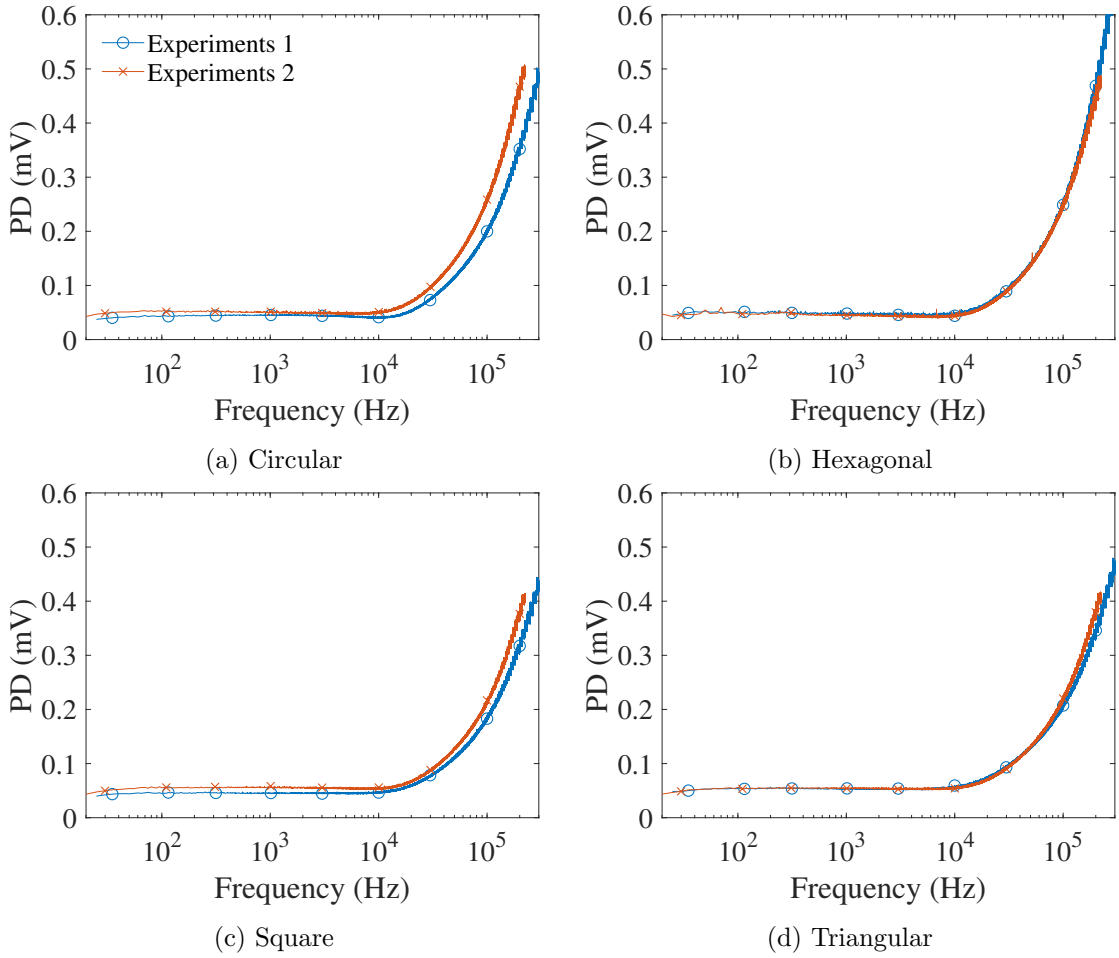
Figure 7.2: Illustration of the repeatability between Experiments 1 & 2 applied to the four plain SS316 samples in Case 1.

Numerical Results

FE models of the four plain SS316 samples were built by following the approaches introduced in Chapter 5 to approximate PDs on certain conductive paths and simulate electric fields within and around the samples. FE results of PD measured from the optimum simulation path, Path-0.8, are shown with related error bars in Fig. 7.3. The definitions of error bars were introduced in Section 5.6 that error bars I & II indicate the impact of different measurement locations and distances on PDs receptively. The sizes of error bars given in Fig. 7.3c-7.3d were calculated in percent of the optimum approximations of PD of Path-0.8.

(a) Effect of measurement locations.

(b) Effect of measurement distances.

(c) Sizes of error bars I in (a).

(d) Sizes of error bars II in (b).
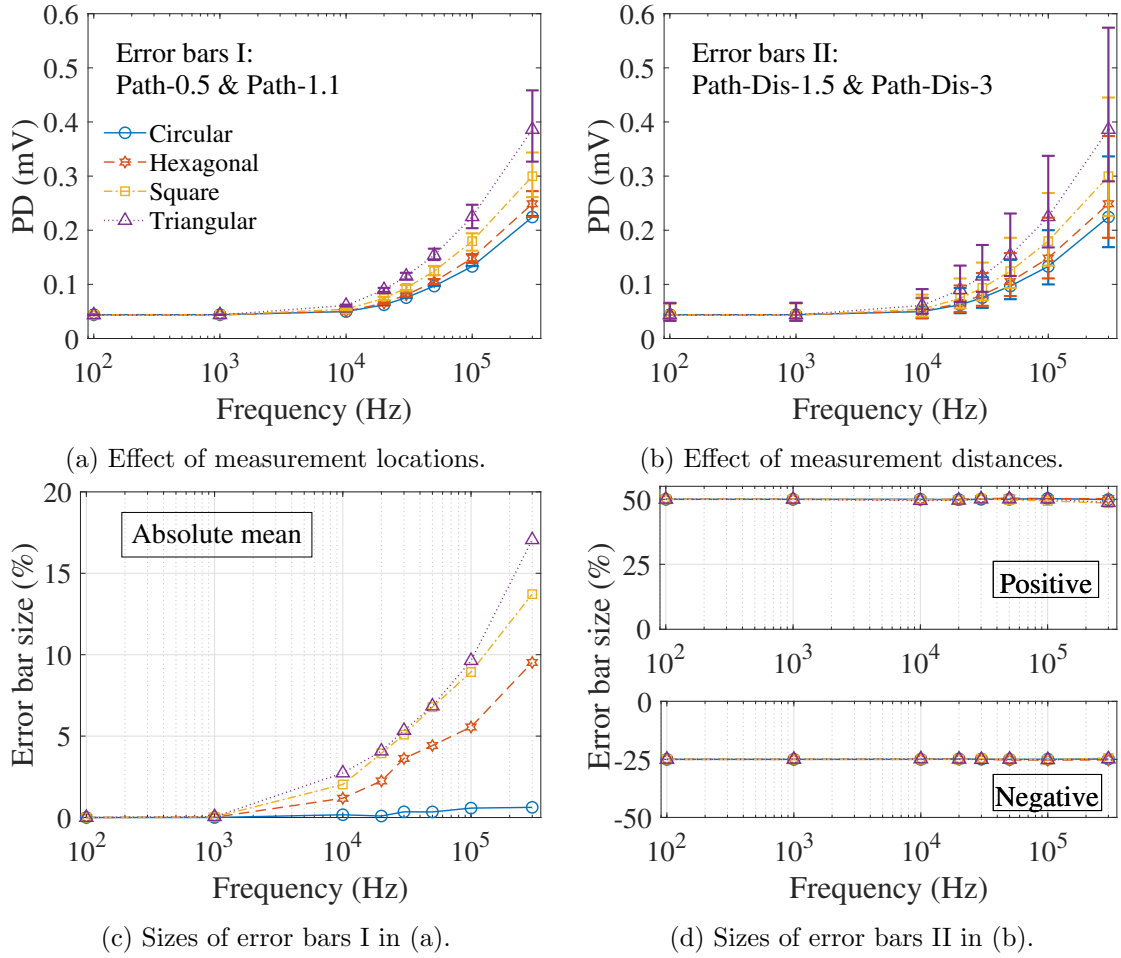
Figure 7.3: FE results of PD of Path-0.8 (the optimum simulation path) and related error bars I & II approximated by the PS SS316 models.

In Fig. 7.3a-7.3b, PDs measured from the uniform paths on the four models, i.e. Path-0.8, show a distinct order in magnitudes among different cross-sectional shapes. PDs consistently increase as the cross-sectional shape varies from circular to triangular for the whole frequency range. At the highest frequency of 300 kHz, the triangular model produces the highest result of 0.39 mV while the circular model gives the lowest value of 0.22 mV. In other words, by sampling the frequency of current injections to 300 kHz, the ACPD method should be able to identify the cross-sectional shapes of SS316 conductors, with the maximum difference of results between the triangular and circular shape of 77% (based on the smaller value). In Fig. 7.3a & 7.3c, error bars I given by the four models have significantly different sizes. Fig. 7.3c shows that at 300 kHz, the size of error bars I averaged from positive and negative parts in the triangular model is upto 17%, whereas that in the circular model is only 0.6% (almost invisible in Fig. 7.3a). With respect to error bars II, sizes of error bars are consistently to be +50% in positive sides and -25% in negative on all models for the whole frequency range, see in Fig. 7.3d.

In addition to investigate around the optimum simulation path close to the edges, Path-4.2 were created to approximate the ACPD results at the positions

far from the edges and close to the surface center. FE results of PD of Path-4.2 and related error bars are shown in Fig. 7.4. PDs of Path-4.2 given by the four models display an inverse order in magnitudes to the results of Path-0.8 shown in Fig. 7.3. At 300 kHz, the circular model gives the highest PD of 0.22 mV (almost identical to the results of Path-0.8), whereas the triangular model outputs the lowest result of 0.14 mV, resulting in the maximum difference of 57%. The sizes of error bars I around Path-4.2 in Fig. 7.3a are much smaller than those around Path-0.8, with sizes smaller than 6% on the triangular model and within 3% on the other models. Similar to error bars II for Path-0.8, the sizes of error bars II for Path-4.2 are constantly to be +50% and -25% in positive and negative parts regardless of the frequency, as shown in Fig. 7.4b.

(a) Effect of measurement locations.   (b) Effect of measurement distances.
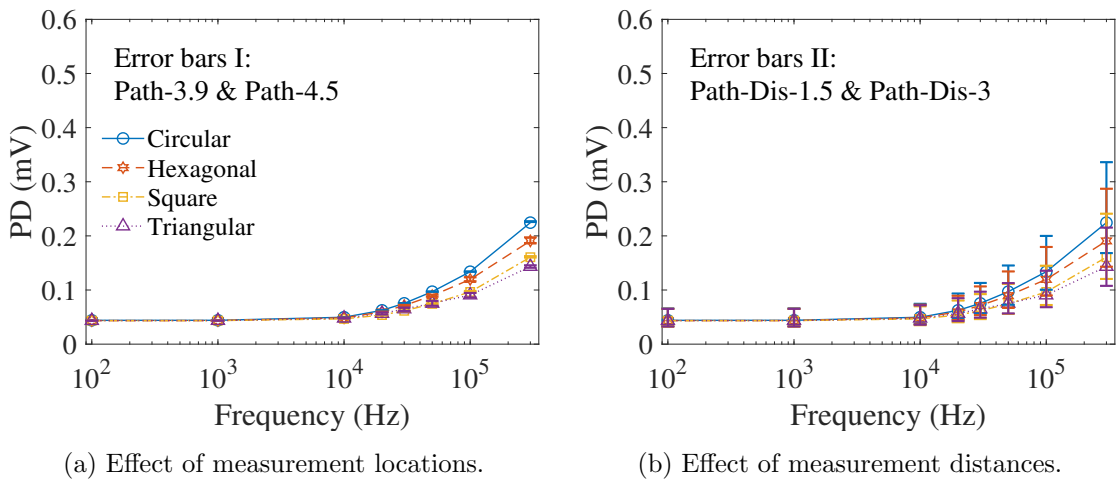
Figure 7.4: FE results of PD of Path-4.2 (far from the edges) and related error bars I & II approximated by the PS SS316 models.

Comparisons of Experimental, Numerical, and Theoretical Results

In addition to the experimental and FE results presented above, theoretical solutions of PD were obtained based on the method of integral equation for current distribution discussed in Section 3.4. Theoretical results of PD were simply calculated by multiplying $R_{ac,InJ}$ per unit length (as shown in Fig. 3.9) by the measurement distance of 2 mm and the total current of 3 A. The calculation assumes the current to be uniformly distributed inside and outside the samples, thereby only provides rough estimations of PD. The ACPD results for the SS316 samples of the four cross-sectional shapes were analysed by comparing the results of PD obtained by the three methodology, combined with error bars related to Path-0.8 approximated by FEA.

Results of comparisons for the sample/model of triangular cross-sectional shape are given in Fig. 7.5. FE PDs measured from two positions close to and far from the edge, i.e. Path-0.8 and Path-4.2, display significant differences at frequencies higher than 10 kHz (e.g. reaching 0.39 mV and 0.14 mV at 300 kHz), with the

theoretical solutions to be located in between. The optimum FE approximations of PD of Path-0.8 show good fitness with experimental results at low frequencies and give slight differences after 10 kHz. The differences between experimental and the optimum FE results are consistently covered by the error bars for the whole frequency range.
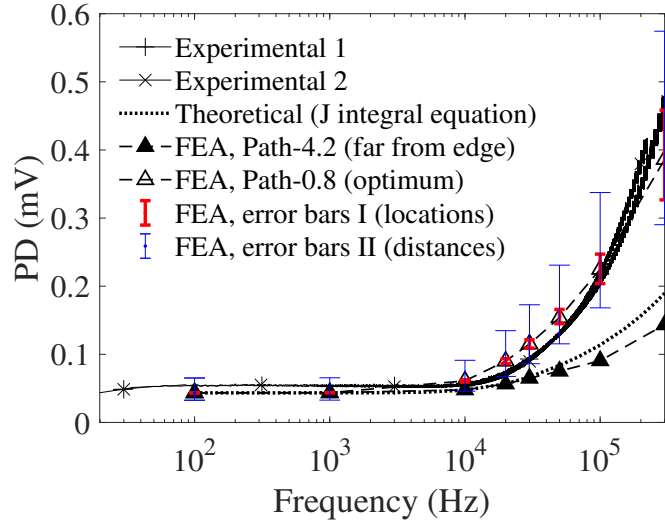
Figure 7.5: Results of PD on the uniform measurement path obtained through various methods for the plain SS316 sample of triangular cross-sectional shape.

Results for the square cross-sectional shape are shown in Fig. 7.6. FE PDs measured from Path-0.8 and Path-4.2 exhibit smaller gaps than those given by the triangular model, leading to the maximum values of 0.30 mV and 0.16 mV at 300 kHz respectively. The theoretical solutions are still located between two sets of FE PDs and very close to the surface measurements of Path-4.2 Experimental results diverge to the optimum FE approximations at frequencies higher than 100 kHz but are still situated within the error bars.
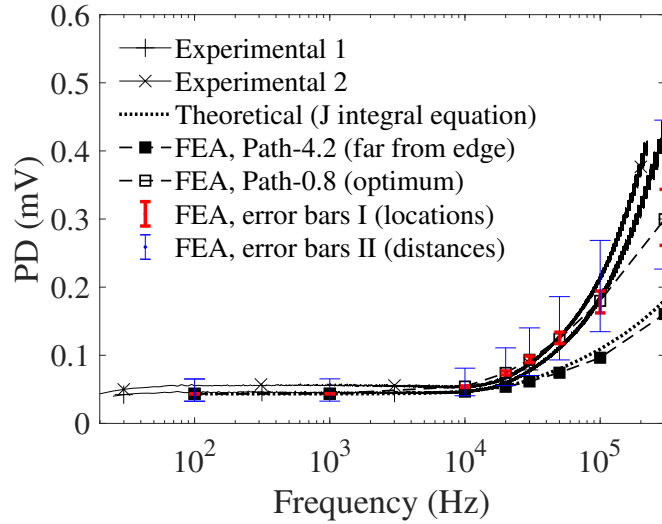
Figure 7.6: Results of PD on the uniform measurement path obtained through various methods for the plain SS316 sample of square cross-sectional shape.

Fig. 7.7-7.8 present results of the hexagonal and the circular cross-sectional shapes. By comparing with FE results in Fig. 7.5-7.6, it can be clearly observed that differences between PDs measured close to and far from the edges decrease as the cross-sectional shape varies from triangular to circular. The theoretical solutions for these two cross-sectional shapes are lower than FE results including the surface measurements of Path-4.2. At 300 kHz, PDs measured from Path-4.2 and Path-0.8 on the hexagonal model are 0.19 mV and 0.25 mV respectively. For the circular model, PDs exported from two paths are similar to be 0.24 mV. Nevertheless, contrasts between experimental and FE results for these two cross-sectional shapes are poor in which experimental results even fall beyond the error bars.
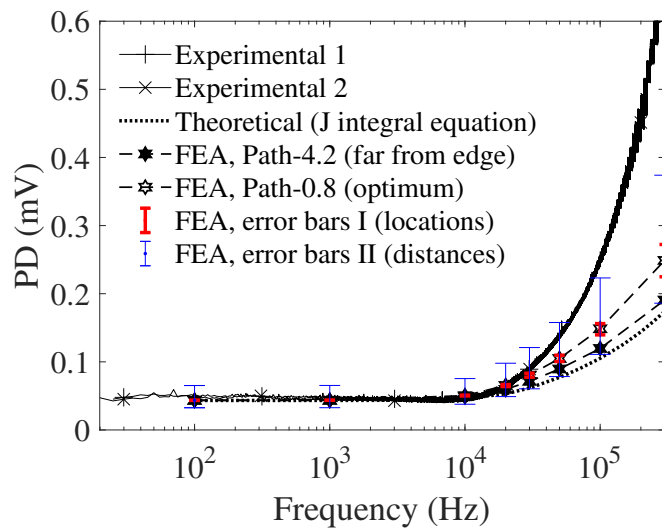
Figure 7.7: Results of PD on the uniform measurement path obtained through various methods for the plain SS316 sample of hexagonal cross-sectional shape.
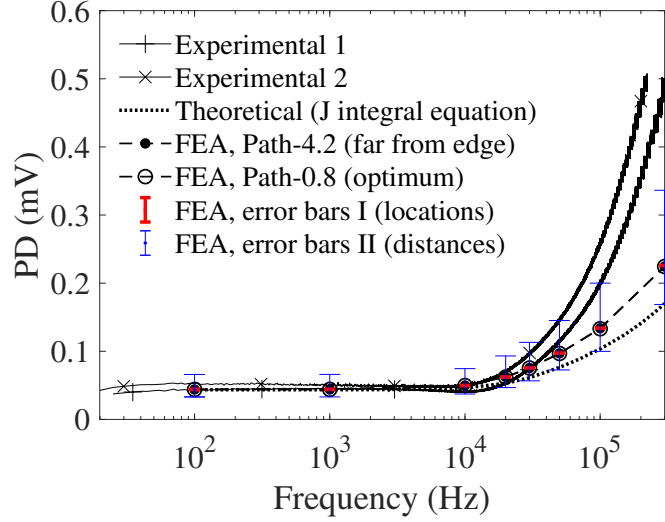
Figure 7.8: Results of PD on the uniform measurement path obtained through various methods for the plain SS316 sample of circular cross-sectional shape.

Indication to Experimental Methodology

Experimental results presented in Fig. 7.1 do not exhibit significant differences between the cross-sectional shapes of SS316 conductors. Such differences have been clearly observed in FEA and are referred as to be current crowding, which will be discussed in detail in Section 7.3. The findings in Case 1 indicate that the measuring methods currently used in the ACPD experiments are incapable of identifying current crowding that occurred in the polygonal SS316 samples with a dimension of 100 mm^2. If the same material of SS316 had been used for specimen manufactured in subsequent experiments involving features, the measurement points (around Path-0.8) would have fallen within the region of non-uniform current distributions caused by the current crowding, meaning measurement uncertainties would have resulted in significant impact on experimental results (similar to the results in Case 1). In other words, it would be difficult to discern whether differences in experimental results between 'featured SS316 samples' were due to various features or measurement uncertainties. Therefore, it was necessary to find a replacement for SS316 to exclude the impact of current crowding, and moreover, the influence of specimen geometry, i.e. to produce stronger skin effect. As a result, the ferromagnetic material of EN1A was selected for the subsequent samples.

The current crowding factor (K_{cc}), which represents the percent increase in R_{ac} of rectangular conductors due to current crowding, was introduced in Section 3.3 as

$$K_{cc} = 1 + 1.2F\left(f\right)\left(e^{\frac{-2.1w_2}{w_1}} + e^{\frac{-2.1w_1}{w_2}}\right) \tag{3.44}$$

where

$$F\left(f\right) = 1 - e^{-0.026p_{sim}} \tag{3.45}$$

$$p_{sim} = \frac{\sqrt{S_0}}{1.2533\delta} \tag{3.46}$$

162

K_{cc} of the square SS316 and EN1A samples were calculated based on above equations, results are shown in Fig. 7.9. Similar to the skin effect in SS316, the current crowding in SS316 is negligible at quasi-DC frequencies but becomes apparent from 1 kHz, causing a maximum increase in R_{ac} of 7% at 300 kHz. Current crowding in EN1A is more significant, which gives 13% of increase in R_{ac} at low frequency of 10 Hz and becomes more prominent as the frequency rises until reaching the limit value of 29% at 1 kHz.
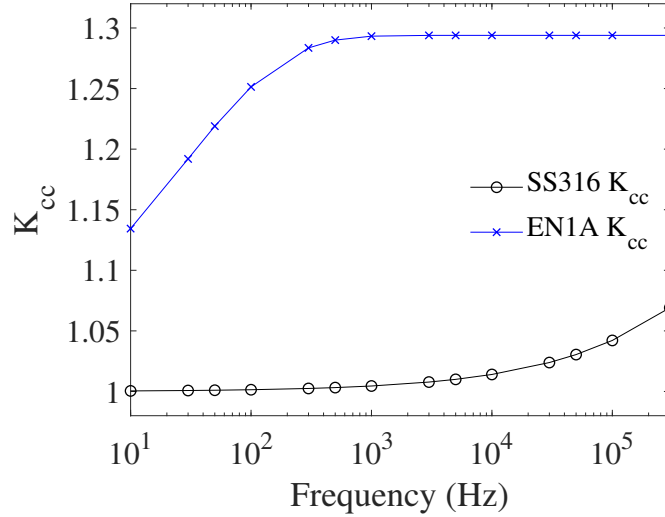
Figure 7.9: Current crowding factor K_{cc} of SS316 and EN1A.

Nevertheless, the pronounced current crowding in EN1A does not affect the current distributions on the conductor surfaces due to the extremely significant skin effect on the surfaces. The factor of skin effect (K_{se}) is introduced to enable comparisons between the magnitudes of the current crowding and skin effect. K_{se} which describes the contribution of resistance increase caused by skin effect can be simplified defined as

$$K_{se} = \frac{S_0}{S_{ac,EAM}} \tag{7.1}$$

The discrepancies between the two factors of the two samples are presented in Fig. 7.10. K_{se} in EN1A does not show a quasi-DC region and rises from 7.6 to 1276 as the frequency increasing, which is considerably greater than K_{cc} in EN1A. Thereby, the current distributions on the EN1A surfaces are dominated by the skin effect and hardly affected by the current crowding.

(a)

(b) Rescaled
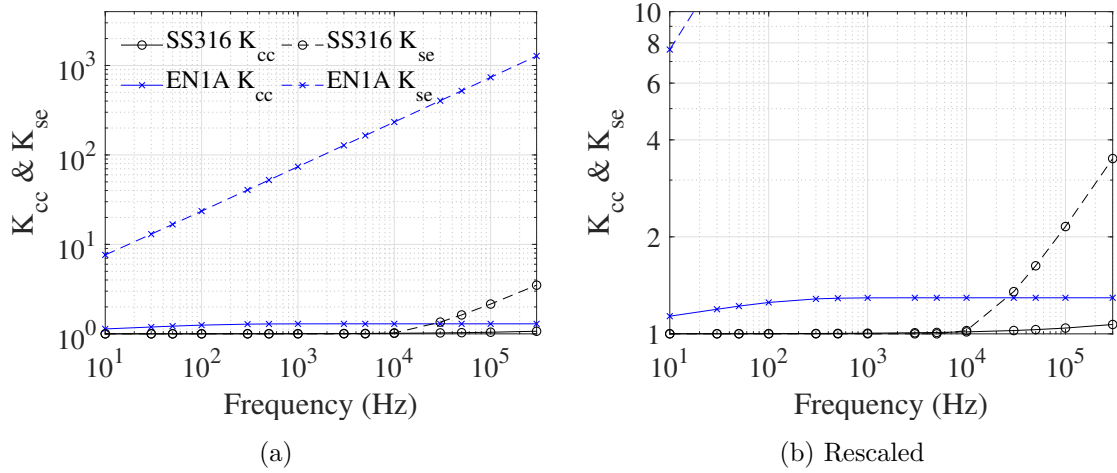
Figure 7.10: Skin effect factor K_{se} of SS316 and EN1A.

Similar conclusions have been noted in FEA. Simulated current fields on the PS SS316 model at 300 kHz and the PS EN1A model at 10 Hz are shown in Fig. 7.11-7.12. The reason for choosing the highest and lowest frequencies (300 kHz & 10 Hz) for the comparison is that these are the only situations that gives close intensity of electromagnetic fields between the two models for frequencies that can be achieved using the Nottingham experimental system, e.g. the minimum δ in SS316 at 300 kHz is 0.77 mm while the maximum δ in EN1A at 10 Hz is 0.34 mm. To comprehensively demonstrate current crowding and skin effect, the maximum magnitudes of current fields (at the edges) on two models are retained in the plotting. In Fig. 7.11-7.12, the skin effect can be clearly observed on both the models through the current decay from the model surfaces on the internal sections. The current crowding on the SS316 model in Fig. 7.11 causes the current to localise on the edge which attenuates not only inwardly but also on the external surfaces. However in Fig. 7.12, the current crowding in EN1A is confined to the inside of the model, resulting in the uniform current distributions on the external surfaces.
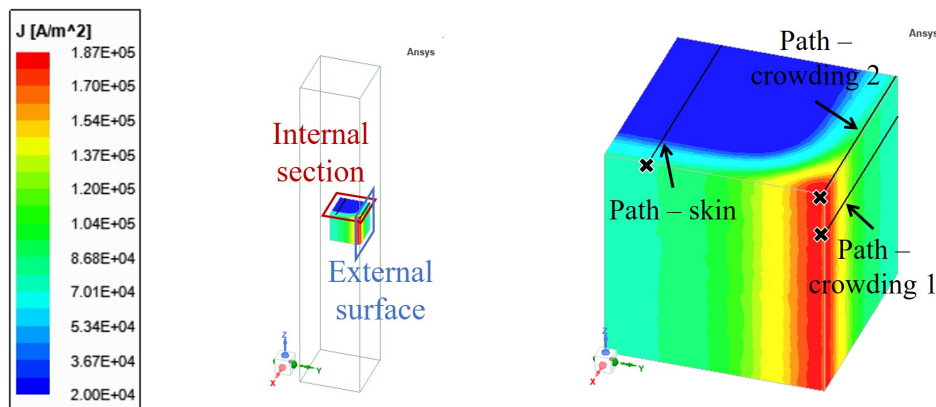
Figure 7.11: FE approximations of the current fields approximated by the PS SS316 models at 300 kHz.

164
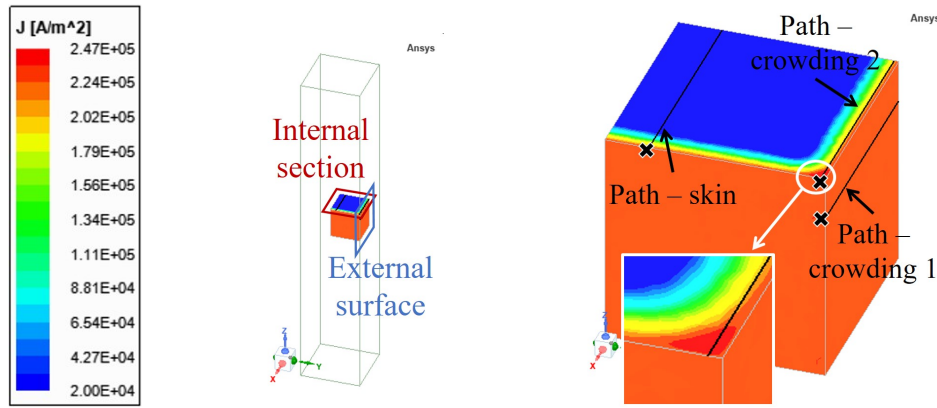
Figure 7.12: FE approximations of the current fields approximated by the PS EN1A models at 10 Hz.

Three paths were created on the internal sections and the external surfaces to illustrate the effects of the two factors on the fields, as marked out in Fig. 7.11-7.12. Fig. 7.13 shows the current fields on the paths starting from the end points on the surfaces/edges (i.e. the crosses in Fig. 7.11-7.12). The Path-crowding 2 are located on the internal sections and very close to the external surfaces with a distance of 0.05 mm. The current fields on the two crowding paths on the SS316 model are almost identical, showing that the current decay with the distances from the surface and edge. In EN1A, the current distributions on the paths on the internal section decrease from the surface/edge due to the skin effect (Path-skin) or the current crowding (Path-crowding 1), while the result of Path-crowding 2 remain constant at 0.247 MA/m^2, which is the maximum magnitude of the whole current field caused by the skin effect, for the whole distance. This suggests that experimental measurements on the square EN1A samples at any frequency should not be affected by current crowding, as it holds for the lowest frequency with the minimum discrepancies between the current crowding and skin effect. Experimental errors due to measurement uncertainties could not be eliminated but was at least reduced by using the EN1A samples and excluding the effect of current crowding.
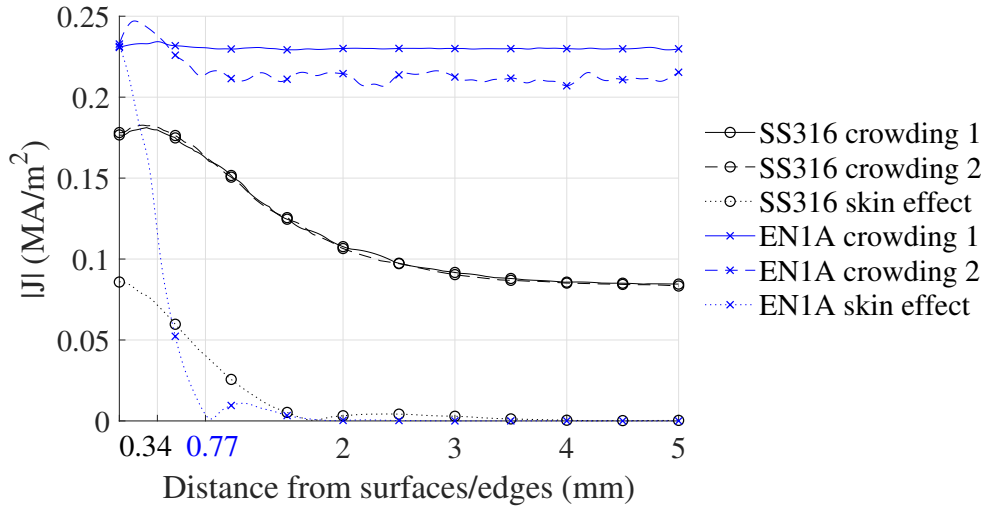
Figure 7.13: Skin effect and current crowding on the SS316 and EN1A models. Paths are marked out in Fig. 7.11.

In addition to the square cross-section at 10 Hz, FEA were applied to simulate the current distributions and ACPD results of EN1A samples of other shapes and at different frequencies. Simulation results of the EN1A models are presented in the same way as given in Fig. 7.3-7.4 for the SS316 models, PDs measured from Path-0.8 & -4.2 are compared between the four cross-sectional shapes with error bars I & II. PDs measured from both the two paths on the EN1A models show similar order of magnitudes to those obtained from Path-4.2 on the SS316 models (in Fig. 7.4). In the absence of current crowding on the sample surfaces, the circular model provides the highest PD measurements, whereas the triangular model gives the lowest values. Furthermore, surface measurements are almost independent of the measurement locations (as indicated by small error bars I in Fig. 7.14a & 7.14c) and proportionally influenced by the measurement distances (as presented by error bars II in Fig. 7.14b & 7.14d).

(a) Path-0.8, effect of measurement locations. (b) Path-0.8, effect of measurement distances.

(c) Path-4.2, effect of measurement locations. (d) Path-4.2, effect of measurement distances.
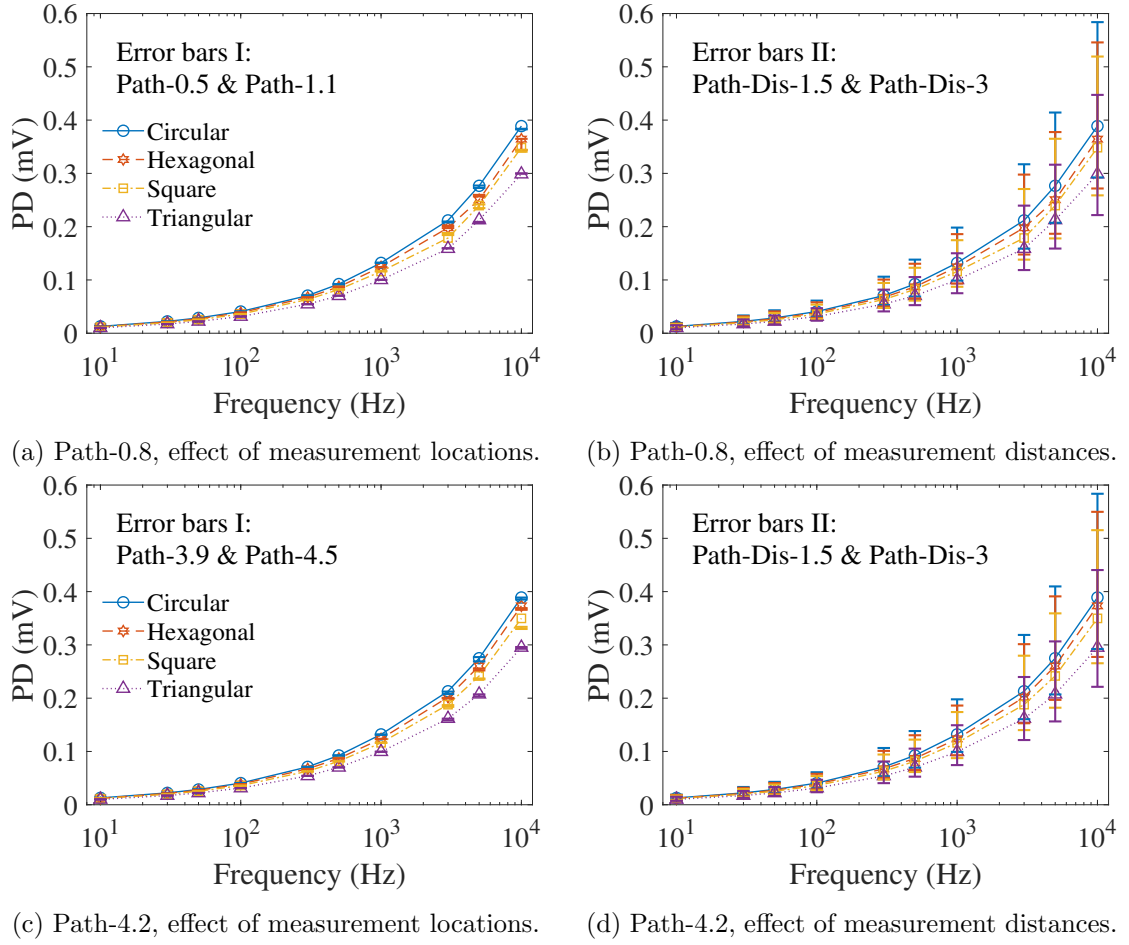
Figure 7.14: FE results of PD of Path-0.8 and Path-4.2 and related error bars I
& II of each approximated by the PS EN1A models.

Subsequent experiments for identifying features only involved square EN1A models. Based on FEA findings discussed above, it can be concluded that ACPD measurements obtained from the featured EN1A sample only contain information about the features and the frequency and are independent of the square cross-sectional shape. In contrast to SS316, the cross-sectional shapes of the EN1A samples do not produce non-uniform current distributions on the sample surfaces, which reduces the influence of measurement uncertainties in experimental results.

7.2.2 Case 2: Various Features with Dissimilar Opening Shapes Contained in Featured Magnetic Samples

The H, N, and NH features in Case 2 have different shapes and dimensions of openings on the sample surfaces. As shown in Fig. 7.15, the opening of the H feature is curved and in a narrow width of 1.06 mm on the surfaces, while that of the N feature is rectangular and more wide to be 4.24 mm in width.

(a) H (b) N (c) NH
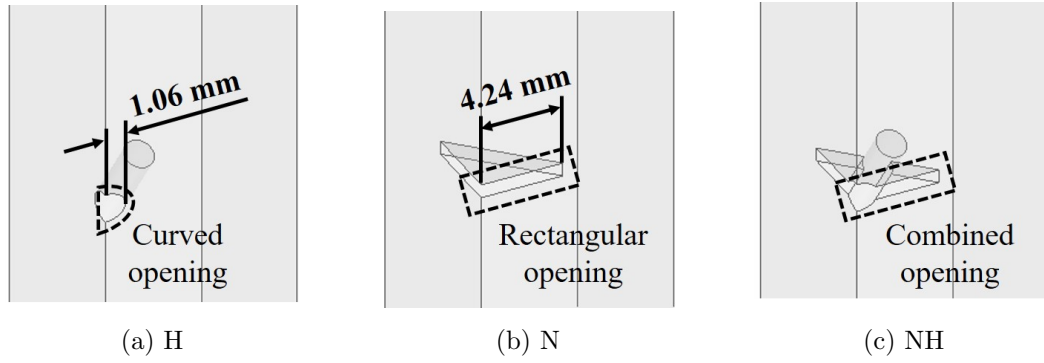
Figure 7.15: Dissimilar openings on the sample surfaces for the H, N, and NH features in Case 2.

Experimental results of PD measured from the three samples at the uniform positions are presented in Fig.7.16. Distinct differences are observed between the samples, and moreover, such differences become more apparent as the frequency increases. PDs measured from the N and NH samples are close and significantly higher than those for the H sample. From 15 Hz, PDs obtained from the N and NH samples are about 0.5 mV, while the low-frequency PDs of the H sample are lower to be 0.32 mV. By sampling the frequency upto 50 kHz, PDs of the H sample reach 0.41 mV, which is smaller than half of results for the other two. By comparing between results of the N and NH samples, two sets of PDs diverge slightly from 1 kHz, which is attributed to the exist of the H drill contained in the NH sample. PDs measured from the NH sample are marginally lower than results of the N sample. At 50 kHz, PDs measured from the N and NH features are about 1.08 mV and 1.02 mV respectively.
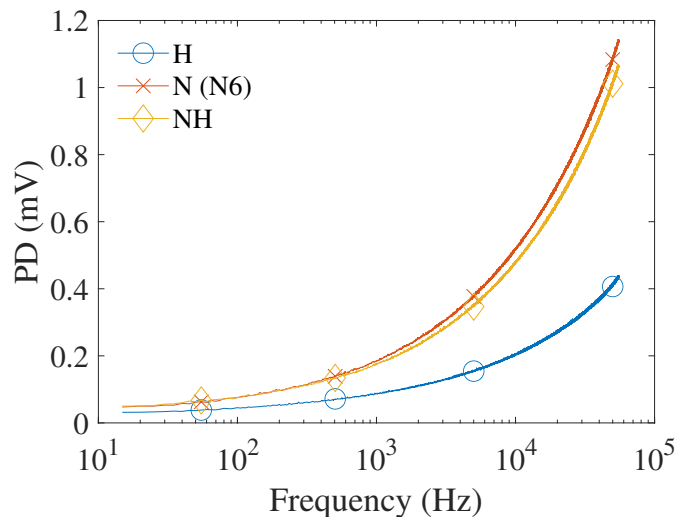
Figure 7.16: Experimental results of PD measured from the uniform positions in 2 mm on the square EN1A samples containing the H, N , and NH features in Case 2.

Based on instructions of FEA presented in Chapter 5, five PS EN1A models

containing various features were built via ANSYS to simulate electric fields produced within and around the samples in Cases 2 & 3. Similar to Case 1, PDs measured from Path-0.8 are assumed as the optimum approximations of experimental results and those obtained from auxiliary paths related to Path-0.8 are used to create error bars I & II. Error bars I contain results from different locations (Path-0.5 and Path-1.1) and bars II are consisted of PDs measured with different distances (Path-Dis-1.5 and Path-Dis-3). Comparisons of experimental and FE results of PD for the samples in Case 2 are demonstrated in Fig. 7.17-7.19. For all the three samples, experimental PDs show good fitness with the optimum FE results based on Path-0.8 and are located inside error bars.
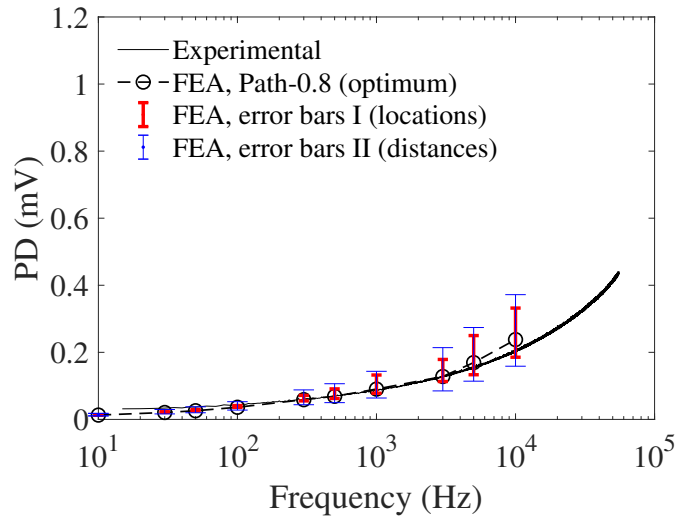
Figure 7.17: Results of PD on the uniform measurement path obtained through various methods for the square EN1A sample containing the H feature.
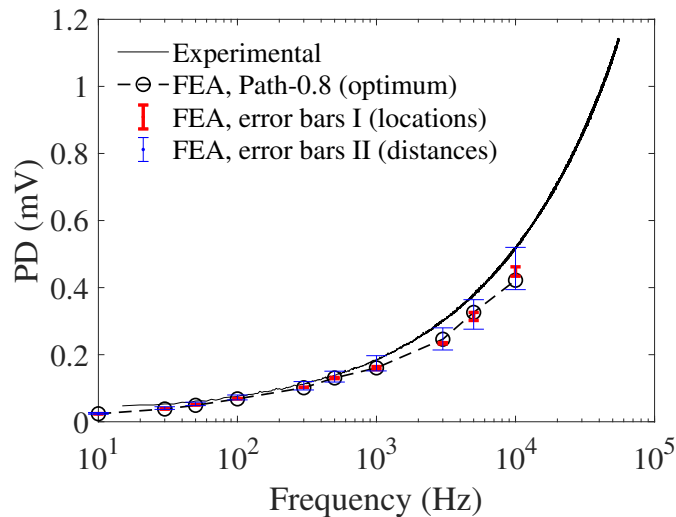
Figure 7.18: Results of PD on the uniform measurement path obtained through various methods for the square EN1A sample containing the N feature.
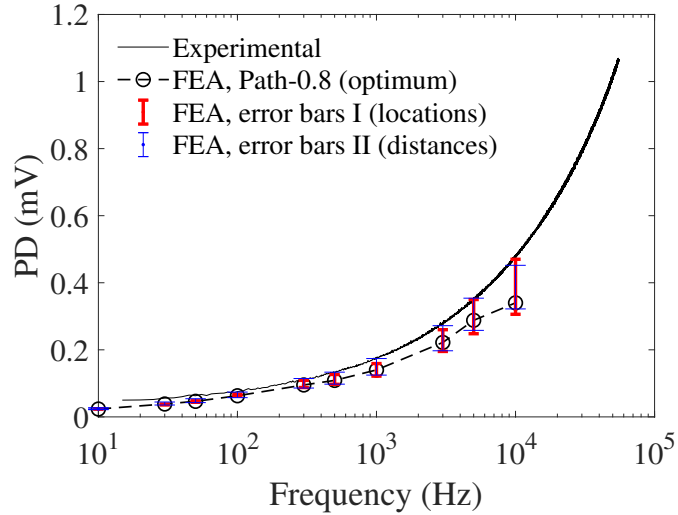
Figure 7.19: Results of PD on the uniform measurement path obtained through various methods for the square EN1A sample containing the NH feature.

Furthermore, error bars I & II in regards to the three features demonstrate significant differences in sizes. To intuitively demonstrate such differences, sizes of error bars were calculated in percent of the optimum approximations of Path-0.8, which are shown in Fig. 7.20-7.21. Error bars I given by the H model rise significantly as the frequency increases, especially in the positive parts based on PDs from Path-1.1. At the highest achievable frequency of 10 kHz, the offsets of ±0.3 mm in measurement locations on the H model introduce differences of -25% to 50% to the optimum approximations of PD. Whereas on the N mode, error bars I have much smaller sizes which cause limited impact on measurements of Path-0.8 for all frequencies from 10 Hz to 10 kHz, giving the sizes of error bars I smaller than ±10%. Error bars I given by the NH model exhibit some similarities to those on the H model that the bars grow with the increasing frequency. Moreover, the positive parts are significant especially at high frequencies, resulting in differences of 40% higher than the optimum approximations at 300 kHz.

(a) Positive parts, Path-1.1.

(b) Negative parts, Path-0.5.
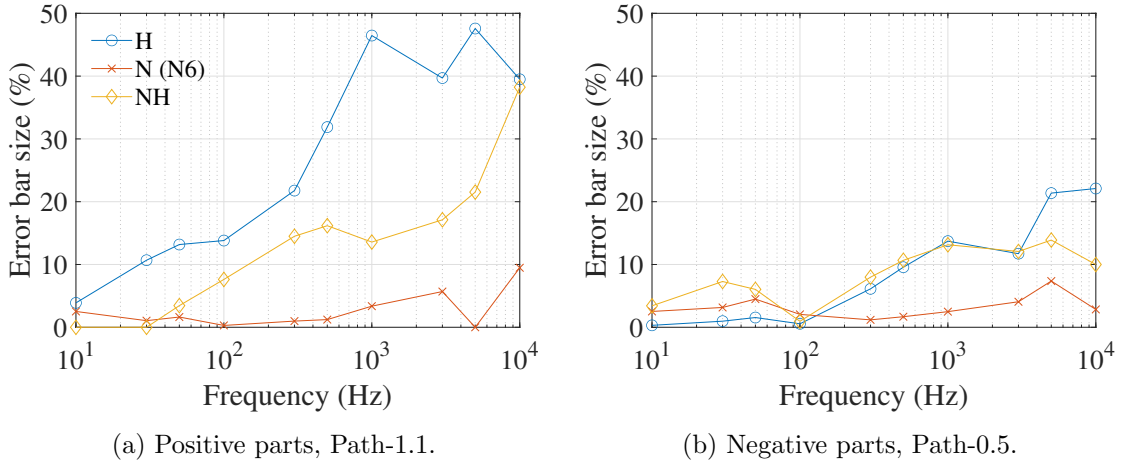
Figure 7.20: Sizes of error bars I related to Path-0.8 (given in Fig. 7.17-7.19) approximated by the PS EN1A models.

(a) Positive parts, Path-Dis-3.

(b) Negative parts, Path-Dis-1.5.
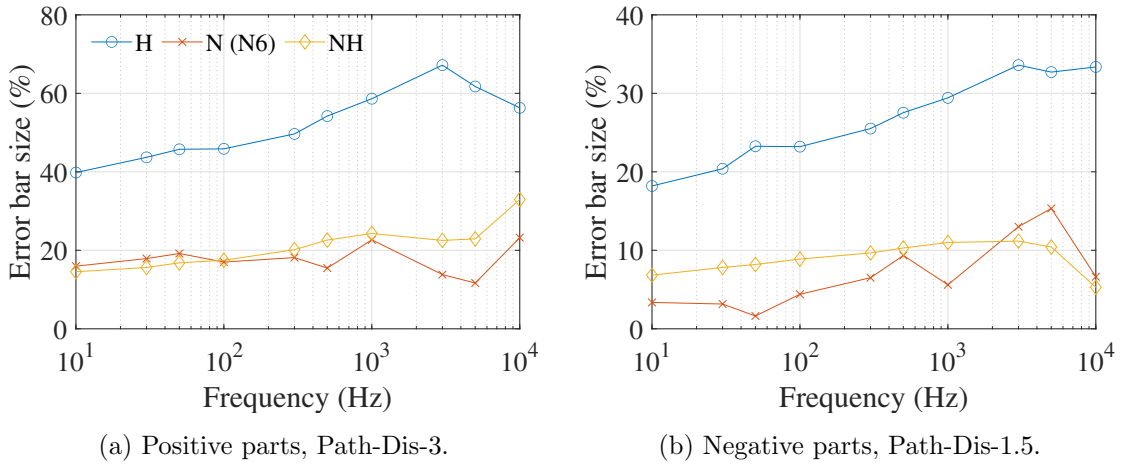
Figure 7.21: Sizes of error bars II related to Path-0.8 (given in Fig. 7.17-7.19) approximated by the PS EN1A models.

Then for error bars II in Fig. 7.21, different measurement distances have great effect on measurements from Path-0.8 on the H model, and furthermore, the effect ascend considerably as frequency increases. Sizes of error bars II given by the H model raise to -35% to 60% at 10 kHz, which are almost twice of those at the beginning of 10 Hz. While on the N and the NH models, sizes of error bars II are limited within smaller extents of -15% to 30% for the whole frequency range.

7.2.3 Case 3: Various Features of the Same Cross-Sectional Area Contained in Featured Magnetic Samples

In Case 3, the openings of the N6, N3, and N1.5 are of the similar shape of rectangular but in various dimensions. As shown in Fig. 7.22, the openings vary from wide to narrow with the widths on surfaces to be 4.24, 2.12, and 1.06 mm respectively. The cross-sectional areas of the three features (as shadowed) are

same to be 9 mm^2.

(a) N6 (N)   (b) N3   (c) N1.5
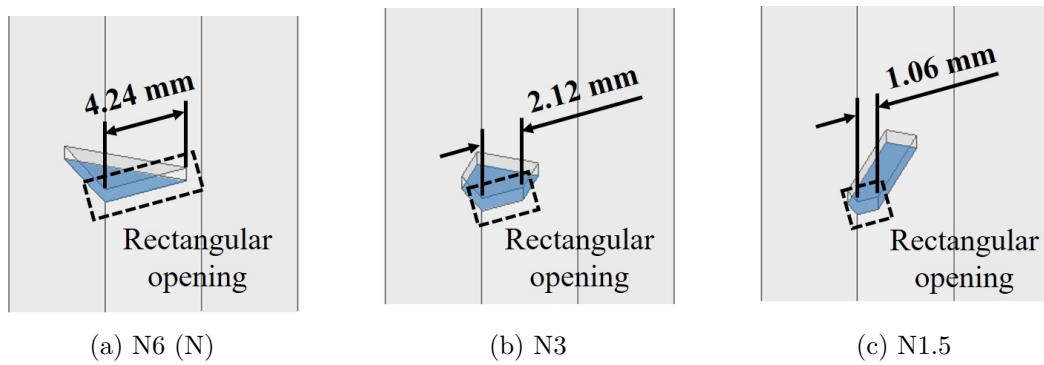
Figure 7.22: Rectangular openings on the sample surfaces for the N6, N3, and
N1.5 features in Case 3.

Experimental PDs measured the three featured samples are shown in Fig. 7.23.
Despite of the same cross-sectional area, ACPD measurements show significant
differences in PDs at high frequencies. The wide and shallow N6 feature has
greatest PDs across while the narrow and deep N1.5 feature has the lowest values.
At 50 kHz, PDs across the N1.5 and the N3 feature reach 0.47 mV and 0.72 mV
respectively.
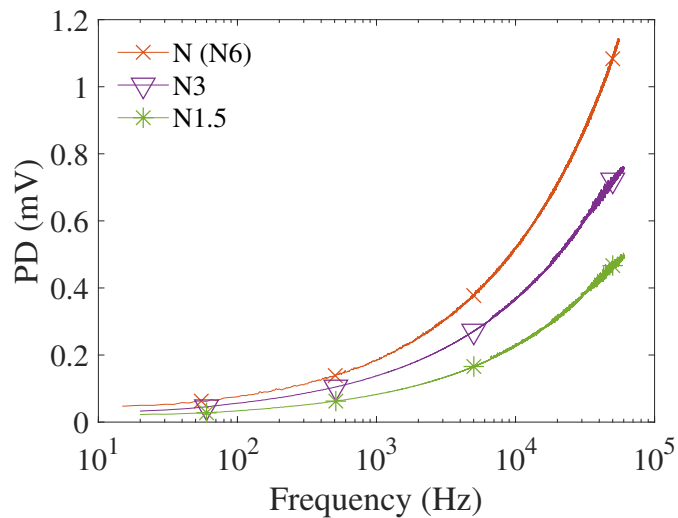
Figure 7.23: Experimental results of PD measured from the uniform positions in
2 mm on the square EN1A samples containing the N6, N3, and N1.5 features in
Case 3.

Comparisons of experimental and FE PDs for the N3 and N1.5 samples are
presented in Fig. 7.24-7.25. Experimental results agree well with the optimum
approximations from FEA for both two samples. Discrepancies between the two
types of results are covered by error bars.
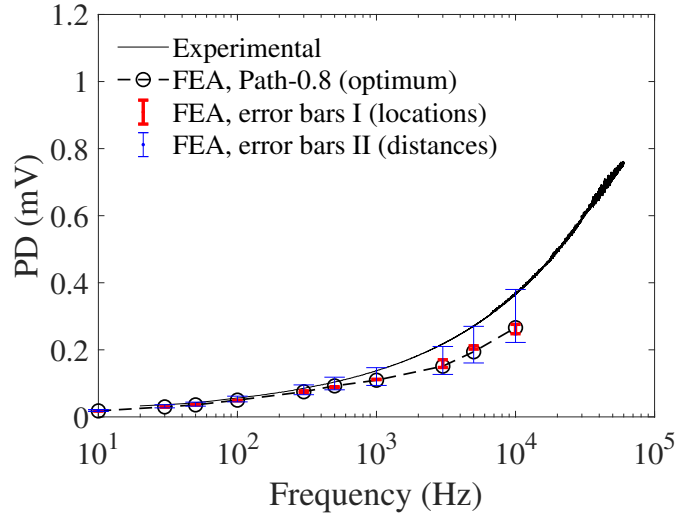
Figure 7.24: Results of PD on the uniform measurement path obtained through various methods for the square EN1A sample containing the N3 feature.
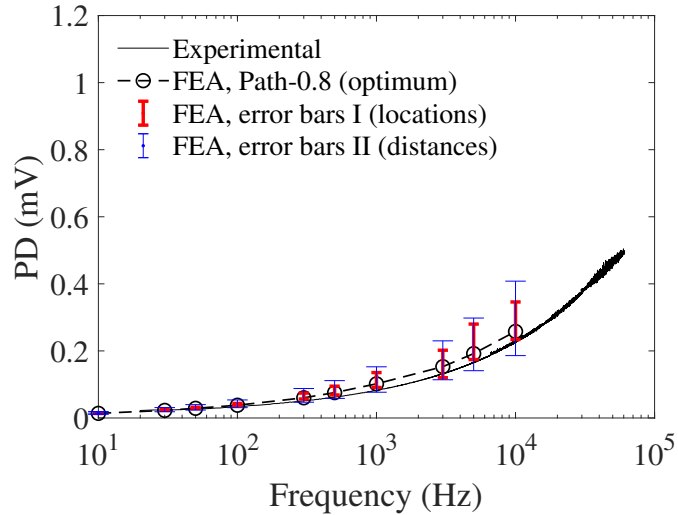
Figure 7.25: Results of PD on the uniform measurement path obtained through various methods for the square EN1A sample containing the N1.5 feature.

Similarly, to clear illustrate effects of measurement uncertainties on ACPD results, sizes of error bars given by the two models are presented in percent of the optimum approximations in Fig. 7.26-7.27. By comparing error bars I on three models, only the positive parts of error bars I predicted by the N1.5 model significantly rise with the increasing frequency, which leads to differences of 40% higher than the optimum results at 10 kHz. On the other two models, the offset of ± 0.3 mm in the measurement locations only have slight impact on measurements, resulting in differences in PDs smaller than $\pm 15\%$ for the whole frequency range. For error bars II in Fig. 7.27, it can be observed that sizes increase as the feature openings become narrower, i.e. the N6 model gives the minimum error bars while the N1.5 model exports the maximum. At 10 kHz, sizes of error bars II on the N6 model is about -15% to 20% of the optimum results, whereas those in the N1.5

model is upto -30% to 60%.

(a) Positive parts, Path-1.1.

(b) Positive parts, Path-0.5.
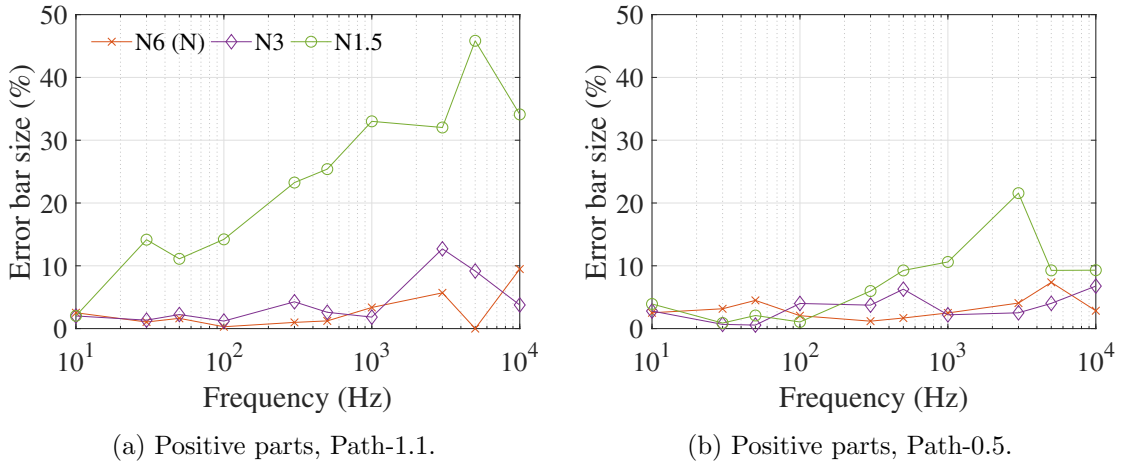
Figure 7.26: Sizes of error bars I related to Path-0.8 (given in Fig. 7.18, 7.24-7.25) approximated by the PS EN1A models.

(a) Positive parts, Path-Dis-3.

(b) Negative parts, Path-Dis-1.5.
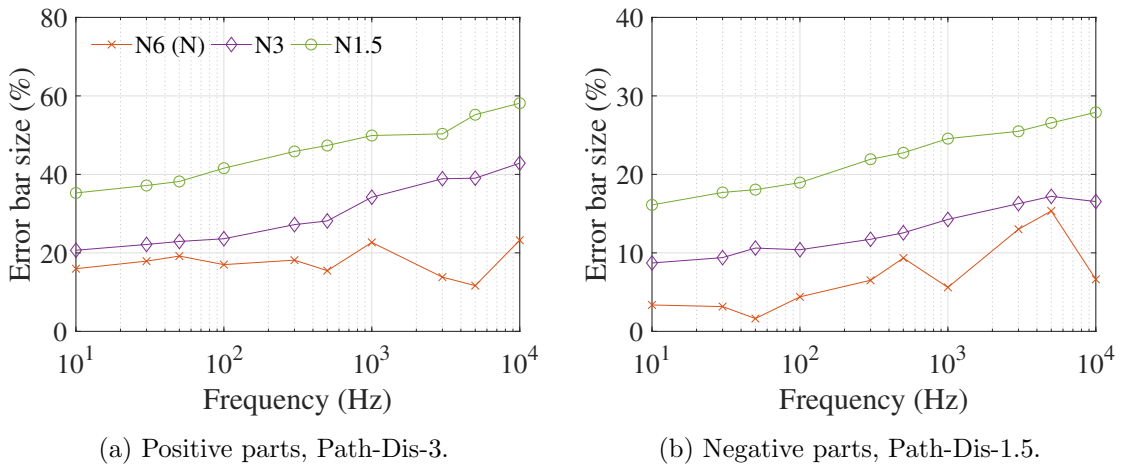
Figure 7.27: Sizes of error bars II related to Path-0.8 (given in Fig. 7.18, 7.24-7.25) approximated by the PS EN1A models.

7.3 Discussions based on Simulated Electric Fields and Current Distributions

In previous sections, experimental results processed from experimentally measured ACPD signals were compared FE approximations for all plain and featured samples. In addition to measure PDs from certain positions on the samples (i.e. conductive paths on models), PS models of ACPD samples were used to produce error bars to demonstrate effects of different measurement locations and distances on PDs from the optimum simulative path. The introduction of error bars provides a justification of deviations between experimental and FE results, i.e. it is

believed to be due to slight uncertainties in welding positions of the PD measurement probes. Error bars are significantly different between the samples, which indicates various influence of the sample cross-sectional shapes and the feature types on the current distributions. This also provide guidance in applying the ACPD experiments, e.g. extra caution is required for measuring across the H feature as ACPD results in this case are highly sensitive to welding errors. Results reported above such as magnitudes of PD from certain positions on the samples and sizes of error bars will be discussed based on the current distributions (and the electric fields) approximated by FEA in the present section. This section will focus on demonstrating the concord between experimental measurements of PD with FE approximations of field solution.

7.3.1 Case 1: Polygonal Cross-sectional Shapes of Plain Samples

ACPD results of the plain SS316 samples in Case 1 will be discussed first. Fig. 7.2a & 7.2c show poor repeatability between Experiments 1 & 2 for the circular and square samples. For the two samples, experimental results obtained from Experiments 2 are constantly higher than those of Experiments 1 from 10 Hz at which ACPD results reflect R_{dc}. The differences in experimental results at low frequencies are independent of the frequency but related to the conductivity, the cross-sectional areas, and the measurement distances. Experiments 1 & 2 were conducted on the same samples by using the same equipments, the only difference was the positions of injection wires and measurement probes which were dismantled and reconnected to the samples in the two experiments. Since the effect of current injection situations on ACPD results are eliminated through FEA in Section 5.4, the repeatability problem is believed to be due to the differences in welding situations of the measurement probes between Experiments 1 & 2. It is assumed that the measurement probes were welded in slightly longer distances on the two samples in Experiment 2 than those in Experiment 1. The limited agreements between experimental and FE results for the circular and hexagonal samples are assumed to be caused by the same reason. It is believed that uncertainties in welding the probes on the two samples were larger than the values indicated by error bars I & II, i.e. more than ±0.3 mm in horizontal positions and -0.25 to +0.5 mm in vertical.

In Fig. 7.3-7.4, FE results of PD measured close to (on Path-0.8) and far from (on Path-4.2) the edges present explicit orders in magnitudes. For results of Path-0.8, the triangular model gives the maximum PDs while the circular model gives the minimum; for results of Path-4.2 an inverse order is exhibited. It suggests that in spite of the same cross-sectional area shared by the samples, the cross-sectional shapes have significant effect on ACPD measurements and current distributions for the non-magnetic material SS316. This impact are clearly demonstrated by the

current fields approximated in FEA, fields at 100 kHz are shown as examples in Fig. 7.28. Path-0.8 and Path-4.2 involved in Fig. 7.3-7.4 are marked out with black lines. Due to the geometrical symmetry of the circular sample and the uniform excitation of surface current, the approximated current field is even everywhere on the surface. Thereby, PDs measured from two paths are almost identical at all frequencies, e.g. the two curves of PD in the Fig. 7.8 are overlapped. For other cross-sectional shapes with edges, the current are consistently concentrated around the edges and less distributed on the surfaces. For example on the triangular model at 300 kHz, PDs of Path-0.8 reaches 0.39 mV and that of the Path-4.2 only gives 0.14 mV. This is the current crowding of AC at high frequencies that was mentioned in Section 3.3.

(a) $\frac{1}{9}$ PS circular model

(b) $\frac{1}{8}$ PS hexagonal model

(c) $\frac{1}{8}$ PS square model

(d) $\frac{1}{4}$ PS triangular model
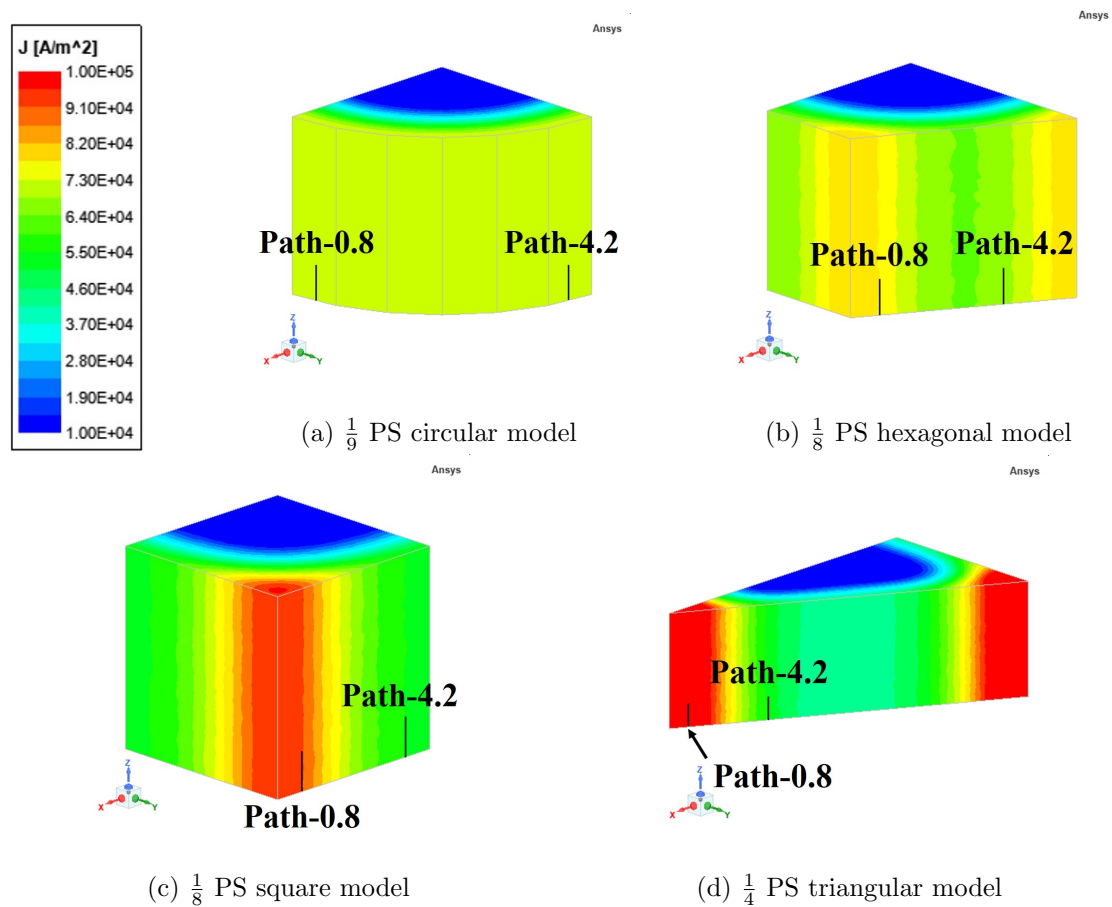
Figure 7.28: FE approximations of the current fields approximated by the PS SS316 models at 100 kHz.

The current fields in Fig. 7.28 also illustrate different error bars for the four cross-sectional shapes. First along the horizontal directions on the model surfaces (i.e. x and y-axis), the current field on the triangular model varies significantly near to the edge and becomes uniform on the surface far from the edge. Whereas in the opposite case of the circular model, the current field is uniform everywhere on the surface as mentioned before. Thereby in Fig. 7.3a & 7.3c, error bars I in the triangular model have the maximum sizes among all models, leading to 17%

of differences to the optimum approximations. While error bars I on the circular model give the minimum sizes and nearly overlap with the optimum results with differences smaller than 0.6%. Error bars I related to Path-4.2 in Fig. 7.4a show limited sizes on all models. This agrees with the field plotting that the current distributions on all models become uniform as moving away to the edges and approaching to the surface center.

Additionally, it is shown that the current fields on four models are consistent along the vertical direction of z-axis. This is because that both the current excitations applied on the top faces and the symmetry boundary conditions assigned on the bottom faces are longitudinal, which enables the fields to remain constant on the vertical direction. As shown in Fig. 7.3b, 7.3d, and 7.4b, error bars II on all models are approximately in the same sizes of -25% to 50% to the optimum results regardless of measurement locations and frequencies. Such differences in PDs are attributed to the measurement distances of 1.5 mm and 3 mm, which are -25% shorter and 50% longer than the optimum distance of 2 mm. In other words, the effects in results caused by uncertainties of the measurement distances is proportional to the magnitudes of the uncertainties. Recalling that the maximum difference of ACPD results occurs in the comparison of PDs close to the edges with strong current crowding (i.e. on Path-0.8) given by the triangular (0.39 mV) and circular (0.22 mV) models at 300 kHz. The maximum difference between two values is 77% (or 44% based on the higher value). However, a minor uncertainty of 0.5 mm in the position of each probe (i.e. 3 mm in the total measurement distance) can result in a significant error in PDs of 50%, which is close to (or larger than) the maximum discernible difference of the ACPD method.

Above discussions of error bars provide indications of conducting ACPD experiments on plain samples of various cross-sectional shapes. In measurements for polygonal samples, it is important to consider the significant impact of measurement locations on experimental results. For example, for the triangular sample in Case 1 that is almost non-magnetic, the measurements on the edge are nearly 3 times larger than those obtained from the surface center at 300 kHz. Furthermore, it was discussed in Section 5.4 that the measurements at the center of SS316 samples are unaffected by the current injections at the ends. Therefore, the measurements of the longitudinal electric fields are directly influenced by the measurement distances, as presented by the consistent error bars II in all SS316 models. To reduce such effect, it is suggested that if the spot welding can be better applied on samples, ACPD signals may be normalised against precisely measured distances between measurement probes to calculate results per unit length. For plain conductors made of other materials and dimensions or sampled at different frequencies, the end effects of current input is suggested to be investigated by numerical methods such as FEA before considering the proportional impact due to uncertainties of measurement locations.

The introduction of theoretical approximations of PD based on the method of

current integral equation not only provides rough comparisons to experimental and FE results, but also indicates the contrast between intensities of current crowding and skin effect. The theoretical approximations were obtained by using the total current of 3 A, which supposes the current to be uniformly distributed within the conductors and on the conductor surfaces. Thereby, both the skin effect and current crowding were ignored in the approximations. On the circular and hexagonal models with no/weak current crowding, the theoretical solutions are consistently smaller than experimental and FE results. This is because that experimental and FE PDs were measured on the sample surfaces at where the current density is the maximum. While on the triangular and square models, the theoretical results are higher than the surface measurements of Path-4.2. It suggests that the current crowding occurring on these two cross-sectional shapes at the frequency of 100 kHz are prominent and even disturb the skin effect on surfaces. This conclusion can be associated with the findings in Section 7.2.1. In ferromagnetic conductors of EN1A, the skin effect consistently dominates the current distributions on surfaces for all frequencies. However, in non-magnetic conductors of polygonal cross-sectional shapes such as the triangular SS316 sample, the current crowding have stronger influence on the current fields on surface than the skin effect at low frequencies.

Nevertheless, ACPD results for various cross-sectional shapes obtained in Experiments 1 & 2 do not shown obvious differences between the samples. This is believed to be due to uncertainties in the welding situations of PD measurements probes especially the measurement distances. Based on FEA, the ACPD method is verified with the capability of distinguishing between various cross-sectional shapes by taking the advantage of the current crowding. The current are consistently concentrated near the sample edges at high frequencies, moreover, the concentrations become more significant as a polygonal cross-sectional shape varies from quasi-circular to triangular. By analysing the current fields and error bars produced in FEA, it is observed that the ACPD measurements with 2 mm in distance on the SS316 samples in dimensions of 55 mm $\times$ 100 mm^2 are greatly affected by measurement uncertainties. If this capability is desired to be verified with experiments, a high-precision approach of signal measurements will be required.

7.3.2   Case 2: Features of H, N, NH

In comparisons shown in Fig. 7.17-7.19, experimental PDs measured from the H, N, and NH samples are all located within error bars approximated by respective models. It suggests that discrepancies between experimental and FE results of PD are due to inevitable uncertainties in welding such as offsets in locations of the measuring probes and varying distances between the pairs of probes. Furthermore, different behaviour of error bars in Fig. 7.17-7.19 indicate that electric fields gen-

erated in the featured models are significantly affected by the feature geometries. For clear explanation, the current distributions around three features at 1 kHz approximated by FEA are displayed in Fig. 7.29-7.31. The optimum simulation path (Path-0.8) and two auxiliary paths constituting error bars I (Path-0.5 & -1.1) are marked out with black lines near the sample edges. The other two auxiliary paths defined for error bars II (Path-Dis-1.5 & -Dis-3) are partly coincided with Path-0.8. To avoid unclear demonstration, these two paths are not marked out here but are clearly shown in Fig. 5.34b. Some similar characteristics of the current distributions around three features are observed: (1) the current fields always sink around the sample corners; (2) but concentrate near the feature roots; (3) dense current distributions around the feature roots descend rapidly towards the features but gently towards the plain surfaces.
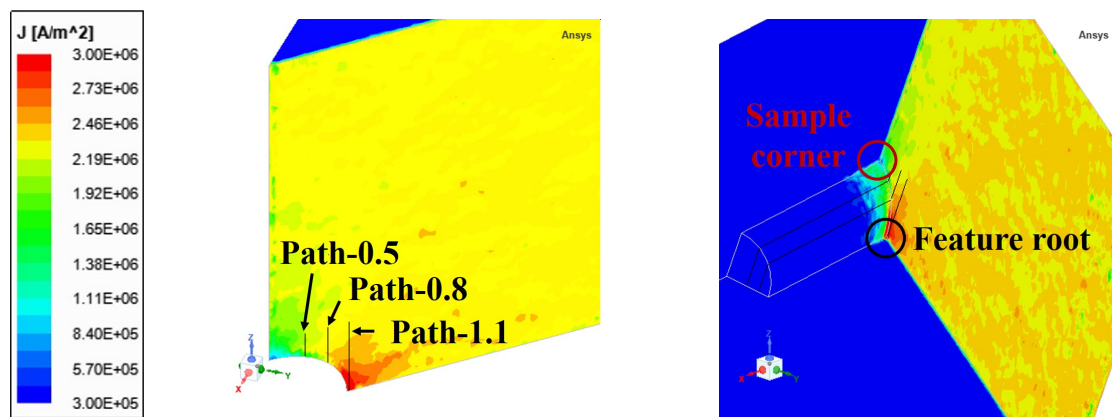
Figure 7.29: FE approximations of the current fields approximated by the PS EN1A model containing the H feature at 1 kHz.
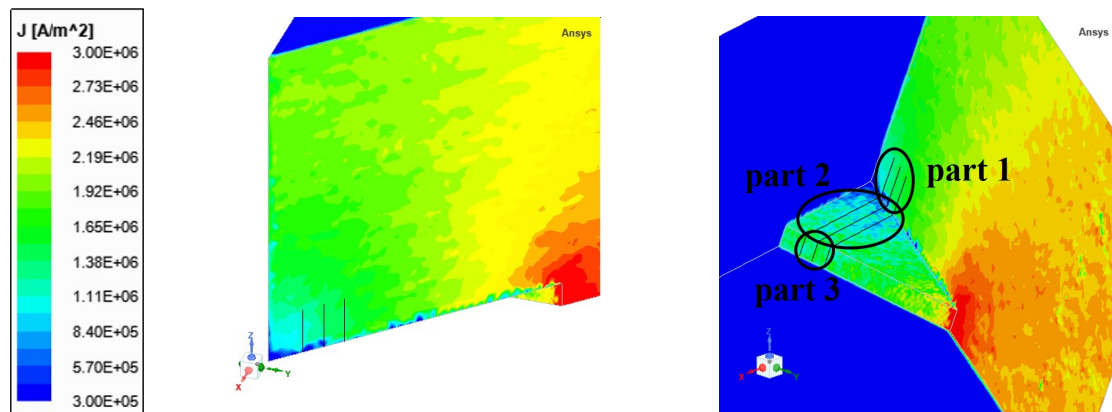
Figure 7.30: FE approximations of the current fields approximated by the PS EN1A model containing the N feature at 1 kHz.

179
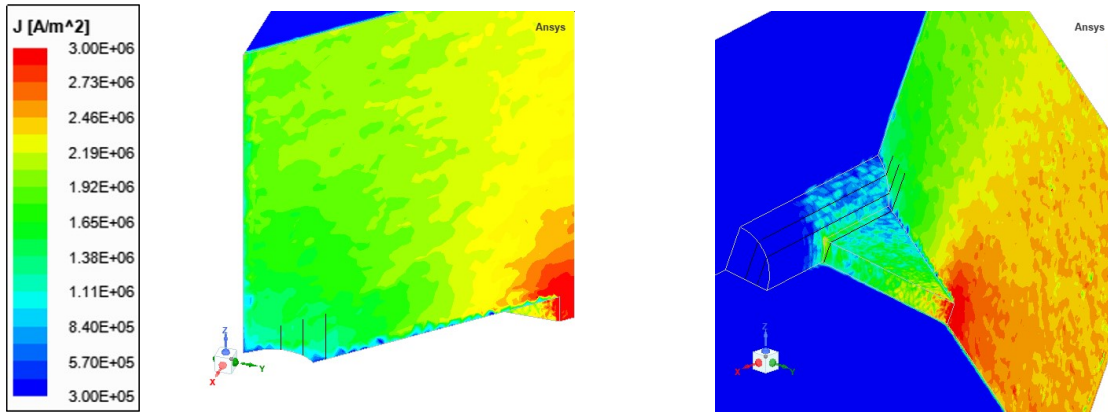
Figure 7.31: FE approximations of the current fields approximated by the PS
EN1A model containing the NH feature at 1 kHz.

Since the conductive paths across features on the featured models are more complex than paths on plain surface on the flawless models, the electric fields along the featured paths are extracted from field plotting in Fig. 7.29-7.31, as shown in Fig. 7.32-7.34. The featured paths are divided into three segments, which are marked out in Fig. 7.30: the vertical distance located on the sample surfaces ('part 1'), the horizontal distance penetrating into the depth of the samples with the features ('part 2'), and the vertical distance on the innermost face of the features ('part 3'). Path-0.5, -0.8, and -1.1 have different total lengths, e.g. on the H model, Path-1.1 is in 1 mm long and much shorter than the other two paths following the feature of about 5.5 mm. To uniformly display results of three paths with a unit distance, magnitudes of electric fields along paths are normalised against respective total lengths. Thereby, integrated areas under the curves of electric fields in Fig. 7.32-7.34 are not the real PDs integrated on the paths. For instance, PDs measured from three paths at 1 kHz around the H feature are 0.035, 0.042, and 0.059 mV, but not as shown in Fig. 7.32 that the area under the curve of Path-1.1 is several times greater than those of the other two.
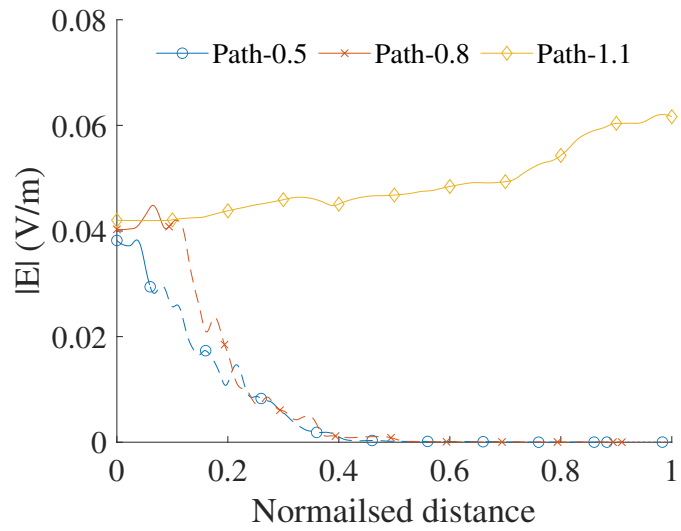
Figure 7.32: FE approximations of the electric fields on conductive paths in the H model. Solid lines: part 1; dash lines: part 2; dash-dotted lines: part 3.
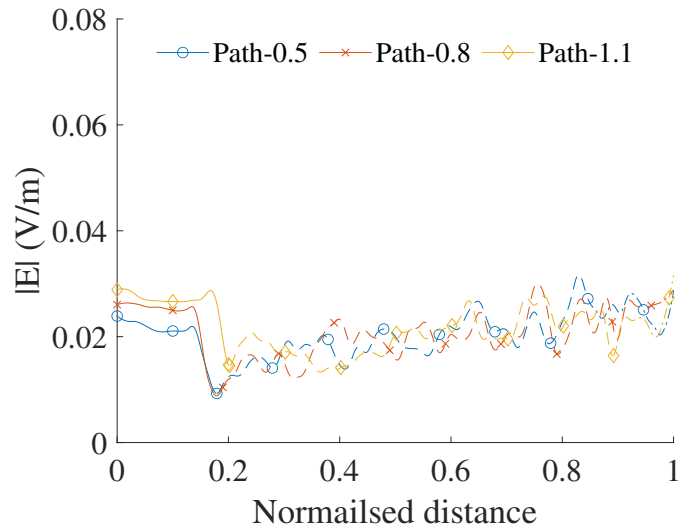
Figure 7.33: FE approximations of the electric fields on the conductive paths in the N model. Solid lines: part 1; dash lines: part 2; dash-dotted lines: part 3.
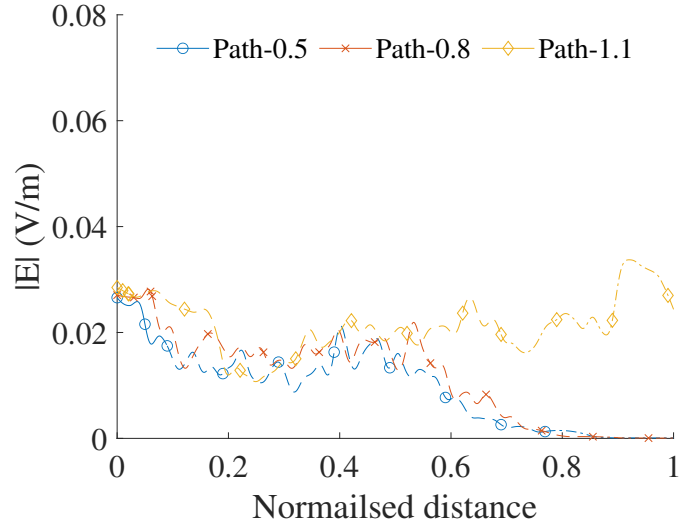
Figure 7.34: FE approximations of the electric fields on the conductive paths in the NH model. Solid lines: part 1; dash lines: part 2; dash-dotted lines: part 3.

In results of the H sample presented in Fig. 7.17, the positive parts of error bars I (based on Path-1.1) are significant and higher than the optimum approximations for 50% at 10 kHz. Although Path-1.1 on the H model has the shortest integrating distance by comparing to Path-0.5 & -0.8, Path-1.1 has the maximum current distributed throughout and provides the highest PDs much greater than the other two paths. This is because Path-1.1 is beyond the feature root at 1.06 mm to the sample edge, thus the full path is situated on the sample surface and passes through the current concentration area near to the root. On the other side, the current distributions on Path-0.5 & -0.8 that extend into the depth of the feature are greatly different. Since the skin effect is significant inside the EN1A samples, and moreover, the H feature causes minor disturbances in the current distributions. The current around the H feature is strongly governed by the skin effect, i.e. mainly concentrated near to the surface and hardly permeates into the depth of the samples, which can be clearly seen on the right of Fig. 7.29. Thereby, the total PDs of Path-0.5 & -0.8 are mainly contributed by part 1 on the surface and the small distances near to the surface of part 2. The remaining parts of the paths have few current distributions, e.g. PDs on part 3 account for less then 0.3% of the total PDs on these two paths. Therefore, PDs from Path-1.1 in the shortest total length are much greater than results from the two featured paths.

For the N feature, the observation region confined by the three paths (i.e. from 0.5 to 1.1 mm to the sample edge) are far from the feature root at 4.24 mm to the edge. Consequently, the electric field inside this region is relatively uniform in the horizontal direction and the magnitudes of the fields on three paths are similar for the whole normalised distance, as presented in Fig. 7.30 & 7.33. This is also indicated by the minimum error bars I of the N feature in Fig. 7.20, causing differences in PDs smaller than ±10% for the whole frequency range.

The current field around the NH feature is distributed in a hybrid way com-

bining the disturbances of the H and N features. It is similar to the H model that the fields on Path-0.5 & -0.8 on the NH model recede and vanish to 0 as the normalised distance increases, i.e. as approaching to the innermost faces of the features inside the samples. However, results on the NH model are greater than those on the H model since the N feature brings in more current distributions on the curved surfaces of the H feature. This difference can be clearly observed by contrasting between field plotting in Fig. 7.29 & 7.31. In Fig. 7.34, the curve of results of Path-1.1 is close to the other two curves in the first half distance, but rises in the second half in which the other two curves gradually reduce to 0. This is because Path-1.1 is beyond the root of the H feature, and thus measures the field on the featured surfaces of the N feature rather than penetrating deeply into the sample with the H feature like Path-0.5 & -0.8. Additionally, Path-1.1 is affected by the slight current concentration near to the root of the H feature.

Above discussions of the measurement locations are related to variations of the electric fields in the horizontal direction, while the impact caused by the measurement distances is attributed to changes of the fields in the vertical direction. The two auxiliary paths (Path-Dis-1.5 & -Dis-3) are different to the optimum path (Path-0.8) in part 1, remaining parts on the featured surfaces are coincident. Thereby, only the electric fields on part 1 of the longest path given by three models are presented against real distances and is displayed in Fig. 7.35. Fields on part 2 & 3 of two auxiliary paths are identical to fields on Path-0.8 shown in Fig. 7.32-7.34, hence these results are not presented to avoid repetitive presentation. In Fig. 7.35, the H model is taken as an example to illustrate the measurement regions of the three paths. The part 1 of the longest Path-Dis-3 measures from the feature edge (at 0.49 mm to the center of the sample) to a position at 1.5 mm to the center. While the part 1 of the shortest Path-Dis-1.5 defines a distance from the feature edge to a closer position at 0.75 mm to the center.
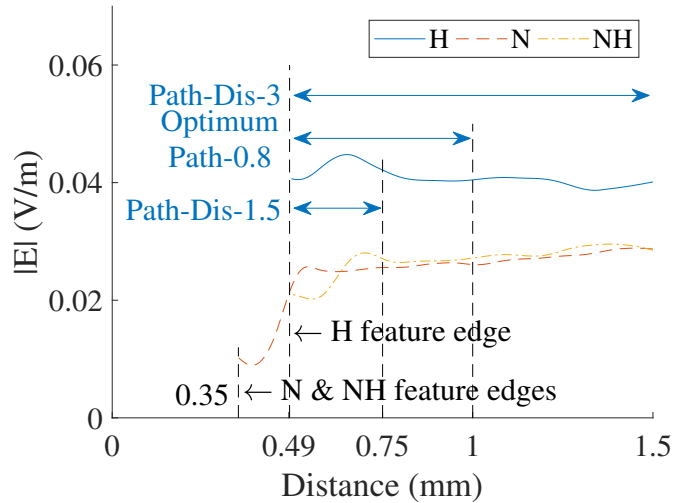
Figure 7.35: FE approximations of the electric fields on part 1 of Path-Dis-3 (starting from 1.5 mm above to the center of the sample) in the EN1A models in Case 2.

Comparing to horizontal variations of the electric fields in Fig. 7.32-7.34, vertical variations in Fig. 7.35 are relatively uniform on the sample surfaces above the features, i.e. on part 1. Because these paths are far from the roots of the N feature but close to the root of the H, magnitudes of the electric field above the H feature are roughly constant at about 0.04 V/m and greater than those for the N and NH. Moreover, the total PDs of paths across the H feature are mainly contributed by the part 1, thus variations in the length of part 1 cause significant differences in the total results. These are the reasons for the largest error bars II in the H model shown in Fig. 7.21. On the N and NH model, the electric fields remain steady from 1.5 mm to the center and drop near the feature edges. It is due to the diffusion of current subsidence near the sample corners, which can be clearly seen in Fig. 7.30.

In a summary, ACPD signals measured across the H, N, and NH features from the uniform positions show concordance with the current/electric fields simulated by FEA. It is shown that PDs are affected by the measurement locations and distances to varying degrees for different features. For example for the H sample, experimental results are particularly sensitive to the measuring situations due to the current concentration near the feature root. The ACPD method is verified with the capability of differentiating between the electric fields generated around features with distinct opening geometries like the H and N features. The similarity between results of the N and NH features is believed to be due to weak disturbance given by the H feature around the observation region.

7.3.3   Case 3: Features of N6, N3, N1.5

In Fig. 7.24-7.25, good comparisons are shown between experimental and FE results for both the N3 and N1.5 samples in which all experimental results of PD are located within error bars. Field solutions approximated by the three featured models are presented in Fig. 7.36-7.39.
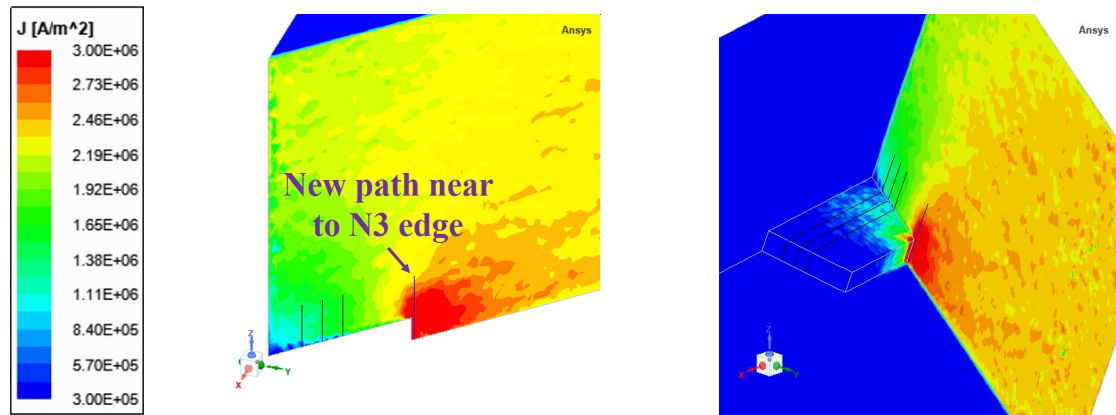
Figure 7.36: FE approximations of the current fields approximated by the PS EN1A model containing the N3 feature at 1 kHz.
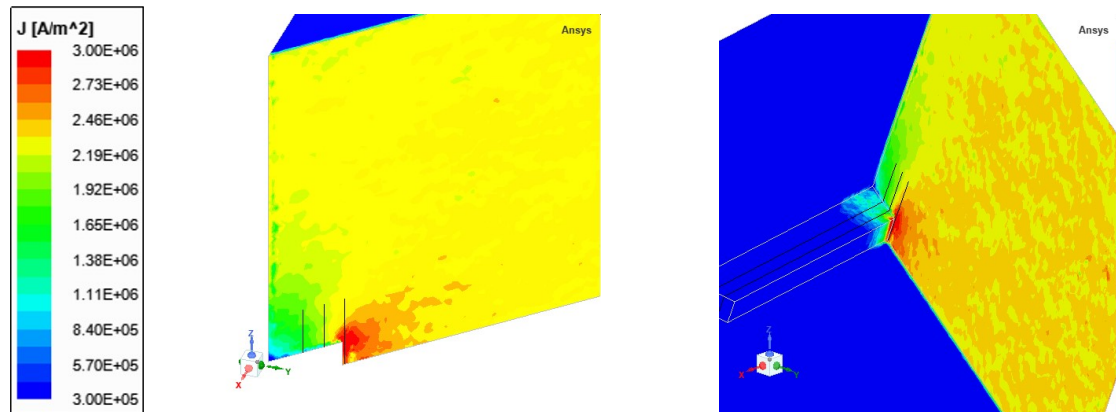
Figure 7.37: FE approximations of the current fields approximated by the PS EN1A model containing the N1.5 feature at 1 kHz.
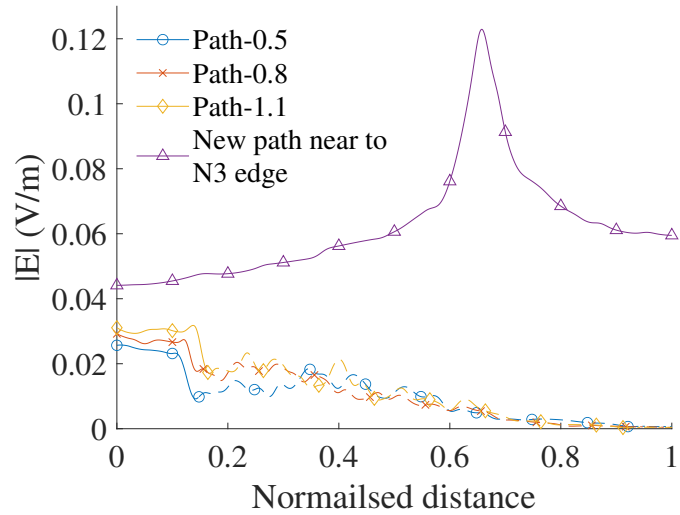
Figure 7.38: FE approximations of the electric fields on the conductive paths in the N3 model. Solid lines: part 1; dash lines: part 2; dash-dotted lines: part 3.
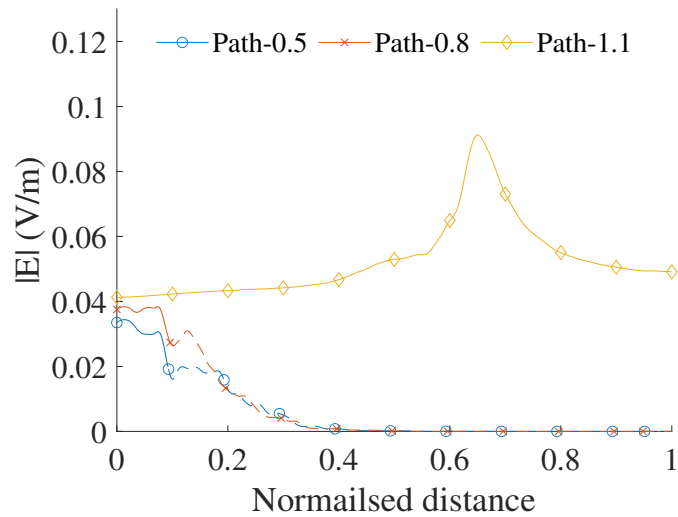
Figure 7.39: FE approximations of the electric fields on the conductive paths in the N1.5 model. Solid lines: part 1; dash lines: part 2; dash-dotted lines: part 3.

With respect to error bars I, it was pointed out in the earlier section that the measurements on the N1.5 model are highly sensitive to positive uncertainties in the measurement locations, which results in a difference of 40% in PDs at 10 kHz. The negative parts of error bars I on the N1.5 model and both the positive and negative parts of error bars I on the other two models show limited divergence (smaller than ±10%) to the optimum results. These conclusions agree with the results of the field solutions shown in Fig. 7.33, 7.38-7.39. In Fig. 7.39, the field on Path-1.1 across the N1.5 feature is apparently different to those on the other two paths. While for the other two models of N6 and N3, field results on three paths are similar to each other and almost overlap for the full distances. This is because Path-1.1 on the N1.5 model is located beyond the feature root at 1.06 mm to the sample edge, which is similar to the situation on the H model. Thereby, the

full path of Path-1.1 passes through the current concentration region on the model surface and contributes to significant positive parts for error bars I. Whereas on the other models, the observation region is far from the features roots (at 4.24 mm and 2.12 mm the N6 and N3 features), therefore, the electric fields within the region are less affected by the current localisations and more uniform.

Additionally, in Fig. 7.39, the electric field on Path-1.1 on the N1.5 model reach the vertex at 0.65 of the normalised distance where is the upper corner of the N1.5 root. To figure out whether there is a similar localisation around the N3 feature, a new conductive path close to the N3 root was defined in the model as marked out in Fig. 7.36. The new path is at 0.04 mm to the root of N3, which is in the same distance between Path-1.1 and the root of N1.5. The electric field along the new path demonstrates similar increase around 0.65 in Fig.7.38. It suggests that the current concentrations near the feature roots are uneven along the vertical edges but localised at the upper corners. This can be assumed as the current crowding around the concave corners of the features, which is similar to the current crowding around the convex corners of polygonal cross-sectional shapes in Case 1.

Then to compare error bars II between the three models, the measurements across the N1.5 feature are the most sensitive to uncertainties in the measurement distances, resulting in differences of -30% to 60% to the optimum results at 10 kHz. This is due to the same reason as for the H feature, the observation region at 0.5-1.1 mm to the edge is close to the feature root on where the current focuses, the electric field is highly asymmetric and hence the measurements within the region are significantly influenced by horizontal and vertical uncertainties in the measurement locations. Vertical variations of the electric fields at 0.8 mm to the sample edges on the three models are shown in Fig. 7.40. Similar to results in Case 2, the electric fields around the three features are distributed in a relative uniform way in the vertical direction. Due to the low densities of the current around the sample corners, the electric fields drop as approaching to the notch edges, which conforms to field plotting given in Fig. 7.30, 7.36-7.37.
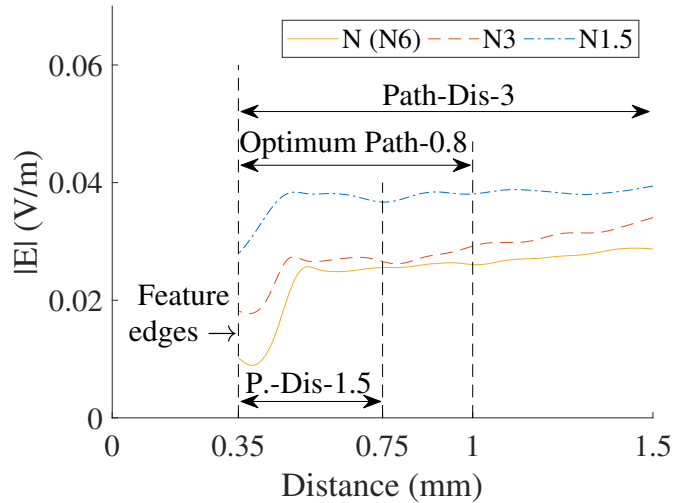
Figure 7.40: FE approximations of the electric fields on part 1 of Path-Dis-3 (starting from 1.5 mm above to the center of the sample) in the EN1A models in Case 3.

In Fig. 7.33, the electric fields on three paths on the N6 model vary around 0.02 mV for the whole lengths of the paths. While in results of the N3 and N1.5 models shown in Fig. 7.38-7.39, the electric fields decrease to 0 as the normalised distances increase, i.e. as going deep into the samples. The electric fields vanish more rapidly in the N1.5 model. It indicates the effect of different feature geometries on the electric fields in the vicinity, i.e. the attenuation of current distributions. To clearly demonstrate this point, PDs of parts 1-3 of Path-0.8 on three models are separately measured and contrasted, as given in Fig. 7.41. Results on part 1 on three models were already compared and discussed above. PDs of parts 2 & 3 on the N model are considerable because the skin effect is interrupted by the wide feature opening and the current around the feature is distributed on all featured surfaces. PDs of these two parts reduce as the opening become narrower, e.g. results of part 3 on the N3 and N1.5 models only contribute to a portion less than 1% to the total PDs. The conclusion summarised for the H feature is further suggested here. The narrow features with small opening widths on surfaces, regardless of the shapes (e.g. a circular drill or a rectangular notch), have less impact on the current surrounding the features, leading to limited penetrating depths of the current. The detection of the ACPD method for inner situations in the depth of narrow features is thus restricted by inadequate information offered by few current distributions.
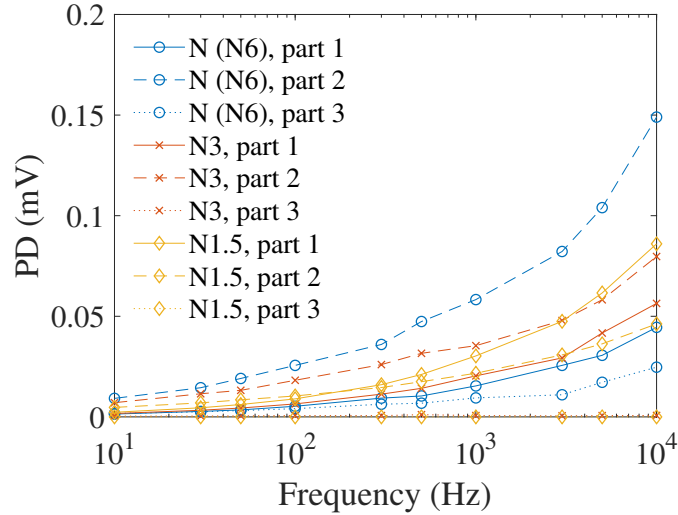
Figure 7.41: FE approximations of PD on 3 parts of Path-0.8 in the EN1A models in Case 3.

The clear differences between experimental PDs measured across the N, N3, and N1.5 features suggest that the ACPD method is able to distinguish between these features even the same cross-sectional area is shared. The detection capability is due to that the distinct opening geometries on the surfaces have various disturbances to skin effect around the features. The current distributions are thereby penetrated into the samples with varying degrees, leading to different results of PD measured across the features. The current penetration depth, i.e. the limitation of detection, is significantly dependent on the opening width. The ACPD method is supposed to be unable to identify inner situations of features beyond the penetrate depth such as the depths due to the lack of current distributions.

7.4 Conclusions

In Case 1, eight sets of experimental results measured from the four SS316 samples were compared based on the cross-sectional shapes. Experimental PDs between various cross-sectional shapes are similar and do not show clear differences, which is believed to be due to the uncertainties in welding of PD measurement probes. By comparing experimental and FE results, good agreement is achieved for the triangular and square samples. While for the hexagonal and circular samples, limited fitness is obtained in which experimental results are located beyond the error bars containing uncertainties of ± 0.3 mm in horizontal positions and -0.25 to +0.5 mm in the vertical positions for each probe. These are assumed to be due to the same reason that actual measurement uncertainties happened on the two samples are considered to be larger the values covered by the error bars.

According to FEA, the capability of the ACPD method of identifying the cross-sectional shapes of the non-magnetic SS316 samples has been validated. By measuring PDs from the uniform positions close to the edges, ACPD results demon-

strate obvious differences between the shapes. At 300 kHz, the highest PD read from the triangular model is 77% higher than that given by the circular model (0.39 mV and 0.22 mV in 2 mm). FE results read from another uniform position far from the edges also show distinct discrepancies between different cross-sectional shapes. The highest result on the circular model is 57% higher than the lowest value from the triangular model (0.22 mV and 0.14 mV in 2 mm). Different results of PD measured from the two positions indicate different sensitivities to uncertainties in the measurement locations, and moreover, uneven current distributions due to polygonal cross-sectional shapes. Measurements of PD close to the edges are more affected by the measurement locations, especially on the triangular model, the ±0.3 mm of offsets in the location lead to a difference in PDs of 17% at 300 kHz. Thereby for applying the ACPD experiments on plain samples, it is suggested to measure near the sample edges due to the maximum magnitudes of results. Meanwhile, the significant sensitivity to the measurement locations in PDs necessitates high-precision for measuring ACPD signals.

The identification capability of the ACPD method is attributed to the current concentrations near the sample edges (i.e. the current crowding) accompanying with the skin effect, which is clearly observed in the fields approximated by FEA. Due to the symmetrical geometries of all cross-sectional shapes and the uniform current injections around the measurement region at the center of samples, the electric fields simulated by FEA are constant in the longitudinal direction, and thus the measured PDs are proportional to the measurement distances. It suggests that minor uncertainties in the distances between the pairs of probes can result in significant errors in ACPD measurements, e.g. 0.5 mm of errors in the vertical position for each probe give rise to a differences in experimental results of 50%. It may be solved by normalising the ACPD results by the measurement distances to calculate results per unit length for the cases in which the spot welding can be applied and hence the distances between probes can be precisely measured.

Therefore, FEA for various cross-sectional shapes validate that the ACPD method benefit from the current crowding and hence is capable of distinguishing between non-magnetic samples in the same cross-sectional area but of various shapes. For experimentally verifying this capability, high-precision measurement approaches are necessary to assure the ACPD signals are measured from absolutely uniform positions on all samples.

For EN1A samples containing features of H, N, and NH, distinct differences are shown in experimental PDs measured from the uniform positions. Results of the N and NH samples are similar for the whole frequency range, reaching 1.08 mV and 1.02 mV at 50 kHz. PDs measured from the H sample are significantly lower than the other two results and give 0.32 mV at 50 kHz. For all samples, experimental results are in good agreement with the optimum FE approximations and located within error bars. Welding uncertainties actually produced in experiments are

believed to be smaller than the predicted values of ±0.3 mm in horizontal positions and -0.25 to 0.5 mm in vertical.

Error bars given by various models show significant differences, which indicates different electric fields induced around these features. At 10 kHz, error bars I & II produced by the H model diverge to the optimum result for -25% to 50% and -35% to 60% respectively. While on the other two models, results are less sensitive to the uncertainties with differences in PDs smaller than ±10% from 10 Hz to 10 kHz. Some similar characteristics of the electric fields around different features are observed: the current fields decrease at the feature corners (on the sample edges) and concentrate at the feature roots. Moreover, for the roots consisting of straight edges like the notches in Case 3 (the root of the H feature is curved), it is shown by FEA that the current focus on, more accurately, the concave corners of the roots. Thus ACPD results near to the feature roots are highly affected by measurement uncertainties due to the highly asymmetric current distributions. The uniform observation region at 0.5-1.1 mm to the edges is close to the root of the H feature at 1.06 mm but far from the roots of N notches at 4.24 mm. This is the reason of various error bars in the different models. This also suggests that extra attention is required in measuring ACPD signals close to the feature roots.

Although the measuring paths on the H model are close to the current concentration region at the root, PDs measured across the H feature are significantly lower than those read from uniform paths across the N and NH features. This is because that the H feature is too narrow to effectively disturb the skin effect inside the sample. The current around the H feature only concentrates beneath the sample surface but hardly penetrate into the depth with the feature. For the N feature, the wide opening on the sample surface strongly interferes with the skin depth and forces the current to flow through all featured surfaces even including the innermost face in the depth of the sample. By comparing the H and NH features, the opening of the N feature greatly increase the current distributions in the depth of the H feature and hence results of the NH feature is similar to those for the N. The involvement of the H feature hardly contributes to the ACPD results of the NH feature, but leads to higher sensitivities of results to measurement uncertainties.

Based on the analysis of experimental and FE results for Case 2, the ACPD method is shown to be able to differentiate between features with distinct opening widths like the narrow H and the wide N.

It was demonstrated by experiments and FEA in Case 3 that the ACPD method is able to identify the features containing the same cross-sectional area. PDs measured from the uniform positions close to the sample edges reduce as the feature openings become narrower from the N6 feature to the N1.5. PDs measured across the N6, N3, and N1.5 features on EN1A samples in a 2 mm distance reach 1.08, 0.72, and 0.47 mV at 50 kHz respectively. The three features have distinct

opening widths of 0.11, 0.21, and 0.42 to the sample size. PDs rise for 53% and 130% as the relative opening width increase from 0.11 to 0.22 and to 0.42. Experimental results are in good comparison to FE approximations with error bars for all three samples. It is similar to the H model in Case 2 that the observation region is close to the root of the N1.5 feature at 1.06 mm, and hence measurements on the N1.5 model are significantly influenced by the measurement uncertainties. By contrasting between PDs contributed by parts 1-3 of the uniform paths in the three models, it is observed that majority parts of the paths across narrow features gain few current distributions and hence offer minor PDs to the total results. The similar conclusion is reached that the ACPD method can be used to differentiate various features with the same cross-sectional area and distinct opening widths by identifying various disturbance in the current distribution and the skin effect caused by openings. However, limitations of the techniques are noticed in the detection of deep and narrow features involving a strong skin effect.

Chapter 8

Conclusions and Future Work

Cracks occur in a significant part of service lifetime of structural components in many engineering applications. The cracks propagate with load cycle, which imperils the structural integrity and may leads to catastrophic failure of the components if the crack reaches the critical size. Reliable predictions of the service lifetime are aimed not only to assure the safe operation of the components but also to maximise the utilisation and thus reduce costs. This significantly depends on quantitative measurements of cracks regarding the depths and shapes inside the structural components by the use of NDT methods. The primary aim of this study was to investigate the capability of the swept ACPD method in distinguishing between, firstly the conductors with the same cross-sectional of various shapes, and secondly the features that have different opening shapes on the conductor surfaces and depths into the conductors.

Several main conclusions relating to the detection capabilities of the swept ACPD method have been obtained from the work. FEA is applied to demonstrate that, by taking the advantage of current crowding, the ACPD method is capable of identifying the cross-sectional shapes of non-magnetic conductors such as SS316 by comparing ACPD results measured from the uniform positions (e.g. at the same distances to the edges) on the conductor surfaces. The current crowding in weak- and non-magnetic materials vary with the cross-sectional shape and are apparent on the surfaces. At 300 kHz, PDs in 2 mm distances close to the edges approximated by the SS316 circular and triangular models reach 0.22 mV and 0.39 mV, respectively, giving a difference of 77%. Nevertheless, the measurement approaches currently used in the project are unable to determine the cross-sectional shapes of the SS316 samples in the scale of 100 mm^2.

Both the experiments and FEA validate the capability of the swept ACPD method to differentiate between the various features. The N1.5, N3, and N6 features were manufactured on the EN1A samples to have the same cross-sectional area and opening height, but different opening widths of 0.11, 0.21, and 0.42 to the sample size. By sampling the frequency to 50 kHz, PDs measured at the uniform positions close to the edges and across the three features are different to be 0.47,

0.72, and 1.08 mV of 2 mm in distance respectively, resulting in increases of 53% and 130%. PDs measured across the H feature, which has a curved opening and the same opening width as N1.5, reach 0.41 mV at 300 kHz. For the NH feature combing the H and N6 features, PDs are slightly lower than those of the N6, giving 1.02 mV at 300 kHz. The ability to detect features of the ACPD method is attributed to the opening widths of features. Narrow features (e.g. H & N1.5) have less impact on the skin effect in the vicinity than wide features, with the current still concentrating near the conductor surfaces and not penetrating into the interior of conductors with the feature depths. Whereas, wide features (e.g. N6 & N3) significantly disturb the current distributions near them, which results in deeper penetration of the current into the conductors and hence producing greater PDs. In the meanwhile, the limitation of the feature detection ability is determined by on the opening situations. Especially for narrow features, the inner situations such as the shapes and depths that exceed the depth of current penetration cannot be detected due to the inadequate information (i.e. the absence of current distribution).

In addition to the aforementioned key conclusions, a summary of findings from other aspects is presented below:

- It has been demonstrated through several distinct theoretical methods and FEA (ANSYS) that Z_{int} of straight non-magnetic SS316 conductors of various cross-sectional shapes slightly increases as the shape varies from circular to hexagonal, square, and triangular. At 300 kHz, Z_{int} of the SS316 samples with the same cross-sectional area of 100 mm^2 reach 0.0284, 0.0290, 0.0301, 0.0315 Ω/m for the four cross-sectional shapes, respectively.

- The two theories relating to discretisation of the conductor cross-sections, integral equations for current distributions and MNT, were adapted for use with cross-sectional shapes other than rectangular and produce the closet comparisons with FE results for the wide frequency range from quasi-DC to 300 kHz (with differences smaller than 4%) . These two methods are recommended as the optimum theoretical solutions for computing Z_{int} of non-magnetic conductors of arbitrary shapes.

- CSMR can be utilised in the data processing (i.e. the MATLAB script) to accurately convert ACPD data measured in the time interval to results of PD and Z in the frequency domain with the frequency range from 10 Hz to 300 kHz. Average differences between processed and manually measured results of PD in all formal experiments are within 8%.

- The reliability of the experimental procedure and the precision of the data processing have been confirmed by conducting the swept ACPD experiments on various types of samples including the R-L circuits and the large-scaled copper wire. For the copper wire, processed $|Z|$ and θ_Z are in good agreement

194

with theoretical solutions based on Bessel Function Method and manually measured results, giving average differences within 3% from 10 Hz to 300 kHz.

- FEA via ANSYS can be used to simulate the swept ACPD experiments on plain and featured samples based on the numerical methodology that includes comprehensive procedures from creating models to the post processing. Parameters of meshing and convergence of SS316 and EN1A models were determined through mesh refinement study, which enables a compromise between the modelling precision and computing costs. PS modelling was applied to improve simulation efficiency after verifying the feasibility.

- The developed FE models can be used to simulate the current distributions generated within and around various plain and featured samples. Current are consistently concentrated at discontinuities on the conductor surfaces, such as the edges of polygonal samples and the feature profiles. Experimental measurements in proximity to these discontinuities may be greatly affected by measurement uncertainties.

- In contrast to ferromagnetic conductors in which current crowding is confined to the conductor interior by skin effect, the ACPD measurements on weak- and non-magnetic materials are more sensitive to measurement uncertainties due to the prominent current crowding on the conductor surfaces.

The present work may be further developed in several aspects in the future. First, future work look to improve the measurement resolution by introducing a new measurement approach to replace manual welding, or alternatively, by using samples in larger scales that adapt to the present measurement method.

Additionally, future research is suggested to focus on quantifying the detection capabilities of the ACPD method, i.e. determining the relation between the feature openings (shapes, dimensions, and positions) and the current attenuation around the features. The attenuation equations of current density with depth around the features could be derived from the 3D current fields simulated by FEA. The research may be focused on basic shapes of the openings, such as elliptical and rectangular like the H and N features. Then each basic shape could be further varied by changing the dimensions, to be more specific, by fixing one dimension (e.g. the horizontal width or the vertical height) and adjusting the other one. Since at this stage the only variable will be the varying dimension, the impact of this dimension on the current distributions could be quantified by comparing the current attenuation equations obtained with different values of the dimension. The impact of the other dimension on the current distributions could be determined by following the same steps. Next, the analyse may be moved on to another basic shapes of openings, and furthermore, different positions of features, e.g. on

conductor surfaces (rather than on corners) or inside conductors without openings on surfaces.

The current attenuation equations around features may be normalised to the current decay equation of skin effect to obtain general equations which will be independent of conductor materials and frequency and dependent on the positions, shapes, and dimensions of feature openings. Such equations could be used to calculate the limitation of detection depth for features with certain openings. Real depth and geometries of deep features beyond the maximum detection depth could not be identified. Whereas, situations of features within the detection region may be detected based on measured PDs (which should be greater than predicted values for the maximum detection depth). Real depths may be approximated by FEA. Alternatively, another approach could be to extend the current attenuation equation to all detections including the bottom surface of the feature, then to calculate the real depths by using the full equitation. For features with shapes varying along the depth (i.e. not constant and straight like features involved in the present research), the shape identification may be conducted by applying AC in multiple directions and constructing several current attenuation equations on these directions. Therefore, the swept ACPD method with comprehensive knowledge of current attenuation equations may be utilised as a powerful NDT technique in practice to identify the depth and shape of a surface feature, or at least to determine whether the depth is larger than the maximum detection depth of the feature opening.

Appendix A

Applications of Theoretical Methods of Internal Impedance

A.1 Integral Equation for Current Distribution

Method 1 of Computing Distance Matrix

```matlab
% Caculating p.u.l R_AC Based on Silvester 'logD' [192]
clc
clear
tic

% Define the number of corners of the conductor
NC = 25; % Approximated cylindircal conductor
% NC = 6;  % Hexagonal conductor
% NC = 4;  % Square conductor
% NC = 3;  % Triangualr conductor

Area = 100e-6;              % Original area = 100 mm^2
alp = pi*(360./NC)/180; % Angle per part at the center
a0 = 2 * sqrt(Area * tan(alp/2) ./ NC); % Side length
r0 = 0.5 * a0 ./ sin(alp/2); % Effective radius
% N = 100;                  % Total number of subbars = N*N
hi = 1e-4;                  % Side length of subsections

% Define positions of corners of the conductor
corner = zeros(NC, 2);
for ii = 1:NC
    corner(ii,1) = r0 * sin(alp/2 + alp*(ii-1)); %
       Positions of corners in x
    corner(ii,2) = r0 * cos(alp/2 + alp*(ii-1)); %
```

```matlab
        Positions of corners in y
end

% Determine positions of subsections/subbars within the
   cross-section
Nr = 2*floor(r0/hi)+2;
posit = zeros(Nr*Nr,2);
for jj = 1:Nr*Nr
    posit(jj,1) = -hi*Nr/2 + hi*(jj-1+0.5) - Nr*hi*floor
       ((jj-1)/Nr);
    posit(jj,2) = -hi*Nr/2 + hi*(floor((jj-1)/Nr)+0.5);
end
in = inpolygon(posit(:,1), posit(:,2), corner(:,1),
   corner(:,2));
subbars(:,1) = posit(in,1); % Positions of subbars in x
subbars(:,2) = posit(in,2); % Positions of subbars in y

temp = subbars(:,1) > 0;
subbars = subbars(temp,:);

% Calculate the matrix of 'logD' based on the positions
   of subsections
N = size(subbars,1);
logDs = zeros(N);    % 'logD' based on Silvester's method
for ii = 1:N
%     Dmms = 2 * subbars(ii,1); % Distance between
   subbar #m and subbar #m_symetry
    logDs(ii,ii) = log(0.44705*hi * 2 * subbars(ii,1));
       % For self-induction
    for jj = 1:N
        if ii ~= jj % For mutual-induction
            Dmn = sqrt((subbars(ii,1) - subbars(jj,1))^2
               + (subbars(ii,2) - subbars(jj,2))^2);   %
               Distance bewteen #m and #n
            Dmns = sqrt((subbars(ii,1) + subbars(jj,1))
               ^2 + (subbars(ii,2) - subbars(jj,2))^2);
               % Distance bewteen #m and #n_sym (
               horizontally symmetrical with #n)
            logDs(ii,jj) = log(Dmn * Dmns); % To reduce
               the matrix size by using 'symmetrical
               subsections'
        end
```

```matlab
        end
    end
toc
clear ii in jj temp

L = 1;                      % Unit length of 1 m
perm = 1.02*4*pi*1e-7;  % Permeability of SS316
cond = 1.38e6;          % Conductivity of SS316
% Rdc = L/(cond*Area);   % R_DC of SS316
I0 = 3;                     % Impressed/Original AC of 3 A
ff=[0.1 0.2 0.5 1 2 5 10 20 30 50 70 100 150 200 250
    300]'*1e3; % Frequency
sd = sqrt(1./(pi .* ff * perm * cond)); % Skin depths

% Calculate p.u.l. R_AC based on 'logDs'
tic
Rs = zeros(size(ff,1),1); % 'R_AC' based on Silvester's
    method
for kk = 1:size(ff,1) % (about 10s per frequency)
    freq = ff(kk);
    const = freq * perm * cond * hi^2; % The constant
        term within X

    Xs = const * logDs;
    U = eye(N);
    G = zeros(N, 1) + I0 / Area;
    Zs = U + Xs * sqrt(-1);
    Js =   Zs^(-1) * G; % Matrix J is calculated by
        inversing Z
    Js_mod = abs(Js);    % Modulus of J
%     Js_ang = angle(Js)*180/pi; % Phase angles of J

%     Calculate p.u.l. R_AC of the conductor
    Rs(kk) = L * sum(Js_mod.^2*hi^2) / (cond*(abs(sum(Js
        ))*hi^2)^2);
    disp(kk);
end
Rs = Rs/2;
toc

Js_circ = Js; Js_mod_circ = Js_mod; Rs_circ(:,1) = ff;
    Rs_circ(:,2) = Rs;
```

```matlab
clearvars -except Js_circ Js_mod_circ Rs_circ
save('Res_Theory_IntJ_Silvester_CIRC.mat')

% Js_hex = Js; Js_mod_hex = Js_mod; Rs_hex(:,1) = ff;
   Rs_hex(:,2) = Rs;
% clearvars -except Js_hex Js_mod_hex Rs_hex
% save('Res_Theory_IntJ_Silvester_HEX.mat')

% Js_sq = Js; Js_mod_sq = Js_mod; Rs_sq(:,1) = ff; Rs_sq
   (:,2) = Rs;
% clearvars -except Js_sq Js_mod_sq Rs_sq
% save('Res_Theory_IntJ_Silvester_SQ.mat')

% Js_tri = Js; Js_mod_tri = Js_mod; Rs_tri(:,1) = ff;
   Rs_tri(:,2) = Rs;
% clearvars -except Js_tri Js_mod_tri Rs_tri
% save('Res_Theory_IntJ_Silvester_TRI.mat')
```

Method 2 of Computing Distance Matrix

```matlab
% Caculating p.u.l. R_AC Based on Antonini 'logD' [217]
clc
clear
tic

% Define the number of corners of the conductor
NC = 25; % Approximated cylindircal conductor
% NC = 6;  % Hexagonal conductor
% NC = 4;  % Square conductor
% NC = 3;  % Triangualr conductor

Area = 100e-6;              % Original area = 100 mm^2
alp = pi*(360./NC)/180; % Angle per part at the center
a0 = 2 * sqrt(Area * tan(alp/2) ./ NC); % Side length
r0 = 0.5 * a0 ./ sin(alp/2); % Effective radius
% N = 100;                  % Total number of subbars = N*N
hi = 1e-4;                  % Side length of subsections

% Define positions of corners of the conductor
corner = zeros(NC, 2);
for ii = 1:NC
    corner(ii,1) = r0 * sin(alp/2 + alp*(ii-1)); %
        Positions of corners in x
```

```matlab
        corner(ii,2) = r0 * cos(alp/2 + alp*(ii-1)); %
            Positions of corners in y
end

% Determine positions of subsections/subbars within the
    cross-section
Nr = 2*floor(r0/hi)+2;
posit = zeros(Nr*Nr,2);
for jj = 1:Nr*Nr
    posit(jj,1) = -hi*Nr/2 + hi*(jj-1+0.5) - Nr*hi*floor
        ((jj-1)/Nr);
    posit(jj,2) = -hi*Nr/2 + hi*(floor((jj-1)/Nr)+0.5);
end
in = inpolygon(posit(:,1), posit(:,2), corner(:,1),
    corner(:,2));
subbars(:,1) = posit(in,1); % Positions of subbars in x
subbars(:,2) = posit(in,2); % Positions of subbars in y

temp = subbars(:,1) > 0;
subbars = subbars(temp,:);

% Calculate the matrix of 'logD' based on positions of
    subsections
N = size(subbars,1);
logDa = zeros(N);   % 'logD' based on Antonini's method
f = zeros(4,1);     % The distance function in Antonini'
    s method
f_sum = 0;
for ii = 1:N  % (about 200s)
    logDa(ii,ii) = log(0.44705*hi * 2 * subbars(ii,1));
    for jj = 1:N
        if ii ~= jj
            P = abs(subbars(ii,2) - subbars(jj,2));
            E = abs(subbars(ii,1) - subbars(jj,1));
%             Ps = abs(subbars(ii,2) - subbars(jj,2));
%             Es = abs(subbars(ii,1) - subbars(jj,1));

            q(1) = E-hi;
            q(2) = E;
            q(3) = E+hi;
            q(4) = E;
            r(1) = P-hi;
```

```matlab
            r(2) = P;
            r(3) = P+hi;
            r(4) = P;

%               qs(1) = Es-hi;
%               qs(2) = Es;
%               qs(3) = Es+hi;
%               qs(4) = Es;
%               rs(1) = Ps-hi;
%               rs(2) = Ps;
%               rs(3) = Ps+hi;
%               rs(4) = Ps;

            for iii = 1:4
                qq = q(iii);
%                   qqs = qs(iii);
                for jjj = 1:4
                    rr = r(jjj);
%                       rrs = rs(jjj);
                    if (rr ~= 0) && (qq ~= 0)
                        f(jjj,1) = (-1)^(iii+jjj)*(((qq*
                            qq*rr*rr)/4 - (qq^4+rr^4)/24)
                            * log(qq^2+rr^2) + ((qq^3*rr
                            )/3)*atan(rr/qq)+ ((qq*rr^3)
                            /3)*atan(qq/rr));
%                           fs(jjj,1) = (-1)^(iii+jjj)*(((
    qqs*qqs*rrs*rrs)/4 - (qqs^4+rrs^4)/24) * log(qqs^2+
    rrs^2) + ((qqs^3*rrs)/3)*atan(rrs/qqs)+ ((qqs*rrs^3)
    /3)*atan(qqs/rrs));
                    elseif (rr == 0) && (qq == 0)
                        f(jjj,1) = 0;
%                           fs(jjj,1) = 0;
                    elseif (rr == 0) || (qq == 0)
                        f(jjj,1) = (-1)^(iii+jjj)*(((qq*
                            qq*rr*rr)/4 - (qq^4+rr^4)/24)
                            * log(qq^2+rr^2));
%                           fs(jjj,1) = (-1)^(iii+jjj)*(((
    qqs*qqs*rrs*rrs)/4 - (qqs^4+rrs^4)/24) * log(qqs^2+
    rrs^2));
                    end
                end
                f_sum = f_sum + sum(f);
```

```matlab
%                        fs_sum = fs_sum + sum(fs);
            end
            logDa (ii,jj) = -25/12 + f_sum/(2*hi^4);
%               logDa (ii,jj) = -25/12 + fs_sum/(2*hi^4);
            f_sum = 0;
%               fs_sum = 0;
        end
    end
    disp(ii);
end
toc
clear ii in jj temp

L = 1;                     % Unit length of 1 m
perm = 1.02*4*pi*1e-7;   % Permeability of SS316
cond = 1.38e6;           % Conductivity of SS316
% Rdc = L/(cond*Area);   % R_DC of SS316
I0 = 3;                    % Impressed/original AC of 3 A
ff=[0.1 0.2 0.5 1 2 5 10 20 30 50 70 100 150 200 250
   300]'*1e3; % Frequency
sd = sqrt(1./(pi .* ff * perm * cond)); % Skin depths

% Calculate p.u.l. R_AC based on 'logDa'
tic
Ra = zeros(size(ff,1),1); % 'R_AC' based on Antonini's
   method
for kk = 1:size(ff,1) % (about 10s per frequency)
    freq = ff(kk);
    const = freq * perm * cond * hi^2; % The constant
        term within X

    Xa = const * logDa;
    U = eye(N);
    G = zeros(N, 1) + I0 / Area;
    Za = U + Xa * sqrt(-1);
    Ja =   Za^(-1) * G; % Matrix J is calculated by
        inversing Z
    Ja_mod = abs(Ja);    % Modulus of J
%      Js_ang = angle(Js)*180/pi; % Phase angles of J

    % Calculate p.u.l. R_AC of the conductor
    Ra(kk) = L * sum(Ja_mod.^2*hi^2) / (cond*(abs(sum(Ja
```

```matlab
        ))*hi^2)^2);
    disp(kk);
end
Ra = Ra/2;
toc


subbars_circ = subbars; Ja_circ = Ja; Ja_mod_circ =
   Ja_mod; Ra_circ(:,1) = ff; Ra_circ(:,2) = Ra;
clearvars -except subbars_circ Ja_circ Ja_mod_circ
   Ra_circ
save('Res_Theory_IntJ_Antonini_CIRC.mat')

% subbars_hex = subbars; Ja_hex = Ja; Ja_mod_hex =
   Ja_mod; Ra_hex(:,1) = ff; Ra_hex(:,2) = Ra;
% clearvars -except subbars_hex Ja_hex Ja_mod_hex Rs_hex
% save('Res_Theory_IntJ_Antonini_HEX.mat')

% subbars_sq = subbars; Ja_sq = Ja; Ja_mod_sq = Ja_mod;
   Ra_sq(:,1) = ff; Ra_sq(:,2) = Ra;
% clearvars -except subbars_sq Ja_sq Ja_mod_sq Ra_sq
% save('Res_Theory_IntJ_Antonini_SQ.mat')

% subbars_tric = subbars; Ja_tri = Ja; Ja_mod_tri =
   Ja_mod; Ra_tri(:,1) = ff; Ra_tri(:,2) = Ra;
% clearvars -except subbars_tric Ja_tri Ja_mod_tri
   Ra_tri
% save('Res_Theory_IntJ_Antonini_TRI.mat')
```

A.2   Modal Network Theory

```matlab
% Calculating p.u.l R_ac Based on MNT
clc
clear
tic


A0 = 100e-6;              % Original area = 100 mm 2
L = 1;                    % Unit length of 1 m
perm = 1.02*4*pi*1e-7;    % Permeability of SS316
cond = 1.38e6;            % Conductivity of SS316
Rdc = L/(cond*A0);        % R_DC of SS316
I0 = 3;                   % Impressed/Original AC of 3A
f=[0.1 0.2 0.5 1 2 5 10 20 30 50 70 100 150 200 250
```

```matlab
   300]'*1e3; % Frequency
sd = sqrt(1./(pi .* f * perm * cond)); % Skin depths

NC = 25;                      % Approximated Circular
d0_circ = sqrt(A0/pi);
d_circ = d0_circ-sd;
tempc = find(d_circ<0);
a_circ(tempc,1) = A0;
a_circ(tempc(end)+1:size(d_circ,1), 1) = A0-pi*d_circ(
   tempc(end)+1:size(d_circ,1)).^2;
Aeff = a_circ;
sd(tempc) = 0;
clear d0_circ d_circ tempc a_circ

% NC = 6;                      % Hexagonal conductor
% d0_hex = sqrt(A0/(1.5*sqrt(3)));
% d_hex = d0_hex-2*sd/sqrt(3);
% temph = find(d_hex<0);
% a_hex(temph,1) = A0;
% a_hex(temph(end)+1:size(d_hex,1), 1) = A0-6*0.25*sqrt
%   (3)*d_hex(temph(end)+1:size(d_hex,1)).^2;
% Aeff = a_hex;
% sd(temph) = 0;
% clear d0_hex d_hex temph a_hex

% NC = 4;                      % Square conductor
% d0_sq = sqrt(A0);
% d_sq = d0_sq-2*sd;
% temps = find(d_sq<0);
% a_sq(temps,1) = A0;
% a_sq(temps(end)+1:size(d_sq,1), 1) = A0-d_sq(temps(end
%   )+1:size(d_sq,1)).^2;
% Aeff = a_sq;
% sd(temps) = 0;
% clear d0_sq d_sq temps a_sq

% NC = 3;                       % Triangualr conductor
% d0_tri = sqrt(A0*4/sqrt(3));
% d_tri = d0_tri-2*sqrt(3)*sd;
% tempt = find(d_tri<0);
% a_tri(tempt,1) = A0;
% a_tri(tempt(end)+1:size(d_tri,1), 1) = A0-0.25*sqrt(3)
```

```matlab
    *d_tri(tempt(end)+1:size(d_tri,1)).^2;
% Aeff = a_tri;
% sd(tempt) = 0;
% clear d0_tri d_tri tempt a_tri

Reff = L./(cond.*Aeff);
alp = pi*(360./NC)/180;                  % Angle per part
    at the center
a0 = 2 * sqrt(A0 * tan(alp/2) ./ NC); % Side length of
    the sample
r0 = 0.5 * a0 ./ sin(alp/2);             % Effective radius
hi = 1e-4;                               % Side length of
    subsections

% Define positions of corners of the conductor
cornerx = zeros(NC,1);
cornery = zeros(NC,1);
for ii = 1:NC
    cornerx(ii,1) = r0 * sin(alp/2 + alp*(ii-1)); %
        Positions of corners in x
    cornery(ii,1) = r0 * cos(alp/2 + alp*(ii-1)); %
        Positions of corners in y
end

% Determine positions of subsections/subbars within the
    cross-section
Nr = 2*floor(r0/hi)+2;
posit = zeros(Nr*Nr,2);
for jj = 1:Nr*Nr
    posit(jj,1) = -hi*Nr/2 + hi*(jj-1+0.5) - Nr*hi*floor
        ((jj-1)/Nr);
    posit(jj,2) = -hi*Nr/2 + hi*(floor((jj-1)/Nr)+0.5);
end
in1 = inpolygon(posit(:,1), posit(:,2), cornerx, cornery
    );
subbars(:,1) = posit(in1,1); % Positions of subbars in x
subbars(:,2) = posit(in1,2); % Positions of subbars in y
temp = subbars(:,1) > 0;
subbars = subbars(temp,:);
clear temp

tic
```

```matlab
N = size(subbars,1);
logDs = zeros;    % 'logD' based on Silvester's method
for ii = 1:N      % (about 43s)
    logDs(ii,ii) = log(0.44705*hi * 2 * subbars(ii,1));
        % For self-induction
    for jj = 1:N
        if ii ~= jj % For mutual-induction
            Dmn = sqrt((subbars(ii,1) - subbars(jj,1))^2 ...
                + (subbars(ii,2) - subbars(jj,2))^2);   %
                Distance bewteen #m and #n
            Dmns = sqrt((subbars(ii,1) + subbars(jj,1)) ...
                ^2 + (subbars(ii,2) - subbars(jj,2))^2);
                % Distance bewteen #m and #n_sym (
                horizontally symmetrical with #n)
            logDs(ii,jj) = log(r0^2/(Dmn * Dmns)); % To
                reduce the matrix size by using '
                symmetrical subsections'
        end
    end
    %      disp(ii);
end
clear ii in jj temp
toc

tic
deno1 = cell(1,size(f,1));
deno2 = cell(1,size(f,1));
A = cell(1,size(f,1));
B = cell(1,size(f,1));
Rac_deno = cell(1,size(f,1));
Z = zeros(size(f,1),1);
deno_sum = zeros(size(f,1),1);
deno_sub = zeros(size(f,1),1);
Z2 = zeros(size(f,1),1);
AA = zeros(size(f,1),1);
BB = zeros(size(f,1),1);
Rac_para = zeros(size(f,1),1);

E = logDs;
num_eig = [10;15;20;30;40;50;60;70;80;100];
Z_eig =zeros(size(f,1), size(num_eig,1));
Z2_eig =zeros(size(f,1), size(num_eig,1));
```

```matlab
for ee = 1:size(num_eig,1)
    [eigVec,eigVal] = eigs(E, num_eig(ee));
    N = 2*size(E,1);
    Omegak   = -2*N./eigVal;
    Omegak_inf = isinf(Omegak);
    Omegak(Omegak_inf) = [];
    alphak = abs(mean(eigVec, 1))*sqrt(0.5*N);
    alphak = alphak';
    temp = abs(mean(eigVec, 1));
    mk = Omegak * Rdc * pi / perm;
    Omega = perm*2.*f / Rdc;
    % p(ff,1) = sqrt(Omega(ff));
    for ff = 1:size(f,1)
        for kk = 1:size(Omegak,2)
            deno1{1,ff}(kk,1) = alphak(kk)^2/(1+sqrt(-1)
                *(Omega(ff)/Omegak(kk)));
            deno2{1,ff}(kk,1) = alphak(kk)^2 ./ (Rdc .*
                (1+sqrt(-1)*2*pi*f(ff) ./ mk(kk)));
        end
        Z(ff,1) = Rdc/sum(deno1{1,ff});
        Z2(ff,1) = 1/sum(deno2{1,ff});
    end
    Z_eig(:,ee) = Z;
    Z2_eig(:,ee) = Z2;
    disp(ee);
end
toc

clearvars -except NC logDs Rdc Reff subbars cond perm A0
    f sd r0 a0 hi Z_eig Z2_eig num_eig
save('Results_ModalTheory_Z_CIRC.mat');
% save('Results_ModalTheory_Z_HEX.mat');
% save('Results_ModalTheory_Z_SQ.mat');
% save('Results_ModalTheory_Z_TRI.mat');
```

Appendix B

The Data Processing and Constant Slope Ratio Method

```matlab
% The Data Processing of ACPD Results Measured in
    Experiments.
%% Prepare the processing data
clear
clc
I_amp = 3;              % Current mplitude
fs = 4e6;              % Sampling frequency
t = (0:1/fs:2)';       % Time, total time interval is 2
    seconds
t = t(1:end-1);
load('Feature Data Mean.MAT', 'I_Mean', 'V_Mean') % Load
    experimental data
I = I_Mean;
V = V_Mean;
cut = 0.18*fs; %Find out the time position of the first
    curent peak 'cut' of the processing data and delete
    current signals before the first peak
I = I(cut:end);
V = V(cut:end);
t = t(cut:end);

clearvars -except I V t I_amp
%% Find out band part-1 by using tolerance ratio = 1/3
tic
tr = 1/3;
I_tol = tr*I_amp; % Tolerance of band part
upper_I_lim = find(I<=I_tol);
lower_I_lim = find(I>=-I_tol);
```

```matlab
bands = intersect(upper_I_lim,lower_I_lim); % Signal
    bands

heads = zeros;
heads(1,1) = 1;
kk = 1;
for ii = 1:length(bands)
    if ii == 1
        O = [t(bands(ii)), I(bands(ii))]; % The 1st
            signal of band (ii)
    elseif sign(I(bands(ii))) ~= sign(O(2))
        if exist('A','var')==0 % Calculate slope of
            band_OA
            A = [t(bands(ii)), I(bands(ii))];
            jj = 1;
            kAsum = zeros;
            kAsum(jj,1) = (A(2)-O(2))/(A(1)-O(1));
            kA = mean(kAsum);
            jj = jj+1;
        else
            B = [t(bands(ii)), I(bands(ii))]; %
                Calculate slope of band_OB
            kB = (B(2)-O(2))/(B(1)-O(1));
            kr = kA/kB;
            if kr > 4 % The constant slope ratio of tr =
                1/3 is 4.62
                heads(kk+1,1) = ii;
                O = [t(bands(ii)), I(bands(ii))]; % THIS
                    IS THE FINAL SIGNAL OF THE BAND
                clear A kA
                kk = kk+1;
            else
                A = B;
                kAsum(jj,1) = kB;
                kA = mean(kAsum);
                jj = jj+1; % Continue to identify the
                    next signal
            end
        end
    end
    disp(length(bands)-ii);
end
```

```matlab
toc

band_part1 = cell(length(heads)+1,1);
for ii = 1:length(heads)-1
    band_part1{ii,1} = [t(bands(heads(ii)):(bands(heads(
        ii+1)-1))), I(bands(heads(ii)):(bands(heads(ii+1)
        -1)))];
end

% band_part_size1 = zeros(length(band_part1),1); % Check
    if needed
% for ii = 1:length(band_part1)
%    band_part_size1(ii,1) = size(band_part1{ii,1},1);
% end
% band_part_check1 = zeros(length(band_part_size1)-1,1);
% for ii = 1:length(band_part_size1)-1
%    band_part_check1(ii,1) = band_part_size1(ii)/
    band_part_size1(ii+1);
% end
% ccheck1 = find(band_part_check1>1.5);

clearvars -except I V t band_part1 band_part_size1
%% Continue to find out band parts-2 by using tr=2/3
tic
% ns = find(band_part_size1==3);
% if isempty(ns) == 1
%     clear ns
%     %Then there is no need to find out band parts-2!
% end

ns1_bp = min(find(band_part_size1==4));
ns1 = find(t==band_part1{ns1_bp,1}(1,1));
I = I(ns1:end); I_amp=3;
V = V(ns1:end);
t = t(ns1:end);
tr = 2/3;
I_tol = tr*I_amp;
upper_I_lim = find(I<=I_tol);
lower_I_lim = find(I>=-I_tol);
bands = intersect(upper_I_lim,lower_I_lim);

heads = zeros;
```

```matlab
heads(1,1) = 1;
kk = 1;
for ii = 1:length(bands)
    if ii == 1
        O = [t(bands(ii)), I(bands(ii))];
    elseif sign(I(bands(ii))) ~= sign(O(2))
        if exist('A','var') == 0
            A = [t(bands(ii)), I(bands(ii))];
            jj = 1;
            kAsum = zeros;
            kAsum(jj,1) = (A(2)-O(2))/(A(1)-O(1));
            kA = mean(kAsum);
            jj = jj+1;
        else
            B = [t(bands(ii)), I(bands(ii))];
            kB = (B(2)-O(2))/(B(1)-O(1));
            kr = kA/kB;
            if kr > 1.5 % The constant slope ratio of tr
                % = 1/3 is 2.15
                heads(kk+1,1) = ii;
                O = [t(bands(ii)), I(bands(ii))]; % THIS
                    % IS THE FINAL SIGNAL OF THE BAND
                clear A kA
                kk = kk+1;
            else
                A = B;
                kAsum(jj,1) = kB;
                kA = mean(kAsum);
                jj = jj+1;
            end
        end
    end
    disp(length(bands)-ii);
end
toc

band_part2 = cell(length(heads)+1,1);
for ii = 1:length(heads)-1
    band_part2{ii,1} = [t(bands(heads(ii)):(bands(heads(
        ii+1)-1))), I(bands(heads(ii)):(bands(heads(ii+1)
        -1)))];
end
```

```matlab
% band_part_size2 = zeros(length(band_part2),1); % Check
    if needed
% for ii = 1:length(band_part2)
%     band_part_size2(ii,1) = size(band_part2{ii,1},1);
% end
%
% band_part_check2 = zeros(length(band_part_size2)-1,1);
% for ii = 1:length(band_part_size2)-1
%     band_part_check2(ii,1) = band_part_size2(ii)/
   band_part_size2(ii+1);
% end
% ccheck2 = find(band_part_check2 >1.5);

clearvars -except I V t band_part1 band_part_size1
   band_part2 band_part_size2 ns1_bp
%% Continue to find out band parts -3 by using tr=1 (1'')
 tic
% ns = find(band_part_size2 ==3);
% if isempty(ns) == 1
%     clear ns
%      %Then there is no need to find out band part -3!
% end

ns_t = zeros;
kk = 1;
for ii = 1:length(ns)
    tt1 = band_part2{ns(ii),1}(1,2);
    tt2 = band_part2{ns(ii),1}(end,2);
    if round(tt1) ~= (-round(tt2))
        ns_t(kk,1) = ns(ii);
        kk = kk+1;
    end
end
ns2_bp = ns_t(1);
ns2 = find(t==band_part2{ns_t(1),1}(1,1));
I = I(ns2:end);
V = V(ns2:end);
t = t(ns2:end);

heads = zeros;
heads(1,1) = 1;
```

```matlab
kk = 1;
for ii = 3:length(I)-1 %NOTE: part3{1,1} is not a repeat
    of part2{ns2_bp,1}
    if (I(ii)>I(ii-1)) ~= (I(ii-1)>I(ii-2))
        heads(kk,1) = ii;
        kk = kk+1;
    end
end

% band_part3 = cell(length(heads)+1,1); % Check if
    needed
% for ii = 1:length(heads)-1
%     band_part3{ii,1} = [t(heads(ii):(heads(ii+1)-1)), I
    (heads(ii):(heads(ii+1)-1))];
% end
%
% band_part_size3 = zeros(length(band_part3),1);
% for ii = 1:length(band_part3)
%     band_part_size3(ii,1) = size(band_part3{ii,1},1);
% end
% band_part_check3 = zeros(length(band_part_size3)-1,1);
% for ii = 1:length(band_part_size3)-1
%     band_part_check3(ii,1) = band_part_size3(ii)/
    band_part_size3(ii+1);
% end
% ccheck3 = find(band_part_check3>1.5);
% toc

 clearvars -except I V t band_part1 band_part_size1
    band_part2 band_part_size2 band_part3
    band_part_size3 ns1_bp ns2_bp
%% Combine band part-1,2,3 into a total band part

%If band part-3 has been run:
band_part = cell(ns1_bp+ns2_bp+length(band_part3)-1,1);
band_part(1:ns1_bp-1,1) = band_part1(1:ns1_bp-1,1);
band_part(ns1_bp:ns1_bp+ns2_bp-1,1) = band_part2(1:
    ns2_bp,1);
band_part(ns1_bp+ns2_bp:end,1) = band_part3;
band_part(end-1:end) = []; %It has two '[]' at the end
    of band_part
```

```matlab
% %If band part-3 has not been run:
% band_part = cell(ns1_bp+length(band_part2)-1,1);
% band_part(1:ns1_bp-1,1) = band_part1(1:ns1_bp-1,1);
% band_part(ns1_bp:end,1) = band_part2;
% band_part(end-1:end) = []; %It has two '[]' at the end
%     of band_part

%If band part-2 (and band part-3) has not been run:
% band_part = band_part1;
% band_part(end-1:end) = []; %It has two '[]' at the end
%     of band_part
% band_part_size = zeros(length(band_part),1);
% for ii = 1:length(band_part)
%     band_part_size(ii,1) = size(band_part{ii,1},1);
% end
% band_part_check = zeros(length(band_part_size)-1,1);
% for ii = 1:length(band_part_size)-1
%     band_part_check(ii,1) = band_part_size(ii)/
%   band_part_size(ii+1);
% end

if any(band_part_check>1.5)
    ccheck = find(band_part_check>1.5);
    %So find out the wrong bands, check kB/kA there,
        then change the 'if'
    %condition () above.
end

clearvars -except band_part I V t I_amp
%% Find out I-zeros in each band (both rising and
   dropping)

tzerosI = zeros(size(band_part,1),2);
tzerosI_pos = zeros(size(band_part,1),2);
tzerosI0 = zeros(size(band_part,1),1);
tic
for ii = 1:(size(band_part,1))
    temp = band_part{ii,1};
    p = polyfit(temp(:,1),temp(:,2),1);
    cal0 = -p(2)/p(1);
    temp(:,3) = abs(temp(:,1)-cal0);
    ins = min(temp(:,3));
```

```matlab
        insp = find(temp(:,3)==ins);
        if p(1)<0
            tzerosI(ii,1) = temp(insp,1); % Measured zeros
            tzerosI(ii,2) = cal0;          % Calculated zeros
        elseif p(1)>0
            tzerosI_pos(ii,1) = temp(insp,1);
            tzerosI_pos(ii,2) = cal0;
        else
            tzerosI0(ii,1) = -p(2)/p(1);
        end
        disp((size(band_part,1))-ii);
    end

    if any(tzerosI0~=0)==0
        clear tzerosI0
    end
    toc
    % tzerosI(find(tzerosI(:,1)==0),:)=[];
    % tzerosI_pos(find(tzerosI_pos(:,1)==0),:)=[];

    clearvars -except I V t tzerosI tzerosI_pos tzerosI0
    %% Find out V-zeros based on I-zeros
    tic
    fs = 4e6;
    ts = 1/fs;

    tzerosV = zeros(length(tzerosI)-1,1);
    Iamp = zeros(length(tzerosI)-1,1);
    Vamp = zeros(length(tzerosI)-1,1);
    Res=zeros(size(tzerosI,1), 3);
    for ii = 2:length(tzerosI)-1 % ii doesn't run from 1 as
       there are phase shifts at the beginning
        t1 = tzerosI(ii,1);
        t2 = tzerosI(ii+1,1);
        p1 = find(t==t1);
        p2 = find(t==t2);
        ti = t2-t1;
        if V(p1)>0
            t3 = t1;
        else
            jjmax = ti/(2*ts); % Assume V doesn't lead I
                more than half period
```

```matlab
        insp = find(temp(:,3)==ins);
        if p(1)<0
            tzerosI(ii,1) = temp(insp,1); % Measured zeros
            tzerosI(ii,2) = cal0;          % Calculated zeros
        elseif p(1)>0
            tzerosI_pos(ii,1) = temp(insp,1);
            tzerosI_pos(ii,2) = cal0;
        else
            tzerosI0(ii,1) = -p(2)/p(1);
        end
        disp((size(band_part,1))-ii);
    end

    if any(tzerosI0~=0)==0
        clear tzerosI0
    end
    toc
    % tzerosI(find(tzerosI(:,1)==0),:)=[];
    % tzerosI_pos(find(tzerosI_pos(:,1)==0),:)=[];

    clearvars -except I V t tzerosI tzerosI_pos tzerosI0
    %% Find out V-zeros based on I-zeros
    tic
    fs = 4e6;
    ts = 1/fs;

    tzerosV = zeros(length(tzerosI)-1,1);
    Iamp = zeros(length(tzerosI)-1,1);
    Vamp = zeros(length(tzerosI)-1,1);
    Res=zeros(size(tzerosI,1), 3);
    for ii = 2:length(tzerosI)-1 % ii doesn't run from 1 as
       there are phase shifts at the beginning
        t1 = tzerosI(ii,1);
        t2 = tzerosI(ii+1,1);
        p1 = find(t==t1);
        p2 = find(t==t2);
        ti = t2-t1;
        if V(p1)>0
            t3 = t1;
        else
            jjmax = ti/(2*ts); % Assume V doesn't lead I
                more than half period
```

```matlab
        for jj = 1:jjmax
            if sign(V(p1-jj))~=sign(V(p1)) && abs(V(p1-
                jj))>=abs(V(p1))
                break;
            end
        end
        psv = p1-jj+1;
        temp = [t(psv:p1), V(psv:p1)];
        poly = polyfit(temp(:,1),temp(:,2),1);
        if poly(1) == 0
            cal0 = temp(:,1);
        else
            cal0 = -poly(2)/poly(1);
        end
        temp(:,3) = abs(temp(:,1)-cal0);
        ins = min(temp(:,3));
        insp = find(temp(:,3)==ins);
        t3 = temp(insp,1);
        tzerosV(ii,1) = t3;
        tzerosV(ii,2) = cal0;
    end
    Res(ii,1) = 1/ti; % Processed results of f

    p3 = find(t==t3);
    p4 = p3+(p2-p1);
    Ipeak = [max(I(p1:p2)), abs(min(I(p1:p2)))];
    Vpeak = [max(V(p3:p4)), abs(min(V(p3:p4)))];
    Iamp(ii,1) = mean(Ipeak);
    Vamp(ii,1) = mean(Vpeak);
    Res(ii,2) = Vamp(ii,1)/Iamp(ii,1); % Processed
       results of |Z|

    if ii<1993
        Res(ii,3) = (t1-t3)*2*pi*Res(ii,1); % Processed
           results of Z_theta
    else %f>1e4 Hz
        Res(ii,3) = (tzerosI(ii,2)-tzerosV(ii,2))*2*pi*
           Res(ii,1);
    end
    disp(length(tzerosI)-ii);
end
toc
```

```
clearvars -except I V t tzerosI tzerosI_pos tzerosI0 fs
   ts tzerosV Res Iamp Vamp
save('Processed Results.mat');
```

Bibliography

[1] A. A. Griffith, "The phenomena of rupture and flow in solids," *Philosophical transactions of the royal society of london. Series A, containing papers of a mathematical or physical character*, vol. 221, no. 582-593, pp. 163–198, 1921.

[2] T. M. Buss, J. P. Rouse, C. J. Hyde, and S. D. Garvey, "Development of a technique for the real-time determination of crack geometries in laboratory samples," in *MATEC Web of Conferences*, vol. 165. EDP Sciences, 2018, p. 09004.

[3] A. Campagnolo, G. Meneghetti, F. Berto, and K. Tanaka, "Calibration of the potential drop method by means of electric fe analyses and experimental validation for a range of crack shapes," *Fatigue & Fracture of Engineering Materials & Structures*, vol. 41, no. 11, pp. 2272–2287, 2018.

[4] L. Doremus, Y. Nadot, G. Henaff, C. Mary, and S. Pierret, "Calibration of the potential drop method for monitoring small crack growth from surface anomalies–crack front marking technique and finite element simulations," *International Journal of Fatigue*, vol. 70, pp. 178–185, 2015.

[5] A. Gajji and G. Sasikala, "Potential drop method for online crack length measurement during fracture testing: Development of a correction procedure," *Engineering Fracture Mechanics*, vol. 180, pp. 148–160, 2017.

[6] M. R. Hill and D. H. Stuart, "Direct current potential difference correlation for open-hole, single-crack coupons," *Engineering Fracture Mechanics*, vol. 99, pp. 141–146, 2013.

[7] J. Hosdez, J. Witz, C. Martel, N. Limodin, D. Najjar, E. Charkaluk, P. Osmond, and F. Szmytka, "Fatigue crack growth law identification by digital image correlation and electrical potential method for ductile cast iron," *Engineering Fracture Mechanics*, vol. 182, pp. 577–594, 2017.

[8] J. Jones, "Enhancing the accuracy of advanced high temperature mechanical testing through thermography," *Applied Sciences*, vol. 8, no. 3, p. 380, 2018.

[9] S. Kolitsch, H.-P. Gaenser, and R. Pippan, "Experimental and calculation challenges of crack propagation in notches–from initiation to end of lifetime," *International Journal of Fatigue*, vol. 103, pp. 395–404, 2017.

[10] R. Lancaster, M. Whittaker, K. Perkins, and S. Jeffs, "Prediction of fatigue lives at stress raising features in a high strength steel," *International journal of fatigue*, vol. 59, pp. 301–308, 2014.

[11] Y. Li, F. Gan, Z. Wan, J. Liao, and W. Li, "Novel method for sizing metallic bottom crack depth using multi-frequency alternating current potential drop technique," *Measurement Science Review*, vol. 15, no. 5, p. 268, 2015.

[12] P. Ljustell, "The effect of large scale plastic deformation on fatigue crack length measurement with the potential drop method," *Journal of Testing and Evaluation*, vol. 39, no. 6, pp. 985–1002, 2011.

[13] J. Meriaux, S. Fouvry, K. Kubiak, and S. Deyber, "Characterization of crack nucleation in ta6v under fretting–fatigue loading using the potential drop technique," *International Journal of Fatigue*, vol. 32, no. 10, pp. 1658–1668, 2010.

[14] M. K. Raja, S. Mahadevan, B. Rao, S. Behera, T. Jayakumar, and B. Raj, "Influence of crack length on crack depth measurement by an alternating current potential drop technique," *Measurement Science and Technology*, vol. 21, no. 10, p. 105702, 2010.

[15] Y. P. Singh, M. J. Presby, K. Manigandan, and G. N. Morscher, "Multi-lead direct current potential drop (dcpd) for in-situ health monitoring of ceramic matrix composites," in *Turbo Expo: Power for Land, Sea, and Air*, vol. 51128. American Society of Mechanical Engineers, 2018, p. V006T02A006.

[16] V. Spitas, C. Spitas, and P. Michelis, "A three-point electrical potential difference method for in situ monitoring of propagating mixed-mode cracks at high temperature," *Measurement*, vol. 43, no. 7, pp. 950–959, 2010.

[17] G. Sposito, P. Cawley, and P. B. Nagy, "An approximate model for three-dimensional alternating current potential drop analyses using a commercial finite element code," *NDT & E International*, vol. 43, no. 2, pp. 134–140, 2010.

[18] E. Storgärds and K. Simonsson, "Crack length evaluation for cyclic and sustained loading at high temperature using potential drop," *Experimental Mechanics*, vol. 55, no. 3, pp. 559–568, 2015.

[19] K. Tarnowski, K. Nikbin, D. Dean, and C. Davies, "A unified potential drop calibration function for common crack growth specimens," *Experimental Mechanics*, vol. 58, no. 6, pp. 1003–1013, 2018.

[20] ——, "Improvements in the measurement of creep crack initiation and growth using potential drop," *International Journal of Solids and Structures*, vol. 134, pp. 229–248, 2018.

[21] K. Van Minnebruggen, S. Hertelé, M. A. Verstraete, and W. De Waele, "Crack growth characterization in single-edge notched tension testing by means of direct current potential drop measurement," *International Journal of Pressure Vessels and Piping*, vol. 156, pp. 68–78, 2017.

[22] Y. Si, J. Rouse, and C. Hyde, "Potential difference methods for measuring crack growth: A review," *International Journal of Fatigue*, vol. 136, p. 105624, 2020.

[23] P. McIntyre and A. Priest, "Measurement of sub-critical flaw growth in stress corrosion, cyclic loading and high temperature creep by the dc electrical resistance technique," Tech. Rep., 1971.

[24] Y. Nakai and R. Wei, "Measurement of short crack lengths by an ac potential method," *Engineering fracture mechanics*, vol. 32, no. 4, pp. 581–589, 1989.

[25] K.-H. Schwalbe, D. Hellmann, J. Heerens, J. Knaack, and J. Müller-Roos, "Measurement of stable crack growth including detection of initiation of growth using the dc potential drop and the partial unloading methods," in *Elastic-Plastic Fracture Test Methods: The User's Experience*. ASTM International, 1985.

[26] J. Coffey, "Ultrasonic measurement of crack dimensions in laboratory specimens," in *The Measurement of Crack Length and Shape During Fracture and Fatigue[Proc. Conf.], Birmingham, England, May 1979,*, 1980, pp. 345–386.

[27] L. Satyarnarayan, D. Pukazhendhi, A. Kannan, K. Balasubranianiam, and D. R. Murthy, "Comparative studies on phased array ultrasonic, alternating current potential drop and conventional ultrasonic techniques for detection, monitoring and sizing of circumferential fatigue crack growth in pipes," *Journal of Structural Engineering*, vol. 34, no. 2, pp. 104–110, 2007.

[28] T. Lindley and P. McIntyre, "Application of acoustic emission to crack detection and measurement," in *The Measurement of Crack Length and Shape During Fracture and Fatigue[Proc. Conf.], Birmingham, England, May 1979,*, 1980, pp. 285–344.

[29] J. Mackerle, "Finite-element modelling of non-destructive material evaluation: a bibliography (1976-1997)," *Modelling and Simulation in Materials Science and Engineering*, vol. 7, no. 1, p. 107, 1999.

[30] ——, "Finite-element modelling of non-destructive material evaluation, an addendum: a bibliography (1997–2003)," *Modelling and Simulation in Materials Science and Engineering*, vol. 12, no. 5, p. 799, 2004.

[31] A. Lewis, "Electromagnetic methods for nde of metal fatigue cracks: Practical techniques and theoretical models," *Nondestructive Testing and Evaluation*, vol. 6, no. 6, pp. 389–409, 1992.

[32] W. Dover and C. Monahan, "The measurement of surface breaking cracks by the electrical systems acpd/acfm," *Fatigue & Fracture of Engineering Materials & Structures*, vol. 17, no. 12, pp. 1485–1492, 1994.

[33] W. Dover, R. Collins, and D. Michael, "The use of ac-held measurem ents for crack detection and sizing in air and underwater," *Philosophical Transactions of the Royal Society of London. Series A, Mathematical and Physical Sciences*, vol. 320, no. 1554, pp. 271–283, 1986.

[34] W. Dover, F. Charlesworth, K. Taylor, R. Collins, and D. Michael, "The use of ac field measurements to determine the shape and size of a crack in a metal," in *Eddy-current characterization of materials and structures*. ASTM International, 1981.

[35] D. Michael, R. Waechter, and R. Collins, "The measurement of surface cracks in metals by using ac electric fields," *Proceedings of the Royal Society of London. A. Mathematical and Physical Sciences*, vol. 381, no. 1780, pp. 139–157, 1982.

[36] A. Trost, "Ermittlung von rissen and messung der risstiefen in metallischen werkstoffen durch elektrische spannungsmessung," *Metallwirtschaft*, vol. 23, pp. 308–309, 1944.

[37] T. Venkatsubramanian and B. Unvala, "An ac potential drop system for monitoring crack length," *Journal of physics E: scientific instruments*, vol. 17, no. 9, pp. 765–771, 1984.

[38] R. Wei and R. Brazill, "An assessment of ac and dc potential systems for monitoring fatigue crack growth," in *Fatigue crack growth measurement and data analysis*. ASTM International, 1981.

[39] W. D. Dover, R. Collins, and D. H. Michael, "Review of developments in acpd and acfm," *British Journal of Non-Destructive Testing*, vol. 33, no. 3, pp. 121–127, 1991.

[40] N. Merah, "Detecting and measuring flaws using electric potential techniques," *Journal of Quality in Maintenance Engineering*, vol. 9, no. 2, pp. 160–175, 2003.

[41] G. Sposito, C. Ward, P. Cawley, P. Nagy, and C. Scruby, "A review of non-destructive techniques for the detection of creep damage in power plant steels," *Ndt & E International*, vol. 43, no. 7, pp. 555–567, 2010.

[42] B. Freeman and G. Neate, "The measurement of crack length during fracture at elevated temperatures using the d. c. potential drop technique," 1980.

[43] M. Halliday and C. Beevers, "The d. c. electrical potential method for crack length measurement," in *The Measurement of Crack Length and Shape During Fracture and Fatigue[Proc. Conf.], Birmingham, England, May 1979,*, 1980, pp. 85–112.

[44] G. Klintworth and G. Webster, "Optimization of electrical-potential methods of measuring crack growth," *The Journal of Strain Analysis for Engineering Design*, vol. 14, no. 4, pp. 187–192, 1979.

[45] K. Watt, "A consideration of an a. c. potential drop method for crack length measurement," in *The Measurement of Crack Length and Shape During Fracture and Fatigue[Proc. Conf.], Birmingham, England, May 1979,*, 1980, pp. 202–221.

[46] L. Gandossi, S. Summers, N. Taylor, R. Hurst, B. Hulm, and J. Parker, "The potential drop method for monitoring crack growth in real components subjected to combined fatigue and creep conditions: application of fe techniques for deriving calibration curves," *International journal of pressure vessels and piping*, vol. 78, no. 11-12, pp. 881–891, 2001.

[47] A. Antonarulrajah, V. Ramos, S. Fazluddin, and B. Rand, "Evaluation of the electrical potential drop technique in the determination of crack growth resistance-curves of carbon/carbon composites and carbon bonded refractories," *Journal of materials science*, vol. 40, no. 2, pp. 373–380, 2005.

[48] D. Sidey, *The measurement of crack growth in metals by the electrical potential method.* Univ., Engineering Department, 1973.

[49] R. L. Tregoning, "Feasibility study of alternating current potential drop techniques for elastic-plastic fracture toughness testing," in *Applications of Automation Technology to Fatigue and Fracture Testing and Analysis: Third Volume.* ASTM International, 1997.

[50] M. Vassilaros and E. Hackett, "J-integral r-curve testing of high strength steels utilizing the direct-current potential drop method," in *Fracture Mechanics: Fifteenth Symposium.* ASTM International, 1984.

[51] A. Saxena, "Electrical potential technique for monitoring subcritical crack growth at elevated temperatures," *Engineering Fracture Mechanics*, vol. 13, no. 4, pp. 741–750, 1980.

[52] G. A. Hartman and D. A. Johnson, "Dc electric-potential method applied to thermal/mechanical fatigue crack growth," *Experimental mechanics*, vol. 27, no. 1, pp. 106–112, 1987.

[53] K. Schwalbe and W. Sets, "Application of the potential method and the compliance method for the measurement of r curve," in *The Measurement of Crack Length and Shape During Fracture and Fatigue[Proc. Conf.], Birmingham, England, May 1979,*, 1980.

[54] R. Kažys, A. Voleišis, and B. Voleišienė, "High temperature ultrasonic transducers," *Ultragarsas/Ultrasound*, vol. 63, no. 2, pp. 7–17, 2008.

[55] R. Ritchie, *Crack growth monitoring: some considerations on the electrical potential method.* Cambridge Univ., Department of Metallurgy and Materials Science, 1972.

[56] Y. Lu and J. R. Bowler, "Four-point probe measurements of a direct current potential drop on layered conductive cylinders," *Measurement Science and Technology*, vol. 23, no. 11, p. 115603, 2012.

[57] M. Connolly, D. Michael, and R. Collins, "The inversion of surface potential measurements to determine crack size and shape," *Journal of applied physics*, vol. 64, no. 5, pp. 2638–2647, 1988.

[58] G. Aronson and R. Ritchie, "Optimization of the electrical potential technique for crack growth monitoring in compact test pieces using finite element analysis," *Journal of Testing and Evaluation*, vol. 7, no. 4, pp. 208–215, 1979.

[59] R. Ritchie and K. Bathe, "On the calibration of the electrical potential technique for monitoring crack growth using finite element methods," *International Journal of Fracture*, vol. 15, no. 1, pp. 47–55, 1979.

[60] G. Gille, "Die potentialsondenmethode und ihre anwendung auf die zerstorungsfreie priifung grosset werst (icke," 1956.

[61] B. Thornton and W. Thornton, "The measurement of the thickness of metal walls from one surface only, by an electrical method," *Proceedings of the Institution of Mechanical Engineers*, vol. 140, no. 1, pp. 349–398, 1938.

[62] W. J. Barnett and A. Troiano, "Crack propagation in the hydrogen-induced brittle fracture of steel," *JOM*, vol. 9, no. 4, pp. 486–494, 1957.

[63] P. Irving, J. Robinson, and C. Beevers, "Fatigue crack closure in titanium and titanium alloys," *International Journal of Fracture*, vol. 9, no. 1, pp. 105–108, 1973.

[64] T.-T. Shih and R. P.-y. Wei, "A study of crack closure in fatigue," *Engineering Fracture Mechanics*, vol. 6, no. 1, pp. 19–32, 1974.

[65] P. Irving, J. Robinson, and C. Beevers, "A study of the effects of mechanical and environmental variables on fatigue crack closure," *Engineering Fracture Mechanics*, vol. 7, no. 4, pp. 619–630, 1975.

[66] C. Clarke and G. Cassatt, "A study of fatigue crack closure using electric potential and compliance techniques," *Engineering Fracture Mechanics*, vol. 9, no. 3, pp. 675–688, 1977.

[67] V. Bachmann and D. Munz, "Fatigue crack closure evaluation with the potential method," *Engineering Fracture Mechanics*, vol. 11, no. 1, pp. 61–71, 1979.

[68] M. Lafarie-Frenot and C. Gasc, "On the evaluation of crack closure using the potential drop method," *International Journal of Fracture*, vol. 15, no. 3, pp. R121–R123, 1979.

[69] C. Ward-Close, "A new potential-drop method for the measurement of crack closure," *International Journal of Fracture*, vol. 16, no. 4, pp. R211–R213, 1980.

[70] R. Pippan, G. Haas, and H. Stüwe, "Comparison of two methods to measure crack closure in ultra-high vacuum," *Engineering fracture mechanics*, vol. 34, no. 5-6, pp. 1075–1084, 1989.

[71] M. Andersson, T. Hansson, C. Persson, and S. Melin, "Fatigue crack propagation in ti–6al–4v subjected to high strain amplitudes," *Fatigue & Fracture of Engineering Materials & Structures*, vol. 28, no. 3, pp. 301–308, 2005.

[72] M. Andersson, C. Persson, and S. Melin, "Experimental and numerical investigation of crack closure measurements with electrical potential drop technique," *International journal of fatigue*, vol. 28, no. 9, pp. 1059–1068, 2006.

[73] J. Lowes and G. Featnehough, "The detection of slow crack growth in crack opening displacement specimens using an electrical potential method," *Engineering Fracture Mechanics*, vol. 3, no. 2, pp. 103–104, 1971.

[74] N. Okumura, T. Venkatasubramanian, B. Unvala, and T. Baker, "Application of the ac potential drop technique to the determination of r curves of tough ferritic steels," *Engineering Fracture Mechanics*, vol. 14, no. 3, pp. 617–625, 1981.

[75] A. Bakker, "A dc potential drop procedure for crack initiation and r-curve measurements during ductile fracture tests," in *Elastic-Plastic Fracture Test Methods: The User's Experience*. ASTM International, 1985.

[76] G. Gibson, "The use of alternating current potential drop for determining j-crack resistance curves," *Engineering fracture mechanics*, vol. 26, no. 2, pp. 213–222, 1987.

[77] M. Sakane and M. Ohnami, "Electrical potential drop and notch opening displacement methods for detecting high temperature low cycle fatigue cracks

of circumferential notched specimens," *Journal of Engineering Materials and Technology*, vol. 110, no. 3, pp. 247–252, 1988.

[78] Y. Dai, N. Marchand, and M. Hongoh, "Fatigue crack growth measurements in tmf testing of titanium alloys using an acpd technique," in *Special applications and advanced techniques for crack size determination*. ASTM International, 1995.

[79] N. Merah, T. Bui-Quoc, and M. Bernard, "Calibration of dc potential technique using an optical image processing system in lcf testing," *Journal of testing and evaluation*, vol. 23, no. 3, pp. 160–167, 1995.

[80] M. Whittaker, W. Evans, R. Lancaster, W. Harrison, and P. Webster, "The effect of microstructure and texture on mechanical properties of ti6-4," *International journal of fatigue*, vol. 31, no. 11-12, pp. 2022–2030, 2009.

[81] R. Ritchie, G. Garrett, and J. Knott, "Crack-growth monitoring: optimisation of the electrical potential technique using an analogue method," *International Journal of Fracture Mechanics*, vol. 7, no. 4, p. 462, 1971.

[82] G. Clark and J. Knott, "Measurement of fatigue cracks in notched specimens by means of theoretical electrical potential calibrations," *Journal of the Mechanics and Physics of Solids*, vol. 23, no. 4-5, pp. 265–276, 1975.

[83] N. Merah, "Dc potential drop calibration in creep-fatigue loading conditions," *Journal of testing and evaluation*, vol. 28, no. 4, pp. 301–306, 2000.

[84] I. Vasatis and R. Pelloux, "Application of the dc potential drop technique in investigating crack initiation and propagation under sustained load in notched rupture tests," *Metallurgical Transactions A*, vol. 19, no. 4, pp. 863–871, 1988.

[85] N. Tada, T. Kitamura, R. Ohtani, and E. Nakayama, "Evolution of creep-fatigue damage in type 304 stainless steel and its detection by electrical potential method," *Acta Metallurgica Sinica(English Letters*, vol. 11, no. 6, pp. 463–469, 1998.

[86] E. Madhi and P. B. Nagy, "Sensitivity analysis of a directional potential drop sensor for creep monitoring," *Ndt & E International*, vol. 44, no. 8, pp. 708–717, 2011.

[87] J. Corcoran, P. Nagy, and P. Cawley, "Monitoring creep damage at a weld using a potential drop technique," *International Journal of Pressure Vessels and Piping*, vol. 153, pp. 15–25, 2017.

[88] H. Johnson and A. Willner, "Moisture and stable crack growth in a high strength steel," *Applied Materials Research*, vol. 4, no. 1, pp. 35–40, 1965.

[89] E. Hackett, P. Moran, and J. Gudas, "Evaluation of environmentally assisted cracking of a high strength steel using elastic-plastic fracture mechanics techniques," in *Fracture Mechanics: Seventeenth Volume*. ASTM International, 1986.

[90] E. Santos-Leal and R. J. Lopez, "Simultaneous measurement of acoustic emission and electrical resistance variation in stress-corrosion cracking," *Measurement Science and Technology*, vol. 6, no. 2, p. 188, 1995.

[91] G. Hancock and H. Johnson, "Subcritical crack growth in am 350 steel," *Mater Res Stand*, vol. 6, no. 9, pp. 431–435, 1966.

[92] C. Stubbington and S. Pearson, "Effect of dwell on the growth of fatigue cracks in ti-6al-4v alloy bar," *Engineering Fracture Mechanics*, vol. 10, no. 4, pp. 723–756, 1978.

[93] R. Gardiner, "The detection of crack growth during sustained load cracking of ti-6al-4v alloy bar," in *The Measurement of Crack Length and Shape During Fracture and Fatigue[Proc. Conf.], Birmingham, England, May 1979,*, 1980.

[94] J. Lee, M. Saka, and H. Abé, "Loading effect on acpd of a crack in ferromagnetic material," *Experimental mechanics*, vol. 37, no. 2, pp. 132–136, 1997.

[95] N. Bowler, "Electric field due to alternating current injected at the surface of a metal plate," *Journal of applied physics*, vol. 96, no. 8, pp. 4607–4613, 2004.

[96] ——, "Analytical solution for the electric field in a half space conductor due to alternating current injected at the surface," *Journal of applied physics*, vol. 95, no. 1, pp. 344–348, 2004.

[97] N. Bowler and Y. Huang, "Model-based characterization of homogeneous metal plates by four-point alternating current potential drop measurements," *IEEE transactions on magnetics*, vol. 41, no. 6, pp. 2102–2110, 2005.

[98] N. Bowler, "Theory of four-point alternating current potential drop measurements on a metal half-space," *Journal of Physics D: Applied Physics*, vol. 39, no. 3, p. 584, 2006.

[99] J. R. Bowler and N. Bowler, "Theory of four-point alternating current potential drop measurements on conductive plates," *Proceedings of the Royal Society A: Mathematical, Physical and Engineering Sciences*, vol. 463, no. 2079, pp. 817–836, 2007.

[100] J. R. Bowler, Y. Huang, H. Sun, J. Brown, and N. Bowler, "Alternating current potential-drop measurement of the depth of case hardening in steel rods," *Measurement Science and Technology*, vol. 19, no. 7, p. 075204, 2008.

[101] Y. Lu, N. Bowler, J. R. Bowler, and Y. Huang, "Edge effects in four-point direct current potential drop measurements on metal plates," *Journal of Physics D: Applied Physics*, vol. 42, no. 13, p. 135004, 2009.

[102] D. Pulle, "Crack length measurement: Analysis of the electropotential method using a finite element method," *The Journal of Strain Analysis for Engineering Design*, vol. 21, no. 3, pp. 127–134, 1986.

[103] D. T. Read and M. Pfuff, "Potential drop in the center-cracked panel with asymmetric crack extension," *International journal of fracture*, vol. 48, no. 3, pp. 219–229, 1991.

[104] P. C. McKeighan, W.-X. Zhu, and D. J. Smith, "A full field dc potential drop calibration for an asymmetrically cracked m (t) specimen," *Journal of testing and evaluation*, vol. 23, no. 2, pp. 102–110, 1995.

[105] K. Ohji, S. Kubo, and T. Sakagami, "Electric potential ct method for measuring location and size of two-and three-dimensional cracks (development of boundary element inverse analysis method for electric potential problems and its application to non-destructive crack measurement)," *Trans. Jpn. Soc. Mech. Eng., Ser. A*, vol. 51, pp. 1818–1827, 1985.

[106] T. SAKAGAMI, S. KUBO, T. HASHIMOTO, H. YAMAWAKI, and K. OHOJI, "Quantitative measurement of two-dimensional inclined cracks by the electric-potential ct method with multiple current applications," *JSME international journal. Ser. 1, Solid mechanics, strength of materials*, vol. 31, no. 1, pp. 76–86, 1988.

[107] N. Tada, "Monitoring of a surface crack in a finite body by means of electrical potential technique," *International Journal of fracture*, vol. 57, no. 3, pp. 199–220, 1992.

[108] R. Ghajarieh, M. Saka, T. Sugawara, H. Abe, I. Komura, and H. Sakamoto, "Nde of multiple cracks on the surface of materials by means of the potential drop technique," *NDT & E International*, vol. 27, no. 3, pp. 143–150, 1994.

[109] R. Ghajarieh, M. Saka, H. Abe, I. Komura, and H. Sakamoto, "Simplified nde of multiple cracks by means of the potential drop technique," *NDT & E International*, vol. 28, no. 1, pp. 23–28, 1995.

[110] N. Tada, Y. Hayashi, T. Kitamura, and R. Ohtani, "Analysis of direct current potential field around multiple random cracks," *International journal of fracture*, vol. 75, no. 1, pp. 69–84, 1996.

[111] ——, "Analysis on the applicability of direct current electrical potential method to the detection of damage by multiple small internal cracks," *International Journal of Fracture*, vol. 85, no. 1, pp. 1–9, 1997.

[112] H. Liu, M. Saka, H. Abe', I. Komura, and H. Sakamoto, "Analysis of interaction of multiple cracks in a direct current field and nondestructive evaluation," *Journal of applied mechanics*, vol. 66, no. 2, pp. 468–475, 1999.

[113] N. Tada, E. Nakayama, T. Kitamura, and R. Ohtani, "Analysis of direct current potential field around multiple spherical defects," *JSME International Journal Series A Solid Mechanics and Material Engineering*, vol. 43, no. 2, pp. 109–116, 2000.

[114] R. Ghajar, "Crack interaction in nde of multiple cracks by means of potential drop technique," *NDT & E International*, vol. 36, no. 8, pp. 581–585, 2003.

[115] ——, "An alternative method for crack interaction in nde of multiple cracks by means of potential drop technique," *NDT & E International*, vol. 37, no. 7, pp. 539–544, 2004.

[116] N. Tada, "Evaluation of the distribution of multiple circular cracks with random radii and angles by direct current electrical potential difference method," *International journal of fracture*, vol. 141, no. 1, pp. 49–62, 2006.

[117] M. Ritter and R. Ritchie, "On the calibration, optimization and use of dc electrical potential methods for monitoring mode iii crack growth in torsionally-loaded samples," *Fatigue & Fracture of Engineering Materials & Structures*, vol. 5, no. 1, pp. 91–99, 1982.

[118] V. Spitas, C. Spitas, and P. Michelis, "Real-time measurement of shear fatigue crack propagation at high-temperature using the potential drop technique," *Measurement*, vol. 41, no. 4, pp. 424–432, 2008.

[119] R. Smith, "Calibrations for the electrical potential method of crack growth measurement by a direct electrical analogy," *Strain*, vol. 10, no. 4, pp. 183–187, 1974.

[120] R. Smith and A. Cameron, "A three dimensional wax analogue for the calibration of the electrical potential technique of crack growth monitoring," in *Fracture 84*. Elsevier, 1984, pp. 3371–3376.

[121] W.-H. Chen, J.-S. Chen, and H.-L. Fang, "A theoretical procedure for detection of simulated cracks in a pipe by the direct current–potential drop technique," *Nuclear engineering and design*, vol. 216, no. 1-3, pp. 203–211, 2002.

[122] N. Tada, M. Uchida, A. Funakoshi, and H. Ishikawa, "Experimental study of three-dimensional identification of semi-elliptical crack on the back surface by means of direct-current electrical potential difference method of multiple-point measurement type," *Journal of pressure vessel technology*, vol. 133, no. 1, 2011.

[123] K. Tarnowski, D. Dean, K. Nikbin, and C. Davies, "Predicting the influence of strain on crack length measurements performed using the potential drop method," *Engineering Fracture Mechanics*, vol. 182, pp. 635–657, 2017.

[124] M. Hicks and A. Pickard, "A comparison of theoretical and experimental methods of calibrating the electrical potential drop technique for crack length determination," *International Journal of Fracture*, vol. 20, no. 2, pp. 91–101, 1982.

[125] W. Soboyejo, R. Reed, and J. Knott, "On the calibration of the direct current potential difference method for the determination of semi-elliptical crack lengths," *International journal of fracture*, vol. 44, no. 1, pp. 27–41, 1990.

[126] I. Hwang, "A multi-frequency ac potential drop technique for the detection of small cracks," *Measurement Science and Technology*, vol. 3, no. 1, pp. 62–74, 1992.

[127] G. Belloni, E. Gariboldi, A. L. Conte, M. Tono, and P. Speranzoso, "On the experimental calibration of a potential drop system for crack length measurements in a compact tension specimen," *Journal of testing and evaluation*, vol. 30, no. 6, pp. 461–469, 2002.

[128] K. Yu, S. Nahm, and Y. Kim, "Toughness degradation evaluation of 1cr-1mo-0.25 v steel by electrical resistivity," *Journal of materials science letters*, vol. 18, no. 14, pp. 1175–1176, 1999.

[129] A. A. Anctil, E. B. Kula, and E. DiCesare, "Electric-potential technique for determining slow crack growth," ARMY MATERIALS RESEARCH AGENCY WATERTOWN MA, Tech. Rep., 1963.

[130] N. Micone and W. De Waele, "On the application of infrared thermography and potential drop for the accelerated determination of an sn curve," *Experimental Mechanics*, vol. 57, no. 1, pp. 143–153, 2017.

[131] H. Johnson, "Calibrating the electric potential method for studying slow crack growth," *Materials Research and Standards*, vol. 5, no. 1, pp. 442–445, 1965.

[132] W. Wilson, "On the electrical potential analysis of a cracked fracture mechanics test specimen using the finite element method," *Engineering Fracture Mechanics*, vol. 18, no. 2, pp. 349–358, 1983.

[133] J. Gu and L. Yu, "The influence of geometric factors on crack depth measurement using the potential drop technique," *NDT international*, vol. 23, no. 3, pp. 161–164, 1990.

[134] I. Verpoest, E. Aernoudt, A. Deruyttere, and M. Neyrinck, "An improved ac potential drop method for detecting surface microcracks during fatigue tests of unnotched specimens," *Fatigue & Fracture of Engineering Materials & Structures*, vol. 3, no. 3, pp. 203–217, 1980.

[135] S. Tiku, N. J. Marchand, and B. Unvala, "An advanced multiple frequency acpd system for crack detection and calibration," in *Nontraditional methods of sensing stress, strain, and damage in materials and structures*.   ASTM International, 1997.

[136] V. Bachmann and D. Munz, "Unusual potential drop during the application of the electrical potential method in a fracture mechanics test," *Journal of Testing and Evaluation*, vol. 4, no. 4, pp. 257–260, 1976.

[137] I. Cerny, M. Kneifl, and V. Linhart, "Measurement of crack length and profile in thick specimens and components using modified dcpd method," *WIT Transactions on Engineering Sciences*, vol. 19, 1998.

[138] B. Kluttig, H. Steinmill, W. Stoppler, and H. Keller, "Crack growth measurements on components under cyclic loading: comparison of different methods," *Nuclear Engineering and Design*, vol. 151, no. 2, pp. 523–530, 1994. [Online]. Available: https://www.sciencedirect.com/science/article/pii/0029549394901937

[139] J. Davies, D. Cannon, and R. J. Allen, "Measurements of electrical potential for detecting crack extension in cod tests," *Nature*, vol. 225, no. 5239, pp. 1240–1242, 1970.

[140] Z.-J. Lu, P. Nicholas, and W. Evans, "Calibration of an acpd monitoring system for small crack growth in corner crack specimens," *Engineering fracture mechanics*, vol. 50, no. 4, pp. 443–456, 1995.

[141] R. Wei and R. Brazill, "An a. c. potential system for crack length measurement," in *The Measurement of Crack Length and Shape During Fracture and Fatigue[Proc. Conf.], Birmingham, England, May 1979,*, 1980, pp. 190–201.

[142] Ø. Persvik and J. R. Bowler, "Evaluation of four-point transient potential drop on conductive plates," *Applied Physics Letters*, vol. 110, no. 8, p. 084102, 2017.

[143] S. S. Rao, M. Liu, F. Peng, B. Zhang, and H. Zhao, "Signal sensitivity of alternating current potential drop measurement for crack detection of

conductive substrate with tunable coating materials through finite element modeling," *Measurement Science and Technology*, vol. 27, no. 12, p. 125004, 2016.

[144] E. C. Jordan, *Electromagnetic waves and radiating systems / Edward C. Jordan, Keith G. Balmain.*, 2nd ed., ser. Prentice-Hall electrical engineering series.   Englewood Cliffs, N.J.: Prentice-Hall, 1968.

[145] I. S. Grant and W. R. Phillips, *Electromagnetism.*   John Wiley & Sons, 2013.

[146] H. Saguy and D. Rittel, "Alternating current flow in internally flawed conductors: A tomographic analysis," *Applied physics letters*, vol. 89, no. 9, p. 094102, 2006.

[147] E. Madhi, G. Sposito, C. Davies, P. Cawley, and P. Nagy, "In-situ creep monitoring using the potential drop method," in *AIP Conference Proceedings*, vol. 1335, no. 1.   American Institute of Physics, 2011, pp. 1631–1638.

[148] S. Prajapati, P. B. Nagy, and P. Cawley, "Potential drop detection of creep damage in the vicinity of welds," *NDT & E International*, vol. 47, pp. 56–65, 2012.

[149] J. Corcoran, P. Hooper, C. Davies, P. B. Nagy, and P. Cawley, "Creep strain measurement using a potential drop technique," *International Journal of Mechanical Sciences*, vol. 110, pp. 190–200, 2016.

[150] M. S. Loveday, M. F. Day, and B. F. Dyson, "Measurement of high temperature mechanical properties of materials: Based on the edited proceedings of a symposium held from 3–5 june 1981 at the national physical laboratory, teddington, england."   H.M.S.O., London, UK, 1982, pp. 58–82.

[151] K. Ikeda, M. Yoshimi, and C. Miki, "Electrical potential drop method for evaluating crack depth," *International Journal of Fracture*, vol. 47, no. 1, pp. 25–38, 1991.

[152] H.-M. Bauschke and K.-H. Schwalbe, "Measurement of the depth of surface cracks using the direct current potential drop method," *Materialwissenschaft und Werkstofftechnik*, vol. 16, no. 5, pp. 156–165, 1985.

[153] H. Saguy and D. Rittel, "Flaw detection in metals by the acpd technique: Theory and experiments," *NDT & E International*, vol. 40, no. 7, pp. 505–509, 2007.

[154] I. Austen and E. Walker, "Calibration of the electrical resistance technique for crack growth monitoring in cks type test pieces," *BSC Tech. Rep.*, p. PMC/6795/6/76/B, 1976.

[155] D. Green, J. Kendall, and J. Knott, "Analytic and analogue techniques for determining potential distributions around angled cracks," *International journal of fracture*, vol. 37, no. 1, pp. R3–R12, 1988.

[156] M. Enmark, G. Lucas, and G. Odette, "An electric potential drop technique for characterizing part-through surface cracks," *Journal of nuclear materials*, vol. 191, pp. 1038–1041, 1992.

[157] C. Gilbert, J. McNaney, R. Dauskardt, and R. Ritchie, "Back-face strain compliance and electrical-potential crack length calibrations for the disk-shaped compact-tension dc (t) specimen," *Journal of testing and evaluation*, vol. 22, no. 2, pp. 117–120, 1994.

[158] J. Liu and P. Bowen, "Dc potential drop calibration in matrix-cladded ti mmc specimens with a corner notch," *International journal of fatigue*, vol. 25, no. 7, pp. 671–676, 2003.

[159] S. Na, D. Yoon, J. Kim, H. Kim, and D. Kim, "An evaluation of the fatigue crack propagation rate for powder metallurgical nickel-based superalloys using the dcpd method at elevated temperatures," *International Journal of Fatigue*, vol. 101, pp. 27–35, 2017.

[160] D. Gilbey and S. Pearson, "Measurement of the length of a central or edge crack in a sheet of metal by an electrical resistance method," *RAE Technical Report No. 66402*, 1966.

[161] J. Knott, "The use of analogue and mapping techniques with particular reference to detection of short cracks," in *The Measurement of Crack Length and Shape During Fracture and Fatigue[Proc. Conf.], Birmingham, England, May 1979,*, 1980, pp. 113–135.

[162] C.-Y. Li and R. Wei, "Calibrating the electrical potential method for studying slow crack growth(electric potential method used to study slow crack growth in center-notched plate specimens)," *Materials Research and Standards*, vol. 6, pp. 392–394, 1966.

[163] K.-H. Schwalbe and D. Hellmann, "Application of the electrical potential method to crack length measurements using johnson's formula," *Journal of Testing and Evaluation*, vol. 9, no. 3, pp. 218–220, 1981.

[164] G. Baudin and H. Policella, "Progress in potential drop technique- application to three-dimensional crack fronts," *ONERA, TP no. 1981-14, 1981. 9 p*, 1981.

[165] F. Riemelmoser, R. Pippan, H. Weinhandl, and O. Kolednik, "The influence of irregularities in the crack shape on the crack extension measurement by

means of the direct-current-potential-drop method," *Journal of testing and evaluation*, vol. 27, no. 1, pp. 42–46, 1999.

[166] P. C. McKeighan and D. J. Smith, "Determining the potential drop calibration of a fatigue crack growth specimen subject to limited experimental observations," *Journal of testing and evaluation*, vol. 22, no. 4, pp. 291–301, 1994.

[167] E. Hay and M. Brown, "A dc potential drop method to monitor crack growth in notches subjected to torsion," *Fatigue & Fracture of Engineering Materials & Structures*, vol. 4, no. 3, pp. 287–290, 1981.

[168] C. You, "Electric tank simulation of the potential drop technique for crack length determinations," *International Journal of Fracture*, vol. 23, pp. R139–R141, 1983.

[169] M. E. Orazem, "Calculation of the electrical resistance of a compact tension specimen for crack-propagation measurements," *Journal of the Electrochemical Society*, vol. 132, no. 9, pp. 2071–2076, 1985.

[170] M. E. Orazem and W. Ruch, "An improved analysis of the potential drop method for measuring crack lengths in compact tension specimens," *International journal of fracture*, vol. 31, no. 4, pp. 245–258, 1986.

[171] O. Hiroshi, Z. Wei, S. N. Atluri, and S. Sampath, "A computational approach to determining the depth of surface flaws by the acpd technique," *Engineering fracture mechanics*, vol. 43, no. 6, pp. 911–921, 1992.

[172] D. Harrington, R. Bell, and C. Tan, "Calibration of the localized dcpd method for crack shape measurement using the boundary element method," *Fatigue & Fracture of Engineering Materials & Structures*, vol. 18, no. 7-8, pp. 875–884, 1995.

[173] C. Aliberti, N. Fokas, and Y. Lee, "Multi-parametric sensitivity analysis of an electrical potential difference gear crack sensor using finite elements," *International Journal of Mechanical Engineering and Robotics Research*, vol. 6, no. 4, pp. 272–278, 2017.

[174] G. Garrett, Ph.D. dissertation, University of Cambridge, 1973.

[175] I. Austen, "Measurement of crack length and data analysis in corrosion fatigue." in *n The Measurement of Crack Length and Shape During Fracture and Fatigue[Proc. Conf.], Birmingham, England, May 1979.*, 1980, pp. 164–179.

[176] Y. Iwamura and K. Miya, "Numerical approach to inverse problem of crack shape recognition based on the electrical potential method (of ndt)," *IEEE transactions on magnetics*, vol. 26, no. 2, pp. 618–621, 1990.

234

[177] Y. Hashimoto, Y. Urabe, S. Masamori, Y. Kamiwaki, and K. Baba, "Procedure of crack shape determination by reversing dc potential method," *Nuclear engineering and design*, vol. 138, no. 3, pp. 259–268, 1992.

[178] Y. Sato, T. Atsumi, and T. Shoji, "Application of induced current potential drop technique for measurements of cracks on internal wall of tube-shaped specimens," *NDT & E International*, vol. 40, no. 7, pp. 497–504, 2007.

[179] H. Abé, M. Saka, T. Wachi, and Y. Kanoh, "An inverse problem in nondestructive inspection of a crack in a hollow cylinder by means of electrical potential method," in *Computational Mechanics' 88*. Springer, 1988, pp. 342–345.

[180] H. Abé and Y. Kanoh, "An inverse problem in nondestructive inspection of a crack in a plate with an inhomogeneity by means of the electrical potential method," in *Micromechanics and Inhomogeneity*. Springer, 1990, pp. 1–15.

[181] N. Tada, M. Okada, and J. Iwamoto, "Three-dimensional identification of semi-elliptical surface crack by means of direct-current electrical potential difference method with multiple-probe sensor," *Journal of Pressure Vessel Technology*, vol. 129, no. 3, pp. 441–448, 2007.

[182] N. Tada and A. Funakoshi, "Three-dimensional identification of semi-elliptical crack on the back surface by means of direct-current electrical potential difference method with multiple-probe sensor (pvp2006-icpvt-11-93359)," *Journal of Pressure Vessel Technology*, vol. 131, no. 2, 2009.

[183] D. Harrington and R. Bell, "A mobile dcpd probe arrangement for improved crack profile measurements," *British Journal of Non-Destructive Testing*, vol. 35, no. 9, pp. 497–501, 1993.

[184] I. Černỳ, "The use of dcpd method for measurement of growth of cracks in large components at normal and elevated temperatures," *Engineering Fracture Mechanics*, vol. 71, no. 4-6, pp. 837–848, 2004.

[185] F. Takeo, M. Saka, S. R. Ahmed, S. Hamada, and M. Hayakawa, "Selecting suitable probes distances for sizing deep surface cracks using the dcpd technique," *Journal of Pressure Vessel Technology*, vol. 129, no. 1, pp. 205–210, 2007.

[186] A. Tumanov, V. Shlyannikov, and J. C. Kishen, "An automatic algorithm for mixed mode crack growth rate based on drop potential method," *International Journal of Fatigue*, vol. 81, pp. 227–237, 2015.

[187] Y. Dai, N. Marchand, and M. Hongoh, "Study of fatigue crack initiation and growth in titanium alloys using an acpd technique," *Canadian aeronautics and space journal*, vol. 39, no. 1, pp. 35–44, 1993.

[188] C. Omprakash, B. Srivathsa, M. Kamaraj, and D. Satyanarayana, "Creep damage evaluation of ds cm247 nickel base superalloy using alternate current potential drop technique," *Transactions of the Indian Institute of Metals*, vol. 69, no. 2, pp. 241–245, 2016.

[189] Y. J. Oh, J. H. Kim, and I. S. Hwang, "Dynamic loading fracture tests of ferritic steel using the direct current potential drop method," *Journal of testing and evaluation*, vol. 30, no. 3, pp. 221–227, 2002.

[190] N. Ida, *Engineering electromagnetics / Nathan Ida.*, 3rd ed. Cham: Springer, 2015.

[191] D. K. D. K. Cheng, *Field and wave electromagnetics / David K. Cheng.*, 2nd ed., ser. Addison-Wesley series in electrical engineering. Reading, Mass. ; Wokingham: Addison-Wesley, 1989.

[192] D. D. E. Dugdale, *Essentials of electromagnetism / David Dugdale.*, ser. Macmillan physical science series. Basingstoke: Macmillan, 1993.

[193] P. Silvester, *Modern Electromagnetic Fields*, ser. Microwaves and fields series. Prentice-Hall, 1968. [Online]. Available: https://books.google.co.uk/books?id=ViNRAAAAMAAJ

[194] A. E. Kennelly, F. A. Laws, and P. H. Pierce, "Experimental researches on skin effect in conductors," *Transactions of the American Institute of Electrical Engineers*, vol. 34, no. 2, pp. 1953–2021, 1915.

[195] A. Kennelly and H. Affel, "Skin-effect resistance measurements of conductors, at radio-frequencies up to 100,000 cycles per second," *Proceedings of the Institute of Radio Engineers*, vol. 4, no. 6, pp. 523–574, 1916.

[196] H. B. Dwight, "Skin effect in tubular and flat conductors," *Transactions of the American Institute of Electrical Engineers*, vol. 37, no. 2, pp. 1379–1403, 1918.

[197] ——, "Skin effect and proximity effect in tubular conductors," *Transactions of the American Institute of Electrical Engineers*, vol. 41, pp. 189–198, 1922.

[198] H. Forbes and L. Gorman, "Skin effect in rectangular conductors," *Electrical Engineering*, vol. 52, no. 9, pp. 636–639, 1933.

[199] S. Haefner, "Alternating-current resistance of rectangular conductors," *Proceedings of the Institute of Radio Engineers*, vol. 25, no. 4, pp. 434–447, 1937.

[200] J. D. Cockcroft, "Skin effect in rectangular conductors at high frequencies," *Proceedings of the Royal Society of London. Series A, Containing Papers*

236

of a Mathematical and Physical Character, vol. 122, no. 790, pp. 533–542, 1929.

[201] H. A. Wheeler, "Formulas for the skin effect," *Proceedings of the IRE*, vol. 30, no. 9, pp. 412–424, 1942.

[202] C. Hoer and Y. Love, "Exact inductance equations for rectangular conductors with applications to more compli-cated geometries," *J. Res. Nat. Bureau Standards-C. Eng. Instrum.*, vol. 69, no. 2, pp. 127–137, 1965.

[203] A. E. Ruehli, "Inductance calculations in a complex integrated circuit environment," *IBM journal of research and development*, vol. 16, no. 5, pp. 470–481, 1972.

[204] W. Weeks, L.-H. Wu, M. McAllister, and A. Singh, "Resistive and inductive skin effect in rectangular conductors," *IBM Journal of Research and Development*, vol. 23, no. 6, pp. 652–660, 1979.

[205] P. Silvester, "Modal network theory of skin effect in flat conductors," *Proceedings of the IEEE*, vol. 54, no. 9, pp. 1147–1151, 1966.

[206] ——, "Ac resistance and reactance of isolated rectangular conductors," *IEEE Transactions on Power Apparatus and Systems*, no. 6, pp. 770–774, 1967.

[207] ——, "The accurate calculation of skin effect in conductors of complicated shape," *IEEE transactions on Power Apparatus and Systems*, no. 3, pp. 735–742, 1968.

[208] ——, "Skin effect in multiple and polyphase conductors," *IEEE Transactions on Power Apparatus and Systems*, no. 3, pp. 231–238, 1969.

[209] P. Waldow and I. Wolff, "The skin-effect at high frequencies," *IEEE Transactions on Microwave Theory and Techniques*, vol. 33, no. 10, pp. 1076–1082, 1985.

[210] ——, "Dual bounds variational formulation of skin effect problems," in *1987 IEEE MTT-S International Microwave Symposium Digest*, vol. 1.   IEEE, 1987, pp. 333–336.

[211] G. Costache, "Finite element method applied to skin-effect problems in strip transmission lines," *IEEE transactions on microwave theory and techniques*, vol. 35, no. 11, pp. 1009–1013, 1987.

[212] M. J. Tsuk and J. A. Kong, "A hybrid method for the calculation of the resistance and inductance of transmission lines with arbitrary cross sections," *IEEE Transactions on microwave Theory and Techniques*, vol. 39, no. 8, pp. 1338–1347, 1991.

[213] S. Ramo, *Fields and waves in communication electronics / Simon Ramo, John R. Whinnery, Theodore Van Duzer.*, 3rd ed. New York: Wiley, 1994.

[214] C. R. Paul, *Analysis of multiconductor transmission lines.* John Wiley & Sons, 2007.

[215] M. S. Raven, "Experimental measurements of the skin effect and internal inductance at low frequencies," *Acta Technica*, vol. 60, no. 1, 2015.

[216] W. Heinrich, "Comments on" internal impedance of conductors of rectangular cross section"," *IEEE Transactions on Microwave Theory and Techniques*, vol. 49, no. 3, pp. 580–581, 2001.

[217] F. Medina, R. Marques, G. Antonini, A. Orlandi, and C. Paul, "Comments on" internal impedance of conductors of rectangular cross section"[and author's reply]," *IEEE Transactions on Microwave Theory and Techniques*, vol. 49, no. 8, pp. 1511–1513, 2001.

[218] G. Antonini, A. Orlandi, and C. R. Paul, "Internal impedance of conductors of rectangular cross section," *IEEE Transactions on Microwave Theory and Techniques*, vol. 47, no. 7, pp. 979–985, 1999.

[219] M. Matsuki and A. Matsushima, "Improved numerical method for computing internal impedance of a rectangular conductor and discussions of its high frequency behavior," *Progress In Electromagnetics Research M*, vol. 23, pp. 139–152, 2012.

[220] A. Hu, W. Ma, and Z. Zhao, "New numerical methods of computing internal inductance of conductors of rectangular cross section," in *2008 Asia-Pacific Symposium on Electromagnetic Compatibility and 19th International Zurich Symposium on Electromagnetic Compatibility.* IEEE, 2008, pp. 674–677.

[221] T. Schellenberg, G. Xu, M. El-Arabied, and M. Schneider, "Accelerated methods for computing internal inductances of rectangular conductors," in *International Symposium on Electromagnetic Compatibility-EMC EUROPE.* IEEE, 2012, pp. 1–6.

[222] A. Rong and A. C. Cangellaris, "Note on the definition and calculation of the per-unit-length internal impedance of a uniform conducting wire," *IEEE transactions on electromagnetic compatibility*, vol. 49, no. 3, pp. 677–681, 2007.

[223] T. Demeester and D. De Zutter, "Internal impedance of composite conductors with arbitrary cross section," *IEEE transactions on electromagnetic compatibility*, vol. 51, no. 1, pp. 101–107, 2009.

[224] Y. Zhilichev, "Ac field and impedance of short cylindrical conductors," *IEEE transactions on applied superconductivity*, vol. 23, no. 4, pp. 8 201 810–8 201 810, 2013.

[225] A. Payne. Skin effect, proximity effect and the resistance of circular and rectangular conductors. [Online]. Available: https://www.researchgate.net/publication/ 351306996_SKIN_EFFECT_PROXIMITY_EFFECT_AND_THE_ RESISTANCE_OF_CIRCULAR_AND_RECTANGULAR_CONDUCTORS

[226] ——. The ac resistance of rectangular conductors. [Online]. Available: https://www.researchgate.net/publication/351307928_THE_AC_ RESISTANCE_OF_RECTANGULAR_CONDUCTORS

[227] J. J. Thomson, *Notes on recent researches in electricity and magnetism: intended as a sequel to Professor Clerk-Maxwell's Treatise on electricity and magnetism.* Clarendon Press, 1893.

[228] F. E. Terman. McGraw-Hill, New York, 1943.

[229] S. Ramo, J. R. Whinnery, and T. Van Duzer, *Fields and waves in communication electronics.* John Wiley & Sons, 2008.

[230] M. A. Heald and J. B. Marion, *Classical electromagnetic radiation.* Courier Corporation, 2012.

[231] N. W. McLachlan, "Bessel functions for engineers," 1955.

[232] G. N. Watson, "A treatise on the theory of bessel functions," 1966.

[233] S. Butterworth, "Iii. eddy-current losses in cylindrical conductors, with special applications to the alternating current resistances of short coils," *Philosophical Transactions of the Royal Society of London. Series A, Containing Papers of a Mathematical or Physical Character*, vol. 222, no. 594-604, pp. 57–100, 1922.

[234] ——, "On the alternating current resistance of solenoidal coils," *Proceedings of the Royal Society of London. Series A, Containing Papers of a Mathematical and Physical Character*, vol. 107, no. 744, pp. 693–715, 1925.

[235] *ANSYS Maxwell 3D Field Simulator v15 User's Guide*, ANSYS Inc., Southpointe, 275 Technology Drive, Canonsburg, PA 15317, 2012.

[236] C. Moosbrugger, *ASM ready reference: electrical and magnetic properties of metals.* Asm International, 2000. [Online]. Available: https://app.knovel.com/hotlink/toc/id:kpASMRREMQ/ asm-ready-reference-electrical/asm-ready-reference-electrical

[237] E. U. Condon and H. Odishaw, *Handbook of Physics.* New York, McGraw-Hill, 1958.